The University of
Nottingham

UNITED KINGDOM · CHINA · MALAYSIA

Ainslie-Malik, Gregory R. (2013) Mathematical analysis of PWM processes. PhD thesis, University of Nottingham.

Access from the University of Nottingham repository:
http://eprints.nottingham.ac.uk/13021/1/Mathematical_Analysis_of_PWM_Processes.pdf

Mathematical Analysis of PWM Processes

Gregory R. Ainslie-Malik, MMath.

Thesis submitted to The University of Nottingham
for the degree of Doctor of Philosophy

July 2013

Abstract

Pulse width modulation (PWM) inverters convert a direct current (DC) power supply to an alternating current (AC) supply by means of high frequency switching between two DC sources. Undesirable high-frequency components are generated in the frequency spectra of the voltages and currents of PWM inverters. The high-frequency components are ultimately removed from the input and output waveforms by filters. PWM inverters are used in a wide variety of electrical devices, ranging from microwave ovens to the electrical parts of aircraft. In many of these devices, minimising the size and weight of the electrical parts is important, and, consequently, it is desirable to design efficient filters for PWM inverters. Identification of the unwanted high-frequency components allows for optimal filter design.

In this thesis we use alternative methods to calculate the voltages and currents of PWM inverters. Mathematical models are developed for several PWM inverter designs, and Fourier analysis of the mathematical expressions for the currents and voltages allow us to determine frequency spectra. The methods used in this thesis are shown to be more suitable to the calculation of spectra for complex inverter designs, compared to conventional techniques. In particular, input current spectra are calculated for PWM inverters that incorporate dead time and space vector modulation (SVM) inverters for the first time here.

Acknowledgements

I would like to thank all the people who have put up with my rambling thoughts and long-winded explanations during the course of my PhD. In particular I would like to extend my gratitude to Dr. Steve Cox and Dr. Stephen Creagh for their excellent support and guidance, and without whom this thesis would not have been possible. Indeed, if it weren't for Dr. Cox (and his vast array of coloured pens) I would never have had the opportunity to study for a PhD.

My acknowledgements also go out to the academic, administrative and technical support from the School of Mathematical Sciences and staff at the University of Nottingham. I would also like to acknowledge the EPSRC for providing the financial support for this research.

I would also like to thank all the friends and family, new and old, that have kept me entertained for the duration of my research. Hopefully I won't bore you with any more maths stories. Finally, and above all else, I would like reserve special thanks for my fiancée Bex, who has made my PhD the most worthwhile experience of my life.

Contents

1

INTRODUCTION

Conversion from a *direct current* (DC) power supply to an *alternating current* (AC) power supply is required in many applications. For example, wind turbines and fuel cells generate DC power supplies (see [91] and [82], respectively), but most household electrical devices require an AC power supply [84].

An electrical device that converts a DC supply to an AC supply is called an *inverter* [92]. As described in [49], in modern inverters, there are two DC sources of prescribed voltages. An AC supply is generated by switching between the DC sources in the inverter at a high frequency. In addition, switching between the two DC sources generates a voltage output that switches between two prescribed voltages.

High-frequency inverter switching is achieved using semiconductor-based switches (such as transistors). The way the switches are operated in an inverter is known as a *modulation strategy*. The aim of the modulation strategy is that the voltage output is generated with similar low-frequency behaviour to a desired low-frequency *signal wave*. In this thesis we examine inverters that use a modulation strategy known as *pulse width modulation* (PWM). Inverters using PWM have excellent power efficiency, making PWM advantageous compared to other modulation strategies (see [50] and the references therein). In addition, PWM can be designed so that the low-frequency components of the voltage output approximate, and in some cases match, the signal wave.

Despite the advantages of PWM, considerable high-frequency distortion is generated in the output voltage of PWM inverters (see [49], for example). In our analysis, voltage distortion is any harmonic deviation of the voltage output from the desired signal wave. An example of an inverter malfunction is if the voltage output is generated with large amounts of distortion [39]. Furthermore, undesirable high-frequency components are generated in the currents of PWM inverters (see [31, 40], for a few examples). There are electrical problems associated with high-frequency currents, such as electro-magnetic interference (EMI) [55]. Filtering out the high-frequency components improves inverter performance (see [4], and the references therein) and reduces EMI (see [59, 67], for example).
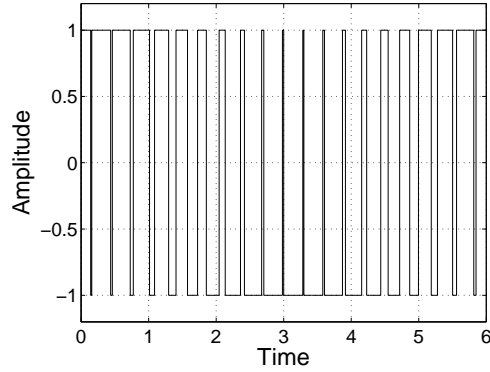
Figure 1.1: *Sample square-wave output of a PWM inverter.*

In this thesis, we calculate frequency spectra for the voltages and currents of a wide variety of PWM inverters. Knowledge of spectra informs effective filter design for the removal of high-frequency components, without recourse to bulky, or weighty filters. Optimal filters are of particular importance for electrical components of an aircraft, for example, where minimising size and weight of the electrical parts of the aircraft reduces operating costs (by reducing fuel consumption) [102].

1 Inverter Design

We now discuss the different inverter designs in this thesis following the accounts in [49]. Industrial demands for efficient, high-voltage power supplies have led to extensive use of PWM inverters to provide power. There are a multitude of inverter designs, and we examine three in this thesis: single-phase inverters, two-phase inverters and three-phase inverters.

Before we detail the different inverter designs, we first describe the electronic components used in inverter circuits. All inverter circuits are supplied by an upper DC source of a prescribed voltage, and a lower DC source of a prescribed voltage (in this thesis, we non-dimensionalise the supply voltage to be ± 1). Semiconductor-based switches are used in inverter circuits to switch between the DC sources and generate a square-wave output (illustrated in figure 1.1). Additionally, the electrical impedance on the circuit is referred to as the *load*, and we discuss the load further in section 1.1. Note that we assume that there is an insignificant voltage drop across the semiconductor switches. If this assumption was not satisfied the inverter would suffer from *switching losses* [37] (switching losses are not considered in this thesis).

By wiring semiconductor switches between an upper DC source and a lower DC source, a *phase-leg* is produced. A phase-leg is illustrated in figure 1.2, where, in order to prevent a short circuit of the input power supply, each semiconductor switch is open while the other is closed. In other words, if S_+ is open, S_- is closed (similarly, if S_- is open, S_+ is closed). Phase-legs are the fundamental building blocks of inverters.
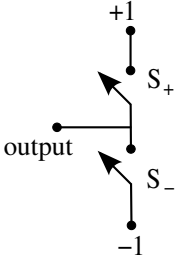
Figure 1.2: *Circuit diagram of a phase-leg, where the upper DC source is denoted by +1, the lower DC source by −1 and the semi-conductor switches are denoted S_+ and S_-. The AC output is also illustrated.*

(a) *Single-phase inverter.*   (b) *Two-phase inverter.*   (c) *Three-phase inverter.*
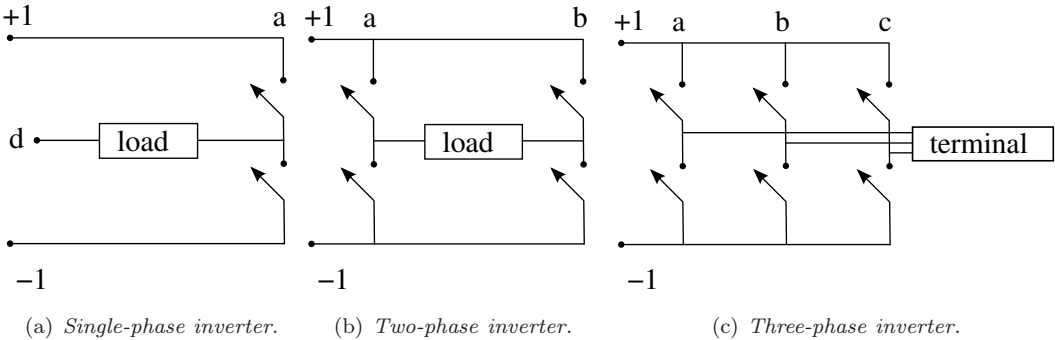
Figure 1.3: *Circuit diagrams for: (a) a single-phase inverter, (b) a two-phase inverter and (c) a three-phase inverter. In (c), the part of the circuit labelled terminal can be wired in two ways, as illustrated in figure 1.4.*

In order for the phase-leg to generate an AC power supply, the circuit must be closed. A phase-leg connected to a neutral point (a point held at 0V, such as an earth wire [84]) by a load is called a single-phase inverter. The circuit diagram of a single-phase inverter is illustrated in figure 1.3(a), where a load is connected between phase-leg a and neutral point d. High-frequency switching between the two DC sources in a single-phase inverter using PWM generates a high-frequency voltage output that switches between ±1.

Multi-phase inverters are produced by connecting phase-legs together with loads. In a multi-phase inverter, each phase-leg generates a voltage output that is out of phase with the voltage outputs generated by the other phase-legs. There are a wide range of multi-phase inverters, and in this thesis we examine two types: two-phase and three-phase inverters, comprising, respectively, two or three phase-legs that generate two or three output voltages. As documented in [62, 80, 95], compared to single-phase inverters, two-phase and three-phase inverters are desirable because: the voltages generated across the loads have reduced harmonic distortion; the input currents have fewer high-frequency components; they operate at a lower switching frequency; and they are better suited to high-voltage power supplies.

A two phase inverter is illustrated in figure 1.3(b), where a load is connected between phase-leg a and phase-leg b. This type of inverter is sometimes known as a single-phase full-bridge inverter,

(a) Δ *configuration.*   (b) *Y configuration.*
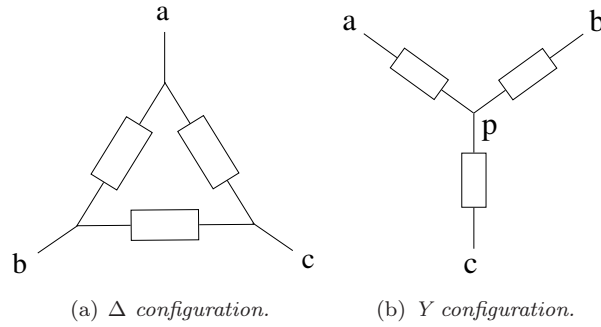
Figure 1.4: *Wiring designs for a three-phase inverter.*

or an H-bridge inverter. H-bridge inverters are often found in robots, as they are capable of running DC motors in two directions [110].

Three-phase inverters are commonly used for variable-frequency drive applications, which control the speed of an AC motor by adjusting the frequency of the electrical power supply. Variable-frequency drives are extensively used, for example in both water and gas supplies to save energy by efficiently controlling motorised pumps to match pipeline demands [23]. A three-phase PWM inverter is illustrated in figure 1.3(c), where each phase-leg is connected to a load in the part of the circuit labelled "terminal". The terminal can be wired in two ways: in the "Δ configuration", or in the "Y configuration". Both the Δ and the Y wiring configurations are illustrated in figure 1.4. In this thesis we predominantly examine the Δ configuration (shown in figure 1.4(a)), where a load is connected between each pair of phase-legs. The Y configuration is more complicated to analyse because each load is connected to a floating point p, as illustrated in figure 1.4(b). Sometimes the Y configuration is wired so that the floating point p is connected to a neutral point, though the extra wiring increases the cost of the inverter [42]. The Y configuration is equivalent to the Δ configuration when all the load impedances are equal (see [44], for example).

1.1   Load Choice

In this thesis, the load on an inverter is composed of passive electrical components (resistors and inductors). These passive electrical components filter the current waveforms, reducing or amplifying the amplitude of some harmonics. Additionally, the electrical impedance determines the relationship between the voltage drop across the load and the output current through the load [52]. From this relationship we can directly evaluate the output currents from the output voltages. Subsequently, because the input currents are functions of the output currents, we are able to determine the input currents.

We now describe the passive electronic components examined in this thesis. All circuits have a natural resistance to the current flow from the wire that is used to manufacture them. We illustrate a circuit symbol of a resistor in figure 1.5(a). The voltage drop across a resistor determines the current through the resistor by Ohm's law ($V = IR$, where R is the resistance measured in ohms) [38]. The circuit symbol of a pure inductor is shown in figure 1.5(b). Pure

(a) *Resistor.*   (b) *Inductor.*
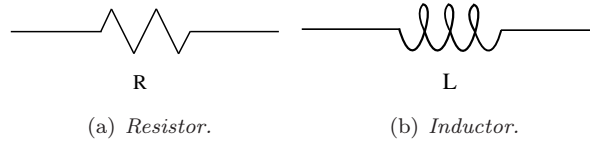
Figure 1.5: *Circuit symbols of the passive electrical components that make up a load in a PWM inverter.*

(a)   (b)
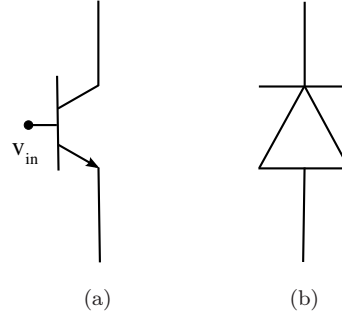
Figure 1.6: *Circuit symbol of: (a) a transistor, and (b) a diode. The operation of the transistor is controlled by a low voltage power supply, v_{in}.*

inductors are used in an inverter to resist changes to the current flow [81]. The voltage drop across a pure inductor determines current through

$$V = L\frac{\mathrm{d}I}{\mathrm{d}t},$$

where the inductance L is measured in henrys. Note that in this thesis we assume both R and L are *constants.*

In this thesis, we examine inverters with series resistive-inductive (RL) loads. Inverters with series RL loads are common, with examples of previous analysis in [31, 40, 94]. The voltage drop across a series RL load and the current through the load are related by

$$V = IR + L\frac{\mathrm{d}I}{\mathrm{d}t}.$$

We will also examine inverters with general output impedance.

1.2 Inverter Switch Control

In this thesis there are two models that describe the mechanics of the operation of the switches in the inverter. In order to describe the two switching models, it is useful to examine a single phase-leg of an inverter (shown in figure 1.2). We assume in this section that the phase-leg is attached to a well defined output terminal.

The first switching model is analysed in chapters 2, 3, 4, 7 and 8. For this first model, we assume that the switches operate instantaneously. Additionally, the two switches on each phase-leg are assumed to operate in a complementary fashion. In other words, with reference to figure 1.2,

S_+ opens when S_- closes (similarly, S_+ closes when S_- opens). This type of inverter switching is well documented and analysed. For example, output voltages, output currents and input currents have been determined in [49], [94] and [31], respectively. In practice, the operation of the switches in an inverter is more complex than described by this model, however, and we also model a more physical switching model.

In order to describe the second switching model, we first of all examine the composition of the semiconductor switches in more detail. From [42], semiconductor switches used in inverters comprise a transistor and a diode connected in parallel. Transistors are fundamental components of most modern electronic devices (see [66], for example). As described in [6], a transistor has three terminals, and, in an inverter, one is connected to an input, one to an output, and one is connected to a low-voltage power supply (shown in figure 1.6(a)). The low-voltage supply to the transistor controls when the transistor conducts between the input and output. More specifically, when the oscillatory voltage output of the low-voltage supply is within certain thresholds, the transistor will conduct. Diodes were first developed as rectifiers (electronic devices that convert an AC power supply to a DC supply), and are self-operating semiconductor switches that allow current to pass in one direction only [57]. A diode is illustrated in figure 1.6(b), and has two terminals, one connected to an output and one to an input.

Because diodes are self operational, we can only control the transistors. Transistors do not switch instantly, but have a transition phase [61]. Therefore, if the transistors on a phase-leg operate simultaneously, there is a possibility that both transistors will conduct at the same time, which will cause a short circuit of the input power supply. To avoid a short circuit, both transistors are briefly open between switching transitions. The period of time when both transistors are open is known as *dead time* [78]. The voltage output during dead time is dependent on the operation of the diodes, and we discuss this further in chapter 5.

The second switching model incorporates dead time, and we examine inverters that incorporate dead time in chapters 5 and 6. With this switching model, with reference to figure 1.2, we assume that when one of the transistors of S_+ or S_- opens, there is a small delay before the transistor on the other switch closes. Note that we assume that transistors switch instantaneously.

Mathematical models for inverters with dead time are more sophisticated than models for inverters without dead time, and are not as well documented. The output voltages of single-phase inverters with dead time have been calculated, however, in [34]. Output voltages have also been calculated in [111] and [27] (for two-phase and single-phase inverters, respectively), but these calculations either contain approximations or give no immediate insight to the frequency spectrum. In this thesis, we extend the results of [34] to the case of two-phase and three-phase inverters in chapter 5. Input currents have *never* been calculated for inverters that incorporate dead time. In chapter 6 of this thesis we address this, and calculate the input currents of a single-phase inverter that incorporates dead time for the *very first time*.
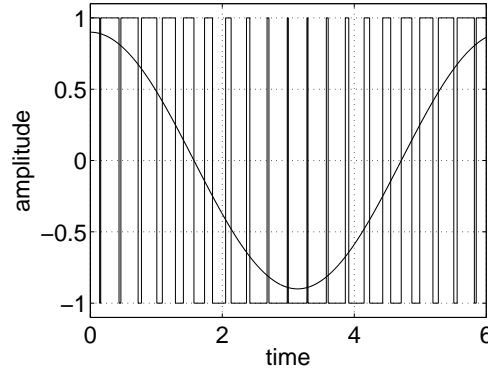
Figure 1.7: *Sample square wave output from a PWM device, characterising a given signal wave (a cosine wave).*

2 PWM Methods

PWM is a high-frequency modulation strategy, made feasible by transistors, which can operate at the required high frequencies. Furthermore, because transistors are mass produced at a low cost (per transistor), PWM has become commonly used for regulating power supplies [15]. Mathematically, PWM generates a square wave that switches between two values at a high frequency, modulating the width of the pulses (the length of time spent at each value) at a low frequency. This low frequency is the frequency of the required signal wave. An example of a PWM square wave is illustrated in figure 1.7, where the signal wave is also shown. Note that the generated square wave tends to be positive (on average) when the signal wave is positive, and negative otherwise. More specifically, the square wave is constructed to have low-frequency components that provide a good approximation to the signal wave. In order to achieve this, the switch times of the square wave are determined by samples of the signal wave. There are two common sampling methods, known as *uniform* (or *regular*) sampling and *natural* sampling. PWM inverters use both uniform and natural sampling.

Samples of the signal wave are taken at fixed intervals when using uniform sampling. The switch times of the square wave are the times when the value of a given high-frequency *carrier wave* is equal to the sampled value of the signal wave (shown in figure 1.8(a)). The regularity of the sampling makes uniform sampling ideally suited to digital applications. This digital compatibility, coupled with advances in digital solid-state electronics, has led to PWM devices being predominantly uniformly sampled [66]. Therefore, in this thesis, we are most interested in uniformly sampled PWM inverters. Note that, using uniform sampling, there is a delay between the sampling of the signal wave and the switching of the square wave. This delay generates tolerable low-frequency distortion in the PWM square wave output (see [49], for example).

We also briefly examine natural sampling in this thesis. Natural sampling is older than uniform sampling, being an analogue modulation strategy, and was used as early as 1964 in a Sinclair x-10 amplifier [3]. Using natural sampling, the times when the signal wave and the carrier wave

(a) *Uniform sampling.*   (b) *Natural sampling*
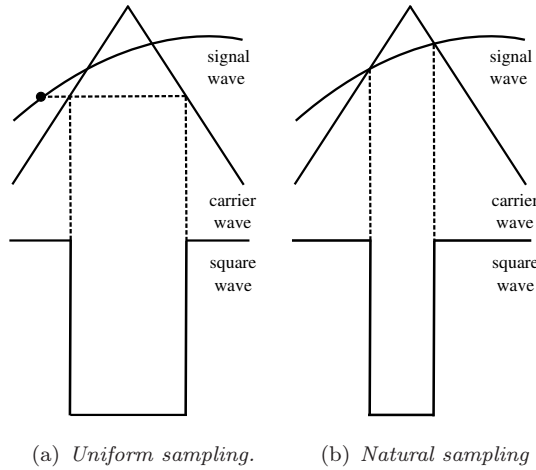
Figure 1.8: *Illustration of how the switch times of the square wave output of a PWM device are determined by the signal wave the carrier wave, for uniform and natural sampling.*

intersect are the switch times of the square wave, as illustrated in figure 1.8(b). PWM square waves generated with natural sampling do not have any low-frequency distortion [49]. This makes natural sampling well suited to modern (class-D) audio amplifiers [32, 112].

In this thesis, we also examine a specific type of PWM, known as space vector modulation (SVM). SVM is limited to inverters with three or more phase-legs, and is shown in [20] to be advantageous because SVM inverters generate lower current harmonics compared to standard PWM inverters. Both natural and uniform sampling are used in SVM inverters, but, because SVM is better suited to digital devices, uniform sampling is more common (see [114], for example).

Note that, in this thesis, we assume that for all PWM methods the carrier wave and the square wave have identical amplitudes (as illustrated in figure 1.8). This assumption has been made in previous studies, such as those in [49].

3 Identification of High-Frequency Components Generated by PWM Inverters

In all the inverter designs discussed in section 1, use of PWM generates high-frequency components in the output voltages, output currents and input currents. Note that high-frequency components are also generated in the inputs and outputs of inverters by the load impedance. Filters are used to remove unwanted frequency components from the voltages and the currents. To design appropriate filters, we require knowledge of the undesirable high-frequency components of the voltages and currents. The high-frequency components that require filtering are identified from frequency spectra. Mathematical models that represent the inverter allow us to obtain spectra for the voltages and currents.

In section 3.1, we discuss methods of determining frequency spectra for the voltage outputs (and hence output currents) of several inverters. We review previous calculations of input current

spectra in section 3.2. Finally, in section 3.3, we outline calculations of voltage and current spectra in this thesis.

3.1 Calculations of Output Voltages and Currents

In this section, we explore the different methods used to find the output voltages of PWM inverters in a form that tells us about their frequency spectrum. Output currents are straightforward to determine, provided both the output voltage and the load are known (see [13], for example).

The most common technique used to find output voltages is *Black's method*, first used by Harold S. Black in [14]. This is an algebraically complex method that, through a partly geometrical argument, derives a double Fourier series for the voltage output. Black's method is the standard engineering method, but is cumbersome, because each Fourier coefficient is determined by a double integral. We instead use the *Poisson re-summation method* [31], which is more direct and gets precisely the same results as Black's method, but at a smaller analytical cost. There are also a few other non-standard methods that have been employed by engineers, which we will discuss briefly here.

The book by Holmes and Lipo [49] provides a comprehensive catalogue of frequency spectra for the output voltages of several types of PWM inverter, and is a good reference for both simple and complex calculations using Black's method. In [49], they examine single-phase, two-phase and three-phase inverters using both natural and uniform sampling, including a type of uniform sampling known as asymmetrical uniform sampling, where the signal wave is sampled twice as often as standard uniform sampling. Asymmetrical uniform sampling is shown to be advantageous to standard uniform sampling, because of greater harmonic cancellation. Applications of Black's method by Bowes [17, 18] and Holmes [48] have been used to determine spectra for a further range of PWM inverters using both natural and uniform sampling. Black's method has been used, more recently, in [83], to calculate spectra for PWM inverters that have signal waves dependent on multiple frequencies. A comparison, in [46], for a naturally sampled single-phase PWM inverter, shows that the analytical frequency spectrum generated using Black's method is virtually indistinguishable from a spectrum derived from experimental data.

Black's method has also been used to calculate voltage spectra for more complex inverter designs. Voltage spectra for a two-phase inverter that incorporates dead time have been calculated using Black's method in [111]. In this paper, to simplify the calculation, an approximation is made to one of the integration bounds in the double Fourier integral necessitated by Black's method. This approximation accounts for the errors between their analytical and simulated results. Additionally, Black's method has been used to determine Fourier series expressions for the voltage output of SVM inverters in [49, 77]. Studies (in [19], for example) have shown the agreement between theoretical and experimental spectra for SVM inverters.

In this thesis, we mainly use the Poisson re-summation method. This method involves writing the voltage output as a discrete switching function in the time domain, then taking a Fourier transform. Use of the Poisson re-summation formula then allows us to identify a Fourier series expression for the voltage output. An early version of this calculation is found in [32] for a

simple type of PWM device: an audio amplifier. A more refined version of this calculation was introduced in [33] to find spectra for a matrix power converter (a complex AC/AC PWM device). This method is also used in [31] for single-phase and two-phase inverters. More recently, the Poisson re-summation method has been used to calculate the output voltage of a single-phase inverter that incorporates dead time in [34]. The advantage of the Poisson re-summation method over Black's method is that it is more direct, which makes complicated calculations (as carried out here) feasible.

Even though Black's method is the engineering standard, there have been several attempts to develop more direct methods of determining output voltages. In [41], the voltage outputs of PWM inverters are determined through the use of Kepler's equation. Kepler's equation is typically used to describe the motion of planetary orbits (such as in [30]), but is used in [41] to describe the switching instants of a naturally sampled three-phase inverter as infinite series of Bessel functions, across a switching period, using Kapteyn series. Another method, used in [88] and [99], describes the voltage output as a discrete switching function in the time domain before taking a Fourier transform, similar to the Poisson re-summation method. To derive spectra, they approximate the switch times of the inverter with Taylor series expansions. This method has also been used in [27] for a single-phase inverter that incorporates dead time. In [27], expressions for the voltage output are left in terms of switching times, however, and spectra are not provided. Most recently, in [76], a method with similarities to the Poisson re-sumation method is used to calculate the output voltage of a single-phase inverter. It is noted in this paper that Black's method can only be applied to PWM inverters with periodic signal waves, whereas a Fourier transform method (such as the Poisson re-summation method) is not so rigid. We note that the methods of [27, 41, 76, 88, 99] are difficult to generalise, and are mathematically over-complicated compared to the Poisson re-summation method.

We have discussed several methods of finding frequency spectra for the voltage output of PWM inverters, and observed that Black's method is widely used by engineers. In particular, [17, 49] contain comprehensive catalogues of frequency spectra for single-phase, two-phase and three-phase PWM inverters using both natural and uniform sampling. Calculation of spectra for inverters that incorporate dead time is, however, very difficult using Black's method. The more direct Poisson re-summation method makes complex calculation of spectra for inverters with dead time possible, as shown in [34].

3.2 Input Current Calculations

We discuss the methods used to calculate input current spectra for PWM inverters in this section. An inverter has two input currents, one drawn from the upper DC source and one drawn from the lower. Calculating input currents is difficult, because they are complex switching functions, that involve the output currents.

Inductors resist change in currents, therefore, for an inverter with a high inductance the output currents appear sinusoidal. Therefore, in order to mitigate the difficulty of finding expressions for the input currents, output currents have been approximated as sinusoidal in most analysis

so far [36, 70, 74, 106]. These papers model inverters with series RL loads. Approximating output currents as sinusoidal leads to accurate mathematical models for the input currents only in certain limiting cases. There has also been analysis for SVM with sinusoidal approximations of the output currents in [60], which when compared to experimental data are found to have acceptable error under very specific operating (highly inductive) conditions.

The *direct method* calculates input currents without making additional mathematical approximations. Using the direct method, a double Fourier series is derived for each input current. The double Fourier series is determined by multiplying a Fourier series for the output currents with a Fourier series that describes the switching of the input current. Both Fourier series approximate discontinuous square waves, and converge slowly. Consequently, the double Fourier series for the input current converges extremely slowly. The direct method is, however, a powerful technique of finding accurate input current spectra, which is easily adaptable to most PWM inverter designs.

The direct method is used in [40] to determine input currents for a single-phase and a three-phase inverter with a series RL load. Theoretical input current spectra determined by the direct method were compared to experimental data and were found to agree in [94], and in [86]. The direct method has also been applied to matrix converters in [71], which illustrates how effective this method is, even for complicated PWM devices.

In order to avoid the problem of slow convergence, we use the *single-sum method*. Using the single-sum method, the output currents are first determined as discrete switching functions in the time domain. To obtain a discrete, time-dependent function for each input current, we then multiply the output currents with a discrete time-dependent function that describes the switching of the input current. This expression for the input currents is evaluated over two separate infinite sums, and careful rearranging of these sums allows us to compute one sum exactly, leaving a single, discontinuous, function. A Fourier series approximating a single, discontinuous, function converges much faster than the product of two Fourier series approximating discontinuous functions. Therefore, Fourier series for the input currents calculated using the single-sum method converge much faster than those calculated using the direct method.

The single-sum method was first used to calculate input currents in [33] for a matrix converter with a resistive-only load and a series RL load. In [31], input spectra are calculated for a single-phase and a two-phase inverter with a series RL load.

So far, in the literature, there have been no calculations of the input currents for inverters that incorporate dead time, or for SVM inverters (except with approximations in [60]).

3.3   Outline of Calculations in This Thesis

In order to set out the key ideas that will be fundamental to the Fourier analysis in this thesis, we begin by using Black's method and the Poisson re-summation method to calculate the output voltages for single-phase, two-phase and three-phase PWM inverters for natural and uniform sampling in chapter 2. While these are known results, it is the exposition of the more direct Poisson re-summation method that is of greatest importance in this chapter (forming the foundation of the calculations in all the following chapters).

Following on from chapter 2, we calculate the input and output currents of single-phase, two-phase and three-phase uniformly sampled PWM inverters with series RL loads in chapter 3, using the single-sum method. In this chapter, we extend the work of [31], using the single-sum method to calculate input currents for a three-phase inverter for the first time. These calculations determine Fourier series for the input currents with Fourier coefficients that converge faster than the Fourier coefficients for the input currents in [40] determined using the direct method. The increased speed of convergence means that input current spectra are provided at a lower numerical cost in chapter 3 than in [40]. Chapter 3 also presents a comparison of the single-sum method and the direct method, to illustrate the relative merits of both methods.

In chapter 4, we build upon work in chapter 3 by calculating input currents for single-phase, two-phase and three-phase PWM inverters with general output impedance using the single-sum method. All previous calculations of input currents have been for specific output impedances, and this chapter generalises these results. The single-sum method is algebraically involved, and calculating input currents for PWM inverters with general output impedance increases the algebraic complexity of the single-sum method. For this reason, in this thesis, we introduce the single-sum method in chapter 3 for a specific impedance before calculations with general output impedance in chapter 4.

We examine a more realistic inverter design in chapter 5: inverters that incorporate dead time. The mathematical models that represent inverters with dead time are more sophisticated than those in earlier chapters. To illustrate the main steps in the calculation of output voltages for inverters with dead time, we begin by reviewing the calculation of the output voltage of a single-phase inverter with dead time, as described in [34]. We then extend [34] and determine the output voltages for the more complicated cases of two-phase and three-phase inverters with dead time.

The effects of dead time on the input currents of PWM inverters have been investigated in the time domain in [16, 24] by simulating the input current waveform, but the effects of dead time on the frequency spectrum of the input currents have never been calculated before. We rectify this in chapter 6, calculating input currents for a single-phase PWM inverter. Calculations are presented for single-phase inverters with general output impedance, which are then developed to determine spectra for inverters with series RL loads.

To illustrate that the Poisson re-summation method can be applied to other complex modulation strategies, we calculate the output voltages of a three-phase SVM inverter in chapter 7. Despite the fact that this chapter contains known results, it is evident that the Poisson re-summation method significantly reduces the analytical cost of calculating the output voltages of SVM inverters, by comparison with calculations using Black's method in [49].

In chapter 8, we calculate the input currents of a three-phase SVM inverter with a series RL load. This extends [60], where the input currents of SVM inverters are calculated for highly inductive loads. Highly resistive loads are also important (see [71, 86], for example), and the analysis in chapter 8 treats the case of highly resistive loads, amongst others (such as equally resistive and inductive loads).

Finally, in chapter 9, we summarise the results of this thesis, and suggest avenues for future research.

Voltage Spectra for PWM Inverters

1 Introduction

In this chapter we determine frequency spectra for the output voltages of several inverter designs. Frequency spectra of the output voltages are used to quantify the deviation of the low-frequency components from the intended signal wave, and to identify the high-frequency components, which will ultimately be filtered out. We examine two methods of determining the frequency spectra of PWM inverters here: *Black's method* and the *Poisson re-summation method*. The presentation of the newer method (the Poisson re-summation method) is of most importance here, since it is the basis of our calculations in later chapters.

Black's method is the most widely used method of determining frequency spectra, first used in [14]. Black's method uses a partly geometrical argument to derive a double Fourier series for the voltage output, but is algebraically cumbersome. In [49] there is a comprehensive catalogue of calculations using Black's method to find the frequency spectra of several PWM inverters. In fact there are many engineering papers (see [17, 18, 43, 48, 83], for example) that contain calculations using Black's method to find frequency spectra for a wide variety of switching devices. Calculations using Black's method have been shown to be accurate when compared with simulated and experimental results (see [19, 46], for example).

The Poisson re-summation method is more direct than Black's method, and avoids the calculation of a double integral. We provide calculations using the Poisson re-summation method in this chapter in order to illustrate the relative compactness of this method in comparison to Black's method. An early version of the Poisson re-summation method can be found in [32], with more refined versions of the method in [31, 33].

1.1 Structure of Chapter

In section 2 we determine frequency spectra for a single-phase inverter using both the Poisson re-summation method and Black's method to demonstrate the relative merits of the separate
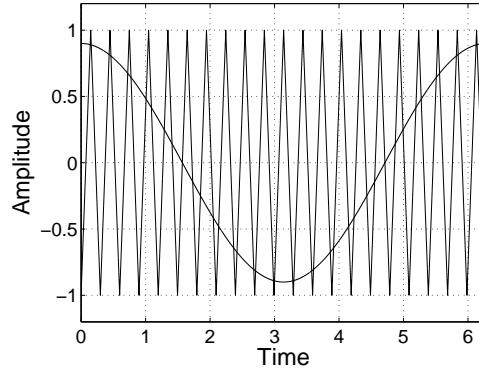
Figure 2.1: *High-frequency triangle carrier wave and low-frequency sinusoidal signal wave, where $M = 0.9$, $\omega_s = 1$ and $\omega_c = 21\omega_s$.*

approaches to calculating spectra to a practitioner. Two-phase and three-phase inverters are discussed in section 3, and the voltages across the loads are determined. Finally, in section 4, we sum up our conclusions.

2   Single-phase Inverter

In this section we examine a single-phase inverter (illustrated in figure 1.3(a)). Using PWM, high-frequency modulation of the switches generates a voltage output, $v_a(t)$, with low-frequency components that closely approximate a low-frequency signal wave, $s_a(t)$. We define the signal wave as

$$s_a(t) = M \cos \omega_s t, \tag{2.1}$$

where $|M| < 1$ is the *modulation index*, or (constant) amplitude, and ω_s is the frequency. In order to determine the switch times of $v_a(t)$, the signal wave is then sampled according to uniform sampling, or natural sampling. In fact, uniform sampling is categorised into two further types: *symmetrical* uniform sampling, and *asymmetrical* uniform sampling. The switch times of $v_a(t)$ are given as the times when the sampled values of $s_a(t)$ are equal to a carrier wave, $w(t)$, which in our analysis is given by

$$w(t) = \begin{cases} -1 + \frac{4(t-mT)}{T}, & \text{for } mT < t < (m + \frac{1}{2})T, \\ 3 - \frac{4(t-mT)}{T}, & \text{for } (m + \frac{1}{2})T < t < (m+1)T, \end{cases} \tag{2.2}$$

where m is any integer and $T = 2\pi/\omega_c$ is the switching period (and $\omega_c > \omega_s$ is the switching frequency). In practice, the ratio between ω_s and ω_c can vary quite widely, and studies in [101] examine the relationship between the ratio of switching and signal frequencies and the power losses of an inverter. For low power devices, $\omega_c \gg \omega_s$ (for example, $\omega_c = 100\omega_s$), however, for very high-volage devices ω_c can be as low as 5 times ω_s. The signal wave and the carrier wave are illustrated in figure 2.1. Note that there are several types of carrier wave, but the one we
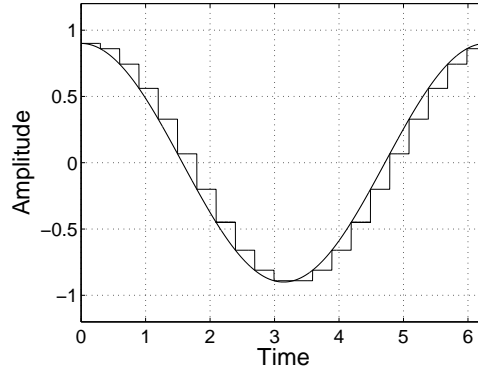
Figure 2.2: *Signal wave $s_a(t)$ and the discontinuous uniform signal wave $s_u(t)$, where $s_a(t)$ is given in (2.1), $M = 0.9$, $\omega_s = 1$ and $\omega_c = 21\omega_s$. Note that the length of each horizontal step in $s_u(t)$ is equal to the switching period T.*

are choosing to examine generates a voltage output with the least high-frequency components (see [49], for example).

We also note that in this thesis we assume that the signal and carrier waves are synchronised. If the signal wave were at some constant phase angle to the carrier wave there is a phase-shift term in the Fourier series of the voltage outputs (and consequently the input and output currents), but the Fourier coefficients are not affected [49]. Since we are interested in frequency spectra in this thesis, the assumption that the carrier and signal wave are synchronised does not affect our results.

In section 2.1, we determine the frequency spectrum of the voltage output of a single-phase PWM inverter with symmetrical uniform sampling using both Black's method and the Poisson re-summation method. Then, in section 2.2, we provide the frequency spectrum for a single-phase PWM inverter using asymmetrical uniform sampling. Finally, we examine natural sampling in section 2.3, using both Black's method and the Poisson re-summation method to determine frequency spectra for the voltage output of a naturally sampled single-phase PWM inverter.

2.1 Symmetrical Uniform Sampling

Symmetrical uniform sampling (normally referred to as uniform sampling) is associated with digital devices, and is a more recently developed technique than natural sampling for generation of PWM signals (see [87, 88], for example). The regularity of the sampling times makes uniform sampling more suitable to digital inverters than natural sampling [49]. Uniform sampling incurs a delay between sampling the reference wave and switching the inverter, however, which generates low-frequency distortion in the voltage output [49].

The principle of uniform sampling is that the reference wave $s_a(t)$ is sampled at the start of every switching period mT to determine $s(mT)$ for $m = 0, \pm1, \pm2\ldots$, and these sampled values are used to define the uniform signal wave $s_u(t) = s_a(mT)$ for $mT < t < (m+1)T$, as illustrated

(along with $s_a(t)$) in figure 2.2. The voltage output of a uniformly sampled PWM inverter is described as

$$v_a(t) = \begin{cases} +1, & \text{if } s_u(t) > w(t), \\ -1, & \text{if } s_u(t) < w(t), \end{cases}$$

as shown in figure 2.3. During each switching period T there are two switching times, $\mathcal{A}_m^a$ and $\mathcal{B}_m^a$: $t = \mathcal{A}_m^a$ when the upward slope of $w(t)$ crosses $s_u(t)$; and $t = \mathcal{B}_m^a$ when the downward slope of $w(t)$ crosses $s_u(t)$. Thus, we have an alternative definition for $v_a(t)$, given by

$$v_a(t) = \begin{cases} -1, & \text{if } \mathcal{A}_m^a < t < \mathcal{B}_m^a, \\ +1, & \text{if } \mathcal{B}_m^a < t < \mathcal{A}_{m+1}^a, \end{cases} \tag{2.3}$$

where m is any integer and the switch times $\mathcal{A}_m^a$ and $\mathcal{B}_m^a$ are the times when $s_u(t) = w(t)$, in other words they are given *explicitly* as

$$\mathcal{A}_m^a = mT + \frac{T}{4}(1 + s_a(mT)), \qquad \text{and} \qquad \mathcal{B}_m^a = mT + \frac{T}{4}(3 - s_a(mT)). \tag{2.4}$$

We now determine the frequency spectrum of the voltage output of a uniformly sampled single-phase PWM inverter using both the Poisson re-summation method in section 2.1.1 and Black's method in section 2.1.2. Comparison of sections 2.1.1 and 2.1.2, illustrate that, for inverters that use symmetrical uniform sampling, calculation of the output voltage is more compact using the Poisson re-summation method. We analyse the frequency spectrum of $v_a(t)$ of a uniformly sampled PWM inverter in section 2.1.3.

2.1.1 The Poisson Re-summation Method

Use of the Poisson re-summation method is fundamental to the calculations in this thesis. Previously, the Poisson re-summation method has been used to find spectra for single-phase and two-phase inverters in [31], and to calculate spectra for a matrix converter in [33]. Although not widely used, the Poisson re-summation method has many advantages, for example calculation of a double integral is not required, unlike for Black's method. The relative compactness of calculations involved in the Poisson re-summation method is demonstrated by comparison with the calculations using Black's method in section 2.1.2.

In order to apply the Poisson re-summation method, we require an expression for $v_a(t)$ as a discrete switching function. To this end, we define a *top-hat function* $\psi(t; t_1, t_2)$, given by

$$\psi(t; t_1, t_2) = \begin{cases} 1, & \text{for } t_1 < t < t_2, \\ 0, & \text{otherwise}, \end{cases}$$

and, for completeness, $\psi(t; t_1, t_2) = 0$ when $t_1 > t_2$. Therefore, we express $v_a(t)$ as

$$v_a(t) = 1 - 2\sum_m \psi(t; \mathcal{A}_m^a, \mathcal{B}_m^a) \equiv 1 - 2f(t),$$

where the explicit switching times $\mathcal{A}_m^a$ and $\mathcal{B}_m^a$ are in (2.4), and $f(t)$ is introduced to represent the sum (for later convenience). We note that, in this thesis, the sum $\sum_m$ is the sum over all m from ∞ to $-\infty$. This representation of $v_a(t)$ is a discrete time-dependent switching function, and gives no immediate insight to the frequency spectrum. The non-trivial components of the
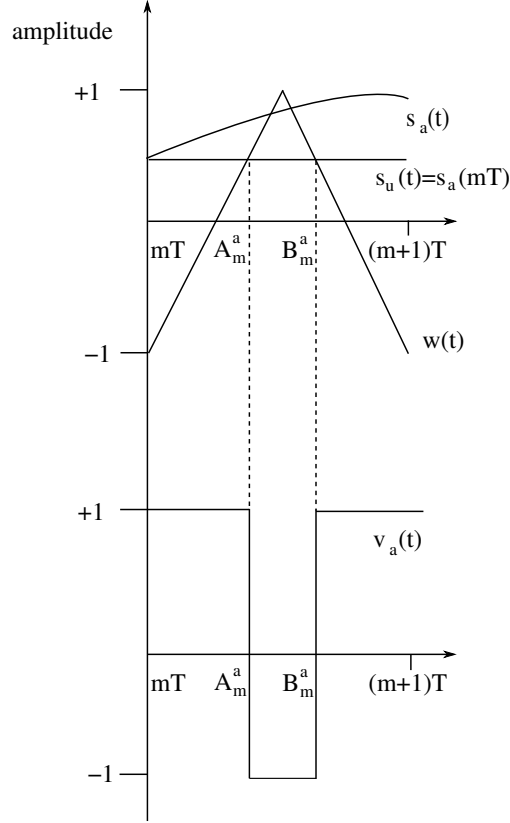
Figure 2.3: *Illustration of how the switch times of the voltage output $v_a(t)$ are determined using uniformly sampled PWM, across a single switching period. Note that $s_a(t)$ is sampled at the start of every switching period mT for $m = 0, \pm 1, \pm 2 \ldots$, and this sampled value $s_a(mT)$ is equal to $s_u(t)$ between mT and $(m+1)T$. The voltage output $v_a(t)$ is $+1$ when $s_u(t) > w(t)$ and is -1 otherwise. The down-switching of $v_a(t)$ occurs at $t = \mathcal{A}_m^a$, when the upward slope of $w(t)$ crosses $s_u(t)$. Similarly, the up-switching of $v_a(t)$ occurs at $t = \mathcal{B}_m^a$, when the downward slope of $w(t)$ crosses $s_u(t)$.*

spectrum reside in $f(t)$. To determine the frequencies that contribute to $f(t)$, we take a Fourier transform of $f(t)$, which gives

$$\hat{f}(\omega) = \sum_m \int_{-\infty}^{\infty} \psi(t; \mathcal{A}_m^a, \mathcal{B}_m^a) e^{-i\omega t} \, dt.$$

Although $\hat{f}(\omega)$ is not integrable, it is locally integrable, and so it does have a Fourier transform in the sense of a distribution. Therefore,

$$\hat{f}(\omega) = \sum_m \frac{1}{i\omega} (e^{-i\omega \mathcal{A}_m^a} - e^{-i\omega \mathcal{B}_m^a}),$$

when $\omega \neq 0$. We now have a function in the frequency domain, but we want it in the time domain in a form that shows the contributions at various frequencies. To this end we use the Poisson re-summation formula, defined in [7] to be

$$\sum_m h(m) = \sum_m \int_{-\infty}^{\infty} e^{2\pi i m \tau} h(\tau) \, d\tau.$$

– 18 –

Note that $h(\tau)$ is a continuous integrable function, which satisfies,

$$|h(\tau)| + |\hat{h}(\tau)| \le C(1 + |\tau|)^{-1-\delta},$$

for some C, $\delta > 0$ and all τ [100].

In order to apply the Poisson re-summation formula, we define continuous functions whose discrete samples give the switching times; such functions are

$$\mathcal{A}(t) = t + \frac{T}{4}(1 + s_a(t)), \qquad \text{and} \qquad \mathcal{B}(t) = t + \frac{T}{4}(3 - s_a(t)).$$

Applying the Poisson re-summation formula to our Fourier transform $\hat{f}(\omega)$ we determine, for $\omega \neq 0$,

$$\begin{aligned}
\hat{f}(\omega) &= \sum_m \int_{-\infty}^{\infty} \frac{e^{2\pi i m t/T}}{i\omega T} \left[e^{-i\omega T(1+s_a(t))/4} - e^{-i\omega T(3-s_a(t))/4} \right] e^{-i\omega t} \, \mathrm{d}t, \\
&= \sum_m \int_{-\infty}^{\infty} \frac{e^{2\pi i m t/T}}{i\omega T} \left[e^{-i\omega T/4} e^{-i\omega MT \cos \omega_s t/4} - e^{-3i\omega T/4} e^{i\omega MT \cos \omega_s t/4} \right] e^{-i\omega t} \, \mathrm{d}t.
\end{aligned}$$

In order to interpret the $e^{\pm i\omega MT \cos \omega_s t/4}$ terms, we consider the Jacobi-Anger expansion, which tells us, from [109], that

$$e^{iz \cos \theta} = \sum_n i^n J_n(z) e^{in\theta}.$$

Therefore, from the Jacobi-Anger expansions of the $e^{\pm i\omega MT \cos \omega_s t/4}$ terms, it follows that, for $\omega \neq 0$,

$$\hat{f}(\omega) = \sum_{mn} \int_{-\infty}^{\infty} \frac{1}{i\omega T} J_n \left(\tfrac{1}{4}\omega MT \right) \left[e^{-in\pi/2} e^{-i\omega T/4} - e^{in\pi/2} e^{-3i\omega T/4} \right] e^{i\Omega_{mn}t} e^{-i\omega t} \, \mathrm{d}t + C,$$

where C is a constant that arises because $\hat{f}(\omega)$ has a δ-function singularity at $\omega = 0$. We can determine this constant directly, but instead treat the $\omega = 0$ case in the following paragraph. Therefore, it is straightforward to see that

$$f(t) = \sum_{mn} \frac{1}{i\Omega_{mn}T} J_n \left(\tfrac{1}{4}\Omega_{mn}MT \right) \left[e^{-in\pi/2} e^{-i\Omega_{mn}T/4} - e^{in\pi/2} e^{-3i\Omega_{mn}T/4} \right] e^{i\Omega_{mn}t},$$

where the terms in the sum which correspond to $\Omega_{mn} = 0$ are omitted. Note that the only non-zero contributions to the frequency spectrum of $f(t)$ are frequencies of the form $\Omega_{mn} = m\omega_c + n\omega_s$.

The contribution to the frequency spectrum of $v_a(t)$ for non-zero Ω_{mn} is contained in $f(t)$. The contribution to $v_a(t)$ when $\Omega_{mn} = 0$ corresponds to the mean value of $v_a(t)$. The mean value of $v_a(t)$ is the mean value of

$$1 - 2\sum_m \psi(t; \mathcal{A}_m^a, \mathcal{B}_m^a),$$

which is zero (see appendix A.1). This means that the voltage output is given by

$$v_a(t) = \sum_{mn} a_{mn} e^{i\Omega_{mn}t},$$

where

$$a_{mn} = \begin{cases} 0, & \text{if } \Omega_{mn} = 0, \\ \frac{2}{i\Omega_{mn}T} J_n \left(\tfrac{1}{4}\Omega_{mn}MT \right) i^{m+n} \left[e^{-3\pi in\omega_s/2\omega_c} - (-1)^{m+n} e^{-\pi in\omega_s/2\omega_c} \right], & \text{if } \Omega_{mn} \neq 0. \end{cases} \tag{2.5}$$

This reproduces the output voltages calculated in [31, 49]. It is straightforward to see that $a_{mn} \to 0$ as m or $n \to \infty$. Note that engineering texts, such as [49], derive real Fourier series, rather than complex Fourier series as we have derived here. We demonstrate how to convert between equivalent real and complex Fourier series in appendix B.

2.1.2 Black's Method

Here we calculate the voltage output of a uniformly sampled single-phase PWM inverter using Black's method, for comparison with the Poisson re-summation method.

Black's method is the primary technique used by engineers for finding frequency spectra of PWM inverters [49]. Black's method involves the derivation of a double Fourier series through a partly geometrical argument. We begin by introducing a fast time-like variable, x, and a slow time-like variable, y, in order to formulate a problem that has $v_a(t) = A(x, y)$, where $A(x, y)$ is 2π-periodic in each of its arguments. It is easily verified, with reference to the the carrier wave $w(t)$ and signal wave $s_a(t)$, respectively, that

$$x = \omega_c t, \qquad \text{and} \qquad y = \omega_s t, \tag{2.6}$$

are fast and slow time-like variables.

Now, from (2.3) and (2.4), we have

$$v_a(t) = \begin{cases} -1, & \text{if } 2\pi n + \frac{\pi}{2} + \frac{\pi M}{2} \cos \omega_s nT < \omega_c t < 2\pi n + \frac{3\pi}{2} - \frac{\pi M}{2} \cos \omega_s nT, \\ +1, & \text{otherwise.} \end{cases}$$

Therefore, in the interval $nT < t < (n+1)T$

$$v_a(t) = A'(x', y') = \begin{cases} -1, & \text{if } 2\pi n + \frac{\pi}{2} + \frac{\pi M}{2} \cos y' < x' < 2\pi n + \frac{3\pi}{2} - \frac{\pi M}{2} \cos y', \\ +1, & \text{otherwise,} \end{cases}$$

where

$$x' = \omega_c t, \qquad \text{and} \qquad y' = \omega_s nT.$$

Note that

$$A'(x' + 2\pi, y') = \begin{cases} -1, & \text{if } 2\pi(n+1) + \frac{\pi}{2} + \frac{\pi M}{2} \cos y' < x + 2\pi' \\ & \qquad < 2\pi(n+1) + \frac{3\pi}{2} - \frac{\pi M}{2} \cos y', \\ +1, & \text{otherwise,} \end{cases}$$

$$= A'(x', y'),$$

$$A'(x', y' + 2\pi) = \begin{cases} -1, & \text{if } 2\pi n + \frac{\pi}{2} + \frac{\pi M}{2} \cos(y' + 2\pi) < x' < 2\pi n + \frac{3\pi}{2} - \frac{\pi M}{2} \cos(y' + 2\pi), \\ +1, & \text{otherwise,} \end{cases}$$

$$= A'(x', y').$$

Therefore $A'(x', y')$ is 2π-periodic in x' and y', however, we do not want to write $A'(x', y')$ as a double Fourier series in x' and y', because y' is a piecewise constant (meaning $e^{iny'}$ is difficult to interpret). We want to write $A'(x', y')$ as a function of x and y (given in (2.6)).

It is obvious that $x = x'$, however how to write y' in terms of x and y is more complicated. We want to write y' in such a way that for $nT < t < (n+1)T$, $y' = \omega_s nT$. If we let

$$y' = y - \frac{\omega_s}{\omega_c}(x - 2\pi n),$$

such that

$$A'(x', y') = A(x, y) = \begin{cases} -1, & \text{if } 2\pi n + \frac{\pi}{2} + \frac{\pi M}{2}\cos y' < x < 2\pi n + \frac{3\pi}{2} - \frac{\pi M}{2}\cos y', \\ +1, & \text{otherwise,} \end{cases}$$

then

$$A(x + 2\pi, y) = \begin{cases} -1, & \text{if } 2\pi(n+1) + \frac{\pi}{2} + \frac{\pi M}{2}\cos(y - \frac{\omega_s}{\omega_c}(x + 2\pi - 2\pi(n+1))) < x + 2\pi \\ & \quad < 2\pi(n+1) + \frac{3\pi}{2} - \frac{\pi M}{2}\cos(y - \frac{\omega_s}{\omega_c}(x + 2\pi - 2\pi(n+1))), \\ +1, & \text{otherwise,} \end{cases}$$

$$= \begin{cases} -1, & \text{if } 2\pi n + \frac{\pi}{2} + \frac{\pi M}{2}\cos(y - \frac{\omega_s}{\omega_c}(x - 2\pi n)) < x \\ & \quad < 2\pi n + \frac{3\pi}{2} - \frac{\pi M}{2}\cos(y - \frac{\omega_s}{\omega_c}(x - 2\pi n)), \\ +1, & \text{otherwise,} \end{cases}$$

$$= A(x, y),$$

$$A(x, y + 2\pi) = \begin{cases} -1, & \text{if } 2\pi n + \frac{\pi}{2} + \frac{\pi M}{2}\cos(y + 2\pi - \frac{\omega_s}{\omega_c}(x - 2\pi n)) < x \\ & \quad < 2\pi n + \frac{3\pi}{2} - \frac{\pi M}{2}\cos(y + 2\pi - \frac{\omega_s}{\omega_c}(x - 2\pi n)), \\ +1, & \text{otherwise,} \end{cases}$$

$$= A(x, y).$$

Therefore $A(x, y)$ is 2π-periodic in x and y, and we are able to write

$$A(x, y) = \sum_{mn} A_{mn} e^{i(mx + ny)},$$

where

$$A_{mn} = \frac{1}{4\pi^2} \int_0^{2\pi} \int_0^{2\pi} A(x, y) e^{-i(mx + ny)} \, \mathrm{d}x \, \mathrm{d}y. \tag{2.7}$$

Unfortunately, it is not easy to directly evaluate these integrals, because the boundaries of the regions in which $A(x, y) = \pm 1$ are given by implicit equations relating to x and y.

To evaluate the integral in (2.7) we transform the integral to one over x' and y'. The boundaries to the region of integration are

$$\left.\begin{array}{l} y = 0 \\ 0 \leq x \leq 2\pi \end{array}\right\} \quad \longleftrightarrow \quad \left\{\begin{array}{l} y' = -\frac{\omega_s}{\omega_c}x' \\ 0 \leq x' \leq 2\pi \end{array}\right.$$

$$\left.\begin{array}{l} y = 2\pi \\ 0 \leq x' \leq 2\pi \end{array}\right\} \quad \longleftrightarrow \quad \left\{\begin{array}{l} y' = 2\pi - \frac{\omega_s}{\omega_c}x \\ 0 \leq x' \leq 2\pi \end{array}\right.$$

$$\left.\begin{array}{l} x = 0 \\ 0 \leq y \leq 2\pi \end{array}\right\} \quad \longleftrightarrow \quad \left\{\begin{array}{l} x' = 0 \\ 0 \leq y' \leq 2\pi \end{array}\right.$$

$$\left.\begin{array}{l} x = 2\pi \\ 0 \leq y \leq 2\pi \end{array}\right\} \quad \longleftrightarrow \quad \left\{\begin{array}{l} x' = 2\pi \\ 0 \leq y' \leq 2\pi \end{array}\right.$$

Thus the domain of the integration is transformed from $D = \{(x, y) : 0 \leq x, y \leq 2\pi\}$ in the xy-plane (shown in figure 2.4(a)) to $D' = \{(x', y') : 0 \leq x' \leq 2\pi, -\frac{\omega_s}{\omega_c}x' \leq y' \leq 2\pi - \frac{\omega_s}{\omega_c}x'\}$ in

(a) *Region D.* (b) Region D'.
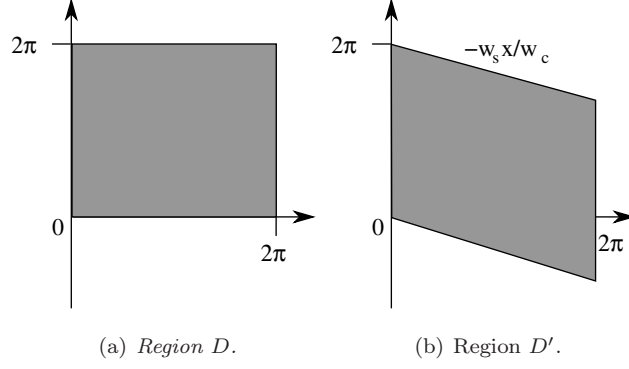
Figure 2.4: *Illustration of the two regions* $D = \{(x, y) : 0 \leq x, y \leq 2\pi\}$ *and* $D' = \{(x', y') : 0 \leq x' \leq 2\pi, -\frac{\omega_s}{\omega_c}x' \leq y' \leq 2\pi - \frac{\omega_s}{\omega_c}x'\}$.

the $x'y'$-plane (shown in figure 2.4(b)), and the Jacobian for this transformation is

$$\frac{\partial(x, y)}{\partial(x', y')} = \left| \begin{array}{cc} \frac{\partial x}{\partial x'} & \frac{\partial x}{\partial y'} \\ \frac{\partial y}{\partial x'} & \frac{\partial y}{\partial y'} \end{array} \right| = \left| \begin{array}{cc} 1 & 0 \\ \frac{\omega_c}{\omega_s} & 1 \end{array} \right| = 1.$$

Since $A'(x', y')$ is 2π-periodic in y', D' can be replaced with $D'' = \{(x', y') : 0 \leq x', y' \leq 2\pi\}$. Therefore, from (2.7), we are able to evaluate, when $mx + ny \neq 0$,

$$
\begin{aligned}
A_{mn} &= \frac{1}{4\pi^2} \int \int_D A(x, y) e^{-i(mx+ny)} \, dx \, dy, \\
&= \frac{1}{4\pi^2} \int \int_{D'} A'(x', y') e^{-i((m+n\omega_s/\omega_c)x' + ny')} \frac{\partial(x, y)}{\partial(x', y')} \, dx' \, dy', \\
&= \frac{1}{4\pi^2} \int \int_{D''} A'(x', y') e^{-i((m+n\omega_s/\omega_c)x' + ny')} \, dx' \, dy', \\
&= \frac{1}{4\pi^2} \int_0^{2\pi} e^{-iny'} \left[\int_0^{\pi/2 + \pi M \cos y'/2} e^{-i(m+n\omega_s/\omega_c)x'} \, dx' \right. \\
&\qquad - \int_{\pi/2 + \pi M \cos y'/2}^{3\pi/2 - \pi M \cos y'/2} e^{-i(m+n\omega_s/\omega_c)x'} \, dx' \\
&\qquad \left. + \int_{3\pi/2 - \pi M \cos y'/2}^{2\pi} e^{-i(m+n\omega_s/\omega_c)x'} \, dx' \right] \, dy'.
\end{aligned}
$$

It follows from the Jacobi-Anger expansion [109] of some of the exponential terms in A_{mn}, that, when $mx + ny \neq 0$,

$$A_{mn} = -\sum_p \frac{1}{\pi i \Omega_{mn} T} \left[(-i)^p e^{-i\Omega_{mn}T/4} - i^p e^{-3i\Omega_{mn}T/4} \right] J_p \left(\tfrac{1}{4} \Omega_{mn} M T \right) \int_0^{2\pi} e^{-i(n-p)y} \, dy',$$

where

$$\int_0^{2\pi} e^{-i(n-p)y} \, dy' = \left\{ \begin{array}{ll} 2\pi, & \text{if } n = p, \\ 0, & \text{otherwise.} \end{array} \right.$$

Therefore, when $\Omega_{mn} \neq 0$,

$$A_{mn} = \frac{2}{i\Omega_{mn}T} J_n \left(\tfrac{1}{4} \Omega_{mn} M T \right) i^{m+n} \left[e^{-3\pi in\omega_s/2\omega_c} - (-1)^{m+n} e^{-\pi in\omega_s/2\omega_c} \right],$$

To evaluate the contribution to A_{mn} when $\Omega_{mn} = 0$ we examine the mean value of A_{mn}, which is

$$A_{mn} = \frac{1}{4\pi^2} \int_0^{2\pi} \int_0^{2\pi} A(x', y') \, \mathrm{d}x' \, \mathrm{d}y' = 0.$$

Therefore the voltage output is

$$v_a(t) = A(x', y') = \sum_{mn} a_{mn} e^{i\Omega_{mn}t},$$

where a_{mn} is given in (2.5). This reproduces the formula we found using the Poisson re-summation method.

The directness of the Poisson re-summation is apparent when we consider that to set up Black's method, for uniform sampling, in terms of the time-like variables given in (2.6) requires algebraic (or geometric) verification of the periodicity of $v_a(t)$ in x and y. Additionally, the Poisson re-summation method does not require a double integral, such as in (2.7). Furthermore, to calculate the double integral in (2.7), we require two transformations of the domain of the integral. Thus, it is clear that the derivation of the voltage output of a uniformly sampled single-phase PWM inverter requires much less analytical cost using the Poisson re-summation method than using Black's method.

2.1.3 Analysis of the Frequency Spectrum

The frequency spectrum of $v_a(t)$ is the representation of $v_a(t)$ in the frequency domain. In this thesis, unless otherwise stated, we present the spectrum as the absolute value of the Fourier coefficients (the *amplitude*) against the *harmonic order*, described mathematically as $\Omega_{mn}/\omega_s = m\omega_c/\omega_s + n$. We also plot frequency spectra that are determined by fast Fourier transforms (FFTs) [65] of Matlab simulations of the voltage output waveform. These simulated results are presented in order to check our analytical results are correct.

Similar to [49], we plot spectra where $\omega_c = 21\omega_s$. This ratio between the carrier and signal frequency is suitable for certain inverter design (see [49], for example), and, for illustrative purposes, it is small enough to make the key features of the spectrum easily identifiable. Although we mainly present spectra for $\omega_c = 21\omega_s$, we draw more general conclusions about the spectra from other numerical results (omitted to avoid an overabundance of similar spectra). The convention of plotting spectra where $\omega_c = 21\omega_s$ to illustrate our general conclusions is followed throughout this thesis to allow for exact comparisons of spectra (where necessary). Note that in this chapter we also present some spectra for $\omega_c = 51\omega_s$.

The simulated results are obtained in Matlab by defining time-dependent expressions for the uniform signal wave, $s_u(t)$, and the carrier wave, $w(t)$. An indicator function, square(t), is then defined to be $+1$ when $s_u(t) > w(t)$, and 0 otherwise. We then take an FFT of $2\,\mathrm{square}(t) - 1$ across a single signal period to determine the spectrum.

The frequency spectrum of a uniformly sampled single-phase PWM inverter is shown in figure 2.5, along with simulated spectra to verify the accuracy of our analytical results. There are clusters of peaks around each multiple of the carrier frequency ω_c, with a dominant central peak only

when m is odd, and two dominant central peaks when m is even. Similar to [49], we refer to each cluster of peaks as a *carrier group*. More specifically, each carrier group is the contribution to the spectrum for a single value of m. For example, for the voltage output $v_a(t)$, the $m = 1$ carrier group is the contribution to the spectrum from a_{1n}. In this chapter, the $m = 0$ carrier group constitutes the *low-frequency* components of the spectrum. Similarly, the $m \neq 0$ carrier groups constitute the *high-frequency* components of the spectrum.

The leading low-frequency contribution to the spectrum is at ω_s, and the leading high-frequency contribution to the spectrum is at ω_c. This implies that the low-frequency behaviour of the voltage output is approximating a sine wave with frequency ω_s, in other words the low-frequency behaviour is a good approximation of the desired signal wave. Low-frequency distortion is present in the spectrum, as expected (see [49], for example). Similarly, the high-frequency behaviour is approximating a sine wave with frequency ω_c.

As the ratio ω_c/ω_s increases, the relative delay between the sampling of the signal wave and the switching of the voltage output decreases. Therefore we expect there to be less low-frequency distortion as ω_c/ω_s increases. From comparison of figures 2.5(a) and 2.5(c), as ω_c/ω_s increases, the low-frequency distortion decreases (as predicted), and the magnitude of the peaks in the spectrum decrease when $m + n$ is even. The decrease in magnitude when $m + n$ is even can be explained from examination of (2.5). It is easily verified that as $\omega_c/\omega_s \to \infty$, $e^{-3\pi i n \omega_s/2\omega_c} \to e^{-\pi i n \omega_s/2\omega_c}$, for small n. Therefore, it is straightforward to see that, from (2.5) (specifically the $e^{-3\pi i n \omega_s/2\omega_c} - (-1)^{m+n} e^{-\pi i n \omega_s/2\omega_c}$ term), for fixed m and n (provided $m+n$ is even and $n \neq 0$), $a_{mn} \to 0$ as $\omega_c/\omega_s \to \infty$.

Note that spectra plotted in [49], for example, are plotted for amplitudes of 10^{-4} and greater, whereas we plot spectra for amplitudes of 10^{-5} and greater. Our spectra account for smaller amplitudes because we are plotting complex Fourier coefficients, rather than real Fourier coefficients (see appendix B).

2.2   Asymmetrical Uniform Sampling

Asymmetrical uniform sampling is similar to uniform sampling, except that the signal wave is sampled twice as often, with each sample being used to determine the subsequent switching time. Therefore in each switching period two samples are taken, one at the start of the switching period and one halfway through. The first and second sample determine the switch times $\mathcal{A}_m^a$ and $\mathcal{B}_m^a$, respectively, to be

$$\mathcal{A}_m^a = mT + \frac{T}{4}(1 + s_a(mT)), \qquad \text{and} \qquad \mathcal{B}_m^a = mT + \frac{T}{4}\left(3 - s_a\left(\left(m + \tfrac{1}{2}\right)T\right)\right). \quad (2.8)$$

Thus the voltage output is described as

$$v_a(t) = \begin{cases} +1, & \text{if } \mathcal{A}_m^a < t < \mathcal{B}_m^a, \\ -1, & \text{otherwise.} \end{cases}$$

We give brief accounts of the calculations for both the Poisson re-summation method and Black's method (in sections 2.2.1 and 2.2.2, respectively), as the details of the calculations are similar

(a) *Analytical.*

(b) *Simulated.*

(c) *Analytical.*

(d) *Simulated.*
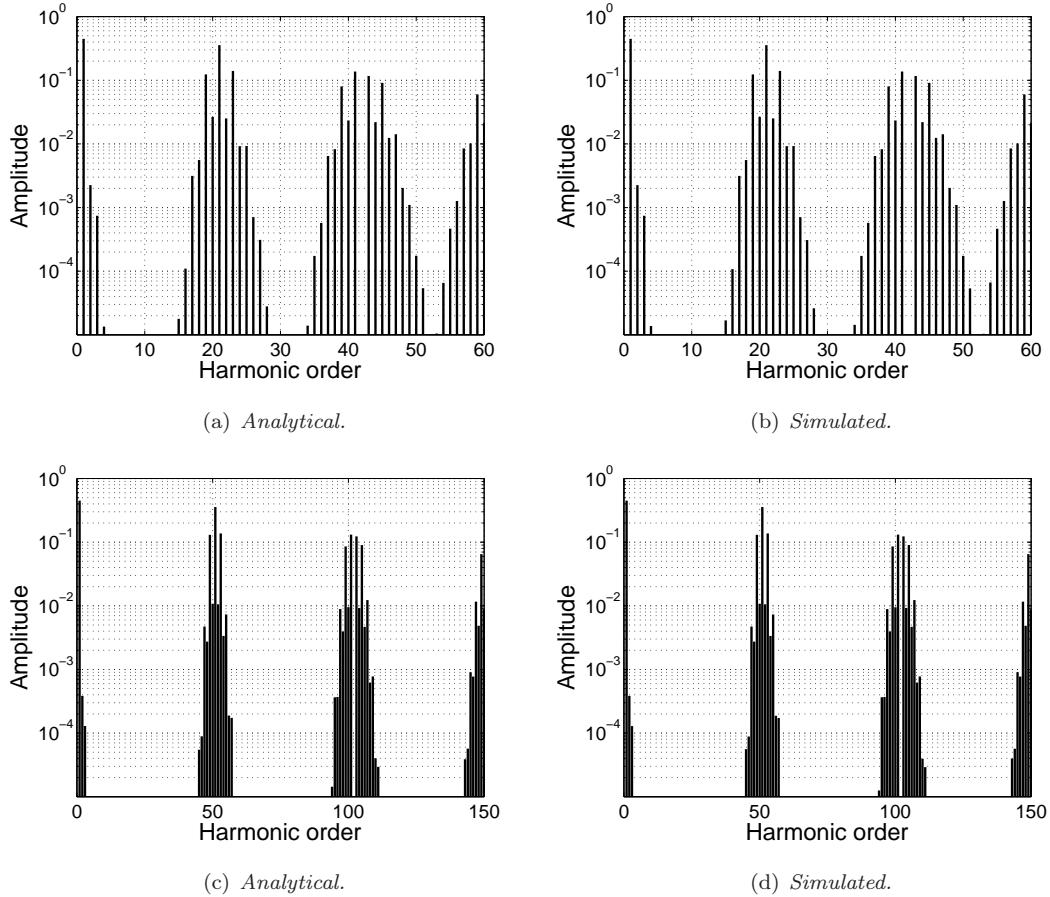
Figure 2.5: *Frequency spectrum of the voltage output of a uniformly sampled PWM inverter, where the x-axis is $m\omega_c/\omega_s + n$, and the y-axis is the absolute value of the Fourier coefficients a_{mn} (given in (2.5)). The parameter values are $M = 0.9$, $\omega_c = 21\omega_s$ in (a) and (b), and $\omega_c = 51\omega_s$ in (c) and (d).*

to those in section 2.1. We also analyse the frequency spectrum of $v_a(t)$ for PWM inverters that use symmetrical uniform sampling in section 2.2.3.

2.2.1 The Poisson Re-summation Method

Determining the voltage output of an inverter with asymmetrical uniform sampling is broadly the same as for symmetrical uniform sampling, with minor algebraic differences. The voltage output $v_a(t)$ is defined, with switch times from (2.8), as

$$v_a(t) = 1 - 2\sum_m \psi(t; \mathcal{A}_m^a, \mathcal{B}_m^a) \equiv 1 - 2f(t).$$

To calculate the non-trivial contribution to the frequency spectrum of $v_a(t)$, we determine the spectrum of $f(t)$. Therefore, for $\omega \neq 0$,

$$
\begin{aligned}
\hat{f}(\omega) &= -2\sum_m \left[-\frac{1}{i\omega} e^{-i\omega t} \right]_{\mathcal{A}_m^a}^{\mathcal{B}_m^a}, \\
&= 2\sum_m \frac{1}{i\omega} e^{-i\omega mT} \left(e^{-i\omega T(3 - M\cos(\omega_s(m+1/2)T))/4} - e^{-i\omega T(1 + M\cos\omega_s mT)/4} \right).
\end{aligned}
$$

From the Jacobi-Anger expansions of the $e^{-i\omega MT \cos\omega_s mT/4}$ and $e^{i\omega MT \cos(\omega_s(m+1/2)T)/4}$ terms, when $\omega \neq 0$,

$$
\hat{f}(\omega) = \sum_{mn} \frac{2}{i\omega} J_n\left(\tfrac{1}{4}\omega MT\right) e^{in\omega_s mT} e^{-in\omega_s T/4} (i^{m+n} - (-i)^{m+n}) e^{-i\omega nT}.
$$

Poisson re-summing in m determines

$$
\hat{f}(\omega) = \sum_{mn} \int_{-\infty}^{\infty} \frac{2}{i\omega T} J_n\left(\tfrac{1}{4}\omega MT\right) (i^{m+n} - (-i)^{m+n}) e^{i\Omega_{mp} t - in\omega_s T/4} e^{-i\omega t} \, \mathrm{d}t.
$$

Therefore

$$
f(t) = \sum_{mn} \frac{2}{i\Omega_{mn} T} J_n\left(\tfrac{1}{4}\Omega_{mn} MT\right) i^{m+n} (1 - (-1)^{m+n}) e^{i\Omega_{mn} t - in\omega_s T/4},
$$

where the terms in the sum that correspond to $\Omega_{mn} = 0$ are omitted. By the same logic as in section 2.1.1, the contribution to $v_a(t)$ when $\Omega_{mn} = 0$ corresponds to the mean value of $v_a(t)$. The mean value of $v_a(t)$ is zero (see appendix A.1). Therefore the output voltage is given by

$$
v_a(t) = \sum_{mn} a_{mn} e^{i\Omega_{mn} t - in\omega_s T/4},
$$

where

$$
a_{mn} = \begin{cases} 0, & \text{if } \Omega_{mn} = 0 \\ \dfrac{2}{i\Omega_{mn} T} J_n\left(\tfrac{1}{4}\Omega_{mn} MT\right) i^{m+n} (1 - (-1)^{m+n}), & \text{if } \Omega_{mn} \neq 0. \end{cases} \tag{2.9}
$$

Our Fourier coefficients agree with [49], except [49] omit the delay in the voltage output, probably due to an implicit shift of their carrier wave by a quarter of a switching period.

2.2.2 Black's Method

This calculation follows the structure of the calculation in section 2.1.2. Similar to symmetrical uniform sampling we want to formulate a problem that has $v_a(t)$ equal to a function that is 2π-periodic in each of its arguments. From (2.8) we write

$$
v_a(t) = \begin{cases} -1, & \text{if } nT + \tfrac{T}{4}(1 + M\cos\omega_s nT) < \omega_c t < nT + \tfrac{T}{4}(3 - M\cos(\omega_s(n+\tfrac{1}{2})T)), \\ +1, & \text{otherwise.} \end{cases}
$$

In the interval $nT < t < (n+1)T$,

$$
v_a(t) = A_1'(x', y_1') + A_2'(x', y_2') = \begin{cases} -1, & \text{if } 2\pi n + \tfrac{\pi}{2} + \tfrac{\pi M}{2}\cos y_1' < x' < 2\pi n + \tfrac{3\pi}{2} - \tfrac{\pi M}{2}\cos y_2', \\ +1, & \text{otherwise,} \end{cases}
$$

where

$$A_1'(x',y_1') = \begin{cases} +1, & 2\pi n < x' < 2\pi n + \frac{\pi}{2} + \frac{\pi M}{2}\cos y_1', \\ -1, & 2\pi n + \frac{\pi}{2} + \frac{\pi M}{2}\cos y_1' < x' < 2\pi(n+\frac{1}{2}), \\ 0, & 2\pi(n+\frac{1}{2}) < x' < 2\pi(n+1) \end{cases}$$

$$A_2'(x',y_2') = \begin{cases} 0, & 2\pi n < x' < 2\pi(n+\frac{1}{2}) \\ -1, & 2\pi(n+\frac{1}{2}) < x' < 2\pi n + \frac{3\pi}{2} - \frac{\pi M}{2}\cos y_2', \\ +1, & 2\pi n + \frac{3\pi}{2} - \frac{\pi M}{2}\cos y_2' < x' < 2\pi(n+1), \end{cases}$$

where

$$x' = \omega_c t, \qquad y_1' = \omega_s n T, \quad \text{and} \quad y_2' = \omega_s\left(n + \frac{1}{2}\right)T.$$

It is straightforward to verify that $A_1'(x',y_1')$ is 2π-periodic in x' and y_1', and similarly $A_2'(x',y_2')$ is 2π-periodic in x' and y_2'. Both y_1' and y_2' are piecewise constants, meaning $e^{iny_1'}$ and $e^{iny_2'}$ are difficult to interpret. Therefore, in order to determine a double Fourier series for $A_1'(x',y_1')$ and $A_2'(x',y_2')$, we first express them as functions of x and y (given in (2.6)). It is obvious that $x' = x$, and similarly to section 2.1.2 we define

$$y_1' = y - \frac{\omega_s}{\omega_c}(x - 2\pi n), \qquad \text{and} \qquad y_2' = y - \frac{\omega_s}{\omega_c}(x - 2\pi(n+\frac{1}{2})).$$

Therefore in the interval $nT < t < (n+1)T$,

$$A_1(x,y) = \begin{cases} +1, & 2\pi n < x < 2\pi n + \frac{\pi}{2} + \frac{\pi M}{2}\cos(y - \frac{\omega_s}{\omega_c}(x - 2\pi n)), \\ -1, & 2\pi n + \frac{\pi}{2} + \frac{\pi M}{2}\cos(y - \frac{\omega_s}{\omega_c}(x - 2\pi n)) < x < 2\pi(n+\frac{1}{2}), \\ 0, & 2\pi(n+\frac{1}{2}) < x < 2\pi(n+1) \end{cases}$$

$$A_2(x,y) = \begin{cases} 0, & 2\pi n < x < 2\pi(n+\frac{1}{2}) \\ -1, & 2\pi(n+\frac{1}{2}) < x < 2\pi n + \frac{3\pi}{2} - \frac{\pi M}{2}\cos(y - \frac{\omega_s}{\omega_c}(x - 2\pi(n=\frac{1}{2}))), \\ +1, & 2\pi n + \frac{3\pi}{2} - \frac{\pi M}{2}\cos(y - \frac{\omega_s}{\omega_c}(x - 2\pi(n+\frac{1}{2}))) < x < 2\pi(n+1). \end{cases}$$

It is straightforward to verify that $A_1(x,y)$ and $A_2(x,y)$ are both 2π-periodic in x and y. Therefore we have

$$A_1(x,y) = \sum_{mn} A_{mn}^1 e^{i(mx+ny)},$$

where

$$A_{mn}^1 = \frac{1}{4\pi^2}\int_0^{2\pi}\int_0^{2\pi} A_1(x,y)e^{-i(mx+ny)}\,\mathrm{d}x\,\mathrm{d}y,$$

and similarly for $A_2(x,y)$ and A_{mn}^2. Unfortunately we cannot directly evaluate these integrals, because the limits of the integrals are given by implicit equations relating x and y. We now transform the integral of A_{mn}^1 to one over x' and y_1', and the integral of A_{mn}^2 to one over x' and y_2'.

We first examine A_{mn}^1, where we are changing the domain of integration from $D = \{(x,y) : 0 \le x, y \le 2\pi\}$ in the xy-plane to $D_1' = \{(x',y_1') : 0 \le x' \le 2\pi, -\frac{\omega_s}{\omega_c}x \le y_1' \le 2\pi - \frac{\omega_s}{\omega_c}x\}$ in the $x'y_1'$-plane (D and D_1' are illustrated in figure 2.4). Since $A_1'(x',y_1')$ is 2π-periodic in y_1', then D_1'

can be replaced with $D_1'' = \{(x', y_1') : 0 \leq x', y_1' \leq 2\pi\}$. Therefore, since $\partial(x, y)/\partial(x', y_1') = 1$,

$$
\begin{aligned}
A_{mn}^1 &= \frac{1}{4\pi^2} \int \int_D A_1(x, y) e^{-i(mx+ny)} \, dx \, dy, \\
&= \begin{cases} 0, & \text{if } \Omega_{mn} = 0 \\ \frac{1}{i\Omega_{mn}T} \left[1 + e^{-i\Omega_{mn}T/2} - 2(-i)^n e^{-i\Omega_{mn}T/4} J_n \left(\frac{1}{4}\Omega_{mn}MT \right) \right], & \text{otherwise.} \end{cases}
\end{aligned}
$$

For A_{mn}^2, we change the domain of integration from $D = \{(x, y) : 0 \leq x, y \leq 2\pi\}$ in the xy-plane to $D_2' = \{(x', y_2') : 0 \leq x' \leq 2\pi, -\pi - \frac{\omega_s}{\omega_c}x \leq y_2' \leq \pi - \frac{\omega_s}{\omega_c}x\}$ in the $x'y_2'$-plane. Since $A_2'(x', y_2')$ is 2π-periodic in x' and y_2', then D_2' can be replaced with $D_2'' = \{(x', y_2') : -\pi \leq x', y_2' \leq \pi\}$. Therefore, since $\partial(x, y)/\partial(x', y_2') = 1$, and similarly to A_{mn}^1,

$$
\begin{aligned}
A_{mn}^2 &= \frac{1}{4\pi^2} \int \int_D A_2(x, y) e^{-i(mx+ny)} \, dx \, dy, \\
&= \begin{cases} 0, & \text{if } \Omega_{mn} = 0 \\ \frac{1}{i\Omega_{mn}T} \left[2i^{m+n} e^{-in\omega_s T/4} J_n \left(\frac{1}{4}\Omega_{mn}MT \right) - e^{in\omega_s T/2}(e^{i\Omega_{mn}T/2} + 1) \right], & \text{otherwise.} \end{cases}
\end{aligned}
$$

Therefore

$$
v_a(t) = \sum_{mn} (A_{mn}^1 + A_{mn}^2) e^{i(mx+ny)} \equiv \sum_{mn} a_{mn} e^{i\Omega_{mn}t} e^{-in\omega_s T/4},
$$

where a_{mn} is given in (2.9).

Note that, by comparison of calculations in section 2.2.1 and 2.2.2, the algebraic complexity of Black's method is highlighted (compared to the Poisson re-summation method). Additionally, Black's method incurs further algebraic difficulty for asymmetrical uniform sampling than for symmetrical uniform sampling (by comparison of sections 2.1.2 and 2.2.2). This is due to the fact we are required to calculate two Fourier coefficients, rather than one, for asymmetrical uniform sampling.

2.2.3 Analysis of the Frequency Spectrum

Frequency spectra plotted here are identical to those in [49], since we plot the absolute value of the Fourier coefficients. We plot frequency spectra for $v_a(t)$ of a PWM inverter that uses asymmetrical uniform sampling in figure 2.6 for a range of ratios ω_c/ω_s. We also include simulated spectra, to verify the accuracy of our analytical results. Carrier groups in even m have one dominant central peak, and carrier groups in odd m have two dominant central peaks. The leading low-frequency contribution to the spectrum is at ω_s, and the leading high-frequency contribution to the spectrum is at ω_c. Therefore, asymmetrical uniform sampling generates a voltage output with low-frequency behaviour that provides a good approximation to the desired signal wave.

Less distortion is generated using asymmetrical uniform sampling, compared to symmetrical uniform sampling, as anticipated by [49], for example. This is a consequence of the signal wave being sampled twice as often (compared to symmetrical uniform sampling). Mathematically, the reduction in distortion is a consequence of the $1 - (-1)^{m+n}$ term, which means there is contribution to the frequency spectrum only when $m + n$ is odd. Similar to output voltage spectra

(a) *Analytical.*

(b) *Simulated.*

(c) *Analytical.*

(d) *Simulated.*
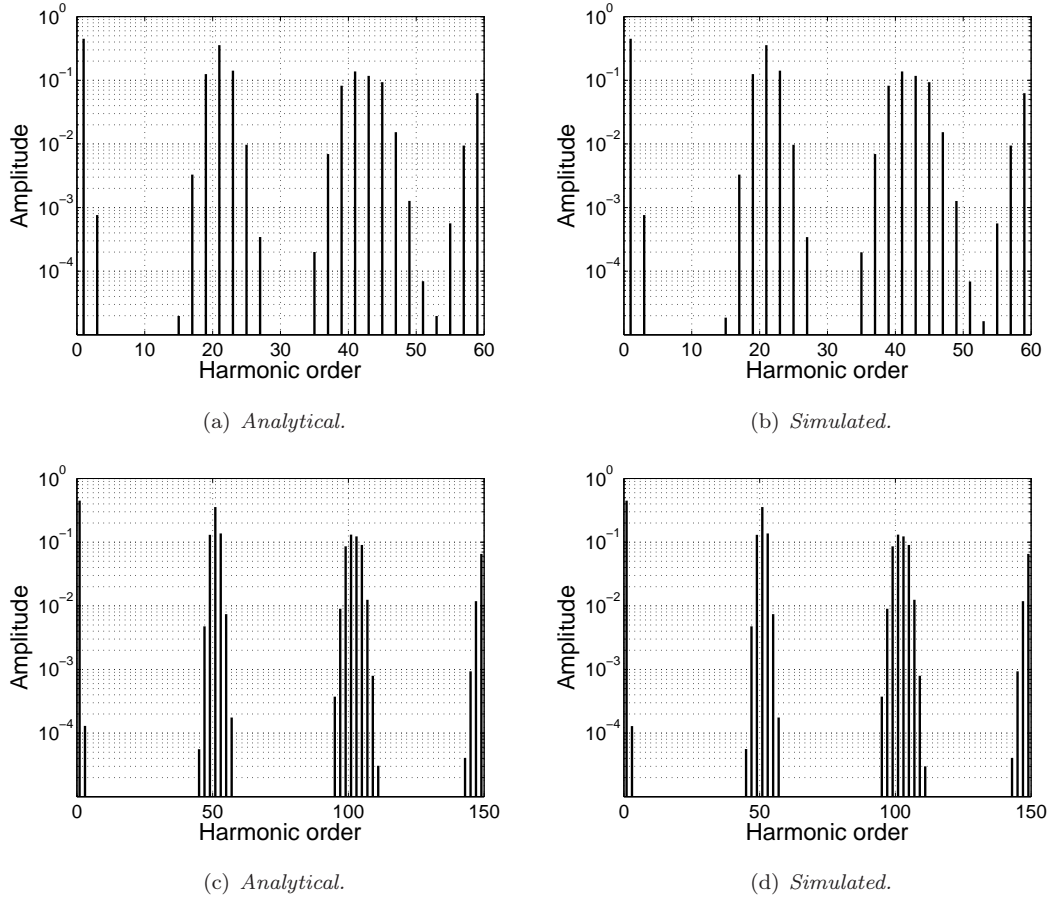
Figure 2.6: *Frequency spectrum of the voltage output of a PWM inverter using asymmetrical uniform sampling, where $M = 0.9$. In (a) and (b), $\omega_c = 21\omega_s$, and in (c) and (d), $\omega_c = 51\omega_s$.*

for inverters with symmetrical uniform sampling, the magnitude of the low-frequency distortion decreases as ω_c/ω_s increases (from comparison of figures 2.8(a) and 2.8(b)). This is expected, because the delay between the sampling of the signal wave, and the switching of the voltage output decreases as ω_c/ω_s increases. The high-frequency distortion remains approximately constant as ω_c/ω_s increases.

2.3 Natural Sampling

In a naturally sampled PWM inverter, switching occurs at the exact points when the signal wave crosses the carrier wave. This instantaneous sampling and switching is what makes natural sampling ideally suited to analogue application, but less suitable for digital implementation [87]. Another consequence of instantaneous sampling and switching is that inverters that use natural sampling generate voltage outputs with insignificant low-frequency distortion [69].

We describe the voltage output $v_a(t)$ as

$$v_a(t) = \begin{cases} +1, & \text{when } s_a(t) > w(t), \\ -1, & \text{when } s_a(t) < w(t), \end{cases}$$
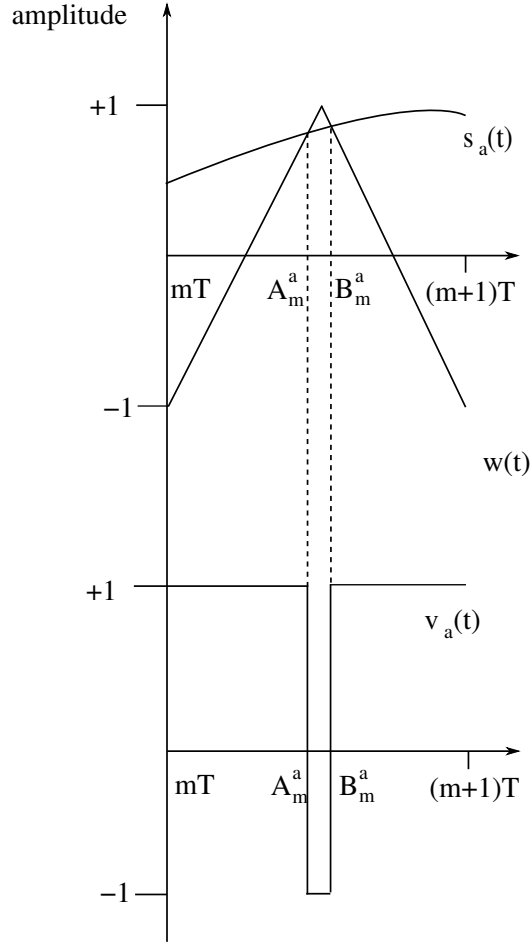
Figure 2.7: *Illustration of how the switch times of the voltage output are determined using naturally sampled PWM over a single switching period. We see that $v_a(t)$ is $+1$ when $s_a(t) > w(t)$ and -1 otherwise, with $t = \mathcal{A}_m^a$, $\mathcal{B}_m^a$ when $s_a(t)$ and $w(t)$ cross. The down-switching and up-switching of the output $v_a(t)$ (corresponding, respectively, to $\mathcal{A}_m^a$ and $\mathcal{B}_m^a$) occur when the graphs of $s_a(t)$ and $w(t)$ intersect.*

as illustrated in figure 2.7. Alternatively, we also define $v_a(t)$ as

$$v_a(t) = \begin{cases} +1, & \text{if } \mathcal{A}_m^a < t < \mathcal{B}_m^a, \\ -1, & \text{otherwise,} \end{cases} \tag{2.10}$$

where the switching times are the times when $s_a(t) = w(t)$, and are defined *implicitly* to be

$$\mathcal{A}_m^a = mT + \frac{T}{4}(1 + s_a(\mathcal{A}_m^a)), \qquad \text{and} \qquad \mathcal{B}_m^a = mT + \frac{T}{4}(3 - s_a(\mathcal{B}_m^a)). \tag{2.11}$$

We now find the frequency spectrum of a naturally sampled single-phase PWM inverter using both Black's method in section 2.3.2, and the Poisson re-summation method in section 2.3.1.

2.3.1 The Poisson Re-summation Method

We now use the Poisson re-summation method to determine a Fourier series for $v_a(t)$. We express $v_a(t)$ as, from (2.10),

$$v_a(t) = 1 - 2\sum_m \psi(t; \mathcal{A}_m^a, \mathcal{B}_m^a) \equiv 1 - 2f(t),$$

where $\mathcal{A}_m^a$ and $\mathcal{B}_m^a$ are given in (2.11). For notational brevity, we determine the frequency spectrum of $f(t)$, because the non-trivial components of the spectrum of $v_a(t)$ are contained in $f(t)$. Unlike uniform sampling, to determine the spectrum of $f(t)$, we first use the Poisson re-summation formula, rather than taking a Fourier transform. In order apply the Poisson re-summation formula to $f(t)$ we introduce functions $t + \alpha(t)$ and $t + \beta(t)$ that when sampled discretely give us $\mathcal{A}_m^a$ and $\mathcal{B}_m^a$. To this end, similar to [99], we introduce functions defined implicitly by

$$\alpha(t) = \frac{T}{4}(1 + s_a(t + \alpha(t))), \qquad \text{and} \qquad \beta(t) = \frac{T}{4}(3 - s_a(t + \beta(t))).$$

Applying the Poisson re-summation to $f(t)$ determines

$$f(t) = \frac{1}{T}\sum_m \int_{-\infty}^{\infty} e^{2\pi i m\tau/T} \psi(t; \tau + \alpha(\tau), \tau + \beta(\tau)) \, \mathrm{d}\tau.$$

Here τ is a time-like variable such that the top-hat function is non-zero only in the interval $\tau + \alpha(\tau) < t < \tau + \beta(\tau)$, however, we need to re-write this interval in the form $\tau_1 < \tau < \tau_2$ in order to determine the appropriate interval over which to integrate. Therefore we introduce $A(t)$ and $B(t)$ such that

$$t = \tau + \alpha(\tau) \iff \tau = t - A(t),$$
$$t = \tau + \beta(\tau) \iff \tau = t - B(t).$$

Thus

$$\tau_1 = t - B(t), \qquad \text{and} \qquad \tau_2 = t - A(t).$$

If we now consider τ such that $\tau = t - A(t)$, and equivalently $t = \tau + \alpha(\tau)$ we see that

$$A(t) = t - \tau = \alpha(\tau) = \frac{T}{4}(1 + s_a(\tau + \alpha(\tau))) = \frac{T}{4}(1 + s_a(t)),$$

and we have an *explicit* expression for $A(t)$. Similarly we see that $B(t) = \frac{T}{4}(3 - s_a(t))$, and hence our expression for $f(t)$ becomes

$$
\begin{aligned}
f(t) &= \frac{1}{T}\sum_m \int_{t-B(t)}^{t-A(t)} e^{2\pi i m\tau/T} \, \mathrm{d}\tau, \\
&= \frac{1}{2}(1 - s_a(t)) + \sum_{m\neq 0} \frac{e^{2\pi i mt/T}}{2\pi i m}(e^{-2\pi i mA(t)/T} - e^{-2\pi i mB(t)/T}).
\end{aligned}
$$

From the Jacobi-Anger expansions [109] of some of the exponential terms in $f(t)$, it is easily verified that

$$f(t) = \frac{1}{2}(1 - s_a(t)) + \sum_{m\neq 0}\sum_n \frac{e^{i\Omega_{mn}t}}{2\pi i m} i^{m+n}(1 - (-1)^{m+n})J_n\left(\tfrac{1}{2}m\pi M\right),$$

where the sum $\sum_{m\neq 0}$ is the sum over all m from ∞ to $-\infty$ except $m = 0$. Therefore the voltage output $v_a(t)$ is given by

$$v_a(t) = s_a(t) + \sum_{mn} a_{mn} e^{i\Omega_{mn}t}, \tag{2.12}$$

where

$$a_{mn} = \begin{cases} 0, & m = 0, \\ \dfrac{1}{\pi im} J_n\left(\tfrac{1}{2} m\pi M\right) i^{m+n} (1 - (-1)^{m+n}), & m \neq 0, \end{cases} \tag{2.13}$$

This reproduces the output voltages determined in [31, 49]. We note that, from (2.12) and (2.13), the contribution to the spectrum of $v_a(t)$ from the $m = 0$ carrier group is exactly the same as the spectrum of the signal wave. In other words, naturally sampled PWM inverters generate no low-frequency distortion in the spectrum of the output voltages (shown previously in [31, 49], for example).

2.3.2 Black's Method

Black's method is most easily applied to natural sampling, as shown in [49]. We reproduce the work of [49] here, and examine how determine the voltage output of a naturally sampled single-phase PWM inverter using Black's method. From the fast time-like variable, x, and slow time-like variable, y, given in (2.6), coupled with the voltage output given in (2.10) (with switch times in (2.11)), we express $v_a(t)$ as

$$v_a(t) = A(x,y) = \begin{cases} +1, & \text{if } 2\pi n + \frac{\pi}{2} + \frac{\pi M}{2}\cos y < x < 2\pi n + \frac{3\pi}{2} - \frac{\pi M}{2}\cos y, \\ -1, & \text{otherwise.} \end{cases}$$

Note that $A(x,y)$ is 2π-periodic with respect to x and y.

Because of the periodicity of $A(x,y)$ in x and y, we can write $A(x,y)$ as a double Fourier series, and rewriting x, y in terms of t from (2.6) determines a double Fourier series for $v_a(t) = A(x,y)$. In other words we want to find

$$A(x,y) = \sum_{mn} A_{mn} e^{i(mx+ny)}.$$

The coefficients A_{mn} are determined by

$$\begin{aligned}
A_{mn} &= \frac{1}{4\pi^2} \int_0^{2\pi} \int_0^{2\pi} A(x,y) e^{-i(mx+ny)} \, \mathrm{d}x \, \mathrm{d}y, \tag{2.14} \\
&= \frac{1}{4\pi^2} \int_0^{2\pi} e^{-iny} \left[\int_0^{\pi/2+\pi M\cos y/2} e^{-imx} \, \mathrm{d}x - \int_{\pi/2+\pi M\cos y/2}^{3\pi/2-\pi M\cos y/2} e^{-imx} \, \mathrm{d}x \right. \\
&\qquad\qquad \left. + \int_{3\pi/2-\pi M\cos y/3}^{2\pi} e^{-imx} \, \mathrm{d}x \right] \mathrm{d}y. \\
&= -\sum_p \frac{1}{2\pi^2 im} J_p\left(\tfrac{1}{2} m\pi M\right) \left(e^{-i(m+p)\pi/2} - e^{i(m+p)\pi/2} \right) \int_0^{2\pi} e^{-i(n-p)y} \, \mathrm{d}y.
\end{aligned}$$

Now

$$\int_0^{2\pi} e^{-i(n-p)y} \, \mathrm{d}y = \begin{cases} 2\pi, & \text{if } n = p, \\ 0, & \text{otherwise.} \end{cases}$$

Therefore we find, for $m \neq 0$,

$$A_{mn} = \frac{1}{\pi i m} J_n \left(\tfrac{1}{2} m \pi M \right) i^{m+n} (1 - (-1)^{m+n}). \tag{2.15}$$

When $m = 0$, (2.14) gives

$$A_{0n} = \frac{M}{4\pi} \int_0^{2\pi} e^{-iny} \cos y \, dy = \begin{cases} \frac{M}{2}, & \text{if } n = \pm 1, \\ 0, & \text{otherwise.} \end{cases}$$

Therefore, the low-frequency contribution to the frequency spectrum from the $m = 0$ terms is identical to the reference wave. In other words no low-frequency distortion is generated in the voltage output of a naturally sampled PWM inverter. Thus the voltage output is

$$v_a(t) = A(x, y) = s_a(t) + \sum_{mn} a_{mn} e^{i\Omega_{mn}t},$$

where, a_{mn} is given in (2.13).

Note that, for natural sampling, while Black's method still requires the derivation of a double integral, setting up the calculation is algebraically simpler than for uniform sampling. Furthermore, unlike with uniform sampling, no changes to the integration bounds are required to calculate the double integral. Therefore, it is clear that Black's method is more straightforward for the calculation of the voltage output of a naturally sampled single-phase inverter, compared to a uniformly sampled single-phase inverter. It can also be argued that both Black's method and the Poisson re-summation method have advantages when calculating the voltage output of naturally sampled inverters, because while Black's method requires a double integral, determining the switch times of the inverter explicitly using the Poisson re-summation method is algebraically complex.

2.3.3   Analysis of the Frequency Spectrum

The frequency spectrum of $v_a(t)$ is plotted in figure 2.8, and, to verify our analytical results, we also illustrate the simulated spectrum of $v_a(t)$. The spectra in this section are identical to those in [49]. We omit plots of the spectrum of $v_a(t)$ for a range of ω_c/ω_s, because, from (2.13), the Fourier coefficients a_{mn} are independent of ω_c and ω_s. Note that the low-frequency behaviour is *exactly* the contribution from the signal wave, with peaks at $\pm\omega_s$ only. In other words, naturally sampled PWM inverters generate voltage outputs with no low-frequency distortion.

Carrier groups with odd m have one dominant central peak, and carrier groups with even m have two dominant central peaks. There are less high-frequency contributions to the spectrum, compared to the spectrum shown in figure 2.5(a). This is a consequence of the signal wave being sampled twice as often using natural sampling compared to uniform sampling. Specifically, there is a contribution to the frequency spectrum only when $m + n$ is even, which is a consequence of the $1 - (-1)^{m+n}$ term. In summary, naturally sampled PWM inverters generate voltage outputs with no low-frequency distortion, and fewer high-frequency components compared to the voltage output of inverters that use symmetrical uniform sampling.

(a) *Analytical.*

(b) *Simulated.*
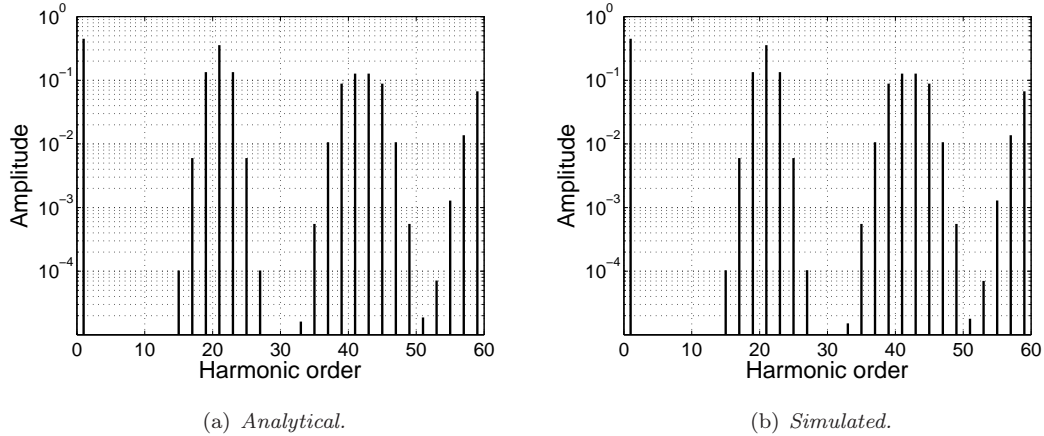
Figure 2.8: *Frequency spectrum of the voltage output of a naturally sampled PWM inverter found using Black's method, where $M = 0.9$. In (a), $\omega_c = 21\omega_s$, and in (b), $\omega_c = 51\omega_s$.*
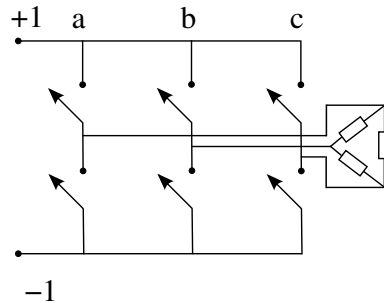
Figure 2.9: *Circuit diagram of a three-phase inverter wired in the Δ configuration.*

3 Two-phase and Three-phase Inverters

In this section we examine two-phase and three-phase inverters (specifically three-phase inverters wired in the Δ configuration). Two-phase and three-phase inverters are more widely used than single-phase inverters, due to more desirable operating conditions and because they generate less high-frequency components in the voltages and currents compared to single-phase inverters (see [62, 80, 95], for example). A two-phase inverter is illustrated in figure 1.3(b), and a three-phase inverter wired in the delta configuration is illustrated in figure 2.9.

Previously, when examining single-phase inverters, we were concerned with the voltage output only. For two-phase and three-phase inverters, we are also interested in the load voltages (the voltages across the loads). In a single-phase inverter, the load voltage is simply the output voltage, but in two-phase and three-phase inverters the load voltage is the difference between output voltages.

In section 3.1, we determine the output voltages of two-phase inverters, and load voltages of two-phase inverters wired in series. The output voltages and load voltages of three-phase inverters are determined in section 3.2. For illustrative purposes, we present voltage spectra for two-phase

and three-phase inverters that use symmetrical uniform sampling in section 3.3.

3.1 Two-phase Inverters

A two-phase inverter has two voltage outputs, one from each phase-leg, and one load voltage. The two phase-legs in a two-phase inverter are generated by signal waves that are π radians out of phase from each other. Therefore, it is straightforward to see that the voltage outputs from each phase-leg are given by

$$
\begin{aligned}
v_a(t) &= 1 - 2 \sum_m \psi(t; \mathcal{A}_m^a, \mathcal{B}_m^a), \\
v_b(t) &= 1 - 2 \sum_m \psi(t; \mathcal{A}_m^b, \mathcal{B}_m^b),
\end{aligned}
$$

where the switch times $\mathcal{A}_m^a$ and $\mathcal{B}_m^a$ are given in (2.4), (2.8) or (2.11) for symmetrical uniform, asymmetrical uniform or natural sampling, respectively. Furthermore, the switch times $\mathcal{A}_m^b$ and $\mathcal{B}_m^b$ are defined similarly to (2.4), (2.8) or (2.11) for symmetrical uniform, asymmetrical uniform or natural sampling, respectively, with signal wave $s_b(t) = M \cos(\omega_s t - \pi)$. It is easily verified, from section 2, that the voltage outputs can be written as

$$
\begin{aligned}
v_a(t) &= \sum_{mn} a_{mn} e^{i\Omega_{mn} t} \\
v_b(t) &= \sum_{mn} a_{mn} e^{i\Omega_{mn} t} (-1)^n,
\end{aligned}
$$

where the Fourier coefficients a_{mn} are given in (2.5) for symmetrical uniform sampling, (2.9) for asymmetrical uniform sampling, and (2.13) for natural sampling. The load voltage $v_{ab}(t)$ of a two-phase inverter is the difference between the output voltages, in other words $v_{ab}(t) = v_a(t) - v_b(t)$. Note that the notation ab denotes the *load connection*, which means the load is connected between phase-leg a and phase-leg b. Therefore,

$$
v_{ab}(t) = \sum_{mn} v_{mn} e^{i\Omega_{mn} t}, \tag{3.1}
$$

where $v_{mn} = a_{mn}(1 - (-1)^n)$. Thus the Fourier coefficients for the voltage difference in a two-phase inverter differ from the Fourier coefficients of the voltage outputs by the $1 - (-1)^n$ term. This term indicates that there is only contribution to the frequency spectrum of the voltage difference when n is odd; this conclusion holds for all sampling methods (as discussed in [49], for example).

3.2 Three-phase Inverters

A three-phase inverter has three voltage outputs (one from each phase-leg) and three loads (thus, three load voltages). The three phase-legs in a three-phase inverter are generated from signal waves that are $2\pi/3$ radians out of phase from each other, respectively. Therefore, we define the

voltage outputs as discrete switching functions in the time domain to be

$$
\begin{aligned}
v_a(t) &= 1 - 2\sum_m \psi(t; \mathcal{A}_m^a, \mathcal{B}_m^a), \\
v_b(t) &= 1 - 2\sum_m \psi(t; \mathcal{A}_m^b, \mathcal{B}_m^b), \\
v_c(t) &= 1 - 2\sum_m \psi(t; \mathcal{A}_m^c, \mathcal{B}_m^c),
\end{aligned}
$$

where the switch times $\mathcal{A}_m^a$, $\mathcal{B}_m^a$, $\mathcal{A}_m^b$, $\mathcal{B}_m^b$, and $\mathcal{A}_m^c$, $\mathcal{B}_m^c$, are given in (2.4), (2.8) or (2.11) for symmetrical uniform, asymmetrical uniform or natural sampling, respectively, with respective signal waves $s_a(t)$ (given in (2.1)), $s_b(t) = M\cos(\omega_s t - 2\pi/3)$ and $s_c(t) = M\cos(\omega_s t + 2\pi/3)$. Therefore, it is easily verified from section 2, that the three voltage outputs are

$$
\begin{aligned}
v_a(t) &= \sum_{mn} a_{mn} e^{i\Omega_{mn} t}, \\
v_b(t) &= \sum_{mn} a_{mn} e^{i\Omega_{mn} t} e^{-2\pi i n/3}, \\
v_c(t) &= \sum_{mn} a_{mn} e^{i\Omega_{mn} t} e^{2\pi i n/3},
\end{aligned}
$$

where a_{mn} is given in (2.5), (2.9) or (2.13) for symmetrical uniform, asymmetrical uniform or natural sampling, respectively. For a three-phase inverter wired in the Δ configuration, it is striaghtforward to see that, from figure 2.9, the load voltages are

$$
\begin{aligned}
v_{ab}(t) &= \sum_{mn} v_{mn} e^{i\Omega_{mn} t}, & (3.2) \\
v_{bc}(t) &= \sum_{mn} v_{mn} e^{i\Omega_{mn} t} e^{-2\pi i n/3}, & (3.3) \\
v_{ca}(t) &= \sum_{mn} v_{mn} e^{i\Omega_{mn} t} e^{2\pi i n/3}, & (3.4)
\end{aligned}
$$

where $v_{mn} = a_{mn}(1 - e^{-2\pi i n/3})$. Similarly, from appendix C, the load voltages of a three-phase inverter wired in the Y configuration are

$$
\begin{aligned}
v_{ap}(t) &= \sum_{mn} v_{mn}^Y e^{i\Omega_{mn} t}, \\
v_{bp}(t) &= \sum_{mn} v_{mn}^Y e^{i\Omega_{mn} t} e^{-2\pi i n/3}, \\
v_{cp}(t) &= \sum_{mn} v_{mn}^Y e^{i\Omega_{mn} t} e^{2\pi i n/3},
\end{aligned}
$$

where $v_{mn}^Y = a_{mn}(2 - e^{-2\pi i n/3} - e^{2\pi i n/3})/3$. Note that the $1 - e^{-2\pi i n/3}$ or $2 - e^{-2\pi i n/3} - e^{2\pi i n/3}$ terms in the Fourier coefficients for the load voltages of three-phase inverters wired in the Δ or the Y configuration, respectively, signify that there is no contribution to the frequency spectrum of any of the voltage differences when n is a multiple of 3, as expected (see [49], for example).

3.3 Spectra for Uniform Sampling

We calculated the frequency spectrum of the voltage output of a symmetrically uniformly sampled single-phase PWM inverter using both the Poisson re-summation method and Black's

(a) *Analytical*

(b) *Simulated.*
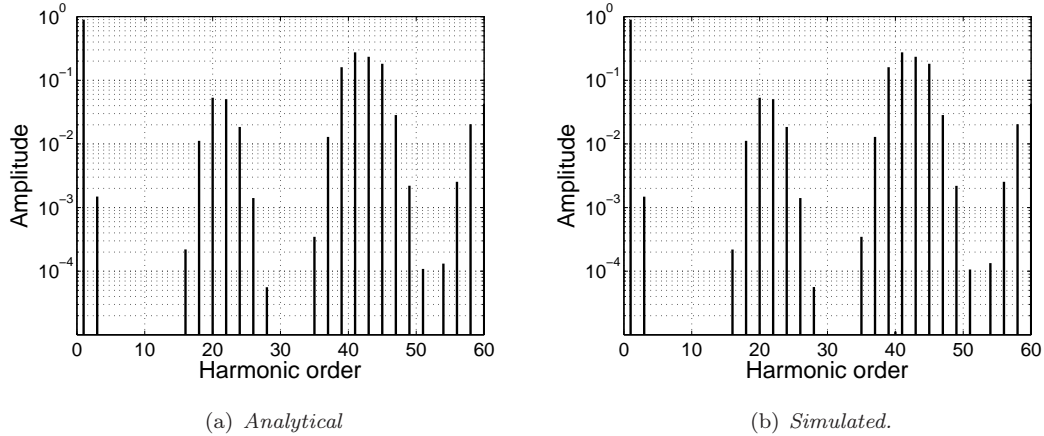
Figure 2.10: *Frequency spectrum of the load voltage a uniformly sampled two-phase PWM inverter wired in series, where $M = 0.9$ and $\omega_c = 21\omega_s$.*

method in section 2.1, and we use the results of those calculations extensively here. In this section, we omit spectra for the load voltages for a range of ratios ω_c/ω_s, because the effects on the spectrum are similar to those shown in figure 2.5 (and described in section 2.1.3).

Because we plot the absolute value of the Fourier coefficients, frequency spectra for the voltage outputs of uniformly sampled two-phase and three-phase inverters are shown in figure 2.5.

The frequency spectrum of the load voltage, $v_{ab}(t)$, of a two-phase inverter is illustrated, from (3.1) and (2.5), in figure 2.10. We also illustrate the spectrum of $v_{ab}(t)$ from simulated results as a check on the accuracy of our calculations. Furthermore, the spectra in figure 2.10 agree with those in [49]. As mentioned in section 3.1, v_{mn} has an extra $1 - e^{in\pi}$ term compared to a_{mn}, which means that there is contribution to the frequency spectrum of $v_{ab}(t)$ only when n is odd. Consequently, each carrier group has two dominant central peaks. Therefore, the spectrum of $v_{ab}(t)$ has less low-frequency distortion and less high-frequency components than the spectrum of $v_a(t)$ or $v_b(t)$.

In a three-phase inverter, there are three load voltages. Because we plot the absolute value of the Fourier coefficients, the frequency spectra of all three load voltages are identical (provided the loads are equal for a three-phase inverter wired in the Y configuration). From (3.2–3.4) and (2.5), we illustrate the frequency spectrum of the load voltages of a three-phase inverter wired in the Δ configuration in figure 2.11(a), which demonstrates our findings from section 3.2 that there is no contribution to the frequency spectrum when n is a multiple of 3. The spectrum of the load voltages of a three-phase inverter wired in the Y configuration, from (3.5–3.5) and (2.5) is shown in figure 2.11(c), where again, as expected, there is no contribution to the spectrum when n is a multiple of 3. We have plotted simulated spectra for the load voltages of three-phase inverters wired in the Δ and the Y configuration in figures 2.11(b) and 2.11(d), respectively, to check our analytical results. Our spectra also agree with those in [49], for the load voltages of three-phase inverters wired in the Δ and the Y configuration.

In the spectra shown in figure 2.11, carrier groups with even m have two dominant central peaks,

(a) *Analytical.*

(b) *Simulated.*

(c) *Analytical.*

(d) *Simulated.*
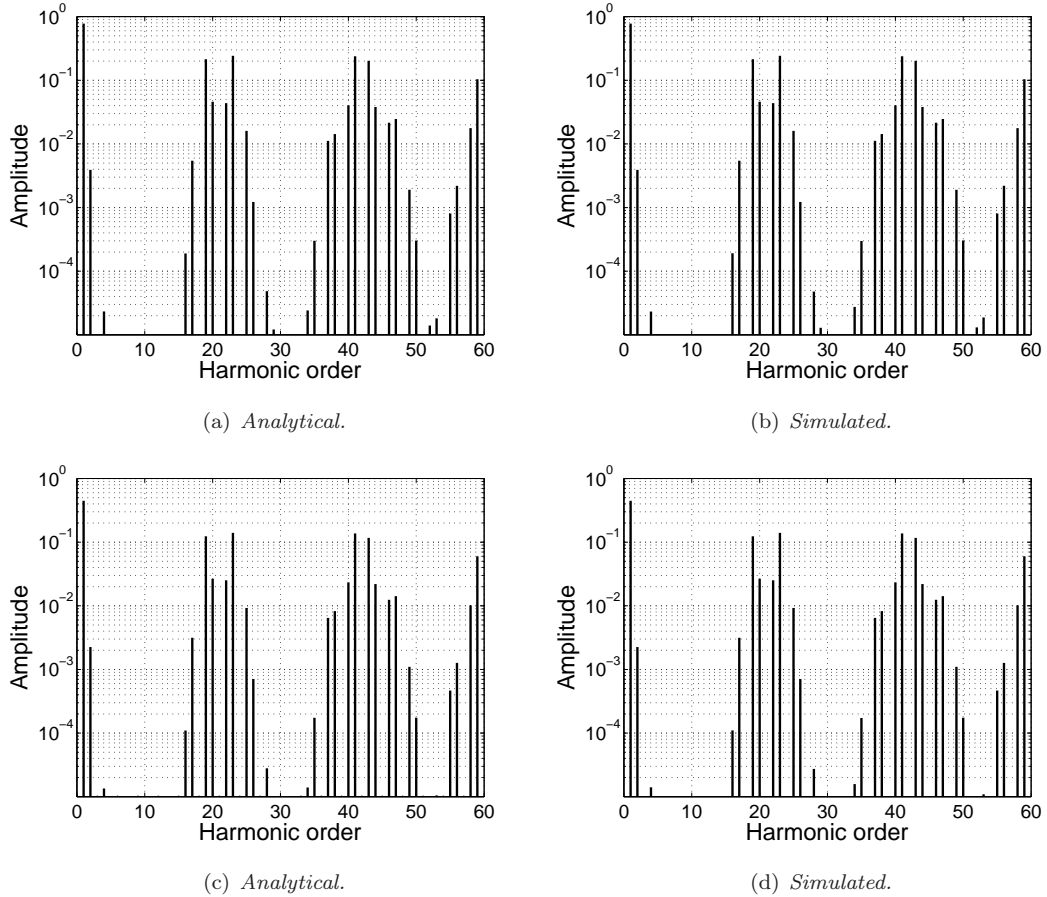
Figure 2.11: *Frequency spectrum of the load voltages of uniformly sampled three-phase PWM inverter, where $M = 0.9$ and $\omega_c = 21\omega_s$. In (a) and (b) we plot spectra for the Δ configuration, and in (c) and (d) we plot spectra for the Y configuration.*

and carrier groups with odd m have two dominant peaks that occur at $m \pm 2n$. Similar to a two-phase inverter, the load voltages of a three-phase inverter have less low-frequency distortion and less high-frequency components than the voltage outputs of a three-phase inverter.

4   Conclusions

In this chapter we have compared two methods of determining frequency spectra for PWM inverters: Black's method [14] and the Poisson re-summation method [31, 33]. Black's method requires the derivation of a double integral, which is algebraically costly, while the Poisson re-summation method requires the derivation of one integral. We have also examined three different types of PWM inverter, a single-phase inverter, a two-phase inverter and a three-phase inverter.

We derived frequency spectra for the voltage outputs of single-phase inverters for natural, symmetrical uniform and asymmetrical uniform sampling. We have performed calculations using both the Poisson re-summation method and Black's method, reproducing analysis in [31] and [49],

respectively. The advantages of the directness of the Poisson re-summation method are most clearly highlighted when calculating frequency spectra for uniformly sampled PWM inverters. For natural sampling, however, due to the algebraic complexity of the Poisson re-summation method, both Black's method and the Poisson re-summation method have advantages. We have also demonstrated that the load voltages of two-phase and three-phase inverters exhibit harmonic cancellation, therefore requiring less filtering of high-frequency components, as shown previously in [49].

The analytical results presented in this chapter have been validated by simulated spectra, from the output voltage. The agreement between the analytical and simulated results is near absolute, for all three sampling methods examined.

We demonstrate in the following chapters that the compactness of the Poisson re-summation method allows for derivation of input current spectra. Prior calculations of input current spectra, that do not use the Poisson re-summation method, are numerically costly (see [40], for example), or involve approximations which limit the scope of the results (see [106], for example). Additionally, calculations of voltage or current spectra for SVM inverters or PWM inverters that incorporate dead time in the switching transitions are made feasible with the Poisson re-summation method.

CURRENT SPECTRA FOR PWM INVERTERS

1   Introduction

In this chapter we derive frequency spectra for the input currents of several PWM inverters using the *single-sum method*. We also derive spectra for the output currents. The input and output currents of PWM inverters have complicated frequency spectra, that contain undesirable high-frequency components. Knowledge of the frequency spectra allows us to identify the high-frequency components, thereby informing filter design. Even though this chapter contains known results, Fourier coefficients for the input currents determined using the single-sum method converge much faster than those determined previously using the *direct method*.

Provided the output voltages and the load are known, output currents are straightforward to determine (see [13], for example). In this chapter, we use the output voltages (calculated in chapter 2) to calculate the output currents of a single-phase, two-phase and three-phase inverter with a series resistive-inductive (RL) load.

Calculating input currents is difficult, because the input currents are complicated switching functions. The switching of the inverter has to be considered twice in order to calculate the input currents. Previous calculations of the input currents have generally contained approximations (see [36, 70, 74, 106], for example), and determine spectra for specific inverter designs (with highly inductive loads). There are two methods that do not make approximations when calculating the input currents: the direct method, which has been used in [40, 71, 86, 94], and the, more sophisticated, Poisson re-summation method, which has been used in [31, 33].

In this chapter, we calculate the input currents of a three-phase inverter with a series RL load, using the single-sum method. This work extends [31], and is an advance on the numerically inefficient calculations of [40, 86] using the direct method. In order to illustrate the main steps in the single-sum calculation, we first review the calculations in [31]. Calculations are also provided using the direct method to calculate the input currents of a single-phase inverter in order to provide a comparison between the single-sum and the direct methods.

1.1 Structure of Chapter

In section 2 we determine the output and input currents of a single-phase inverter with a series RL load using two methods. In section 2.2 we determine input currents using the direct method, and use the single-sum method in section 2.3, comparing both methods in section 2.4. In section 3 the output and input currents are determined for a two-phase inverter with a series RL load. The output and input currents of a three-phase inverter with a series RL load are determined in section 4. Finally, in section 5, we summarise our conclusions.

2 Single-Phase Inverters

In this section we determine the input currents of a single-phase inverter with a series RL load using the direct method of [40] and the single-sum method of [31]. Before calculating any current spectra, we recall the voltage output of a single-phase inverter.

In this chapter we examine inverters that use *uniform* sampling. From section 2.1 of chapter 2, we describe the output voltage $v_a(t)$ of a single-phase inverter mathematically as

$$v_a(t) = 1 - 2 \sum_m \psi(t; \mathcal{A}_m^a, \mathcal{B}_m^a). \tag{2.1}$$

In order to acquire desirable low-frequency behaviour, the switch times $\mathcal{A}_m^a$ and $\mathcal{B}_m^a$ are determined by samples of a low-frequency signal wave $s_a(t) = M \cos \omega_s t$, with amplitude $|M| \leq 1$ and frequency ω_s. The switch times, for uniform sampling, are

$$\mathcal{A}_m^a = mT + \frac{T}{4}\left(1 + s_a(mT)\right), \qquad \text{and} \qquad \mathcal{B}_m^a = mT + \frac{T}{4}\left(3 - s_a(mT)\right), \tag{2.2}$$

where m is any integer and $T = 2\pi/\omega_c$ is the switching period, with switching frequency $\omega_c > \omega_s$. It is easily verified, from section 2.1 of chapter 2, that the Fourier series for $v_a(t)$ is given by

$$v_a(t) = \sum_{mn} a_{mn} e^{i\Omega_{mn}t},$$

where

$$a_{mn} = \begin{cases} 0, & \text{if } \Omega_{mn} = 0, \\ \frac{2}{i\Omega_{mn}T} J_n\left(\frac{1}{4}\Omega_{mn}MT\right)\left[i^n e^{-3i\Omega_{mn}T/4} - (-i)^n e^{-i\Omega_{mn}T/4}\right], & \text{otherwise,} \end{cases} \tag{2.3}$$

are the Fourier coefficients calculated in chapter 2.

Note that there is a modelling issue for the output currents (and hence the input currents), in that there must be a slight delay in the switching of the inverter in order to avoid a short circuit. In this chapter (and, indeed, chapters 4 and 8), we assume that these *dead time* delays are negligible, and do not affect the input and output current spectra. There is an in-depth discussion of the effects of dead time in section 1.1 of chapter 5.

We now calculate the output currents of a single-phase inverter with a series RL load in section 2.1. In section 2.2 we calculate the input currents of a single-phase inverter using the direct

method. In section 2.3 we calculate the input currents of a single-phase inverter using the single-sum method. Then, in section 2.4, we compare the relative merits of the single-sum method and the direct method. Finally, in section 2.5, we examine the spectrum of the input and output currents.

2.1   Output Currents

It is straightforward to derive a Fourier series for the output currents. In this chapter we examine inverters with series RL loads, because series RL loads are a good approximation to a wide variety of loads used in practice (see [52], for example). Furthermore, series RL loads are known to reduce high-frequency current components (see [79], for example). The voltage drop across a series RL load is related to the current through the load by

$$v_{ad}(t) = Ri_{ad}(t) + L\frac{\mathrm{d}i_{ad}(t)}{\mathrm{d}t}, \tag{2.4}$$

where the subscript notation ad denotes that the load is connected between phase-leg a and the neutral point d (as illustrated in figure 1.3(a)). Therefore, we readily determine a Fourier series for the output current, given by

$$i_{ad}(t) = \sum_{mn} i_{mn}e^{i\Omega_{mn}t}, \tag{2.5}$$

where

$$i_{mn} = \frac{a_{mn}}{R + i\Omega_{mn}L}, \tag{2.6}$$

where a_{mn} is given in (2.3). Therefore, the Fourier coefficients for the output currents are easily derived from the Fourier coefficients for the output voltages. It is not as easy to determine the input currents, and we now examine two methods of determining input currents.

2.2   The Direct Method

In a single-phase inverter, there are two input currents: the input current drawn from the upper DC source, and the input current drawn from the lower DC source. By Kirchhoff's current law [103], the upper input current $I(t)$ (the input current drawn from the upper DC source) is equal to the output current across the load $i_{ad}(t)$ when the switch connected to the upper DC source is closed, and the switch connected to the lower DC source is open. Similarly, $I(t) = 0$ when the switch connected to the lower DC source is closed, and the switch connected to the upper DC source is open. In other words,

$$I(t) = i_{ad}(t)\sum_{p}\psi(t;\mathcal{B}_{p}^{a},\mathcal{A}_{p+1}^{a}). \tag{2.7}$$

Similarly, the lower input current $I^{-}(t) = i_{ad}(t)$ when the switch connected to the lower DC source is closed (and the upper switch is open), and $I^{-}(t) = 0$ when the switch connected to the

upper DC source is closed (and the lower switch is open). Therefore

$$
\begin{aligned}
I^-(t) &= i_{ad}(t)\sum_p \psi(t;\mathcal{A}_p^a,\mathcal{B}_p^a), \\
&= i_{ad}(t)\left[1 - \sum_p \psi(t;\mathcal{B}_p^a,\mathcal{A}_{p+1}^a)\right], \\
&= i_{ad}(t) - I(t).
\end{aligned}
$$

As $I^-(t)$ can be written in terms of $I(t)$ we derive only one of $I(t)$ or $I^-(t)$. Here we calculate $I(t)$.

From (2.1), it is straightforward that

$$
\sum_p \psi(t;\mathcal{B}_p^a,\mathcal{A}_{p+1}^a) = \frac{1}{2}(1 + v_a(t)).
$$

Consequently, the upper input current $I(t)$ is

$$
I(t) = \frac{1}{2}i_{ad}(t)(1 + a(t)) = \sum_{mn}\mathcal{I}_{mn}e^{i\Omega_{mn}t},
$$

where,

$$
\mathcal{I}_{mn} = \frac{1}{2}\left[i_{mn} + \sum_{pq}i_{pq}a_{m-pn-q}\right].
$$

These Fourier coefficients reproduce those determined in [31, 40]. To evaluate each Fourier coefficient I_{mn}, we need to compute a double infinite sum that is approximating a square wave. Square waves are discontinuous functions, and consequently the double sum converges slowly (see [90], for example). This makes the direct method numerically inefficient.

2.3 The Single-sum Method

We now calculate the input currents of a single-phase inverter using the more sophisticated single-sum method. The single-sum method is more algebraically involved than the direct method, but is advantageous because the Fourier coefficients converge much faster than those of the direct method [31].

In order to apply the single-sum method, we require an expression for the output currents as a discrete switching function in the time domain. To this end, we derive the current response to a single step voltage pulse. These current responses can then be superposed to give the whole output current. We first write the output current as

$$
i_{ad}(t) = \frac{1}{R}\left[1 - 2\sum_m \phi(t;\mathcal{A}_m^a,\mathcal{B}_m^a)\right], \tag{2.8}
$$

where $\phi(t;\mathcal{A}_m^a,\mathcal{B}_m^a)/R$ is the current response to a single voltage pulse $\psi(t;\mathcal{A}_m^a,\mathcal{B}_m^a)$, and $\mathcal{A}_m^a$ and $\mathcal{B}_m^a$ are given in (2.2). Therefore, from (2.4),

$$
\phi(t;\mathcal{A}_m^a,\mathcal{B}_m^a) + \frac{1}{\gamma}\frac{\mathrm{d}}{\mathrm{d}t}\phi(t;\mathcal{A}_m^a,\mathcal{B}_m^a) = \psi(t;\mathcal{A}_m^a,\mathcal{B}_m^a),
$$

subject to $\phi(t; \mathcal{A}_m^a, \mathcal{B}_m^a) = 0$ for $t < \mathcal{A}_m^a$, where $\gamma = R/L$. It is easily verified that,

$$\phi(t; \mathcal{A}_m^a, \mathcal{B}_m^a) = \begin{cases} 0, & \text{if } t < \mathcal{A}_m^a, \\ 1 - e^{-\gamma(t - \mathcal{A}_m^a)}, & \text{if } \mathcal{A}_m^a < t < \mathcal{B}_m^a, \\ e^{-\gamma(t - \mathcal{B}_m^a)} - e^{-\gamma(t - \mathcal{A}_m^a)}, & \text{if } \mathcal{B}_m^a < t. \end{cases}$$

Therefore, from (2.8), it is straightforward to see that

$$i_{ad}(t) = \frac{1}{R}(1 + 2f_{\mathcal{AB}}(t) + 2f_{\mathcal{A}}(t) - 2f_{\mathcal{B}}(t)), \tag{2.9}$$

where

$$f_{\mathcal{AB}}(t) = -\sum_m \psi(t; \mathcal{A}_m^a, \mathcal{B}_m^a), \tag{2.10}$$

$$f_{\mathcal{A}}(t) = \sum_m e^{-\gamma(t - \mathcal{A}_m^a)} \psi(t; \mathcal{A}_m^a, \infty), \tag{2.11}$$

where $f_{\mathcal{B}}(t)$ is defined similarly to $f_{\mathcal{A}}(t)$.

From (2.7) and (2.9), we determine the input current drawn from the upper DC source of a single-phase inverter as a discrete, time-dependent switching function, given by

$$\begin{aligned} I(t) &= \frac{1}{R}(1 + 2f_{\mathcal{AB}}(t) + 2f_{\mathcal{A}}(t) - 2f_{\mathcal{B}}(t)) \sum_p \psi(t; \mathcal{B}_p^a, \mathcal{A}_{p+1}^a), \\ &= I_0(t) + I_{\mathcal{AB}}(t) + I_{\mathcal{A-B}}(t). \end{aligned}$$

We ultimately determine a Fourier series for $I(t)$. In order to do this, we first determine a Fourier series for each of $I_0(t)$, $I_{\mathcal{AB}}(t)$ and $I_{\mathcal{A-B}}(t)$ in turn. Key to the single-sum method is evaluating one of the infinite sums in $I_0(t)$, $I_{\mathcal{AB}}(t)$ and $I_{\mathcal{A-B}}(t)$ exactly before conducting any Fourier analysis. Once the sum has been evaluated, we follow a process similar to the Poisson re-summation method, and take a Fourier transform to determine the frequency dependence, and then use a Poisson re-summation formula to determine a Fourier series, thereby avoiding having to invert the Fourier transform. Note that a process similar to Black's method could be used instead of the Poisson re-summation method, but the relative algebraic simplicity of the Poisson re-summation method makes the calculations here feasible.

It is straightforward to see that

$$I_0(t) = \frac{1}{R} \sum_p \psi(t; \mathcal{B}_p^a, \mathcal{A}_{p+1}^a) = \frac{1}{2R}(1 + v_a(t)),$$

where the spectrum of $v_a(t)$ is known, with Fourier coefficients in (2.3). From (2.10),

$$I_{\mathcal{AB}}(t) = \frac{2}{R} f_{\mathcal{AB}}(t) \sum_p \psi(t; \mathcal{B}_p^a, \mathcal{A}_{p+1}^a) = 0,$$

since there is no overlap between the intervals $(\mathcal{A}_m^a, \mathcal{B}_m^a)$ and $(\mathcal{B}_p^a, \mathcal{A}_{p+1}^a)$. Examination of (2.11) confirms that $f_{\mathcal{A}}(t)\psi(t; \mathcal{B}_p^a, \mathcal{A}_{p+1}^a)$ is non-zero only when $m \leq p$, and similarly for $f_{\mathcal{B}}(t)\psi(t; \mathcal{B}_p^a, \mathcal{A}_{p+1}^a)$. Subsequently

$$I_{\mathcal{A-B}}(t) = \frac{2}{R} \sum_p \sum_{m=-\infty}^{p} \left[e^{-\gamma(t - \mathcal{A}_m^a)} - e^{-\gamma(t - \mathcal{B}_m^a)} \right] \psi(t; \mathcal{B}_p^a, \mathcal{A}_{p+1}^a).$$

It is straightforward to see that, from evaluation of Jacobi-Anger expansions [109],

$$
\begin{aligned}
e^{\lambda \mathcal{A}_m^a} &= e^{\lambda m T + \lambda T/4} \sum_n (-i)^n J_n\left(\tfrac{1}{4} i \lambda M T\right) e^{i n \omega_s m T}, \\
e^{\lambda \mathcal{B}_m^a} &= e^{\lambda m T + 3\lambda T/4} \sum_n i^n J_n\left(\tfrac{1}{4} i \lambda M T\right) e^{i n \omega_s m T}.
\end{aligned}
$$

Therefore we have

$$
\begin{aligned}
I_{\mathcal{A}-\mathcal{B}}(t) &= \frac{2}{R} \sum_{np} \sum_{m=-\infty}^{p} e^{-\gamma(t-mT)} e^{-3\gamma T/4} J_n\left(\tfrac{1}{4} i\gamma M T\right) \left[(-i)^n e^{-\gamma T/2} - i^n\right] \\
&\qquad e^{i n \omega_s m T} \psi(t; \mathcal{B}_p^a, \mathcal{A}_{p+1}^a).
\end{aligned}
$$

We explicitly evaluate the geometric sum over m to be

$$
\sum_{m=-\infty}^{p} e^{(\gamma + i n \omega_s) m T} = \frac{e^{(\gamma + i n \omega_s) p T}}{1 - e^{-(\gamma + i n \omega_s) T}}.
$$

Consequently,

$$
\begin{aligned}
I_{\mathcal{A}-\mathcal{B}}(t) &= \frac{2}{R} \sum_{np} e^{-\gamma t} e^{-3\gamma T/4} J_n\left(\tfrac{1}{4} i\gamma M T\right) \left[(-i)^n e^{-\gamma T/2} - i^n\right] \\
&\qquad \frac{e^{(\gamma + i n \omega_s) p T}}{1 - e^{-(\gamma + i n \omega_s) T}} \psi(t; \mathcal{B}_p^a, \mathcal{A}_{p+1}^a), \\
&\equiv \frac{2}{R} \sum_n \frac{e^{-3\gamma T/4}}{1 - e^{-(\gamma + i n \omega_s) T}} J_n\left(\tfrac{1}{4} i\gamma M T\right) \left[(-i)^n e^{-\gamma T/2} - i^n\right] F_n(t).
\end{aligned}
$$

We want to know which frequencies $F_n(t)$ depends on. To this end we take a Fourier transform of $F_n(t)$, which gives

$$
\begin{aligned}
\hat{F}_n(\omega) &= -\sum_{pq} \frac{1}{\gamma + i\omega} e^{-i(\omega - (n+q)\omega_s) p T} e^{3\gamma T/4} J_q\left(\tfrac{1}{4}(\omega - i\gamma) M T\right) \\
&\qquad \left[(-i)^q e^{(-\gamma/2 + i(q\omega_s - 5\omega/4))T} - i^q e^{-3i\omega T/4}\right].
\end{aligned}
$$

We now have an expression for $F_n(t)$ in the frequency domain, but we want an expression in the time domain. The Poisson re-summation formula allows us to identify a Fourier series for $F_n(t)$. Poisson re-summing in p we derive

$$
\begin{aligned}
\hat{F}_n(\omega) &= -\sum_{pq} \int_{-\infty}^{\infty} \frac{e^{i\Omega_{p,n+q} t}}{(\gamma + i\omega) T} e^{3\gamma T/4} J_q\left(\tfrac{1}{4}(\omega - i\gamma) M T\right) \\
&\qquad \times \left[(-i)^q e^{(-\gamma/2 + i(q\omega_s - 5\omega/4))T} - i^q e^{-3i\omega T/4}\right] e^{-i\omega t} \, \mathrm{d}t.
\end{aligned}
$$

Therefore we identify a Fourier series for $F_n(t)$, given by

$$
\begin{aligned}
F_n(t) &= -\sum_{pq} \frac{e^{i\Omega_{p,n+q} t}}{(\gamma + i\Omega_{p,n+q}) T} e^{3\gamma T/4} J_q\left(\tfrac{1}{4}(\Omega_{p,n+q} - i\gamma) M T\right) \\
&\qquad \times \left[(-i)^q e^{(-\gamma/2 + i(q\omega_s - 5\Omega_{p,n+q}/4))T} - i^q e^{-3i\Omega_{p,n+q} T/4}\right],
\end{aligned}
$$

where $\Omega_{p,n+q}$ are the only frequencies with a non-zero contribution to $F_n(t)$. Therefore

$$
I_{\mathcal{A}-\mathcal{B}}(t) = \sum_{mn} \mathcal{J}_{mn} e^{i\Omega_{mn} t},
$$

where

$$\mathcal{J}_{mn} = -\frac{2}{R}\sum_q \frac{J_{n-q}\left(\frac{1}{4}i\gamma MT\right)J_q\left(\frac{1}{4}(\Omega_{mn}-i\gamma)MT\right)}{(\gamma+i\Omega_{mn})(1-e^{-(\gamma+i(n-q)\omega_s)T})T}\left((-i)^{n-q}e^{-\gamma T/2}-i^{n-q}\right)$$

$$\times\left[(-i)^q e^{(-\gamma/2+i(q\omega_s-5\Omega_{mn}/4))T}-i^q e^{-3i\Omega_{mn}T/4}\right]. \tag{2.12}$$

Therefore the Fourier series for the input current drawn from the upper DC source of a single-phase inverter with a series RL load is

$$I(t) = \frac{1}{2R}+\sum_{mn}\mathcal{I}_{mn}e^{i\Omega_{mn}t},$$

where

$$\mathcal{I}_{mn} = \frac{a_{mn}}{2R}+\mathcal{J}_{mn}, \tag{2.13}$$

where a_{mn} is defined in (2.3), and $\mathcal{J}_{mn}$ is defined in (2.12). Note that to evaluate each Fourier coefficient $\mathcal{I}_{mn}$, a single infinite sum must be computed. This is an improvement on the Fourier coefficients determined using the direct method, where the evaluation of two infinite sums is required for each Fourier coefficient. Furthermore, the single sum here converges much faster than the double sum for the direct method (we discuss this further in section 2.4). While the Fourier coefficients determined using the single-sum method converge faster than those derived using the direct method, they are very complex functions, involving an infinite sum of Bessel functions.

Finally, the lower input current is given by

$$I^-(t) = -\frac{1}{2R}+\sum_{mn}(i_{mn}-\mathcal{I}_{mn})e^{i\Omega_{mn}t},$$

where i_{mn} is given in (2.6). The Fourier series for upper and lower input currents derived in this section agree with the Fourier series determined in [31].

2.4   Comparison of the Direct Method and the Single-sum Method

We have now calculated Fourier series for the input currents of a single-phase inverter using both the direct and the single-sum method. In this section we illustrate that Fourier coefficients derived using the single-sum method are more numerically efficient than those derived using the direct method.

In section 2.2 we noted that for each Fourier coefficient in the Fourier series for $I(t)$, determined using the direct method, there are two infinite sums over p and q, and these sums converge slowly because they are approximating a square wave (a discontinuous function). In fact, for a Fourier coefficient to be converged to ten decimal places, we sum over approximately 400 p's and q's. In addition to this, a single Fourier coefficient converged up to ten decimal places takes 54.3 seconds to compute in Matlab using the direct method.

For each Fourier coefficient calculated using the single-sum method there is one infinite sum over q. Not only is this a reduction of sums to compute for each coefficient (compared to the

direct method), the single sum also converges quickly. Summing over 21 q computes, in Matlab, a Fourier coefficient in just 0.019 seconds that is converged to more than 15 decimal places.

Note that computations of the Fourier coefficients determined using the direct method and the single-sum method were calculated on the same machine, in order to allow for direct comparison.

It is evident, by comparison of the calculations of section 2.2 and 2.3, that the single-sum method is more algebraically involved than the direct method. This analytical cost, however, is greatly outweighed by the speed of convergence of the Fourier coefficients calculated using the single-sum method. Therefore plotting accurate spectra for the input currents has a low numerical cost when the input currents have been calculated using the single-sum method.

2.5 Analysis of the Frequency Spectrum

In this section, we illustrate frequency spectra for the output current, $i_{ad}(t)$, in section 2.5.1 and spectra for the upper and lower inputs currents, $I(t)$ and $I^-(t)$, respectively, in section 2.5.2. In this chapter, we examine the effects on the spectra of the input and output currents for a range of ratios γ. Because the Fourier coefficients for the input currents are scalar in R, we expect the amplitude of the coefficients to decrease as $R \to \infty$. Therefore, in this thesis, to produce current spectra for a range of γ's, we fix R and vary L.

In the following sections we also include spectra generated by taking fast Fourier transforms of simulations of the output or input current waveform. The results from the numerical simulations were obtained using Matlab.

2.5.1 Output Currents

The frequency spectrum of $i_{ad}(t)$ is illustrated in figure 3.1, along with spectra determined by numerical simulations. There is near perfect agreement between our analytical and simulated results. Furthermore, our spectra agree with those in [13, 40].

In the output current spectra, carrier groups with even m have two dominant central peaks, and carrier groups with odd m have a single dominant central peak. The dominant low-frequency contribution to the spectrum is at ω_s, and the dominant high-frequency contribution to the spectrum is at ω_c. That means the output currents are generated with low-frequency behaviour approximating the signal wave.

We now examine the effects on the spectrum as we vary γ. From comparison of figures 3.1(a) and 3.1(c), as $L \to 0$, for fixed R, the amplitude of the high-frequency components asymptote to the high-frequency components of the voltage output. This implies that as $L \to 0$ with R fixed, the output current approximates the output voltage (scaled by R).

As $L \to \infty$, the amplitude of the high-frequency components in the spectrum of $i_{ad}(t)$ decreases, for fixed R (from comparison of figures 3.1(a) and 3.1(e)). Furthermore, as $L \to \infty$ and R fixed, the non-dominant low-frequency components asymptote to zero. In other words, as $L \to \infty$, the peak at ω_s in the frequency spectrum becomes increasingly dominant (for fixed R), and the output current becomes a better approximation to the signal wave.

(a) $\gamma = 1$, *analytical.*

(b) $\gamma = 1$, *simulated.*

(c) $\gamma = 10$, *analytical.*

(d) $\gamma = 10$, *simulated.*

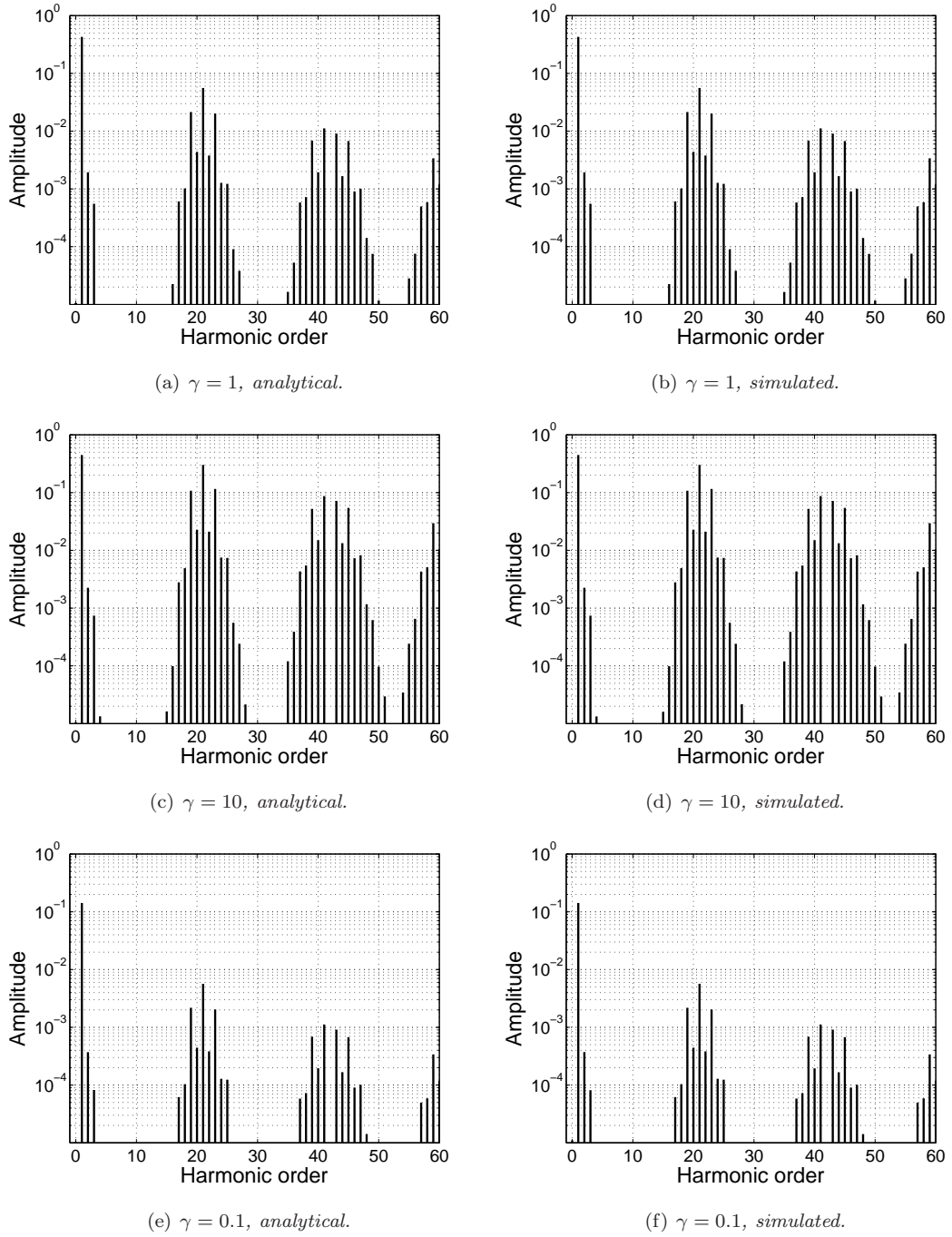(e) $\gamma = 0.1$, *analytical.*

(f) $\gamma = 0.1$, *simulated.*

Figure 3.1: *Frequency spectrum of the output current $i_{ad}(t)$ of a single-phase inverter, where $M = 0.9$, $R = 1$ and $\omega_c = 21\omega_s$. Furthermore, in (a) and (b), $L = 1$, in (c) and (d), $L = 0.1$ and in (e) and (f), $L = 10$.*

Note that we have omitted spectra for a range of ratios ω_c/ω_s here, this is because the effects on the spectrum of $i_{ad}(t)$ as ω_c/ω_s changes are similar to the effects on the spectrum of $v_a(t)$ (discussed in section 2.1.3 of chapter 2). In other words, the non-dominant low-frequency contributions to the spectrum decrease in amplitude as ω_c/ω_s increases. Furthermore, contributions to the spectrum that correspond to the even $m+n$ terms decrease in magnitude as ω_c/ω_s increases.

2.5.2 Input Currents

The frequency spectra for both the input current drawn from the upper and the lower DC source are illustrated in figure 3.2. We also illustrate simulated spectra in figure 3.2. The simulated results agree with our analytical results. In addition to this, the spectra presented here agree with those in [31, 40].

For both the upper input current and the lower input current, there is contribution to the spectrum at 0. This is referred to as the *DC component* [40]. Components in the spectrum other than the DC component are referred to as *current ripple*. Undesirable current ripple is caused by the alternating output waveform [96].

The dominant low-frequency ripple component is at ω_s, and the dominant high-frequency ripple components are at $\omega_c \pm \omega_s$ and $2\omega_c$. The magnitude of the dominant low-frequency ripple components is similar to the magnitude of the DC component.

We have illustrated the frequency spectrum of the upper input current $I(t)$ of a single-phase inverter for a range of ratios γ in figure 3.3 to ascertain the effects of the load composition on the spectrum of $I(t)$. The accuracy of our analytical results has been verifed by simulated results, also shown in figure 3.3. From comparison of figures 3.2(a) and 3.3(a), as $L \to 0$ the number of peaks in each carrier group increases, for fixed R. In other words, as $L \to 0$ with fixed R, there is more current ripple in the spectrum of the input currents. From figure 3.3(c), as $L \to \infty$, carrier groups with odd m are dominated by a one central peak, and carrier groups with even m are dominated by two central peaks (for fixed R). Furthermore, from comparison of figures 3.3(a) and 3.3(c), the DC component for input currents with large γ dominates the low-frequency components of the spectrum, but for small γ it does not. Therefore, as $L \to \infty$ with fixed R, the DC component is suppressed. In other words, the peaks that dominate the spectrum of $I(t)$ are directly affected by γ.

As the ratio ω_c/ω_s increases, the low-frequency current ripple components in the spectrum of $I(t)$ decrease in magnitude. This holds for all γ.

Finally, we comment on the parameter values used to generate results in previous publications. In [86] and [71], inverters are modelled with largely resistive series RL loads (in other words γ is large). The output current spectra in these papers are similar to the spectrum shown in figure 3.1(c), and the spectra for the input currents are similar to the spectrum shown in figure 3.3(a). In [36, 70, 74, 106], however, inverters are modelled with highly inductive series RL loads. The spectra presented in [36, 70, 74, 106] are similar to the spectra illustrated figures 3.1(e) (for output currents) and 3.3(c) (for input currents).

(a) $I(t)$, *analytical.*

(b) $I(t)$, *simulated.*

(c) $I^-(t)$, *analytical.*

(d) $I^-(t)$, *simulated.*
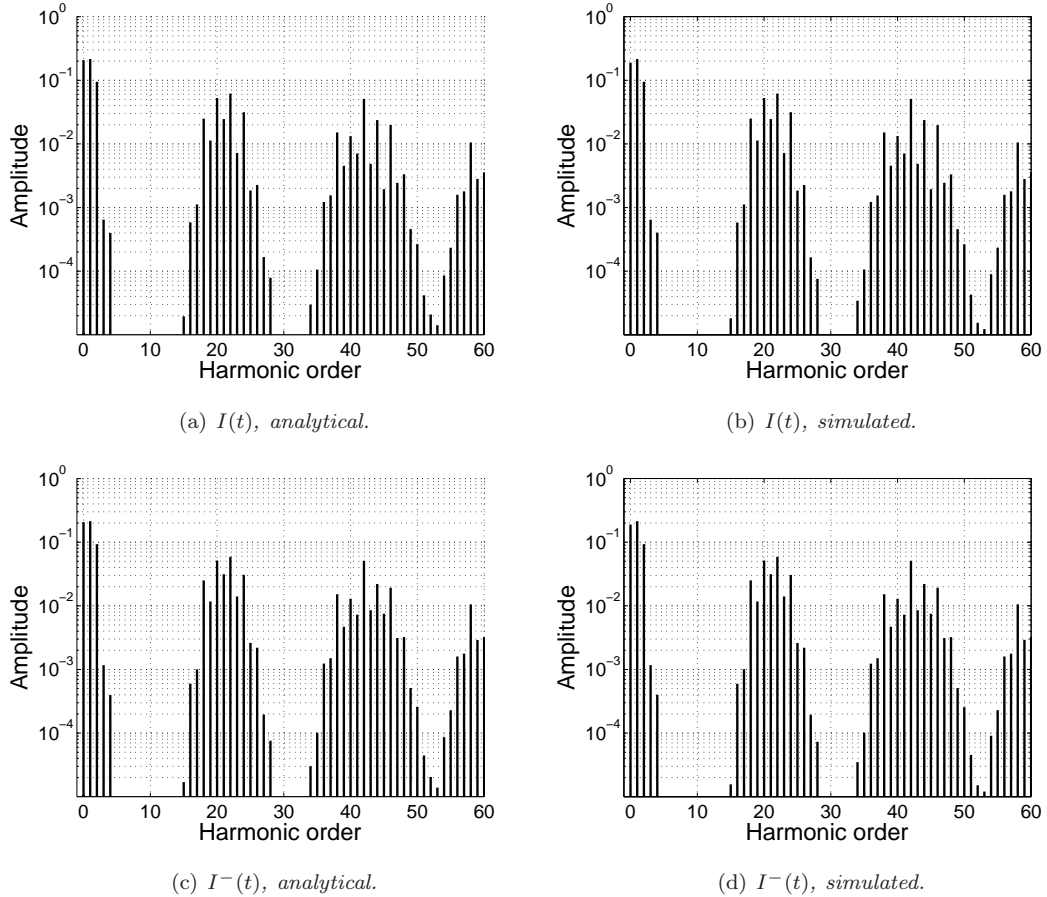
Figure 3.2: *Frequency spectra for the input current drawn from the upper DC source of a single-phase inverter in (a) and (b), and for the input current drawn from the lower DC source in (c) and (d). The parameter values are $M = 0.9$, $\omega_c = 21\omega_s$ and $\gamma = 1$ (specifically, $R = 1$ and $L = 1$).*

3   Two-phase Inverters

A two-phase inverter has two phase-legs, with a load connected between them, as illustrated in figure 1.3(b). The voltage across the load is the difference between the two voltage outputs from either phase-leg. This voltage difference is used to calculate the output current, and, subsequently the input currents. Here we calculate both the output current (in section 3.1) and the input currents (in section 3.2) for a two-phase inverter with a series RL load.

3.1   Output Currents

The voltage difference across the load in a two-phase inverter is $v_{ab}(t) = v_a(t) - v_b(t)$. Thus, the output current through the load satisfies

$$Ri_{ab}(t) + L\frac{\mathrm{d}i_{ab}(t)}{\mathrm{d}t} = v_{ab}(t). \tag{3.1}$$

(a) $\gamma = 10$, *analytical.*

(b) $\gamma = 10$, *simulated.*

(c) $\gamma = 0.1$, *analytical.*

(d) $\gamma = 0.1$, *simulated.*
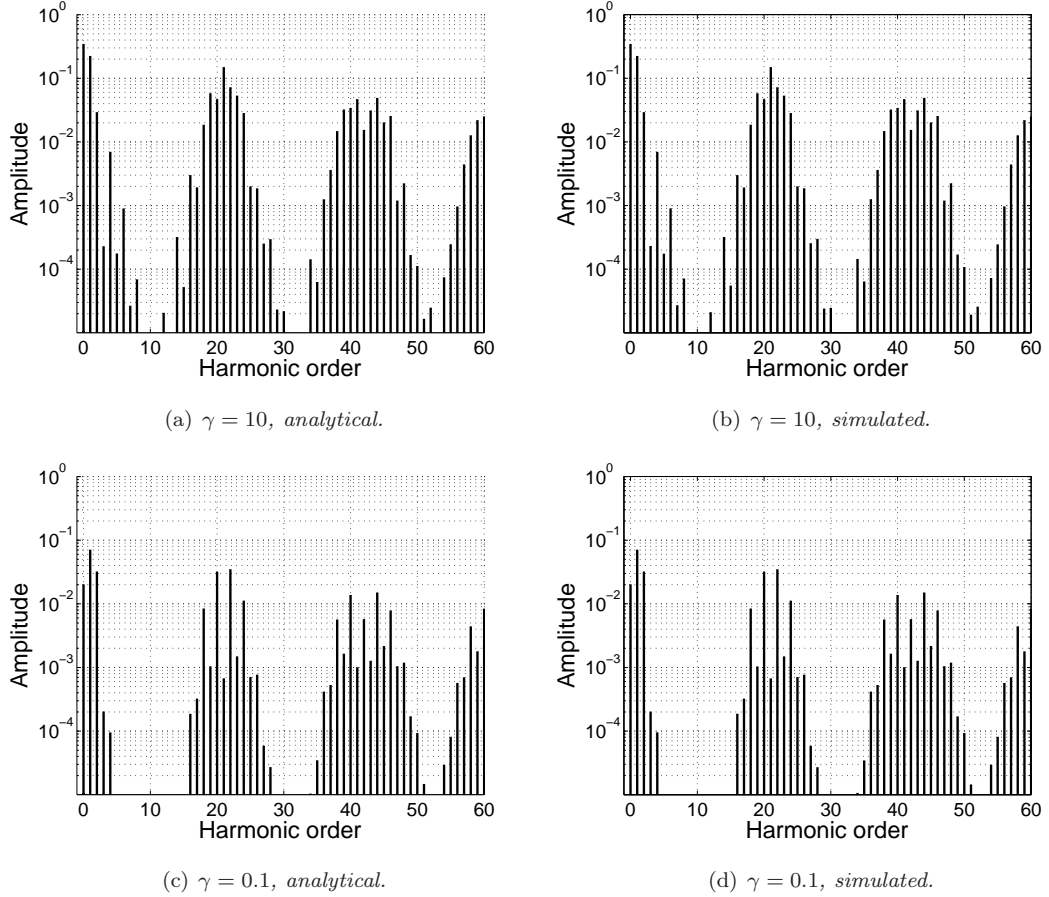
Figure 3.3: *Frequency spectrum of the upper input current $I(t)$ of a single-phase inverter, where $M = 0.9$, $R = 1$ and $\omega_c = 21\omega_s$. Furthermore, in (a) and (b), $L = 0.1$, and in (c) and (d), $L = 10$.*

Because $v_{ab}(t) = v_{ad}(t) - v_{bd}(t)$, it is easily verified that

$$i_{ab}(t) = \sum_{mn} \frac{(1 - (-1)^n)a_{mn}}{R + i\Omega_{mn}L} e^{i\Omega_{mn}t} \equiv \sum_{mn} i_{mn}e^{i\Omega_{mn}t}.$$

The frequency spectrum of $i_{ab}(t)$ is shown in figure 3.4. The frequency spectrum of $i_{ad}(t)$ obtained from FFTs of Matlab simulations of the output current waveform is also included, to corroborate our analytical results. Similar to the spectrum of $i_{ad}(t)$, the dominant low-frequency contribution is at ω_s. As predicted in [13] (for example), there is contribution to the frequency spectrum only when n is odd, which is a consequence of the harmonic cancellation from taking the difference between two currents. Mathematically, it is a consequence of the $1 - (-1)^n$ term. We have omitted the inclusion of spectra for a range of ratios of γ, as the effects on $i_{ab}(t)$ are similar to those on $i_{ad}(t)$, illustrated in figure 3.1 (and discussed in section 2.5.1).

In order to calculate the input currents of a two-phase inverter using the single-sum method, we require expressions for the output currents as discrete, time-dependent switching functions. As a result of $i_{ab}(t) = i_{ad}(t) - i_{bd}(t)$ (where $i_{ad}(t)$ is given in (2.8), and $i_{bd}(t)$ is defined similarly),

(a) *Analytical.* (b) *Simulated.*
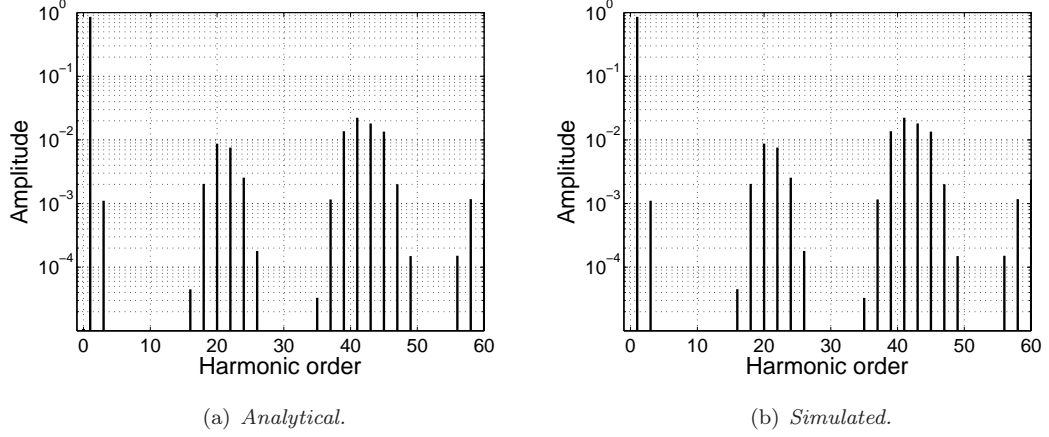
Figure 3.4: *Frequency spectrum of the output current $i_{ab}(t)$ of a two-phase inverter, where $M = 0.9$, $\omega_c = 21\omega_s$ and $\gamma = 1$ (specifically, $R = 1$ and $L = 1$).*

the output current through the load is, from (2.9–2.11),

$$i_{ab}(t) = g_{\mathcal{AB}}(t) + g_{\mathcal{A}}(t) - g_{\mathcal{B}}(t), \tag{3.2}$$

where

$$g_{\mathcal{AB}}(t) = -\frac{2}{R} \sum_m \left[\psi(t; \mathcal{A}_m^a, \mathcal{B}_m^a) - \psi(t; \mathcal{A}_m^b, \mathcal{B}_m^b) \right], \tag{3.3}$$

$$g_{\mathcal{A}}(t) = \frac{2}{R} \sum_m \left[e^{-\gamma(t - \mathcal{A}_m^a)} \psi(t; \mathcal{A}_m^a, \infty) - e^{-\gamma(t - \mathcal{A}_m^b)} \psi(t; \mathcal{A}_m^b, \infty) \right], \tag{3.4}$$

where $\mathcal{A}_m^a$, $\mathcal{B}_m^a$ are given in (2.2), and $\mathcal{A}_m^b$, $\mathcal{B}_m^b$ are defined similarly, with signal wave $s_b(t) = M\cos(\omega_s t - \pi)$. Note that $g_{\mathcal{B}}(t)$ is defined in a similar fashion to (3.4).

3.2 Input Currents

We begin by examining the upper input current $I(t)$ of a two-phase inverter. From examination of Kirchhoff's current law [103], $I(t) = 0$ when the switches on either phase-leg are simultaneously attached to either the upper or lower DC source. Similarly, $I(t) = i_{ab}(t)$ when phase-leg a is attached to the upper DC source and phase-leg b is attached to the lower DC source, and $I(t) = -i_{ab}(t)$ when phase-leg b is attached to the upper DC source and phase-leg a is attached to the lower DC source. In other words,

$$I(t) = i_{ab}(t) \sum_p \left[\psi(t; \mathcal{B}_p^a, \mathcal{A}_{p+1}^a) - \psi(t; \mathcal{B}_p^b, \mathcal{A}_{p+1}^b) \right]. \tag{3.5}$$

By a similar argument, the input current drawn from the lower DC source is

$$
\begin{aligned}
I^-(t) &= i_{ab}(t) \sum_p \left[\psi(t; \mathcal{A}_p^a, \mathcal{B}_p^a) - \psi(t; \mathcal{A}_p^b, \mathcal{B}_p^b) \right], \\
&= i_{ab}(t) \left[\left(1 - \sum_p \psi(t; \mathcal{B}_p^a, \mathcal{A}_{p+1}^a) \right) - \left(1 - \sum_p \psi(t; \mathcal{B}_p^b, \mathcal{A}_{p+1}^b) \right) \right], \\
&= -I(t).
\end{aligned}
$$

Therefore, we calculate only one of the upper or the lower input currents. We choose to examine the upper input current $I(t)$.

The upper input current is, from (3.2–3.14),

$$I(t) = \left[g_{\mathcal{AB}}(t) + g_{\mathcal{A}}(t) - g_{\mathcal{B}}(t) \right] \sum_p \left[\psi(t; \mathcal{B}_p^a, \mathcal{A}_{p+1}^a) - \psi(t; \mathcal{B}_p^b, \mathcal{A}_{p+1}^b) \right],$$

$$= I_{\mathcal{AB}}(t) + I_{\mathcal{A}-\mathcal{B}}(t),$$

where

$$I_{\mathcal{AB}}(t) = -\frac{2}{R} \sum_{mp} \left[\psi(t; \mathcal{A}_m^a, \mathcal{B}_m^a) - \psi(t; \mathcal{A}_m^b, \mathcal{B}_m^b) \right] \left[\psi(t; \mathcal{B}_p^a, \mathcal{A}_{p+1}^a) - \psi(t; \mathcal{B}_p^b, \mathcal{A}_{p+1}^b) \right],$$

$$I_{\mathcal{A}-\mathcal{B}}(t) = \frac{2}{R} \sum_{mp} \left[e^{-\gamma(t-\mathcal{A}_m^a)} \psi(t; \mathcal{A}_m^a, \infty) - e^{-\gamma(t-\mathcal{A}_m^b)} \psi(t; \mathcal{A}_m^b, \infty) - e^{-\gamma(t-\mathcal{B}_m^a)} \psi(t; \mathcal{B}_m^a, \infty) \right.$$

$$\left. + e^{-\gamma(t-\mathcal{B}_m^b)} \psi(t; \mathcal{B}_m^b, \infty) \right] \left[\psi(t; \mathcal{B}_p^a, \mathcal{A}_{p+1}^a) - \psi(t; \mathcal{B}_p^b, \mathcal{A}_{p+1}^b) \right]. \quad (3.6)$$

We now calculate each of $I_{\mathcal{AB}}(t)$ and $I_{\mathcal{A}-\mathcal{B}}(t)$ in turn.

3.2.1 $I_{\mathcal{AB}}(t)$

From examination of the functions $\psi(t; \mathcal{A}_m^a, \mathcal{B}_m^a)$, $\psi(t; \mathcal{A}_m^b, \mathcal{B}_m^b)$, $\psi(t; \mathcal{B}_p^a, \mathcal{A}_{p+1}^a)$ and $\psi(t; \mathcal{B}_p^b, \mathcal{A}_{p+1}^b)$, it is straightforward to see that the sum over p in $I_{\mathcal{AB}}(t)$ can be evaluated directly to give

$$I_{\mathcal{AB}}(t) = \frac{2}{R} \sum_m \left[\psi(t; \mathcal{A}_m^a, \mathcal{A}_m^b) + \psi(t; \mathcal{A}_m^b, \mathcal{A}_m^a) + \psi(t; \mathcal{B}_m^a, \mathcal{B}_m^b) + \psi(t; \mathcal{B}_m^b, \mathcal{B}_m^a) \right].$$

The property $\psi(t; t_1, t_2) = 0$ when $t_2 < t_1$, allows us to write

$$I_{\mathcal{AB}}(t) = \frac{2}{R} \sum_m \left[\psi(t; \min(\mathcal{A}_m^a, \mathcal{A}_m^b), \max(\mathcal{A}_m^a, \mathcal{A}_m^b)) + \psi(t; \min(\mathcal{B}_m^a, \mathcal{B}_m^b), \max(\mathcal{B}_m^a, \mathcal{B}_m^b)) \right].$$

Since $s_a(t) = \cos \omega_s t$ and $s_b(t) = \cos(\omega_s t - \pi) = -\cos \omega_s t$, we introduce

$$s(t) = |\cos \omega_s t|, \quad (3.7)$$

such that

$$I_{\mathcal{AB}}(t) = \frac{2}{R} \sum_m \left[\psi\left(t; mT + \frac{T}{4}(1 - Ms(mT)), mT + \frac{T}{4}(1 + s(mT)) \right) \right.$$

$$\left. + \psi\left(t; mT + \frac{T}{4}(3 - Ms(mT)), mT + \frac{T}{4}(3 + s(mT)) \right) \right]. \quad (3.8)$$

We now take a Fourier transform of $I_{\mathcal{AB}}(t)$, which gives, when $\omega \neq 0$,

$$\hat{I}_{\mathcal{AB}}(\omega) = -\frac{2}{R} \sum_m \frac{1}{i\omega} e^{-i\omega mT} (e^{-i\omega T/4} + e^{-3i\omega T/4})(e^{-i\omega MTs(mT)/4} - e^{i\omega MTs(mT)/4}).$$

We now determine a Fourier series for $e^{-i\omega MTs(mT)/4}$ and $e^{i\omega MTs(mT)/4}$.

Fourier series for $e^{izs(t)}$

From examination of the Jacobi-Anger expansion [109],

$$e^{izs(t)} = \sum_n B_n(z)e^{in\omega_s t}, \tag{3.9}$$

where

$$B_n(z) = \frac{\omega_s}{2\pi} \int_0^{2\pi/\omega_s} e^{izs(t)} e^{-in\omega_s t} \, \mathrm{d}t.$$

It is readily determined that

$$B_n(z) = \begin{cases} 0, & \text{for } n \text{ odd}, \\ J_n(z) + \sum_{p=\pm 1, \pm 3, \ldots} \frac{2J_p(z)}{\pi i(n-p)}, & \text{for } n \text{ even}. \end{cases} \tag{3.10}$$

Note that the coefficient $B_n(z)$ is equal to zero when n is odd, or equal to an infinite sum of Bessel functions when n is even. We now return to our Fourier transform $\hat{I}_{\mathcal{AB}}(\omega)$, giving the Fourier transform in terms of the Fourier coefficients $B_n(z)$.

When computing $B_n(z)$ numerically (and for similar functions later in the thesis) in order to produce spectra, we are required to truncate the infinite sum due to limits on processing power. Therefore, we now briefly examine how quickly the sum over p in (3.10) converges. From calculations in Matlab, truncating the sum over p to a dozen terms either side of 0 to produce coefficients which are accurate up to 15 decimal places.

Fourier Transform

Therefore, when $\omega \neq 0$, the Fourier transform $\hat{I}_{\mathcal{AB}}(\omega)$ is

$$\hat{I}_{\mathcal{AB}}(\omega) = \frac{2}{R} \sum_{mn} \frac{1}{i\omega} e^{-i(\omega - n\omega_s)mT} (e^{-i\omega T/4} + e^{-3i\omega T/4}) \left[B_n\left(\tfrac{1}{4}\omega MT\right) - B_n\left(-\tfrac{1}{4}\omega MT\right) \right].$$

Noting that, for even n,

$$B_n(z) - B_n(-z) = \sum_{p=\pm 1, \pm 3, \ldots} \frac{4J_p(z)}{\pi i(n-p)},$$

and Poisson re-summing in m determines

$$\hat{I}_{\mathcal{AB}}(\omega) = \frac{2}{R} \sum_m \sum_{n=0, \pm 2, \pm 4, \ldots} \int_{-\infty}^{\infty} \frac{e^{-i\omega t}}{i\omega T} e^{i\Omega_{mn}t} (e^{-i\omega T/4} + e^{-3i\omega T/4}) \sum_{p=\pm 1, \pm 3, \ldots} \frac{4J_p\left(\tfrac{1}{4}\omega MT\right)}{\pi i(n-p)} \, \mathrm{d}t.$$

Thus we have a Fourier series for $I_{\mathcal{AB}}(t)$, given by

$$I_{\mathcal{AB}}(t) = \frac{4M}{\pi R} + \sum_m \sum_{n=0, \pm 2, \pm 4, \ldots} \mathcal{I}_{mn} e^{i\Omega_{mn}t},$$

where

$$\mathcal{I}_{mn} = \begin{cases} 0, & \text{if } \Omega_{mn} = 0, \\ \frac{8}{\pi \Omega_{mn} RT} (e^{-i\omega T/4} + e^{-3i\omega T/4}) \sum_{p=\pm 1, \pm 3, \ldots} \frac{J_p\left(\tfrac{1}{4}\Omega_{mn}MT\right)}{p-n}, & \text{otherwise}, \end{cases} \tag{3.11}$$

and the constant term $4M/\pi R$ is the contribution to $I_{\mathcal{AB}}(t)$ when $\Omega_{mn} = 0$, determined by evaluating the mean value of (3.8) (similarly to the accounts in appendix A). Note that the Fourier coefficients $\mathcal{I}_{mn}$ are non-zero when n is even only.

3.2.2 $I_{\mathcal{A}-\mathcal{B}}(t)$

In order to determine a Fourier series for $I_{\mathcal{A}-\mathcal{B}}(t)$ we first split (3.6) into two parts:

$$I_{\mathcal{A}-\mathcal{B}}(t) = I_1(t) + I_2(t),$$

where $I_1(t)$ and $I_2(t)$ are determined by consideration of the sum over m. If $m \leq p$,

$$I_1(t) = \frac{2}{R} \sum_p \left(\psi(t; \mathcal{B}_p^a, \mathcal{A}_{p+1}^a) - \psi(t; \mathcal{B}_p^b, \mathcal{A}_{p+1}^b) \right)$$

$$\times \sum_{m=-\infty}^{p} \left(e^{-\gamma(t-\mathcal{A}_m^a)} - e^{-\gamma(t-\mathcal{A}_m^b)} + e^{-\gamma(t-\mathcal{B}_m^b)} - e^{-\gamma(t-\mathcal{B}_m^a)} \right).$$

When $m > p$,

$$\psi(t; \mathcal{A}_m^a, \infty)[\psi(t; \mathcal{B}_p^a, \mathcal{A}_{p+1}^a) - \psi(t; \mathcal{B}_p^b, \mathcal{A}_{p+1}^b)] = \begin{cases} \psi(t; \mathcal{A}_m^a, \mathcal{A}_m^b), & \text{when } p = m-1, \\ 0, & \text{otherwise,} \end{cases}$$

for example. Therefore, $I_2(t)$, is non-zero when $p = m - 1$ only, in other words

$$I_2(t) = -\sum_m \left[e^{-\gamma(t-\mathcal{A}_m^a)}\psi(t; \mathcal{A}_m^a, \mathcal{A}_m^b) + e^{-\gamma(t-\mathcal{A}_m^b)}\psi(t; \mathcal{A}_m^b, \mathcal{A}_m^a) \right.$$

$$\left. + e^{-\gamma(t-\mathcal{B}_m^a)}\psi(t; \mathcal{B}_m^b, \mathcal{B}_m^a) + e^{-\gamma(t-\mathcal{B}_m^b)}\psi(t; \mathcal{B}_m^a, \mathcal{B}_m^b) \right],$$

which, by the property $\psi(t; t_1, t_2) = 0$ when $t_1 > t_2$, becomes

$$I_2(t) = -\frac{2}{R} \sum_m \left[e^{-\gamma(t-\min(\mathcal{A}_m^a, \mathcal{A}_m^b))}\psi(t; \min(\mathcal{A}_m^a, \mathcal{A}_m^b), \max(\mathcal{A}_m^a, \mathcal{A}_m^b)) \right.$$

$$\left. + e^{-\gamma(t-\max(\mathcal{B}_m^a, \mathcal{B}_m^b))}\psi(t; \min(\mathcal{B}_m^a, \mathcal{B}_m^b), \max(\mathcal{B}_m^a, \mathcal{B}_m^b)) \right].$$

We now calculate a Fourier series for each of $I_1(t)$ and $I_2(t)$ in turn.

From the Jacobi-Anger expansions [109] of the exponential terms in $I_1(t)$,

$$I_1(t) = \frac{2}{R} \sum_p \left(\psi(t; \mathcal{B}_p^a, \mathcal{A}_{p+1}^a) - \psi(t; \mathcal{B}_p^b, \mathcal{A}_{p+1}^b) \right)$$

$$\times \sum_{m=-\infty}^{p} e^{-\gamma(t-mT)} \sum_n e^{in\omega_s mT} e^{-3\gamma T/4} J_n\left(\tfrac{1}{4}i\gamma MT\right) \left[(-i)^n e^{-\gamma T/2} - i^n \right] (1 - (-1)^n).$$

We explicitly evaluate the geometric sum over m to give

$$I_1(t) = \frac{2}{R} \sum_p \left(\psi(t; \mathcal{B}_p^a, \mathcal{A}_{p+1}^a) - \psi(t; \mathcal{B}_p^b, \mathcal{A}_{p+1}^b) \right)$$

$$\times \sum_n e^{-\gamma t} \frac{e^{(\gamma+in\omega_s)pT}}{1 - e^{-(\gamma+in\omega_s)T}} e^{-3\gamma T/4} J_n\left(\tfrac{1}{4}i\gamma MT\right) \left[(-i)^n e^{-\gamma T/2} - i^n \right] (1 - (-1)^n),$$

$$\equiv \frac{2}{R} \sum_{np} \frac{e^{(\gamma+in\omega_s)pT}}{1 - e^{-(\gamma+in\omega_s)T}} e^{-3\gamma T/4} J_n\left(\tfrac{1}{4}i\gamma MT\right) \left[(-i)^n e^{-\gamma T/2} - i^n \right] (1 - (-1)^n) F_p(t).$$

The time dependence in $I_1(t)$ consists of a sum over p of terms

$$F_p(t) = e^{-\gamma t} \left(\psi(t; \mathcal{B}_p^a, \mathcal{A}_{p+1}^a) - \psi(t; \mathcal{B}_p^b, \mathcal{A}_{p+1}^b) \right).$$

Taking a Fourier transform of $F_p(t)$ gives

$$
\begin{aligned}
\hat{F}_p(\omega) &= -\frac{e^{-(\gamma+i\omega)pT}}{\gamma+i\omega}\left[e^{-(\gamma+i\omega)(T+\alpha^a_{p+1})} - e^{-(\gamma+i\omega)(T+\alpha^b_{p+1})} + e^{-(\gamma+i\omega)\beta^b_{p+1}} - e^{-(\gamma+i\omega)\beta^a_{p+1}}\right], \\
&= -\frac{e^{-(\gamma+i\omega)pT}}{\gamma+i\omega}\sum_q e^{iq\omega_s pT}(1-(-1)^q)e^{3\gamma T/4}J_q\left(\tfrac{1}{4}(\omega-i\gamma)MT\right) \\
&\qquad\times\left[(-i)^q e^{(-\gamma/2+i(q\omega_s-5\omega/4))T} - i^q e^{-3i\omega T/4}\right].
\end{aligned}
$$

Therefore

$$
\begin{aligned}
\hat{I}_1(\omega) &= -\frac{2}{R}\sum_{npq}\frac{(1-(-1)^n)(1-(-1)^q)}{(\gamma+i\omega)(1-e^{-(\gamma+in\omega_s)T})}e^{i(n+q)\omega_s pT}J_n\left(\tfrac{1}{4}i\gamma MT\right)J_q\left(\tfrac{1}{4}(\omega-i\gamma)MT\right) \\
&\qquad\times\left[(-i)^n e^{-\gamma T/2}-i^n\right]\left[(-i)^q e^{(-\gamma/2+i(q\omega_s-5\omega/4))T} - i^q e^{-3i\omega T/4}\right]e^{-i\omega pT}.
\end{aligned}
$$

Poisson re-summing in p allows us to identify

$$
I_1(t) = \sum_m \sum_{n=0,\pm 2,\pm 4,\ldots} \mathcal{J}_{mn}e^{i\Omega_{mn}t},
$$

where

$$
\begin{aligned}
\mathcal{J}_{mn} &= -\frac{8}{RT}\sum_{q=\pm 1,\pm 3,\ldots}\frac{1}{(\gamma+i\Omega_{mn})(1-e^{-(\gamma+i(n-q)\omega_s)T})} \\
&\qquad\times J_{n-q}\left(\tfrac{1}{4}i\gamma MT\right)J_q\left(\tfrac{1}{4}(\Omega_{mn}-i\gamma)MT\right)\left[(-i)^{n-q}e^{-\gamma T/2}-i^{n-q}\right] \\
&\qquad\times\left[(-i)^q e^{(-\gamma/2+i(q\omega_s-5\Omega_{mn}/4))T} - i^q e^{-3i\Omega_{mn}T/4}\right].
\end{aligned}
\tag{3.12}
$$

We now calculate a Fourier series for $I_2(t)$.

To begin with, we observe that, from (3.7),

$$\min(\mathcal{A}^a_m,\mathcal{A}^b_m)=mT+\frac{T}{4}(1-Ms(mT)), \qquad\qquad \max(\mathcal{A}^a_m,\mathcal{A}^b_m)=mT+\frac{T}{4}(1+Ms(mT)),$$

$$\min(\mathcal{B}^a_m,\mathcal{B}^b_m)=mT+\frac{T}{4}(3-Ms(mT)), \qquad\text{and}\qquad \max(\mathcal{B}^a_m,\mathcal{B}^b_m)=mT+\frac{T}{4}(3+Ms(mT)).$$

Taking a Fourier transform of $I_2(t)$ gives

$$
\begin{aligned}
\hat{I}_2(\omega) &= \frac{2}{R}\sum_m\frac{e^{-i\omega mT}}{\gamma+i\omega}\left(e^{-i\omega T/4}\left[e^{-MT(2\gamma+i\omega)s(mT)/4}-e^{i\omega MTs(mT)/4}\right]\right. \\
&\qquad\left.+e^{-3i\omega T/4}\left[e^{-i\omega MTs(mT)/4}-e^{MT(2\gamma+i\omega)s(mT)/4}\right]\right).
\end{aligned}
$$

From (3.9), it is easily verified that

$$
\begin{aligned}
\hat{I}_2(\omega) &= \frac{2}{R}\sum_m\sum_{n=0,\pm 2,\pm 4,\ldots}\frac{e^{-i\omega mT}}{\gamma+i\omega}\left(e^{-i\omega T/4}\left[B_n\left(\tfrac{1}{4}(2i\gamma-\omega)MT\right)-B_n\left(\tfrac{1}{4}\omega MT\right)\right]\right. \\
&\qquad\left.+e^{-3i\omega T/4}\left[B_n\left(-\tfrac{1}{4}\omega MT\right)-B_n\left(-\tfrac{1}{4}(2i\gamma-\omega)MT\right)\right]\right)e^{in\omega_s mT},
\end{aligned}
$$

where $B_p(z)$ is given in (3.10). Poisson re-summing in m allows us to identify a Fourier series for $I_2(t)$, given by

$$
I_2(t) = \sum_m \sum_{n=0,\pm 2,\pm 4,\ldots} \mathcal{K}_{mn}e^{i\Omega_{mn}t},
$$

where

$$
\begin{aligned}
\mathcal{K}_{mn} \quad = \quad & \frac{2}{(\gamma + i\Omega_{mn})RT}\Bigg(e^{-i\Omega_{mn}T/4}\bigg[B_n\left(\tfrac{1}{4}(2i\gamma - \Omega_{mn})MT\right) - B_n\left(\tfrac{1}{4}\Omega_{mn}MT\right)\bigg] \\
& + e^{-3i\Omega_{mn}T/4}\bigg[B_n\left(-\tfrac{1}{4}\Omega_{mn}MT\right) - B_n\left(-\tfrac{1}{4}(2i\gamma - \Omega_{mn})MT\right)\bigg]\Bigg). \quad (3.13)
\end{aligned}
$$

The Fourier coefficients $\mathcal{J}_{mn}$ and $\mathcal{K}_{mn}$ are complex functions that involve the sums and differences of Bessel functions. Despite the complexity of $\mathcal{J}_{mn}$ and $\mathcal{K}_{mn}$, they are non-zero when n is even only. We now combine the Fourier series for $I_{\mathcal{AB}}(t)$ and $I_{\mathcal{A-B}}(t)$ to derive a Fourier series for $I(t)$.

3.2.3 Fourier Series and Frequency Spectrum for the Input Current

The upper input current is given by

$$
I(t) = \frac{4M}{\pi R} + \sum_{mn} \mathcal{P}_{mn}e^{i\Omega_{mn}t}, \quad (3.14)
$$

where

$$
\mathcal{P}_{mn} = \begin{cases} \mathcal{I}_{mn} + \mathcal{J}_{mn} + \mathcal{K}_{mn}, & n \text{ even}, \\ 0, & n \text{ odd}, \end{cases}
$$

where $\mathcal{I}_{mn}$, $\mathcal{J}_{mn}$ and $\mathcal{K}_{mn}$ are given in (3.11), (3.12) and (3.13), respectively. This reproduces the Fourier series for the input current of a two-phase inverter determined in [31].

For some values of γ, the coefficients $\mathcal{P}_{mn}$ decay slowly with respect to n (for fixed m). This means that the number of peaks in each carrier group increases. Consequently, for some ratios of ω_c/ω_s (provided $\omega_c/\omega_s \in \mathbb{Q}$), each peak in the frequency spectrum will have a contribution from several carrier groups. Note that, if ω_c/ω_s is irrational, the contribution at each frequency is unique, coming from a single Fourier coefficient.

Each peak in the frequency spectrum of $I(t)$ has amplitude

$$
\left| \sum_{k=-\infty}^{\infty} \mathcal{P}_{m+k,n-\omega_c k/\omega_s} \right|,
$$

for fixed m and n. The coefficients $|\mathcal{P}_{m+k,n-\omega_c k/\omega_s}| \to 0$ as $k \to \infty$, however, and in this thesis we only plot contributions to the spectrum with magnitude 10^{-5} and greater. Therefore, in order to reduce the numerical cost of plotting spectra for $I(t)$, we identify an integer N for which $|\mathcal{P}_{m\pm N,n\mp\omega_c N/\omega_s}| \geq 10^{-5}$ and $|\mathcal{P}_{m\pm(N+1),n\mp\omega_c(N+1)/\omega_s}| < 10^{-5}$ for all m and n. From empirical evidence, for the spectra plotted in this section, $N = 3$. Therefore, we plot the *amplitude*,

$$
\left| \sum_{k=-3}^{3} \mathcal{P}_{m+k,n-\omega_c k/\omega_s} \right|, \quad (3.15)
$$

against the *harmonic number*, Ω_{mn}/ω_s. Note that, from (3.15) and (3.14), if ω_c is a multiple of $2\omega_s$, there is contribution to the frequency spectrum of $I(t)$ only when the harmonic order is even.

We now note that, previously, we described the low-frequency components of the spectrum as those corresponding to the $m = 0$ carrier group, and described the high-frequency components

as those corresponding to the carrier groups with $m \neq 0$. When plotting spectra where several carrier groups contribute to each peak in the spectrum this definition is inadequate, because it is not clear where the high-frequency and low-frequency components in the spectrum begin or end. Therefore, similar to [69], we use an alternative convention for describing the high and low frequency components of the spectrum: the low-frequency components of the spectrum are those with harmonic order less than $\omega_c/2\omega_s$; the high-frequency components are those with harmonic order greater than $\omega_c/2\omega_s$.

The frequency spectrum of $I(t)$ is shown in figure 3.5 for a range of ratios γ. Note that, because we plot the absolute values of the Fourier coefficients, the frequency spectrum for $I^-(t)$ is identical to the spectrum of $I(t)$ (because $|I(t)| = |I^-(t)|$). The spectra plotted in this section agree with those in [31], and, furthermore, we provide spectra determined from FFTs of Matlab simulations of the input current waveform to verify the accuracy of our analytical results.

The agreement between the dominant contributions to the spectrum in the simulated and analytical spectra is near absolute. For the non-dominant contributions, however, the agreement is not as good. In particular, as $L \to 0$ (for R fixed), more errors appear between the simulated and the analytical results.

The dominant low-frequency contribution to the spectra in figure 3.5 is the DC component, and the dominant high-frequency contribution to the spectrum is at $2\omega_c$. Note that the frequencies with a dominant contribution to the spectrum are unaffected by γ.

We now examine how variation of γ affects the spectrum of $I(t)$. From comparison of figures 3.5(a) and 3.5(c), as $L \to 0$, the number of peaks in each carrier group increases for fixed R (and the Fourier coefficients $\mathcal{P}_{mn}$ decay more slowly with respect to n, for fixed m). Conversely, as $L \to \infty$ (with R fixed), the number of peaks in each carrier group decreases (from comparison of figures 3.5(a) and 3.5(e)). Thus, the number of peaks in each carrier group is affected by γ. We also note that, for all γ, the low-frequency current ripple contributions to the spectrum of $I(t)$ asymptote to zero as the ratio ω_c/ω_s increases.

4 Three-Phase Inverters

We now calculate, for the first time using the single-sum method, the input currents of a three-phase inverter wired in the Δ configuration (shown in figure 2.9). This calculation is significantly more difficult than the previous calculations, as there are three loads in a three-phase inverter, all with different output currents that contribute to the input currents differently. We assume, in this section, that all the load impedances are equal in a three-phase inverter.

We begin by calculating the output currents of a three-phase inverter with a series RL load in section 4.1. In section 4.2 we calculate the input currents of a three-phase inverter with a series RL load.

(a) $\gamma = 1$, *analytical.*

(b) $\gamma = 10$, *simulated.*

(c) $\gamma = 10$, *analytical.*

(d) $\gamma = 10$, *simulated.*

(e) $\gamma = 0.1$, *analytical.*

(f) $\gamma = 0.1$, *simulated.*
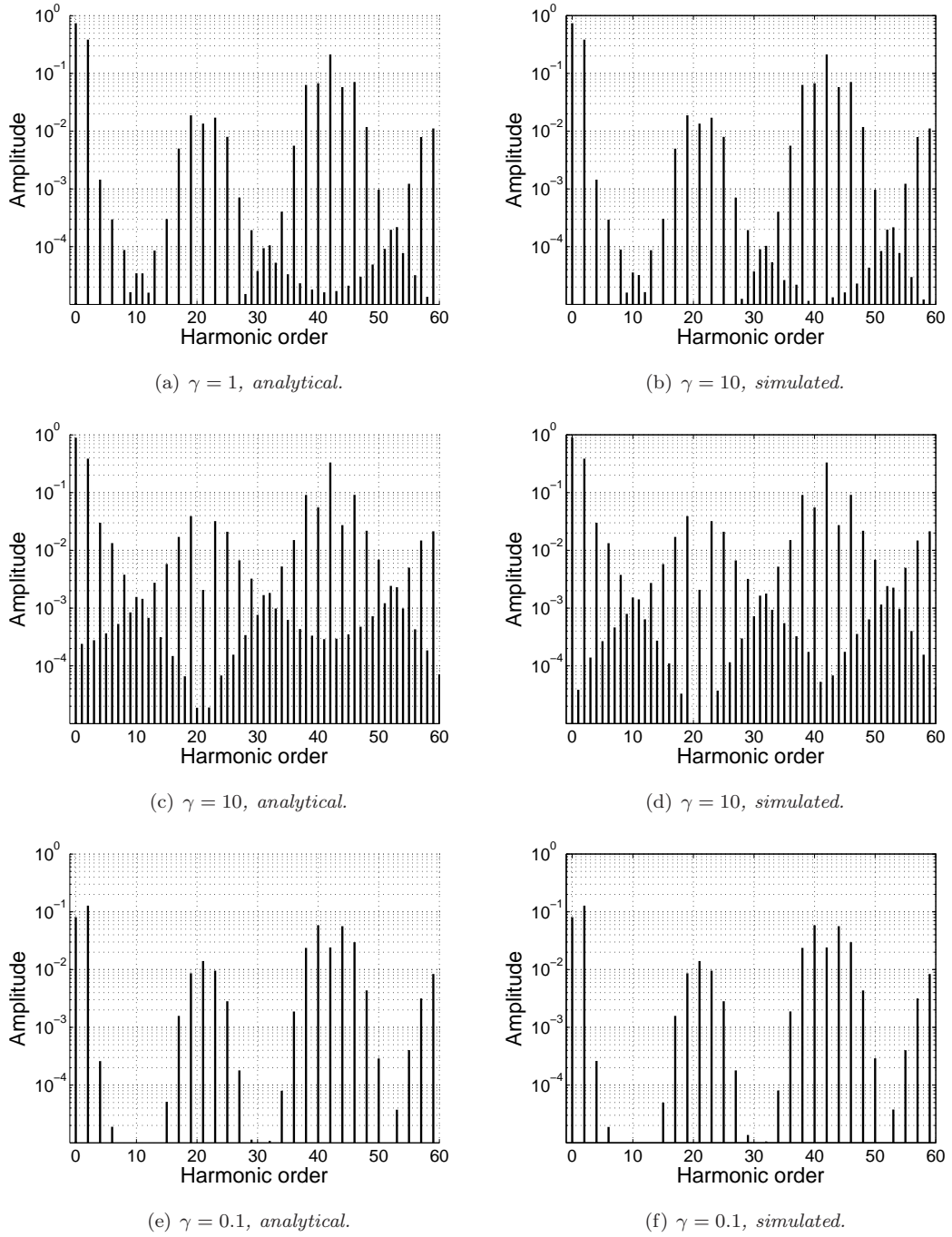
Figure 3.5: *Frequency spectrum of the upper input current $I(t)$ of a two-phase inverter, where $M = 0.9$, $R = 1$ and $\omega_c = 21\omega_s$. Furthermore, in (a) and (b), $L = 1$, in (c) and (d), $L = 0.1$, and in (e) and (f), $L = 10$.*

(a) *Analytical.* (b) *Simulated.*
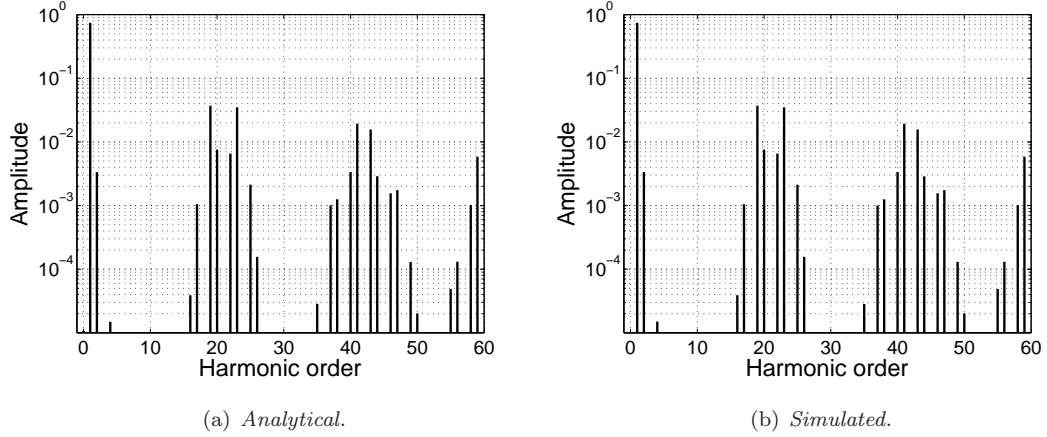
Figure 3.6: *Frequency spectrum of the output current $i_{ab}(t)$ of a three-phase inverter, where $M = 0.9$, $\omega_c = 21\omega_s$ and $\gamma = 1$.*

4.1 Output Currents

There are three loads in a three-phase inverter, and therefore there are three output currents. Each of these output currents can be determined if the voltage difference across the load and the load are known. The three voltage differences are $v_{ab}(t) = v_a(t) - v_b(t)$, $v_{bc}(t) = v_b(t) - v_c(t)$ and $v_{ca}(t) = v_c(t) - v_a(t)$. Therefore, from (3.1), in a three-phase inverter with a series RL load, the three output currents have Fourier series

$$i_{ab}(t) = \sum_{mn} \frac{1 - e^{-2\pi in/3}}{R + i\Omega_{mn}L} a_{mn} e^{i\Omega_{mn}t} \equiv \sum_{mn} i_{mn} e^{i\Omega_{mn}t},$$

$$i_{bc}(t) = \sum_{mn} i_{mn} e^{-2\pi in/3} e^{i\Omega_{mn}t}, \qquad \text{and} \qquad i_{ca}(t) = \sum_{mn} i_{mn} e^{2\pi in/3} e^{i\Omega_{mn}t},$$

where a_{mn} is given in (2.3). All three output currents have identical frequency spectrum, illustrated in figure 3.6. The dominant low-frequency contribution to the spectrum is at ω_s, and when n is a multiple of 3 there is no contribution to the spectrum, caused by taking the difference between two currents, as expected (see [13, 40], for example). Mathematically, the harmonic cancellation is a consequence of the $1 - e^{-2\pi in/3}$ term. We have omitted spectra for the output currents for a range of R/L because the effects on the spectrum are similar to those shown in figure 3.1.

To apply the single-sum method we determine, for each output current, a discrete switching function in the time domain. Since $i_{ab}(t) = i_{ad}(t) - i_{ad}(t)$, we have, from (2.9),

$$i_{ab}(t) = g_{\mathcal{AB}}^{ab}(t) + g_{\mathcal{A}}^{ab}(t) - g_{\mathcal{B}}^{ab}(t), \tag{4.1}$$

where

$$g_{\mathcal{AB}}^{ab}(t) = -\frac{2}{R} \sum_m \left[\psi(t; \mathcal{A}_m^a, \mathcal{B}_m^a) - \psi(t; \mathcal{A}_m^b, \mathcal{B}_m^b) \right], \tag{4.2}$$

$$g_{\mathcal{A}}^{ab}(t) = \frac{2}{R} \sum_m \left[e^{-\gamma(t - \mathcal{A}_m^a)} \psi(t; \mathcal{A}_m^a, \infty) - e^{-\gamma(t - \mathcal{A}_m^b)} \psi(t; \mathcal{A}_m^b, \infty) \right], \tag{4.3}$$

where $\mathcal{A}_m^a$, $\mathcal{B}_m^a$ are given in (2.2), and $\mathcal{A}_m^b$, $\mathcal{B}_m^b$ are defined similarly, with signal wave $s_b(t) = M\cos(\omega_s - 2\pi n/3)$. Note $g_{\mathcal{B}}^{ab}(t)$ is defined similarly to (4.3). The other two input currents, $i_{bc}(t)$ and $i_{ca}(t)$, are defined similarly to (4.1).

4.2 Input Currents

In order to derive the input currents of a three-phase inverter as discrete switching functions in the time domain, it is useful to examine the contribution to the input current from each phase-leg, and then rearrange this expression in terms of the output currents.

To begin with we examine the contribution to the upper input current $I(t)$ from phase-leg a, which we term $I_a(t)$. Figure 3.7 shows the currents flowing out of phase-leg a ($i_{ab}(t)$ and $i_{ac}(t)$) and the input current $I_a(t)$ flowing into phase-leg a from the upper DC source. By Kirchhoff's current law [103], if phase-leg a is connected to the upper DC-source then $I_a(t) = i_{ab}(t) + i_{ac}(t)$, and if phase-leg a is connected to the lower DC source then $I_a(t) = 0$. In other words,

$$I_a(t) = \sum_{p=-\infty}^{\infty} \left(i_{ab}(t) - i_{ca}(t) \right) \psi(t; \mathcal{B}_p^a, \mathcal{A}_{p+1}^a).$$

Note that the input current $I_b(t)$ or $I_c(t)$ flowing into phase-leg b or c, respectively, is defined similarly to $I_a(t)$. Therefore,

$$\begin{aligned} I(t) &= I_a(t) + I_b(t) + I_c(t), \\ &= \sum_{p=-\infty}^{\infty} \left[\left(i_{ab}(t) - i_{ca}(t) \right) \psi(t; \mathcal{B}_p^a, \mathcal{A}_{p+1}^a) + \left(i_{bc}(t) - i_{ab}(t) \right) \psi(t; \mathcal{B}_p^b, \mathcal{A}_{p+1}^b) \right. \\ &\qquad \left. + \left(i_{ca}(t) - i_{bc}(t) \right) \psi(t; \mathcal{B}_p^c, \mathcal{A}_{p+1}^c) \right], \end{aligned}$$

where $\mathcal{B}_p^c$ and $\mathcal{A}_{p+1}^c$ are defined similarly to (2.2), with signal wave $s_c(t) = M\cos(\omega_s t + \frac{2\pi}{3})$. By grouping together the output currents, we have an alternative expression for $I(t)$,

$$I(t) = I_{ab}(t) + I_{bc}(t) + I_{ca}(t), \tag{4.4}$$

where

$$I_{ab}(t) = i_{ab}(t) \sum_{p=-\infty}^{\infty} \left[\psi(t; \mathcal{B}_p^a, \mathcal{A}_{p+1}^a) - \psi(t; \mathcal{B}_p^b, \mathcal{A}_{p+1}^b) \right], \tag{4.5}$$

and $I_{bc}(t)$, $I_{ca}(t)$ are defined similarly. Note that, by a similar argument, the input current drawn from the lower DC source is equal to $-I(t)$. We now determine $I(t)$, by examining each of $I_{ab}(t)$, $I_{bc}(t)$ and $I_{ca}(t)$ in turn.

We write $I_{ab}(t)$ as, from (4.1–4.3),

$$I_{ab}(t) = I_{\mathcal{AB}}^{ab}(t) + I_{\mathcal{A}-\mathcal{B}}^{ab}(t), \tag{4.6}$$
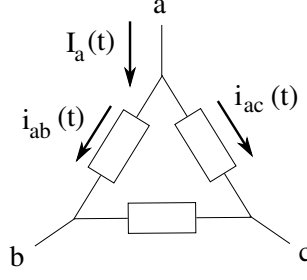
Figure 3.7: *Diagram showing the currents flowing out of ($i_{ab}(t)$ and $i_{ac}(t)$) phase-leg a, and the currents flowing into ($I_a(t)$) phase-leg a from the upper DC source.*

where

$$
I_{\mathcal{AB}}^{ab}(t) = -\frac{2}{R}\sum_{mp}\left[\psi(t;\mathcal{A}_m^a,\mathcal{B}_m^a) - \psi(t;\mathcal{A}_m^b,\mathcal{B}_m^b)\right]\left[\psi(t;\mathcal{B}_p^a,\mathcal{A}_{p+1}^a) - \psi(t;\mathcal{B}_p^b,\mathcal{A}_{p+1}^b)\right],
$$

$$
I_{\mathcal{A}-\mathcal{B}}^{ab}(t) = \frac{2}{R}\sum_{mp}\left[e^{-\gamma(t-\mathcal{A}_m^a)}\psi(t;\mathcal{A}_m^a,\infty) - e^{-\gamma(t-\mathcal{A}_m^b)}\psi(t;\mathcal{A}_m^b,\infty) - e^{-\gamma(t-\mathcal{B}_m^a)}\psi(t;\mathcal{B}_m^a,\infty)\right.
$$

$$
\left. + e^{-\gamma(t-\mathcal{B}_m^b)}\psi(t;\mathcal{B}_m^b,\infty)\right]\left[\psi(t;\mathcal{B}_p^a,\mathcal{A}_{p+1}^a) - \psi(t;\mathcal{B}_p^b,\mathcal{A}_{p+1}^b)\right]. \quad (4.7)
$$

We now calculate each of $I_{\mathcal{AB}}^{ab}(t)$ and $I_{\mathcal{A}-\mathcal{B}}^{ab}(t)$ in turn.

4.2.1 $I_{\mathcal{AB}}^{ab}(t)$

It is straightforward to see that

$$
I_{\mathcal{AB}}^{ab}(t) = \frac{2}{R}\sum_m\left(\psi(t;\mathcal{A}_m^a,\mathcal{A}_m^b) + \psi(t;\mathcal{A}_m^b,\mathcal{A}_m^a) + \psi(t;\mathcal{B}_m^a,\mathcal{B}_m^b) + \psi(t;\mathcal{B}_m^b,\mathcal{B}_m^a)\right)
$$

Therefore, we have, by the property that $\psi(t;t_1,t_2) = 0$ when $t_1 > t_2$,

$$
I_{\mathcal{AB}}^{ab}(t) = \frac{2}{R}\sum_m\left(\psi(t;\min(\mathcal{A}_m^a,\mathcal{A}_m^b),\max(\mathcal{A}_m^a,\mathcal{A}_m^b)) + \psi(t;\min(\mathcal{B}_m^a,\mathcal{B}_m^b),\max(\mathcal{B}_m^a,\mathcal{B}_m^b))\right).
$$

We now introduce two functions $\delta_{\min}(t)$ and $\delta_{\max}(t)$:

$$
\delta_{\min}(t) = \min\{\cos\omega_s t, \cos(\omega_s t - 2\pi/3)\} = \begin{cases} \cos\left(\omega_s t - \frac{2\pi}{3}\right), & -\frac{2\pi}{3} < \omega_s t < \frac{\pi}{3}, \\ \cos\omega_s t, & \frac{\pi}{3} < \omega_s t < \frac{4\pi}{3}, \end{cases} \quad (4.8)
$$

$$
\delta_{\max}(t) = \max\{\cos\omega_s t, \cos(\omega_s t - 2\pi/3)\} = \begin{cases} \cos\omega_s t, & -\frac{2\pi}{3} < \omega_s t < \frac{\pi}{3}, \\ \cos\left(\omega_s t - \frac{2\pi}{3}\right), & \frac{\pi}{3} < \omega_s t < \frac{4\pi}{3}. \end{cases} \quad (4.9)
$$

Thus in terms of $\delta_{\min}(t)$ and $\delta_{\max}(t)$, we have

$$
I_{\mathcal{AB}}^{ab}(t) = \frac{2}{R}\sum_m\left[\psi\left(t; mT + \frac{T}{4}(1 + M\delta_{\min}(mT)), mT + \frac{T}{4}(1 + M\delta_{\max}(mT))\right)\right.
$$

$$
\left. + \psi\left(t; mT + \frac{T}{4}(3 - M\delta_{\max}(mT)), mT + \frac{T}{4}(3 - M\delta_{\min}(mT))\right)\right]. (4.10)
$$

Taking a Fourier transform gives, for $\omega \neq 0$,

$$
\hat{I}_{\mathcal{AB}}^{ab}(\omega) = \frac{2}{R}\sum_m\left(\int_{mT+\frac{T}{4}(1+M\delta_{\min}(mT))}^{mT+\frac{T}{4}(1+M\delta_{\max}(mT))} e^{-i\omega t}\,\mathrm{d}t + \int_{mT+\frac{T}{4}(3-M\delta_{\max}(mT))}^{nT+\frac{T}{4}(3-M\delta_{\min}(mT))} e^{-i\omega t}\,\mathrm{d}t\right).
$$

Thus, for $\omega \neq 0$, we have

$$
\hat{I}_{\mathcal{AB}}^{ab}(\omega) = \frac{2}{R} \sum_m (-i\omega)^{-1} e^{-i\omega mT} \bigg(e^{-i\omega T/4} (e^{-i\omega MT\delta_{\max}(mT)/4} - e^{-i\omega MT\delta_{\min}(mT)/4})
$$
$$
+ e^{-3i\omega T/4} (e^{i\omega MT\delta_{\min}(mT)/4} - e^{i\omega MT\delta_{\max}(mT)/4}) \bigg).
$$

We now determine Fourier series for $e^{i\omega MT\delta_{\min}(t)/4}$ and $e^{i\omega MT\delta_{\max}(t)/4}$.

Fourier Series for $e^{i\lambda\delta_{\min}(t)}$ and $e^{i\lambda\delta_{\max}(t)}$

Fourier series for $e^{i\lambda\delta_{\min}(t)}$ and $e^{i\lambda\delta_{\max}(t)}$ are given by,

$$
e^{i\lambda\delta_{\min}(t)} = \sum_n C_n^+(\lambda) e^{in\omega_s t}, \qquad e^{i\lambda\delta_{\max}(t)} = \sum_n C_n^-(\lambda) e^{in\omega_s t}.
$$

The Fourier coefficients are readily determined to be,

$$
C_n^\pm(\lambda) = \frac{1}{2} J_n(\lambda) (1 + e^{2\pi ip/3}) e^{in\pi/2}
$$
$$
\pm \sum_{p \neq n} \frac{1}{2\pi i(n-p)} J_p(\lambda) (1 - e^{2\pi ip/3}) e^{-i(n-p)\pi/3} (1 - e^{-i(n-p)\pi}) e^{ip\pi/2}. \quad (4.11)
$$

These Fourier coefficients are very complex functions, that are evaluated by taking an infinite sum over Bessel functions. Consequently, the behaviour of $C_n^\pm(\lambda)$ is difficult to interpret.

Fourier Transform

We now return to the Fourier transform of $I_{\mathcal{AB}}^{ab}(t)$. The Fourier transform $\hat{I}_{\mathcal{AB}}^{ab}(\omega)$ is, from (4.11), when $\omega \neq 0$,

$$
\hat{I}_{\mathcal{AB}}^{ab}(\omega) = \frac{2}{R} \sum_{mn} (-i\omega)^{-1} e^{-i\omega mT + in\omega_s mT} \bigg(e^{-i\omega T/4} \Big[C_n^- \left(-\tfrac{1}{4}\omega MT\right) - C_n^+ \left(-\tfrac{1}{4}\omega MT\right) \Big]
$$
$$
+ e^{-3i\omega T/4} \Big[C_n^+ \left(\tfrac{1}{4}\omega MT\right) - C_n^- \left(\tfrac{1}{4}\omega MT\right) \Big] \bigg).
$$

Poisson re-summing in m determines

$$
\hat{I}_{\mathcal{AB}}^{ab}(\omega) = \frac{2}{R} \sum_{mn} \int_{-\infty}^{\infty} (-i\omega T)^{-1} e^{i\Omega_{mn} t} \bigg(e^{-i\omega T/4} \Big[C_n^- \left(-\tfrac{1}{4}\omega MT\right) - C_n^+ \left(-\tfrac{1}{4}\omega MT\right) \Big]
$$
$$
+ e^{-3i\omega T/4} \Big[C_n^+ \left(\tfrac{1}{4}\omega MT\right) - C_n^- \left(\tfrac{1}{4}\omega MT\right) \Big] \bigg) e^{-i\omega t} \, \mathrm{d}t.
$$

Thus we have

$$
I_{\mathcal{AB}}^{ab}(t) = \frac{1}{R} + \sum_{mn} \mathcal{I}_{mn}^{ab} e^{i\Omega_{mn} t},
$$

where $\Omega_{mn} = m\omega_c + n\omega_s$ and

$$
\mathcal{I}_{mn}^{ab} = \begin{cases} 0, & \text{if } \Omega_{mn} = 0, \\[2ex] \dfrac{-2}{i\Omega_{mn}RT} \bigg(e^{-i\Omega_{mn}T/4} \Big[C_n^- \left(-\tfrac{1}{4}\Omega_{mn}MT\right) - C_n^+ \left(-\tfrac{1}{4}\Omega_{mn}MT\right) \Big] & \text{otherwise.} \\ \qquad + e^{-3i\Omega_{mn}T/4} \Big[C_n^+ \left(\tfrac{1}{4}\Omega_{mn}MT\right) - C_n^- \left(\tfrac{1}{4}\Omega_{mn}MT\right) \Big] \bigg), \end{cases} \quad (4.12)
$$

Note that the constant term $1/R$ is the contribution to $I_{\mathcal{AB}}^{ab}(t)$ when $\Omega_{mn} = 0$, determined by taking the average value of (4.10). The Fourier coefficient $\mathcal{I}_{mn}^{ab}$ involves the differences of Fourier coefficients $C_n^{\pm}(\lambda)$, which, as discussed previously, are complex functions. Therefore, the behaviour of $\mathcal{I}_{mn}^{ab}$ is even more complex, as each Fourier coefficient is evaluated by taking the difference between infinite sums of Bessel functions.

4.2.2 $I_{\mathcal{A}-\mathcal{B}}^{ab}(t)$

We now write $I_{\mathcal{A}-\mathcal{B}}^{ab}(t)$ as

$$I_{\mathcal{A}-\mathcal{B}}^{ab}(t) = I_1^{ab}(t) + I_2^{ab}(t),$$

where $I_1(t)$ and $I_2(t)$ are found from consideration of the sum over m. If $m \leq p$,

$$
I_1^{ab}(t) = \frac{2}{R} \sum_p \left(\psi(t; \mathcal{B}_p^a, \mathcal{A}_{p+1}^a) - \psi(t; \mathcal{B}_p^b, \mathcal{A}_{p+1}^b) \right)
$$
$$
\times \sum_{m=-\infty}^{p} \left(e^{-\gamma(t-\mathcal{A}_m^a)} - e^{-\gamma(t-\mathcal{A}_m^b)} + e^{-\gamma(t-\mathcal{B}_m^b)} - e^{-\gamma(t-\mathcal{B}_m^a)} \right).
$$

When $m > p$,

$$
I_2^{ab}(t) = -\frac{2}{R} \sum_m \left[e^{-\gamma(t-\mathcal{A}_m^a)} \psi(t; \mathcal{A}_m^a, \mathcal{A}_m^b) + e^{-\gamma(t-\mathcal{A}_m^b)} \psi(t; \mathcal{A}_m^b, \mathcal{A}_m^a) \right.
$$
$$
\left. + e^{-\gamma(t-\mathcal{B}_m^a)} \psi(t; \mathcal{B}_m^b, \mathcal{B}_m^a) + e^{-\gamma(t-\mathcal{B}_m^b)} \psi(t; \mathcal{B}_m^a, \mathcal{B}_m^b) \right],
$$
$$
= -\frac{2}{R} \sum_m \left[e^{-\gamma(t-\min(\mathcal{A}_m^a, \mathcal{A}_m^b))} \psi(t; \min(\mathcal{A}_m^a, \mathcal{A}_m^b), \max(\mathcal{A}_m^a, \mathcal{A}_m^b)) \right.
$$
$$
\left. + e^{-\gamma(t-\max(\mathcal{B}_m^a, \mathcal{B}_m^b))} \psi(t; \min(\mathcal{B}_m^a, \mathcal{B}_m^b), \max(\mathcal{B}_m^a, \mathcal{B}_m^b)) \right].
$$

We now calculate a Fourier series for each of $I_1^{ab}(t)$ and $I_2^{ab}(t)$ in turn.

By taking Jacobi-Anger expansions of the exponential terms in $I_1^{ab}(t)$,

$$
I_1^{ab}(t) = \frac{2}{R} \sum_p \left(\psi(t; \mathcal{B}_p^a, \mathcal{A}_{p+1}^a) - \psi(t; \mathcal{B}_p^b, \mathcal{A}_{p+1}^b) \right) \sum_{m=-\infty}^{p} e^{-\gamma(t-mT)}
$$
$$
\times \sum_n e^{in\omega_s mT} e^{-3\gamma T/4} J_n \left(\tfrac{1}{4} i\gamma MT \right) \left[(-i)^n e^{-\gamma T/2} - i^n \right] (1 - e^{-2\pi in/3}).
$$

We explicitly evaluate the geometric sum over n to give

$$
I_1^{ab}(t) = \frac{2}{R} \sum_{np} \frac{e^{(\gamma+in\omega_s)pT}}{1 - e^{-(\gamma+in\omega_s)T}} e^{-3\gamma T/4} J_n \left(\tfrac{1}{4} i\gamma MT \right) \left[(-i)^n e^{-\gamma T/2} - i^n \right] (1 - e^{-2\pi in/3}) F_p^{ab}(t),
$$

where

$$
F_p^{ab}(t) = e^{-\gamma t} \left(\psi(t; \mathcal{B}_p^a, \mathcal{A}_{p+1}^a) - \psi(t; \mathcal{B}_p^b, \mathcal{A}_{p+1}^b) \right),
$$

which are the time dependent terms of $I_1^{ab}(t)$. We take a Fourier transform of $F_p^{ab}(t)$, which gives

$$
\hat{F}_p^{ab}(\omega) = -\frac{e^{-(\gamma+i\omega)pT}}{\gamma + i\omega} \sum_q e^{iq\omega_s pT} (1 - e^{-2\pi iq/3}) e^{3\gamma T/4} J_q \left(\tfrac{1}{4}(\omega - i\gamma)MT \right)
$$
$$
\times \left[(-i)^q e^{(-\gamma/2 + i(q\omega_s - 5\omega/4))T} - i^q e^{-3i\omega T/4} \right].
$$

Therefore,

$$
\begin{aligned}
\hat{I}_1^{ab}(\omega) &= -\frac{2}{R}\sum_{npq}\frac{(1-e^{-2\pi in/3})(1-e^{-2\pi iq/3})}{(\gamma+i\omega)(1-e^{-(\gamma+in\omega_s)T})}e^{i(n+q)\omega_s pT}J_n\left(\tfrac{1}{4}i\gamma MT\right)J_q\left(\tfrac{1}{4}(\omega-i\gamma)MT\right) \\
&\quad \times \left[(-i)^n e^{-\gamma T/2}-i^n\right]\left[(-i)^q e^{(-\gamma/2+i(q\omega_s-5\omega/4))T}-i^q e^{-3i\omega T/4}\right]e^{-i\omega pT}.
\end{aligned}
$$

Poisson re-summing in p allows us to identify

$$
I_1^{ab}(t) = \sum_{mn}\mathcal{J}_{mn}^{ab}e^{i\Omega_{mn}t},
$$

where

$$
\begin{aligned}
\mathcal{J}_{mn}^{ab} &= -\frac{8}{RT}\sum_q\frac{(1-e^{-2\pi iq/3})(1-e^{-2\pi ir/3})}{(\gamma+i\Omega_{mn})(1-e^{-(\gamma+i(n-q)\omega_s)T})}J_q\left(\tfrac{1}{4}i\gamma MT\right)J_r\left(\tfrac{1}{4}(\Omega_{mn}-i\gamma)MT\right) \\
&\quad \times \left[(-i)^q e^{-\gamma T/2}-i^q\right]\left[(-i)^r e^{(-\gamma/2+i(q\omega_s-5\Omega_{mn}/4))T}-i^r e^{-3i\Omega_{mn}T/4}\right]. \qquad (4.13)
\end{aligned}
$$

We now calculate a Fourier series for $I_2^{ab}(t)$.

Taking a Fourier transform of $I_2^{ab}(t)$ gives

$$
\begin{aligned}
\hat{I}_2^{ab}(\omega) &= \frac{2}{R}\sum_m\frac{1}{\gamma+i\omega}e^{-i\omega mT}\Bigg[e^{-i\omega T/4}e^{-i\gamma MT\delta_{\min}(mT)/4}\bigg(e^{-(\gamma+i\omega)MT\delta_{\max}(mT)/4} \\
&\quad -e^{-(\gamma+i\omega)MT\delta_{\min}(mT)/4}\bigg)+e^{-3i\omega T/4}e^{\gamma MT\delta_{\min}(mT)/4} \\
&\quad \times\bigg(e^{(\gamma+i\omega)MT\delta_{\min}(mT)/4}-e^{(\gamma+i\omega)MT\delta_{\max}(mT)/4}\bigg)\Bigg],
\end{aligned}
$$

where $\delta_{\min}(t)$ and $\delta_{\max}(t)$ are given in (4.8) and (4.9), respectively. Therefore we have

$$
\begin{aligned}
\hat{I}_2^{ab}(\omega) &= \frac{2}{R}\sum_m\frac{1}{\gamma+i\omega}e^{-i\omega mT}\Bigg[e^{-i\omega T/4}\bigg(e^{\gamma MT(\delta_{\min}(mT)-\delta_{\max}(mT))/4}e^{-i\omega MT\delta_{\max}(mT)/4} \\
&\quad -e^{-i\omega MT\delta_{min}(mT)/4}\bigg)+e^{-3i\omega T/4}\bigg(e^{i\omega\delta_{\min}(mT)/4} \\
&\quad -e^{-\gamma MT(\delta_{\min}(mT)-\delta_{\max}(mT))/4}e^{i\omega MT\delta_{\max}(mT)/4}\bigg)\Bigg].
\end{aligned}
$$

We now determine Fourier series for some of the exponential terms in $\hat{I}_2^{ab}(\omega)$.

Fourier Series for $e^{z(\delta_{\min}(t)-\delta_{\max}(t))}$

The Fourier series for $e^{z(\delta_{\min}(t)-\delta_{\max}(t))}$ is given by,

$$
e^{z(\delta_{\min}(t)-\delta_{\max}(t))} = \sum_n D_n(z)e^{in\omega_s t}.
$$

In order to determine the Fourier coefficients $D_n(z)$ that are not expressed as the product of Bessel functions, we require an alternative expression for $\delta_{\min}(t)-\delta_{\max}(t)$. Now, from (4.8)

and (4.9), we have

$$\delta_{\min}(t) - \delta_{\max}(t) = \begin{cases} \cos\left(\omega_s t - \frac{2\pi}{3}\right) - \cos\omega_s t, & -\frac{2\pi}{3} < \omega_s t < \frac{\pi}{3}, \\ \cos\omega_s t - \cos\left(\omega_s t - \frac{2\pi}{3}\right), & \frac{\pi}{3} < \omega_s t < \frac{4\pi}{3}, \end{cases}$$

$$= \begin{cases} \sqrt{3}\cos\left(\omega_s t - \frac{5\pi}{6}\right), & -\frac{2\pi}{3} < \omega_s t < \frac{\pi}{3}, \\ -\sqrt{3}\cos\left(\omega_s t - \frac{5\pi}{6}\right), & \frac{\pi}{3} < \omega_s t < \frac{4\pi}{3}, \end{cases}$$

$$= -\sqrt{3}\left|\cos\left(\omega_s t - \frac{5\pi}{6}\right)\right|.$$

Therefore,

$$D_n(z) = \frac{\omega_s}{2\pi} \int_{2\pi/\omega_s}^{0} e^{-\sqrt{3}z|\cos(\omega_s t - 5\pi/6)|} e^{-in\omega_s t}\, \mathrm{d}t,$$

$$= \frac{\omega_s}{2\pi}\left[\int_{-2\pi/3\omega_s}^{\pi/3\omega_s} e^{\sqrt{3}z\cos(\omega_s t - 5\pi/6)} e^{-in\omega_s t}\, \mathrm{d}t + \int_{\pi/3\omega_s}^{4\pi/3\omega_s} e^{-\sqrt{3}z\cos(\omega_s t - 5\pi/6)} e^{-in\omega_s t}\, \mathrm{d}t\right].$$

Taking Jacobi-Anger expansions of the exponential terms,

$$D_n(z) = \sum_q \frac{\omega_s}{2\pi} e^{-iq\pi/3} J_q(\sqrt{3}iz)\left[(-1)^q \int_{-2\pi/3\omega_s}^{\pi/3\omega_s} e^{-i(n-q)\omega_s t}\, \mathrm{d}t + \int_{pi/3\omega_s}^{4\pi/3\omega_s} e^{-i(n-q)\omega_s t}\, \mathrm{d}t\right].$$

Now,

$$\int_{-2\pi/3\omega_s}^{\pi/3\omega_s} e^{-i(n-q)\omega_s t}\, \mathrm{d}t = \begin{cases} \dfrac{\pi}{\omega_s}, & \text{if } q = n, \\ \dfrac{e^{-i(n-q)\pi/3}}{i(n-q)\omega_s}(e^{i(n-q)\pi} - 1), & \text{if } q \neq n. \end{cases}$$

Therefore,

$$D_n(z) = \begin{cases} 0, & n \text{ odd}, \\ e^{-i\pi n/3} J_n(\sqrt{3}iz) - \displaystyle\sum_{q=\pm1,\pm3,\pm5,\ldots} \frac{2}{i\pi(n-q)} e^{-i\pi n/3} J_q(\sqrt{3}iz), & n \text{ even}. \end{cases} \tag{4.14}$$

The Fourier coefficient $D_n(z)$ is a complex function. It is either equal to 0 when n is odd, or equal to an infinite sum of Bessel functions when n is even.

Fourier Transform

The Fourier transform of $I_2^{ab}(t)$ is, from (4.11) and (4.14),

$$\hat{I}_2^{ab}(\omega) = \frac{2}{R}\sum_{mn} \frac{e^{in\omega_s mT}}{\gamma + i\omega} e^{-i\omega mT}\left[e^{-3i\omega T/4}C_n^+\left(\tfrac{1}{4}\omega MT\right) - e^{-i\omega T/4}C_n^+\left(-\tfrac{1}{4}\omega MT\right)\right.$$

$$+ \sum_p e^{ip\omega_s mT}\left(e^{-i\omega T/4}C_n^-\left(-\tfrac{1}{4}\omega MT\right) D_p\left(\tfrac{1}{4}\gamma MT\right)\right.$$

$$\left.\left. - e^{-3i\omega T/4}C_n^-\left(\tfrac{1}{4}\omega MT\right) D_p\left(-\tfrac{1}{4}\gamma MT\right)\right)\right],$$

Poisson re-summing in m allows us to identify a Fourier series for $I_2^{ab}(t)$, given by

$$I_2^{ab}(t) = \sum_{mn} \mathcal{K}_{mn}^{ab} e^{i\Omega_{mn}t},$$

where

$$
\begin{aligned}
\mathcal{K}_{mn}^{ab} \;=\;& \frac{2}{(\gamma + i\Omega_{mn})RT}\Bigg[e^{-3i\Omega_{mn}T/4}C_n^+\left(\tfrac{1}{4}\Omega_{mn}MT\right) - e^{-i\Omega_{mn}T/4}C_n^+\left(-\tfrac{1}{4}\Omega_{mn}MT\right) \\
&+ \sum_p \left(e^{-i\Omega_{mn}T/4}C_{n-p}^-\left(-\tfrac{1}{4}\Omega_{mn}MT\right)D_p\left(\tfrac{1}{4}\gamma MT\right) \right. \\
&\left. - e^{-3i\Omega_{mn}T/4}C_{n-p}^-\left(\tfrac{1}{4}\Omega_{mn}MT\right)D_p\left(-\tfrac{1}{4}\gamma MT\right) \right)\Bigg].
\end{aligned}
\tag{4.15}
$$

The Fourier ceofficients $\mathcal{K}_{mn}^{ab}$ are functions of $C_n^{\pm}(\lambda)$ and $D_n(z)$, which are complicated functions that invovle infinite sums of Bessel functions. Therefore, because $\mathcal{K}_{mn}^{ab}$ involves an infinte sum over multiples of $C_n^{\pm}(\lambda)$ and $D_n(z)$, it's behaviour is even more difficult to interpret than the behaviour of $C_n^{\pm}(\lambda)$ or $D_n(z)$. Although each Fourier coefficient $\mathcal{K}_{mn}^{ab}$ involves two infinite sums (one over p, and an additional one for each of $C_n^{\pm}(z)$ and $D_p(z)$), these sums converge quickly.

4.2.3 Fourier Series and Frequency Spectrum for the Input Current

We have now derived a Fourier series for $I_{ab}(t)$, which, from (4.6),

$$
I_{ab}(t) = \frac{1}{R} + \sum_{mn}(\mathcal{I}_{mn}^{ab} + \mathcal{J}_{mn}^{ab} + \mathcal{K}_{mn}^{ab})e^{i\Omega_{mn}t},
\tag{4.16}
$$

where $\mathcal{I}_{mn}^{ab}$, $\mathcal{J}_{mn}^{ab}$ and $\mathcal{K}_{mn}^{ab}$ are given in (4.12), (4.13) and (4.15), respectively. To establish a Fourier series for $I(t)$ we also require, from (4.4), Fourier series for $I_{bc}(t)$ and $I_{ca}(t)$. There is a simple relationship between the Fourier coefficients for $I_{ab}(t)$, $I_{bc}(t)$ and $I_{ca}(t)$, which we highlight using the direct method. It is straightforward that, from (4.5),

$$
I_{ab}(t) = \tfrac{1}{2}i_{ab}(t)(v_a(t) - v_b(t)) \;=\; \sum_{mn}\mathcal{Q}_{mn}e^{i\Omega_{mn}t},
$$

$$
I_{bc}(t) = \sum_{mn}\mathcal{Q}_{mn}e^{i\Omega_{mn}t}e^{-2\pi in/3}, \qquad \text{and} \qquad I_{ca}(t) = \sum_{mn}\mathcal{Q}_{mn}e^{i\Omega_{mn}t}e^{2\pi in/3},
$$

where

$$
\mathcal{Q}_{mn} = \frac{1}{2}\sum_{pq}(1 - e^{-2\pi i(n-q)/3})(1 - e^{-2\pi iq/3})\frac{a_{m-p,n-q}a_{pq}}{R + i\Omega_{mn}L},
$$

where a_{mn} is given in (2.3). Consequently, from (4.16),

$$
\begin{aligned}
I_{bc}(t) &= \frac{1}{R} + \sum_{mn}(\mathcal{I}_{mn}^{ab} + \mathcal{J}_{mn}^{ab} + \mathcal{K}_{mn}^{ab})e^{i\Omega_{mn}t}e^{-2\pi in/3}, \\
I_{ca}(t) &= \frac{1}{R} + \sum_{mn}(\mathcal{I}_{mn}^{ab} + \mathcal{J}_{mn}^{ab} + \mathcal{K}_{mn}^{ab})e^{i\Omega_{mn}t}e^{2\pi in/3}.
\end{aligned}
$$

Therefore, from (4.4),

$$
\begin{aligned}
I(t) &= \frac{3}{R} + \sum_{mn}(1 + e^{-2\pi in/3} + e^{2\pi in/3})(\mathcal{I}_{mn}^{ab} + \mathcal{J}_{mn}^{ab} + \mathcal{K}_{mn}^{ab})e^{i\Omega_{mn}t}, \\
&= \frac{3}{R} + \sum_{mn}\mathcal{P}_{mn}e^{i\Omega_{mn}t},
\end{aligned}
\tag{4.17}
$$

where

$$
\mathcal{P}_{mn} = \begin{cases} 3(\mathcal{I}_{mn}^{ab} + \mathcal{J}_{mn}^{ab} + \mathcal{K}_{mn}^{ab}), & \text{if } \mod(n,3) = 0, \\ 0, & \text{otherwise,} \end{cases}
$$

(a) $\gamma = 1$, *analytical.*

(b) $\gamma = 1$, *simulated.*

(c) $\gamma = 10$, *analytical.*

(d) $\gamma = 10$, *simulated.*

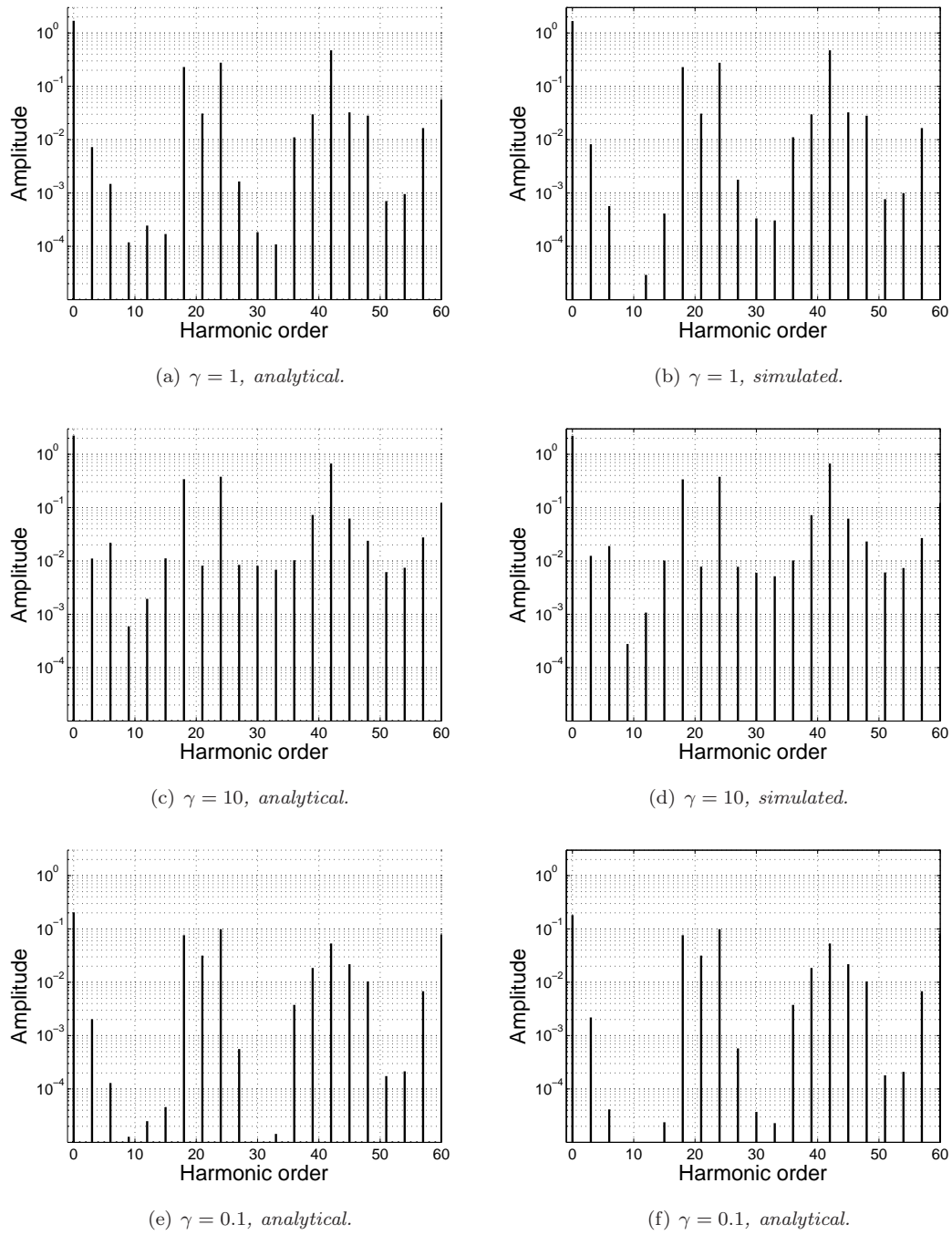(e) $\gamma = 0.1$, *analytical.*

(f) $\gamma = 0.1$, *analytical.*

Figure 3.8: *Frequency spectrum of the upper input current $I(t)$ of a three-phase inverter, where $M = 0.9$, $\omega_c = 21\omega_s$ and $R = 1$. Furthermore, in (a) and (b), $L = 1$, in (c) and (d), $L = 0.1$, and in (e) and (f), $L = 10$.*

where $\mathcal{I}_{mn}^{ab}$, $\mathcal{J}_{mn}^{ab}$ and $\mathcal{K}_{mn}^{ab}$ are given in (4.12), (4.13) and (4.15), respectively.

Similar to the input currents of a two-phase inverter, the Fourier coefficients $\mathcal{P}_{mn}$ for the input currents of a three-phase inverter decay slowly with respect to n (for fixed m). Therefore, provided $\omega_c/\omega_s \in \mathbb{Q}$, for certain ratios ω_c/ω_s, each peak in the spectrum of $I(t)$ will have contribution from several carrier groups. In order to ensure all contributions with magnitude 10^{-5} and greater are accounted for in our spectra, we plot the amplitude (given in (3.15)) against the harmonic number (Ω_{mn}/ω_s) in this section.

The frequency spectrum of $I(t)$ is illustrated in figure 3.8 for a range of ratios γ. Because we plot the absolute value of the Fourier coefficients, the spectrum for the upper input current is identical to the spectrum of the lower input current. Additionally, because $\omega_c = 21\omega_s$, it is easily verified, from (4.17) and (3.15), that there is only contribution to the spectrum when the harmonic order is a multiple of 3. When ω_c is not a multiple of $3\omega_s$, more frequencies will contribute to the spectrum. Therefore, in a three-phase inverter, the input currents have maximum harmonic cancellation when ω_c is a multiple of $3\omega_s$.

We also illustrate, in figure 3.8, frequency spectra generated by taking fast Fourier transforms of simulations of the input current waveform. The agreement between the dominant peaks in the simulated spectra and the analytical spectra is very good, but the agreement is not as good for the non-dominant peaks. We note that our spectra agree with those in [40], generated using the direct method.

From comparison of the spectra in figure 3.8, for all values of γ we examine, the leading low-frequency contribution to the spectrum is the DC component, and the amplitude of this peak increases as $\gamma \to \infty$. Similarly, the leading high-frequency contribution to the spectrum is at $2\omega_c$ for the values of γ we have illustrated spectra for. We also note that the number of peaks in each carrier group decreases as $\gamma \to 0$. Finally, we note that, as the ratio ω_c/ω_s increases, the non-dominant low-frequency contributions to the spectrum of $I(t)$ asymptote to zero. We also note that this is the case for all γ.

5 Conclusions

In this chapter we determined frequency spectra for the input currents a three-phase PWM inverter using the single-sum method for the first time. Previously, the input currents have been determined for three-phase inverters in [40, 86, 94] using the direct method. The direct method is algebraically compact, but Fourier coefficients for the input currents determined using the direct method converge slowly. The more sophisticated single-sum method is algebraically complex, but determines Fourier coefficients that converge much faster than those derived using the direct method. Therefore, the work in this chapter is an advance on previous calculations in [40, 86, 94], as it reduces the numerical cost of plotting input current spectra.

We also determined the input currents for single-phase and two-phase inverters, reviewing the calculations of [31]. In addition to the analysis in [31], we provided a comparison of the single-sum method and the direct method when determining input current spectra for a single-phase

inverter, demonstrating the numerical efficiency of the single-sum method.

The analytical results in this chapter have been corroborated by numerical simulations of the inputs of single-phase, two-phase and three-phase inverters. Furthermore, our results agree with those in [31, 40, 86, 94] for single-phase, two-phase and three-phase inverters.

During the course of our analysis, we demonstrated the known result that, for a two-phase inverter, provided ω_c is a multiple of $2\omega_s$, there is only contribution to the spectrum when the harmonic order is even. We also demonstrated, for a three-phase inverter, only harmonic orders that are a multiple of 3 have a non-zero contribution to spectra of the input currents (provided ω_c is a multiple of $3\omega_s$), as expected (see [40], for example).

In all previous analysis using the direct method [40, 86, 94] and using the single-sum method [31], calculations of input currents have been for specific impedances. In the next chapter, we extend our analysis by calculating input currents for PWM inverters with general output impedance.

PWM Inverters With General Output Impedance

1 Introduction

In this chapter we present calculations to determine frequency spectra for the input currents of several PWM inverters with general output impedance $Z(\omega)$ using the single-sum method, generalising prior calculations for specific output impedances. Examples of previous calculations for specific impedances are in [13, 40, 86, 94] (using the direct method), and in [31, 33] (using the single-sum method).

The calculations in this chapter will be of practical use when determining, analytically, the input currents of PWM inverters with loads we have not examined in this thesis. More specifically, time-consuming analysis will be avoided for future applications of the single-sum method to inverters with loads that are not examined in this thesis.

In order to determine the input currents of an inverter with general output impedance $Z(\omega)$ using the single-sum method, we first derive the output currents by examining the Fourier transform of the current response generated by a single step pulse in the output voltage, and then superpose these currents. Once the output currents have been determined, we then follow the single-sum method (described in chapter 3 and [31, 33]) to determine the input currents for single-phase, two-phase and three-phase PWM inverters with general output impedance $Z(\omega)$.

1.1 Structure of Chapter

In section 2 we derive expressions for the output current of a single phase-leg of a PWM inverter. We first calculate the output current for an inverter with general output impedance $Z(\omega)$ in section 2.1, then determine the current responses to a single voltage pulse for some specific loads in section 2.2. Fourier series for the input current drawn from the upper DC source are derived in section 3 for a range of inverters. Calculations are performed for single-phase inverters with
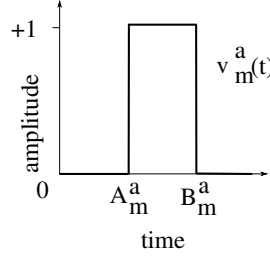
Figure 4.1: *A single voltage pulse $v_m^a(t)$.*

general output impedance $Z(\omega)$ in section 3.1, and then we calculate the input currents for two-phase and three-phase inverters in section 3.2.

2 Output Currents

In this section we determine the output currents of a single-phase inverter by examining the Fourier transform of the current response generated by a single step pulse in the output voltage of the inverter, and then superpose these currents. This method has been used previously in [33]. In section 2.1 we calculate the output current for an inverter with general output impedance $Z(\omega)$. Then, in section 2.2, we plot the current response to a single voltage pulse for a series RL load.

2.1 Output Current with General Impedance

Here we calculate the output current of a single-phase PWM inverter with output impedance $Z(\omega)$. A circuit diagram of a single-phase inverter is illustrated in figure 1.3(a), where the load is connected between phase-leg a and a neutral point d.

We begin by calculating the current response to a single voltage pulse, generated by phase-leg a, before summing these current responses to determine the full output current of a PWM inverter. A single voltage pulse $v_m^a(t)$ is shown in figure 4.1. We describe $v_m^a(t)$ mathematically as

$$v_m^a(t) = \psi(t; \mathcal{A}_m^a, \mathcal{B}_m^a) = \begin{cases} +1, & \text{if } \mathcal{A}_m^a < t < \mathcal{B}_m^a, \\ 0, & \text{otherwise,} \end{cases}$$

where, $\psi(t; \mathcal{A}_m^a, \mathcal{B}_m^a) = 0$ if $\mathcal{A}_m^a > \mathcal{B}_m^a$. The switch times $\mathcal{A}_m^a$ and $\mathcal{B}_m^a$ are determined by samples of a low-frequency signal wave $s_a(t) = M \cos \omega_s t$, with amplitude $|M| \leq 1$ and frequency ω_s. The switch times, for uniform sampling, are

$$\mathcal{A}_m^a = mT + \frac{T}{4}\left(1 + s^a(mT)\right), \qquad \text{and} \qquad \mathcal{B}_m^a = mT + \frac{T}{4}\left(3 - s^a(mT)\right), \qquad (2.1)$$

where m is any integer and $T = 2\pi/\omega_c$ is the switching period, with switching frequency $\omega_c \gg \omega_s$.

To determine the current response to $v_m^a(t)$ we first take a Fourier transform of $v_m^a(t)$, which is

$$\hat{v}_m^a(\omega) = \frac{1}{i\omega}[e^{-i\omega \mathcal{A}_m^a} - e^{-i\omega \mathcal{B}_m^a}].$$

(a) $\Gamma_{r,\rho}$. (b) $C_{r,\rho}^+$. (c) $C_{r,\rho}^-$.
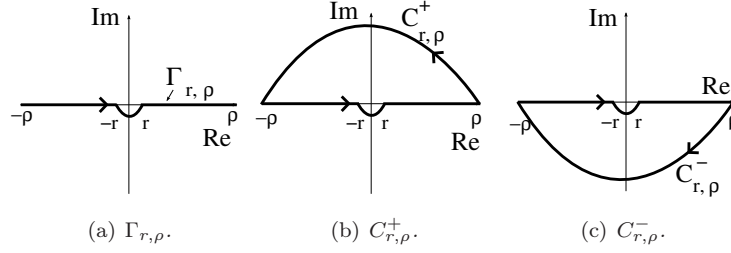
Figure 4.2: *Contours in the complex plane*

We assume the current is 0 before $t = \mathcal{A}_m^a$. Therefore, for a load with general output impedance $Z(\omega)$, the current response $i(t)$ to $v_m^a(t)$ has Fourier transform

$$\hat{\imath}(\omega) = \frac{\hat{v}_m^a(\omega)}{Z(\omega)}.$$

Note that we assume that $Z(\omega)$ is a rational function, which is realistic for a discrete finite circuit of resistors, inductors and capacitors, but is not true in general. An inverse Fourier transform determines

$$i(t) = \frac{1}{2\pi i} \int_{-\infty}^{\infty} \frac{1}{\omega Z(\omega)} (e^{i\omega(t-\mathcal{A}_m^a)} - e^{i\omega(t-\mathcal{B}_m^a)})\, \mathrm{d}\omega.$$

In order to evaluate this integral we use contour integration (see [1], for example). We consider the integral along the contour $\Gamma_{r,\rho}$ (shown in figure 4.2(a)); then

$$i(t) = \lim_{r\to 0,\ \rho\to\infty} \frac{1}{2\pi i} \int_{\Gamma_{r,\rho}} \frac{1}{\omega Z(\omega)} (e^{i\omega(t-\mathcal{A}_m^a)} - e^{i\omega(t-\mathcal{B}_m^a)})\, \mathrm{d}\omega. \qquad (2.2)$$

We calculate the integral in (2.2) by closing the contour and applying Cauchy's residue theorem. The contour $\Gamma_{r,\rho}$ can be closed in two ways: along $C_{r,\rho}^+$ as shown in figure 4.2(b), or along $C_{r,\rho}^-$ as shown in figure 4.2(c).

The functions $e^{i\omega(t-\mathcal{A}_m^a)}$ and $e^{i\omega(t-\mathcal{B}_m^a)}$ are entire functions, so the only poles in the integrand of (2.2) arise from $1/\omega Z(\omega)$. We denote the poles of $1/\omega Z(\omega)$ by ω_j for $j = 1, \ldots, N$. Note that there is a pole at 0 in $1/\omega Z(\omega)$, unless $Z(\omega)$ has a singularity at 0. To ensure all the poles lie within $C_{r,\rho}^+$ we choose the semi-circle of radius r to be below, rather than above, the real axis (either choice makes no difference to the outcome of the integral). We also choose ρ large enough and r small enough so that all the poles lie within $C_{r,\rho}^+$.

We now split the integral in (2.2) into two separate parts,

$$i(t) = i_{\mathcal{A}}(t) - i_{\mathcal{B}}(t),$$

where

$$i_{\mathcal{A}}(t) = \lim_{r\to 0,\ \rho\to\infty} \frac{1}{2\pi i} \int_{\Gamma_{r,\rho}} \frac{e^{i\omega(t-\mathcal{A}_m^a)}}{\omega Z(\omega)}\, \mathrm{d}\omega,$$

and $i_{\mathcal{B}}(t)$ is defined similarly. The choice of contour $C_{r,\rho}^\pm$ over which to evaluate $i_{\mathcal{A}}(t)$ or $i_{\mathcal{B}}(t)$ is determined by our desire that the contribution to the integral from the large curved section of $C_{r,\rho}^\pm$ tends to zero as $\rho \to \infty$ (for fixed r).

We now evaluate the integral $i_{\mathcal{A}}(t)$, as described in [33]. There are two cases to consider: $t < \mathcal{A}_m^a$ and $t > \mathcal{A}_m^a$. In the two cases we close the contour in two different ways. When $t < \mathcal{A}_m^a$ we

evaluate $i_\mathcal{A}(t)$ along $C_{r,\rho}^-$, and when $t > \mathcal{A}_m^a$ we evaluate $i_\mathcal{A}(t)$ along $C_{r,\rho}^+$. There are no poles in $C_{r,\rho}^-$, so when $t < \mathcal{A}_m^a$, $i_\mathcal{A}(t) = 0$ by Cauchy's residue theorem. In $C_{r,\rho}^+$ there are N poles, therefore by Cauchy's residue theorem, when $t > \mathcal{A}_m^a$,

$$
\begin{aligned}
i_\mathcal{A}(t) &= \lim_{\rho \to \infty} \frac{1}{2\pi i} \int_{C_{r,\rho}^+} \frac{e^{i\omega(t - \mathcal{A}_m^a)}}{\omega Z(\omega)} \, d\omega, \\
&= \sum_{j=1}^N \mathrm{Res}\left(\frac{e^{i\omega(t - \mathcal{A}_m^a)}}{\omega Z(\omega)} ; \omega_j \right), \\
&= \sum_{j=1}^N \frac{e^{i\omega_j(t - \mathcal{A}_m^a)}}{Z(\omega_j) + \omega_j Z'(\omega_j)}.
\end{aligned}
$$

Therefore

$$
i_\mathcal{A}(t) = \begin{cases} 0, & \text{if } t < \mathcal{A}_m^a, \\ \displaystyle\sum_{j=1}^N \frac{e^{i\omega_j(t - \mathcal{A}_m^a)}}{Z(\omega_j) + \omega_j Z'(\omega_j)}, & \text{if } t > \mathcal{A}_m^a, \end{cases}
$$

and $i_\mathcal{B}(t)$ is defined similarly.

Thus, the current response to a single voltage pulse is

$$
i(t) = \begin{cases} 0, & \text{if } t < \mathcal{A}_m^a, \\ \displaystyle\sum_{j=1}^N \frac{e^{i\omega_j(t - \mathcal{A}_m^a)}}{Z(\omega_j) + \omega_j Z'(\omega_j)}, & \text{if } \mathcal{A}_m^a < t < \mathcal{B}_m^a, \\ \displaystyle\sum_{j=1}^N \frac{e^{i\omega_j(t - \mathcal{A}_m^a)} - e^{i\omega_j(t - \mathcal{B}_m^a)}}{Z(\omega_j) + \omega_j Z'(\omega_j)}, & \text{if } t > \mathcal{B}_m^a. \end{cases} \tag{2.3}
$$

The current response has three stages: before the up-switching at $t = \mathcal{A}_m^a$ of the voltage from 0 to $+1$; between the up-switching and the down-switching at $t = \mathcal{B}_m^a$, from $+1$ to 0; and after the down-switching. Before the up-switching there is no current flow. Both the up-switching and the down-switching generate a current response (that decays in proportion to $e^{i\omega_j t}$).

The voltage output of a single-phase inverter, $v_a(t)$, is described mathematically as an infinite sum of voltage pulses. In other words

$$
v_a(t) = 1 - 2 \sum_m v_m^a(t).
$$

The steady-state current response, after transients, to a unit voltage is equal to $\frac{1}{Z(0)}$. Summing the current responses to single voltage pulses $v_n^a(t)$, the output current $i_{ad}(t)$ is, from (2.3),

$$
i_{ad}(t) = \frac{1}{Z(0)} - f_\mathcal{A}(t) + f_\mathcal{B}(t), \tag{2.4}
$$

where the subscript ad denotes the load connection, and

$$
f_\mathcal{A}(t) = \sum_{j=1}^N \frac{2}{Z(\omega_j) + \omega_j Z'(\omega_j)} \sum_m e^{i\omega_j(t - \mathcal{A}_m^a)} \psi(t; \mathcal{A}_m^a, \infty), \tag{2.5}
$$

and $f_\mathcal{B}(t)$ is defined similarly. Note that the term $f_\mathcal{A}(t)$ is the sum of current responses to the down-switching from $+1$ to -1 of $v_a(t)$ at the times $t = \mathcal{A}_m^a$, and $f_\mathcal{B}(t)$ is the sum of current responses to the up-switching from -1 to $+1$ of $v_a(t)$ at the times $t = \mathcal{B}_m^a$.

2.2 Current Responses for a Series RL Load

In this section we examine some of the physical attributes of the current response to a single voltage pulse. To achieve this, we plot a number of current responses to single voltage pulses using (2.3). To calculate the current response to a single voltage pulse we first determine the poles of (2.2), which occur when $\omega Z(\omega) = 0$. Therefore for each load we examine in this section we study $Z(\omega)$ before we plot the current response.

The voltage drop across a series RL load determines current in the frequency domain through

$$\hat{v}(\omega) = \left[R + i\omega L\right]\hat{\imath}(\omega) \equiv Z(\omega)\hat{\imath}(\omega).$$

Therefore, for an inverter with a series RL load $\omega Z(\omega) = 0$ when $\omega = 0$ and when $\omega = iR/L \equiv i\gamma$. Thus, from (2.3),

$$i(t) = \begin{cases} 0, & \text{if } t < \mathcal{A}_m^a, \\ \frac{1}{R}(1 - e^{-\gamma(t-\mathcal{A}_m^a)}), & \text{if } \mathcal{A}_m^a < t < \mathcal{B}_m^a, \\ \frac{1}{R}(e^{-\gamma(t-\mathcal{B}_m^a)} - e^{-\gamma(t-\mathcal{A}_m^a)}), & \text{if } t > \mathcal{B}_m^a. \end{cases}$$

Inductors generate a continuous current response (see [85], and the references therein). Current initially exponentially decays towards $1/R$ as a response to the up-switching of the voltage pulse, before exponentially decaying to 0 after the down-switching of the voltage pulse.

We illustrate, in figure 4.3, how the rates of decay are affected for a range of γ. Because the magnitude of $i(t)$ is scalar in R, we fix R and vary L to plot the current response for a range of γ. In all of these figures the time variable has been scaled by the length of the voltage pulse $(\mathcal{B}_m^a - \mathcal{A}_m^a)$. In other words the current responses are plotted against $\tau = \frac{t}{\mathcal{B}_m^a - \mathcal{A}_m^a}$, rather than t. It is straightforward to see that $i(t) \to v_m^a(t)/R$ as $\gamma \to \infty$. In other words, current responses to a voltage pulse through a highly-resistive series RL load approximate the discontinuous voltage pulse (as predicted by [98], for example). As γ decreases, the rate of decay and the magnitude of current response decreases. Thus it is easily verified that the current response to a voltage pulse through a highly inductive load is resistant to change, and decays slowly, as expected (see [85], for example).

3 Input Currents

In this section we determine the input currents of a single-phase, two-phase and three-phase inverter with general output impedance $Z(\omega)$ using the output currents determined in section 2. We calculate the input currents using the single-sum method of [31, 33], which we have used previously, in chapter 3 of this thesis. In fact, the principal steps in the following calculations are the same as in chapter 3, and we just highlight the main differences here.

In this section we use (2.4) and (2.5) to determine the upper input current (the input current drawn from the upper DC source) of a single-phase, two-phase and three-phase inverter with general output impedance $Z(\omega)$. We first find the input current of a single-phase inverter in section 3.1, and then determine the input currents of two-phase and three-phase inverters in section 3.2.

(a) $\gamma = 1$.

(b) $\gamma = 10$.

(c) $\gamma = 0.1$.
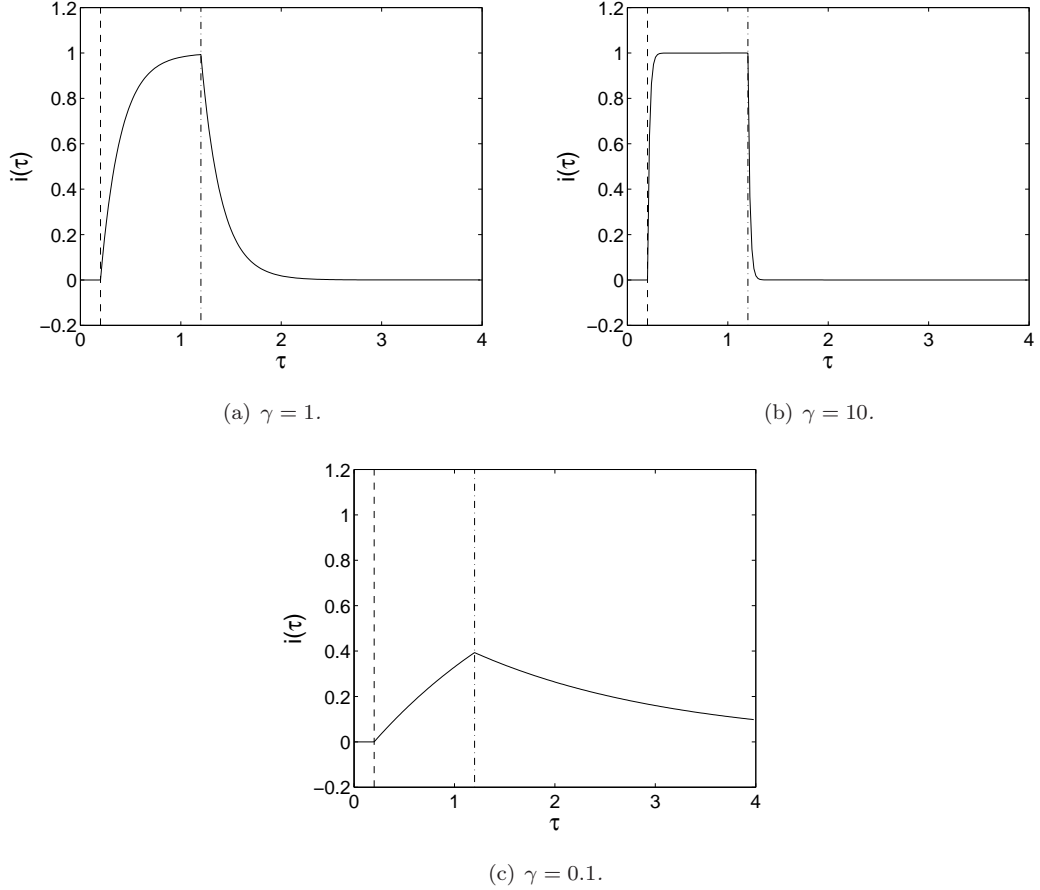
Figure 4.3: *Current response $i(\tau)$ to a single voltage pulse $v_m^a(\tau)$, where $M = 0.9$, $R = 1$ and $\omega_c = 21\omega_s$. The dashed lines indicate when the voltage pulse switches from 0 to +1, and the dot-dash line indicates when the voltage pulse changes from +1 to 0.*

3.1 Single-phase Inverter

The following calculation deriving the upper input current of a single-phase inverter with output impedance $Z(\omega)$ follows the structure of the calculation in section 2 of chapter 3 (where the upper input current of a single-phase inverter with a series resistive-inductive load is derived).

A single-phase inverter is illustrated in figure 1.3(a). By Kirchhoff's current law [103], the upper input current $I(t)$ (the input current drawn from the upper DC source) is equal to the output current $i_{ad}(t)$ (given in (2.4)) when the inverter switch is connected to the upper DC source, and is zero otherwise. In other words,

$$I(t) = i_{ad}(t) \sum_p \psi(t; \mathcal{B}_p^a, \mathcal{A}_{p+1}^a),$$

where, from (2.4),

$$
\begin{aligned}
I(t) &= \left[\frac{1}{Z(0)} - f_\mathcal{A}(t) + f_\mathcal{B}(t) \right] \sum_p \psi(t; \mathcal{B}_p^a, \mathcal{A}_{p+1}^a), \\
&= I_0(t) + I_{\mathcal{A}\mathcal{B}}(t),
\end{aligned}
$$

where

$$I_0(t) \quad = \quad \frac{1}{Z(0)} \sum_p \psi(t; \mathcal{B}_p^a, \mathcal{A}_{p+1}^a), \tag{3.1}$$

$$I_{\mathcal{AB}}(t) \quad = \quad \left[-f_{\mathcal{A}}(t) + f_{\mathcal{B}}(t) \right] \sum_p \psi(t; \mathcal{B}_p^a, \mathcal{A}_{p+1}^a). \tag{3.2}$$

Similarly the lower input current $I^-(t)$ (the input current drawn from the lower DC source) is

$$I^-(t) = i_{ad}(t) - I(t).$$

Therefore we derive the upper input current $I(t)$ only.

We now derive Fourier series for $I_0(t)$ and $I_{\mathcal{AB}}(t)$. Noting that $\sum_p \psi(t; \mathcal{B}_p^a, \mathcal{A}_{p+1}^a) = \frac{1}{2}(1 + v_a(t))$, we have, from (3.1),

$$I_0(t) = \frac{1}{2Z(0)}(1 + v_a(t)),$$

where the spectrum of $v_a(t)$ has been calculated previously (in chapter 2). Examination of (2.5) indicates that $f_{\mathcal{A}}(t)\psi(t; \mathcal{B}_p^a, \mathcal{A}_{p+1}^a)$ is non-zero only when $m \leq p$ (similarly for $f_{\mathcal{B}}(t)\psi(t; \mathcal{B}_p^a, \mathcal{A}_{p+1}^a)$). Therefore, from (3.2),

$$\begin{aligned}
I_{\mathcal{AB}}(t) \quad &= \quad \left[f_{\mathcal{B}}(t) - f_{\mathcal{A}}(t) \right] \sum_p \psi(t; \mathcal{B}_p^a, \mathcal{A}_{p+1}^a), \\
&= \quad \sum_{j=1}^N \frac{2}{Z(\omega_j) + \omega_j Z'(\omega_j)} \sum_p \sum_{m=-\infty}^p \left(e^{i\omega_j(t - \mathcal{B}_m^a)} - e^{i\omega_j(t - \mathcal{A}_m^a)} \right) \psi(t; \mathcal{B}_p^a, \mathcal{A}_{p+1}^a).
\end{aligned}$$

It follows from use of the Jacobi-Anger expansion [109] that

$$\begin{aligned}
I_{\mathcal{AB}}(t) \quad &= \quad -\sum_{j=1}^N \frac{2}{Z(\omega_j) + \omega_j Z'(\omega_j)} \sum_{np} \sum_{m=-\infty}^p e^{i\omega_j(t - mT)} e^{3i\omega_j T/4} J_n(\tfrac{1}{4} i\omega_j MT) \\
&\qquad\qquad \times [(-i)^n e^{i\omega_j T/2} - i^n] e^{in\omega_s mT} \psi(t; \mathcal{B}_p^a, \mathcal{A}_{p+1}^a), \\
&= \quad -\sum_{j=1}^N \frac{2}{Z(\omega_j) + \omega_j Z'(\omega_j)} \sum_n \frac{e^{3i\omega_j T/4}}{1 - e^{-(-i\omega_j + in\omega_s)T}} J_m(\tfrac{1}{4} i\omega_j MT) \\
&\qquad\qquad \times [(-i)^n e^{i\omega_j T/2} - i^m] F_n^j(t),
\end{aligned}$$

where

$$F_n^j(t) = \sum_p e^{i\omega_j t + (-i\omega_j + in\omega_s)pT} \psi(t; \mathcal{B}_p^a, \mathcal{A}_{p+1}^a).$$

The Fourier transform of $F_n^j(t)$ is given by

$$\begin{aligned}
\hat{F}_n^j(\omega) \quad &= \quad \sum_{pq} \frac{1}{i\omega_j - i\omega} e^{-i(\omega - (n+q)\omega_s)pT} e^{-3i\omega_j T/4} J_q(\tfrac{1}{4}(\omega - \omega_j)MT) \\
&\qquad\qquad \times \left[(-i)^q e^{i(\omega_j/2 + q\omega_s - 5\omega/4)T} - i^q e^{-3i\omega T/4} \right].
\end{aligned}$$

Poisson re-summing in p,

$$\begin{aligned}
\hat{F}_n^j(\omega) \quad &= \quad \sum_{pq} \int_{-\infty}^\infty \frac{1}{i(\omega_j - \omega)T} e^{-3i\omega_j T/4} J_q(\tfrac{1}{4}(\omega - \omega_j)MT) \\
&\qquad\qquad \left[(-i)^q e^{i(\omega_j/2 + q\omega_s - 5\omega/4)T} - i^q e^{-3i\omega T/4} \right] e^{i\Omega_{p,n+q} t} e^{-i\omega t} \, dt.
\end{aligned}$$
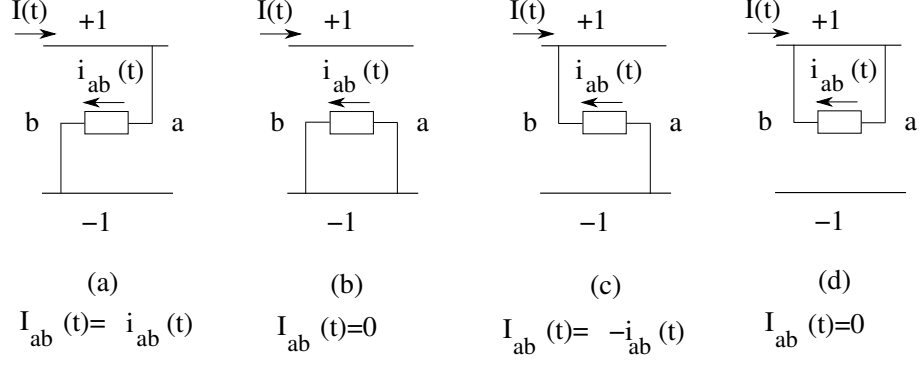
Figure 4.4: *Diagram to show the contribution $I_{ab}(t)$ to the input current $I(t)$ from the load connected between phase-leg a and phase-leg b. The switch state of the two phase-legs determines $I_{ab}(t)$. There are four possible combinations for the phase-legs: (a) phase-leg a attached to the upper DC source and b to the lower ($I_{ab}(t) = i_{ab}(t)$), (b) both attached to the lower DC rail ($I_{ab}(t) = 0$), (c) a attached to the lower and b attached to the upper ($I_{ab}(t) = -i_{ab}(t)$), and (d) both attached to the upper DC rail ($I_{ab}(t) = 0$).*

Therefore, we identify

$$I(t) = \frac{1}{2Z(0)} + \sum_{mn} \mathcal{I}_{mn} e^{i\Omega_{mn}t}, \tag{3.3}$$

where

$$\mathcal{I}_{mn} = \frac{a_{mn}}{2Z(0)} - \sum_{j=1}^{N} \frac{2}{(Z(\omega_j) + \omega_j Z'(\omega_j))T} \sum_q \frac{J_{n-q}(\frac{1}{4}i\omega_j MT)[(-i)^{n-q}e^{i\omega_j T/2} - i^{n-q}]}{(i\omega_j - i\Omega_{mn})(1 - e^{i(\omega_j - (n-q)\omega_s)T})}$$

$$\times J_q(\tfrac{1}{4}(\Omega_{mn} - \omega_j)MT)\left[(-i)^q e^{i(\omega_j/2 + q\omega_s - 5\Omega_{mn}/4)T} - i^q e^{-3i\Omega_{mn}T/4}\right], \tag{3.4}$$

where

$$a_{mn} = \frac{2}{i\Omega_{mn}T} J_n\left(\tfrac{1}{4}\Omega_{mn}MT\right)\left(e^{in\pi/2 - 3i\Omega_{mn}T/4} - e^{-in\pi/2 - i\Omega_{mn}T/4}\right),$$

are the Fourier coefficients of the voltage output $v_a(t)$ of a single-phase inverter (from chapter 2).

The Fourier series for the upper input current of a single-phase inverter given in (3.3) (with coefficients in (3.4)) is given in terms of the general output impedance $Z(\omega)$. We can determine input current spectra from (3.3) and (3.4) for specific output impedances without resorting to lengthy calculations.

3.2   Two-phase and Three-phase Inverter

In a multi-phase inverter the upper input current is equal to minus the lower input current. Therefore for any multi-phase inverter we derive one of the upper or lower input currents only. In this section we derive the upper input current $I(t)$ of a two-phase and a three-phase inverter.

Before we examine either a two-phase or three-phase inverter, we examine the contribution $I_{ab}(t)$ to the upper input current $I(t)$ from a load connected between two phase-legs, a and b.

By Kirchhoff's current law [103], $I_{ab}(t)$ is equal to plus or minus the output current $i_{ab}(t)$ or zero depending on the switch state of the two phase-legs, as illustrated in figure 4.4. In other words, $I_{ab}(t) = 0$ when phase-leg a and phase-leg b are simultaneously connected to either the upper or the lower DC source. Similarly, $I_{ab}(t) = i_{ab}(t)$ if phase-leg a is connected to the upper DC source and b to the lower, and $I_{ab}(t) = -i_{ab}(t)$ if a is connected to the lower and b to the upper. Therefore the contribution to the input current from the load connected between phase-leg a and phase-leg b is

$$I_{ab}(t) = i_{ab}(t) \sum_p \left[\psi(t; \mathcal{B}_p^a, \mathcal{A}_{p+1}^a) - \psi(t; \mathcal{B}_p^b, \mathcal{A}_{p+1}^b) \right],$$

where, from (2.4),

$$i_{ab}(t) = -g_{\mathcal{A}}(t) + g_{\mathcal{B}}(t),$$

and, from (2.5),

$$g_{\mathcal{A}}(t) = \sum_{j=1}^{N} \frac{2}{Z(\omega_j) + \omega_j Z'(\omega_j)} \sum_m \left[e^{i\omega_j(t - \mathcal{A}_m^a)} \psi(t; \mathcal{A}_m^a, \infty) - e^{i\omega_j(t - \mathcal{A}_m^b)} \psi(t; \mathcal{A}_m^b, \infty) \right],$$

and $g_{\mathcal{B}}(t)$ is defined similarly. Note that $\mathcal{A}_m^a$, $\mathcal{B}_m^a$ are defined in (2.1), and $\mathcal{A}_m^b$, $\mathcal{B}_m^b$ are defined similarly, with signal wave $s_b(t) = M\cos(\omega_s t + \phi)$, with phase $\phi \neq 0$.

We now write $I_{ab}(t)$ as

$$
\begin{aligned}
I_{ab}(t) &= \sum_{j=1}^{N} \frac{2}{Z(\omega_j) + \omega_j Z'(\omega_j)} \sum_{mp} \left[e^{i\omega_j(t - \mathcal{A}_m^a)} \psi(t; \mathcal{A}_m^a, \infty) - e^{i\omega_j(t - \mathcal{A}_m^b)} \psi(t; \mathcal{A}_m^b, \infty) \right] \\
&\qquad \left[\psi(t; \mathcal{B}_p^a, \mathcal{A}_{p+1}^a) - \psi(t; \mathcal{B}_p^b, \mathcal{A}_{p+1}^b) \right], \\
&\quad \sum_{j=1}^{N} \frac{2}{Z(\omega_j) + \omega_j Z'(\omega_j)} \left(I_1^j(t) + I_2^j(t) \right),
\end{aligned}
$$

where $I_1^j(t)$ and $I_2^j(t)$ are found from consideration of the sum over m. If $m \leq p$, it is easily verified that

$$
\begin{aligned}
I_1^j(t) &= -\sum_p \left(\psi(t; \mathcal{B}_p^a, \mathcal{A}_{p+1}^a) - \psi(t; \mathcal{B}_p^b, \mathcal{A}_{p+1}^b) \right) \\
&\qquad \times \sum_{m=-\infty}^{p} \left(e^{i\omega_j(t - \mathcal{A}_m^a)} - e^{i\omega_j(t - \mathcal{A}_m^b)} + e^{i\omega_j(t - \mathcal{B}_m^b)} - e^{i\omega_j(t - \mathcal{B}_m^a)} \right).
\end{aligned}
$$

When $m > p$,

$$\psi(t; \mathcal{A}_m^a, \infty)[\psi(t; \mathcal{B}_p^a, \mathcal{A}_{p+1}^a) - \psi(t; \mathcal{B}_p^b, \mathcal{A}_{p+1}^b)] = \begin{cases} \psi(t; \mathcal{A}_m^a, \mathcal{A}_m^b), & \text{when } p = m-1, \\ 0, & \text{otherwise,} \end{cases}$$

for example. Therefore, $I_2^j(t)$, is non-zero when $p = m - 1$ only, in other words

$$
\begin{aligned}
I_2^j(t) &= \sum_m \left[e^{i\omega_j(t - \mathcal{A}_m^a)} \psi(t; \mathcal{A}_m^a, \mathcal{A}_m^b) + e^{i\omega_j(t - \mathcal{A}_m^b)} \psi(t; \mathcal{A}_m^b, \mathcal{A}_m^a) \right. \\
&\quad \left. + e^{i\omega_j(t - \mathcal{B}_m^a)} \psi(t; \mathcal{B}_m^b, \mathcal{B}_m^a) + e^{i\omega_j(t - \mathcal{B}_m^b)} \psi(t; \mathcal{B}_m^a, \mathcal{B}_m^b) \right], \\
&= \sum_m \left[e^{i\omega_j(t - \min(\mathcal{A}_m^a, \mathcal{A}_m^b))} \psi(t; \min(\mathcal{A}_m^a, \mathcal{A}_m^b), \max(\mathcal{A}_m^a, \mathcal{A}_m^b)) \right. \\
&\quad \left. + e^{i\omega_j(t - \max(\mathcal{B}_m^a, \mathcal{B}_m^b))} \psi(t; \min(\mathcal{B}_m^a, \mathcal{B}_m^b), \max(\mathcal{B}_m^a, \mathcal{B}_m^b)) \right].
\end{aligned}
$$

We now determine Fourier series for each of $I_1^j(t)$ and $I_2^j(t)$ in turn.

We examine $I_1^j(t)$ with use of the Jaocbi-Anger expansion [109]. From examination of this expansion, it is easily verified that

$$
\begin{aligned}
I_1^j(t) &= -\sum_{np} e^{i\omega_j t} J_n\left(\tfrac{1}{4}\omega_j MT\right) \left[(-i)^n e^{i\omega_j T/2} - i^n \right] \left[1 - e^{in\phi} \right] \\
&\quad \times \left[\psi(t; \mathcal{B}_p^a, \mathcal{A}_{p+1}^a) - \psi(t; \mathcal{B}_p^b, \mathcal{A}_{p+1}^b) \right] \sum_{m=-\infty}^p e^{i(n\omega_s - \omega_j)mT}. \\
&= -\sum_n \frac{e^{3i\omega_j T/4}}{1 - e^{-i(n\omega_s - \omega_j)T}} J_n\left(\tfrac{1}{4}\omega_j MT\right) \left[(-i)^n e^{i\omega_j T/2} - i^n \right] \left[1 - e^{in\phi} \right] F_n^j(t), \quad (3.5)
\end{aligned}
$$

where

$$
F_n^j(t) = \sum_p e^{i\omega_j t + i(n\omega_s - \omega_j)pT} \left[\psi(t; \mathcal{B}_p^a, \mathcal{A}_{p+1}^a) - \psi(t; \mathcal{B}_p^b, \mathcal{A}_{p+1}^b) \right].
$$

The Fourier transform of $F_n^j(t)$ is given by

$$
\begin{aligned}
\hat{F}_n^j(\omega) &= \sum_{pq} \frac{1}{i(\omega_j - \omega)} e^{-i(\omega - (n+q)\omega_s)pT - 3i\omega_j T/4} J_q\left(\tfrac{1}{4}(\omega - \omega_j)MT\right) \left[1 - e^{iq\phi} \right] \\
&\quad \times \left[(-i)^q e^{i(\omega_j/2 + q\omega_s - 5\omega/4)T} - i^q e^{-3i\omega T/4} \right].
\end{aligned}
$$

We now use the Poisson re-summation formula to give

$$
\begin{aligned}
\hat{F}_n^j(\omega) &= \sum_{pq} \int_{-\infty}^{\infty} \frac{e^{-3i\omega_j T/4}}{i(\omega_j - \omega)T} J_q\left(\tfrac{1}{4}(\omega - \omega_j)MT\right) \left[1 - e^{iq\phi} \right] \\
&\quad \times \left[(-i)^q e^{i(\omega_j/2 + q\omega_s - 5\omega/4)T} - i^q e^{-3i\omega T/4} \right] e^{i\Omega_{p,n+q}t} e^{-i\omega t} \, dt.
\end{aligned}
$$

Thus, we identify a Fourier series for $I_1^j(t)$, given by

$$
\sum_{j=1}^N \frac{2}{Z(\omega_j) + \omega_j Z'(\omega_j)} I_1^j(t) = \sum_{mn} \mathcal{I}_{mn} e^{i\Omega_{mn}t},
$$

where

$$
\begin{aligned}
\mathcal{I}_{mn} &= \sum_{j=1}^N \frac{2}{(Z(\omega_j) + \omega_j Z'(\omega_j))T} \sum_q \frac{(1 - e^{i(n-q)\phi})(1 - e^{iq\phi})((-i)^{n-q} e^{i\omega_j T/2} - i^{n-q})}{(i\Omega_{mn} - i\omega_j)(1 - e^{i(\omega_j - (n-q)\omega_s)T})} \\
&\quad \times J_{n-q}\left(\tfrac{1}{4}\omega_j MT\right) J_q\left(\tfrac{1}{4}(\Omega_{mn} - \omega_j)MT\right) \\
&\quad \times ((-i)^q e^{i(\omega_j/2 + q\omega_s - 5\Omega_{mn}/4)T} - i^q e^{-3i\Omega_{mn}T/4}). \quad (3.6)
\end{aligned}
$$

We now determine a Fourier series for $I_2^j(t)$.

Taking a Fourier transform of $I_2^j(t)$ determines

$$
\hat{I}_2^j(\omega) = \sum_m \frac{1}{i\omega_j - i\omega} e^{-i\omega mT}\left[e^{-i\omega T/4} e^{-i\omega_j MT\delta_{\min}(mT)/4}\left(e^{(i\omega_j - i\omega)MT\delta_{\max}(mT)/4} \right.\right.
$$
$$
\left. -e^{(i\omega_j - i\omega)MT\delta_{\min}(mT)/4} \right) + e^{-3i\omega T/4} e^{i\omega_j MT\delta_{\min}(mT)/4}
$$
$$
\left. \times \left(e^{-(i\omega_j - i\omega)MT\delta_{\min}(mT)/4} - e^{-(i\omega_j - i\omega)MT\delta_{\max}(mT)/4} \right) \right],
$$

where

$$
\delta_{\min}(t) = \min\left\{ \cos\omega_s t, \cos(\omega_s t + \phi) \right\} = \begin{cases} \cos(\omega_s t + \phi), & \text{when } -\pi - \frac{\phi}{2} < \omega_s t < -\frac{\phi}{2} \\ \cos\omega_s t, & \text{when } -\frac{\phi}{2} < \omega_s t < \pi - \frac{\phi}{2}, \end{cases}
$$
$$
\delta_{\max}(t) = \max\left\{ \cos\omega_s t, \cos(\omega_s t + \phi) \right\} = \begin{cases} \cos\omega_s t, & \text{when } -\pi - \frac{\phi}{2} < \omega_s t < -\frac{\phi}{2} \\ \cos(\omega_s t + \phi), & \text{when } -\frac{\phi}{2} < \omega_s t < \pi - \frac{\phi}{2}. \end{cases}
$$

Therefore we have

$$
\hat{I}_2^j(\omega) = \sum_m \frac{1}{i\omega_j - i\omega} e^{-i\omega mT}\left[e^{-i\omega T/4}\left(e^{-i\omega_j MT(\delta_{\min}(mT) - \delta_{\max}(mT))/4} e^{-i\omega MT\delta_{\max}(mT)/4} \right.\right.
$$
$$
\left. -e^{-i\omega MT\delta_{min}(mT)/4} \right) + e^{-3i\omega T/4}\left(e^{i\omega\delta_{\min}(mT)/4} \right.
$$
$$
\left.\left. -e^{i\omega_j MT(\delta_{\min}(mT) - \delta_{\max}(mT))/4} e^{i\omega MT\delta_{\max}(mT)/4} \right) \right],
$$
$$
= \sum_{mn} \frac{e^{in\omega_s mT}}{i\omega_j - i\omega} e^{-i\omega mT}\left[e^{-3i\omega T/4} C_n^+\left(\tfrac{1}{4}\omega MT\right) - e^{-i\omega T/4} C_n^+\left(-\tfrac{1}{4}\omega MT\right) \right.
$$
$$
+ \sum_p e^{ip\omega_s mT}\left(e^{-i\omega T/4} C_n^-\left(-\tfrac{1}{4}\omega MT\right) D_p\left(-\tfrac{1}{2} i\omega_j \sin\tfrac{\phi}{2} MT\right) \right.
$$
$$
\left.\left. -e^{-3i\omega T/4} C_n^-\left(\tfrac{1}{4}\omega MT\right) D_p\left(\tfrac{1}{2} i\omega_j \sin\tfrac{\phi}{2} MT\right) \right) \right],
$$

where the functions $C_n^{\pm}(z)$ and $D_p(z)$ are the coefficients in the following Fourier series:

$$
e^{iz\delta_{\min}(t)} = \sum_n C_n^+(z) e^{in\omega_s t}, \qquad\qquad e^{iz\delta_{\max}(t)} = \sum_n C_n^-(z) e^{in\omega_s t},
$$
$$
e^{z(\delta_{\min}(t) - \delta_{\max}(t))} = \sum_p D_p\left(2i\sin\tfrac{\phi}{2} z\right) e^{ip\omega_s t}.
$$

It is easily verified that

$$
C_n^{\pm}(z) = \frac{i^n}{2} J_n(z)(1 + e^{in\phi}) \pm \sum_{q \neq n} \frac{J_q(z)}{2\pi i(n - q)} e^{iq\pi/2}(1 - e^{iq\phi})(1 - (-1)^{n-q}) e^{i(n-q)\phi/2} \tag{3.7}
$$

$$
D_p(z) = \begin{cases} 0, & p \text{ odd}, \\ e^{-i\pi p/3} J_p(i\sqrt{3}z) - \displaystyle\sum_{q = \pm 1, \pm 3, \pm 5, \ldots} \frac{2}{\pi i(p - q)} e^{-i\pi p/3} J_q(i\sqrt{3}z), & p \text{ even}. \end{cases} \tag{3.8}
$$

Poisson re-summing $\hat{I}_2^j(\omega)$ in m allows us to identify

$$
\begin{aligned}
I_2^j(t) &= \sum_{mn} \frac{e^{i\Omega_{mn}t}}{i\omega_j - i\omega}\Bigg[e^{-3i\Omega_{mn}T/4}C_n^+\left(\tfrac{1}{4}\Omega_{mn}MT\right) - e^{-i\Omega_{mn}T/4}C_n^+\left(-\tfrac{1}{4}\Omega_{mn}MT\right) \\
&\quad + \sum_p \left(e^{-i\Omega_{mn}T/4}C_{n-p}^-\left(-\tfrac{1}{4}\Omega_{mn}MT\right) D_p\left(-\tfrac{1}{2}i\omega_j\sin\tfrac{\phi}{2}MT\right) \right. \\
&\quad \left. - e^{-3i\Omega_{mn}T/4}C_{n-p}^-\left(\tfrac{1}{4}\Omega_{mn}MT\right) D_p\left(\tfrac{1}{2}i\omega_j\sin\tfrac{\phi}{2}MT\right) \right)\Bigg].
\end{aligned}
$$

Therefore,

$$
\sum_{j=1}^N \frac{2}{Z(\omega_j)+\omega_j Z'(\omega_j)} I_2^j(t) = \sum_{mn} \mathcal{J}_{mn} e^{i\Omega_{mn}t},
$$

where

$$
\begin{aligned}
\mathcal{J}_{mn} &= -\sum_{j=1}^N \frac{2}{(Z(\omega_j)+\omega_j Z'(\omega_j))(i\Omega_{mn}-i\omega_j)T}\Bigg[e^{-3i\Omega_{mn}T/4}C_n^+\left(\tfrac{1}{4}\Omega_{mn}MT\right) \\
&\quad - e^{-i\Omega_{mn}T/4}C_n^+\left(-\tfrac{1}{4}\Omega_{mn}MT\right) + \sum_p \left(e^{-i\Omega_{mn}T/4}C_{n-p}^-\left(-\tfrac{1}{4}\Omega_{mn}MT\right) \right. \hspace{2em} (3.9) \\
&\quad \left. \times D_p\left(-\tfrac{1}{2}i\omega_j\sin\tfrac{\phi}{2}MT\right) - e^{-3i\Omega_{mn}T/4}C_{n-p}^-\left(\tfrac{1}{4}\Omega_{mn}MT\right) D_p\left(\tfrac{1}{2}i\omega_j\sin\tfrac{\phi}{2}MT\right) \right)\Bigg].
\end{aligned}
$$

Thus the contribution to the input current from the load connected between phase-leg a and phase-leg d is

$$
I_{ad}(t) = \sum_{mn} (\mathcal{I}_{mn} + \mathcal{J}_{mn}) e^{i\Omega_{mn}t},
$$

where $\mathcal{I}_{mn}$ and $\mathcal{J}_{mn}$ are defined in (3.6) and (3.9), respectively. We now use the Fourier coefficients and Fourier series for $I_{ad}(t)$ to determine a Fourier series for the input currents of two-phase and three-phase inverters.

3.2.1 Two-phase inverter

We now determine the upper input current of a two-phase inverter with general output impedance, using the calculations of the previous section (section 3.2). As illustrated in figure 1.3(b), there is one load in a two-phase inverter, and it is connected between phase-leg a and phase-leg b. The output current across the load in a two-phase inverter is, from (2.4),

$$
i_{ab}(t) = -g_\mathcal{A}(t) + g_\mathcal{B}(t),
$$

where, from (2.5),

$$
g_\mathcal{A}(t) = \sum_{j=1}^N \frac{2}{Z(\omega_j)+\omega_j Z'(\omega_j)} \sum_m \left[e^{i\omega_j(t-\mathcal{A}_m^a)}\psi(t;\mathcal{A}_m^a,\infty) - e^{i\omega_j(t-\mathcal{A}_m^b)}\psi(t;\mathcal{A}_m^b,\infty) \right],
$$

and $g_\mathcal{B}(t)$ is defined similarly. Note that $\mathcal{A}_m^a$, $\mathcal{B}_m^a$ are defined in (2.1), and $\mathcal{A}_m^b$, $\mathcal{B}_m^b$ are defined similarly, with signal wave $s_b(t) = M\cos(\omega_s t - \pi)$. Therefore $I(t)$ is

$$
\begin{aligned}
I(t) &= i_{ab}(t) \sum_p \left[\psi(t;\mathcal{B}_p^a,\mathcal{A}_{p+1}^a) - \psi(t;\mathcal{B}_p^b,\mathcal{A}_{p+1}^b) \right], \\
&= \sum_{mn} \mathcal{P}_{mn} e^{i\Omega_{mn}t}, \hspace{8em} (3.10)
\end{aligned}
$$

where

$$\mathcal{P}_{mn} = \begin{cases} \mathcal{I}_{mn} + \mathcal{J}_{mn}, & n \text{ even,} \\ 0, & n \text{ odd.} \end{cases}$$

From (3.6),

$$\mathcal{I}_{mn} = \sum_{j=1}^{N} \frac{8}{(Z(\omega_j) + \omega_j Z'(\omega_j))T} \sum_{q=\pm1,\pm3,\pm5,\dots} \frac{((-i)^{n-q}e^{i\omega_j T/2} - i^{n-q})}{(i\Omega_{mn} - i\omega_j)(1 - e^{i(\omega_j-(n-q)\omega_s)T})}$$
$$\times J_{n-q}\left(\tfrac{1}{4}\omega_j MT\right) J_q\left(\tfrac{1}{4}(\Omega_{mn} - \omega_j)MT\right)$$
$$\times((-i)^{q+m}e^{i(\omega_j/2+q\omega_s-5n\omega_s/4)T} - i^{q+m}e^{-3in\omega_s T/4}), \quad (3.11)$$

and, from (3.9),

$$\mathcal{J}_{mn} = -\sum_{j=1}^{N} \frac{2}{(Z(\omega_j) + \omega_j Z'(\omega_j))(i\Omega_{mn} - i\omega_j)T}\left[e^{-3i\Omega_{mn}T/4}C_n^+\left(\tfrac{1}{4}\Omega_{mn}MT\right) \right.$$
$$-e^{-i\Omega_{mn}T/4}C_n^+\left(-\tfrac{1}{4}\Omega_{mn}MT\right) + \sum_p \left(e^{-i\Omega_{mn}T/4}C_{n-p}^-\left(-\tfrac{1}{4}\Omega_{mn}MT\right) \right.$$
$$\left. \left. \times D_p\left(\tfrac{1}{2}i\omega_j MT\right) - e^{-3i\Omega_{mn}T/4}C_{n-p}^-\left(\tfrac{1}{4}\Omega_{mn}MT\right) D_p\left(-\tfrac{1}{2}i\omega_j MT\right) \right)\right],(3.12)$$

where, from (3.7),

$$C_n^{\pm}(z) = i^n J_n(z) \pm \sum_{q=\pm1,\pm3,\pm5,\dots} \frac{2}{\pi i(n-q)}i^n J_q(z), \quad (3.13)$$

and $D_p(z)$ is given in (3.8). Note that for a two-phase inverter, only multiples of the second harmonic contribute to $I(t)$. By symmetry, if both voltage outputs are shifted by half of the phase of signal wave (π/ω_s) the input current will be the same, which is why only multiples of the second harmonic contribute to $I(t)$.

3.2.2 Three-phase inverter

We now calculate the input currents of a three-phase inverter with general output impedance using the calculations of section 3.2. Specifically we examine the input currents of a three-phase inverter wired in the Δ configuration, where a load is connected between each pair of phase-legs. A three-phase inverter wired in the Δ configuration is illustrated in figure 2.9.

In order to determine the input current $I(t)$ of a three-phase inverter wired in the Δ configuration, we examine the contribution to the input current from each phase-leg. We begin by examining the contribution of phase-leg a. Figure 3.7 shows the currents flowing out of phase-leg a ($i_{ab}(t)$ and $i_{ac}(t)$) and the input current $I_a(t)$ flowing into phase-leg a. By Kirchhoff's current law [103], if phase-leg a is connected to the upper DC source then $I_a(t) = i_{ab}(t) + i_{ac}(t)$, and if phase-leg a is connected to the lower DC source then $I_a(t) = 0$. In other words,

$$I_a(t) = \sum_p \left(i_{ab}(t) - i_{ca}(t) \right)\psi(t; \mathcal{B}_p^a, \mathcal{A}_{p+1}^a),$$

where $\mathcal{B}_p^a$, $\mathcal{A}_{p+1}^a$ are defined in (2.1). Note that the input current $I_b(t)$ or $I_c(t)$ flowing into

phase-leg b or c, respectively, is defined similarly to $I_a(t)$. Therefore,

$$
\begin{aligned}
I(t) &= I_a(t) + I_b(t) + I_c(t), \\
&= \sum_p \left[\left(i_{ab}(t) - i_{ca}(t) \right) \psi(t; \mathcal{B}_p^a, \mathcal{A}_{p+1}^a) + \left(i_{bc}(t) - i_{ab}(t) \right) \psi(t; \mathcal{B}_p^b, \mathcal{A}_{p+1}^b) \right.
\end{aligned}
$$

$$
\left. + \left(i_{ca}(t) - i_{bc}(t) \right) \psi(t; \mathcal{B}_p^c, \mathcal{A}_{p+1}^c) \right],
$$

where $\mathcal{B}_p^b, \mathcal{A}_{p+1}^b$ and $\mathcal{B}_p^c, \mathcal{A}_{p+1}^c$ are defined similarly to (2.1), with respective signal waves $s_b(t) = M\cos(\omega_s t - \frac{2\pi}{3})$ and $s_c(t) = M\cos(\omega_s t + \frac{2\pi}{3})$. By grouping together the output currents, we have an alternative expression for $I(t)$,

$$
I(t) = I_{ab}(t) + I_{bc}(t) + I_{ca}(t),
$$

where

$$
I_{ab}(t) = i_{ab}(t) \sum_p \left[\psi(t; \mathcal{B}_p^a, \mathcal{A}_{p+1}^a) - \psi(t; \mathcal{B}_p^b, \mathcal{A}_{p+1}^b) \right],
$$

and $I_{bc}(t)$, $I_{ca}(t)$ are defined similarly. The output current $i_{ab}(t)$ is, from (2.4),

$$
i_{ab}(t) = i_{az}(t) - i_{bz}(t) = -g_{\mathcal{A}}(t) + g_{\mathcal{B}}(t),
$$

where, from (2.5),

$$
g_{\mathcal{A}}(t) = \sum_{j=1}^{N} \frac{2}{Z(\omega_j) + \omega_j Z'(\omega_j)} \sum_m \left[e^{i\omega_j(t - \mathcal{A}_m^a)} \psi(t; \mathcal{A}_m^a, \infty) - e^{i\omega_j(t - \mathcal{A}_m^b)} \psi(t; \mathcal{A}_m^b, \infty) \right],
$$

and $g_{\mathcal{B}}(t)$ is defined similarly. Therefore, because of the symmetry of the signal waves $s_a(t)$, $s_b(t)$ and $s_c(t)$, and with reference to section 4.2.3 of chapter 3,

$$
\begin{aligned}
I(t) &= I_{ab}(t) + I_{bc}(t) + I_{ca}(t), \\
&= \sum_{mn} \left[1 + e^{-2\pi in/3} + e^{2\pi in/3} \right] (\mathcal{I}_{mn} + \mathcal{J}_{mn}) e^{i\Omega_{mn}t}, \\
&= \sum_{mn} \mathcal{P}_{mn} e^{i\Omega_{mn}t}, \tag{3.14}
\end{aligned}
$$

where

$$
\mathcal{P}_{mn} = \begin{cases} 3(\mathcal{I}_{mn} + \mathcal{J}_{mn}), & \text{if} \quad \mod(n,3) = 0, \\ 0, & \text{otherwise.} \end{cases}
$$

The Fourier coefficients $\mathcal{I}_{mn}$ and $\mathcal{J}_{mn}$ are, from (3.6) and (3.9), respectively,

$$
\begin{aligned}
\mathcal{I}_{mn} &= \sum_{j=1}^{N} \frac{2}{(Z(\omega_j) + \omega_j Z'(\omega_j))T} \sum_q \frac{(1 - e^{-2\pi i(n-q)/3})(1 - e^{2\pi iq/3})}{(i\Omega_{mn} - i\omega_j)(1 - e^{i(\omega_j - (n-q)\omega_s)T})} \\
&\quad \times J_{n-q}\left(\tfrac{1}{4}\omega_j MT\right) J_q\left(\tfrac{1}{4}(\Omega_{mn} - \omega_j)MT\right) \left[(-i)^{q+m} e^{i(\omega_j/2 + q\omega_s - 5n\omega_s/4)T} \right. \\
&\quad \left. - i^{q+m} e^{-3in\omega_s T/4} \right] ((-i)^{n-q} e^{i\omega_j T/2} - i^{n-q}), \tag{3.15}
\end{aligned}
$$

$$
\begin{aligned}
\mathcal{J}_{mn} \quad = \quad & -\sum_{j=1}^{N} \frac{2}{(Z(\omega_j) + \omega_j Z'(\omega_j))(i\Omega_{mn} - i\omega_j)T} \Bigg[e^{-3i\Omega_{mn}T/4} C_n^+ \left(\tfrac{1}{4}\Omega_{mn}MT \right) \\
& -e^{-i\Omega_{mn}T/4} C_n^+ \left(-\tfrac{1}{4}\Omega_{mn}MT \right) + \sum_p \left(e^{-i\Omega_{mn}T/4} C_{n-p}^- \left(-\tfrac{1}{4}\Omega_{mn}MT \right) \right. \\
& \left. \times D_p \left(\tfrac{\sqrt{3}}{4} i\omega_j MT \right) - e^{-3i\Omega_{mn}T/4} C_{n-p}^- \left(\tfrac{1}{4}\Omega_{mn}MT \right) D_p \left(-\tfrac{\sqrt{3}}{4} i\omega_j MT \right) \right) \Bigg].
\end{aligned}
\tag{3.16}
$$

where, from (3.7),

$$
C_n^{\pm}(z) = \frac{i^n}{2} J_n(z)(1 + e^{-2\pi in/3}) \pm \sum_{q \neq n} \frac{J_q(z)}{2\pi i(n-q)} e^{iq\pi/2}(1 - e^{2\pi iq/3})(1 - (-1)^{n-q}) e^{i(n-q)\pi/3}, \tag{3.17}
$$

and $D_p(z)$ is given in (3.8). Note that for $I(t)$, only multiples of the third harmonic (multiples of three of the signal frequency) contribute to the input currents of a three-phase inverter (as observed in [40], for example). This harmonic cancellation is due to the $1 + e^{-2\pi in/3} + e^{2\pi in/3}$ term, which is a consequence of the fact that the input currents are the same if all three voltage outputs are shifted by a third of the phase of the signal wave $(2\pi/3\omega_s)$.

Because we plot the absolute value of the Fourier coefficients, the frequency spectrum of $I(t)$ (the input current drawn from the upper DC source) is identical to the spectrum of $-I(t)$ (the input current drawn from the lower DC source). In addition to this, frequency spectra for the input currents of three-phase inverters wired in the Δ and Y configurations are identical, with the appropriate scaling, provided all load impedances are equal. This is because, from appendix C, the Fourier coefficients for $I(t)$ are three times the magnitude of the Fourier coefficients of $I_Y(t)$ (the input current drawn from the upper DC source of a three-phase inverter wired in the Y configuration).

4 Conclusions

In this chapter we have calculated, using the single-sum method, Fourier series expressions for the input currents for single-phase, two-phase and three-phase PWM inverters with general output impedance. There are a wide range of input current calculations for specific loads in [31, 40, 94], for example, whereas input currents have only been calculated for general output impedance (in [33]) for a matrix converter. The calculations in this chapter are the first to determine the input currents of PWM inverters with general output impedance. The calculations here determine expressions for the input currents that can be specialised for any given load, thus generalising previous calculations (in [31, 40, 94], for example) for specific loads.

The calculations in this chapter will be of interest to engineers who want to design efficient input filters for inverters for a range of passive loads. Examples of passive loads not examined in this thesis (because they are overly simplistic, or not as common) are resistive only loads (see [33], for example), or series RLC loads (see [105, 107], for example). In practice, however, more work is necessary to extract input current spectra for specific impedances (to inform filter design) from expressions for the input currents calculated in this chapter. Specialising the expressions for the input currents in this chapter to determine spectra for a specific impedance is significantly less

time consuming than calculating input current spectra for each specific impedance individually, however. Furthermore, all calculations in this chapter have been for the single-sum method, which determines Fourier series for the input currents that converge much faster than Fourier series for the input currents derived using the direct method.

This concludes our analysis of inverters without dead time. We next examine a more comprehensive mathematical model for inverters that incorporate dead time. Analytical calculation of voltage and current spectra for inverters with dead time is limited, because the mathematical models required to determine voltage and current spectra are more complex.

Voltage Spectra for PWM Inverters With Dead Time

1 Introduction

In this chapter we determine frequency spectra for the output voltages of more realistic inverter models; inverters that incorporate *dead time*. In practice, the operation of the switches in inverters with dead time is delayed in order to prevent a short circuit. The effects of dead time on the voltage output were first examined in [45], and the dead time delays, although slight, generate distortion in the frequency spectrum of the voltage output, as documented in [25, 27, 29, 34, 64, 78, 93, 111], for example.

Various methods of compensating for the dead time effects on the voltage output are discussed in [25, 29, 64, 93], for example. It is observed in [29] that it is not necessary to insert dead time for every switching moment. In order to avoid unnecessary dead time, control algorithms are examined that decide when to insert dead time in [25, 29, 93]. The control algorithms minimise the dead time effects. In [64] a circuit with an output current feedback loop is discussed, and shown to reduce the dead time effects. Output filters also reduce the dead time effects.

Knowledge of the frequency spectra of the voltage outputs allow us to identify the harmonic components caused by dead time that require filtering. The mathematical models required to determine spectra for inverters with dead time are more sophisticated than those we have determined in previous chapters of this thesis. Most previous calculations of the output voltages of inverters with dead time determine spectra for naturally sampled inverters only.

In [111], spectra are determined using Black's method for a naturally sampled two-phase inverter with dead time. In order to allow for calculation of spectra, an approximation is made to one of the integration bounds of the double integral necessitated by Black's method. This approximation accounts for the difference in the analytical and simulated results they provide. In [27], a Fourier series for the voltage output of a single-phase inverter is calculated, but
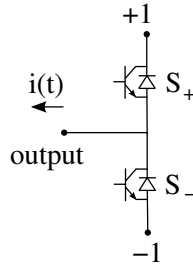
Figure 5.1: *A circuit diagram of a single phase-leg of an inverter. The semiconductor switches are indicated by S_+ and S_-, and the output current, $i(t)$, is also shown (here $i(t) > 0$, and flows out of the phase-leg into the output terminal).*

contains terms that involve the switching times (and therefore give no immediate insight to the frequency spectrum). Spectra are provided for natural sampling, however, and this is achieved by approximating the switching times by a Taylor series (similar to the method used in [99]). Voltage outputs calculated with approximations are accurate only in certain, limiting cases.

In this chapter, we calculate, for the first time, frequency spectra for the voltage outputs of two-phase and three-phase inverters with dead time. These calculations extend calculations in [34], where the voltage output of a single-phase inverter with dead time is determined using the single-sum method. We review the calculations of [34] here, as they form the basis of our calculations of the voltage outputs of two-phase and three-phase inverters.

1.1 Dead Time

In order to explain dead time in more detail, it is useful to examine a single phase-leg of a PWM inverter (illustrated in figure 5.1). More specifically, we examine the operation of each switch in the phase-leg. The switches in the phase-leg comprise a transistor and a diode connected in parallel. Ideally, the transistors of S_+ or S_- operate in a complementary fashion. In practice, the transistors of S_+ and S_- do not switch simultaneously. This is because transistors do not switch instantaneously, but have a transition stage [61]. When the transistors switch simultaneously, there is a potential for short-circuiting of the input power supply during the switching between ± 1. To avoid a short circuit, switch times of the transistors of S_+ and S_- are altered so that both transistors are briefly open at the same time during switching transitions. The period of time during which both transistors are open is known as dead time.

There are two methods used to alter the switch times of the transistors to insert dead time (see [111], for example). To distinguish between the two methods, we introduce some new terminology: *delay-only* switching, and *delay-advance* switching. In comparison to inverters without dead time, for delay-only switching, the times when transistors close are delayed, and the opening times of the transistors are the same. For delay-advance switching, the closing times of the transistors are delayed, and the opening times of the transistors are advanced (compared to inverters without dead time).
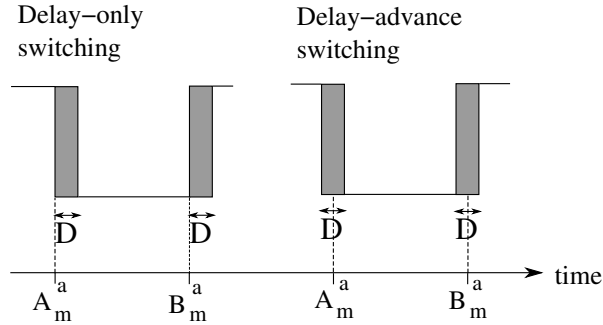
Figure 5.2: *Illustration of when, across a single switching period, dead time of length D (illustrated by the shaded grey areas) will affect the voltage output of a phase-leg when altering the switch times of the transistors according to delay-only switching and delay-advance switching. We also indicate, for reference, the switch times $\mathcal{A}_m^a$ and $\mathcal{B}_m^a$ of the voltage output of an inverter that does not incorporate dead time.*

We now discuss the voltage output during dead time. We illustrate, in figure 5.2, when insertion of dead time into the switching transitions of a phase-leg affects the voltage output of the phase-leg. We want to ensure that the voltage output during dead time is well defined (either ± 1), as an undefined output voltage is an example of an open circuit fault [35].

Because diodes allow current to pass in only one direction, the voltage output during dead time depends upon the direction of current flow during the dead time. Examining figure 5.1, when the output current is positive, it passes out of the phase-leg into the output terminal. When this is the case, during dead time, current flow from the upper DC source is blocked by the diode of S_+ and current flow from the lower DC source passes through the diode of S_-. Therefore, when the output current is positive, the output voltage during dead time is -1. Similarly, when the output current is negative, it passes from the output terminal into the phase-leg, and, during dead time, current flow to the upper DC source passes through the diode of S_+ and current flow to the lower DC source is blocked by the diode of S_-. Therefore, the voltage output during dead time is $+1$ when the output current is negative.

We note at this point that because the high-frequency nature of the switching in an inverter leads to high-frequency oscillations in the output voltages, this can, in turn, lead to high-frequency oscillations in the output currents [63]. If the magnitude of these oscillations is large, the output current can switch between positive and negative values at a high frequency. Determining the output voltage during dead time is analytically difficult if the associated output current is rapidly switching sign.

By Faraday's law of electromagnetic induction [53], the rate of change of the current flowing through an inductor is proportional to the voltage across the inductor, divided by the inductance. Thus, as the inductance increases, the current response to a voltage decreases, and is less likely to oscillate at a high frequency. In fact, inverters with highly inductive loads are preferable, as they reduce high-frequency currents, which can cause problems such as electromagnetic interference (see [59, 67], for example). Therefore, to simplify our analysis, we examine inverters with highly

inductive loads. Note that we discuss what it means for a load to be highly inductive in section 2.1 of chapter 6.

1.2 Structure of the Chapter

In section 2 we calculate a Fourier series for the voltage output of a single-phase inverter that incorporates dead time. Section 3 details the calculation of the voltage outputs of a two-phase inverter that incorporates dead time. In section 4 we determine the voltage outputs of a three-phase inverter. We summarise our conclusions in section 5.

2   Single-phase Inverter

Before calculating the voltage output of a single-phase inverter that incorporates dead time, we recall the output voltage of a single-phase inverter without dead time. An inverter without dead time is assumed to have instantaneous and simultaneous switching. In other words, with reference to figure 5.3, at $t = \mathcal{A}_m^a$, S_+ opens, S_- closes and the voltage output, $v_a(t)$, switches from $+1$ to -1. Similarly, at $t = \mathcal{B}_m^a$, S_+ closes, S_- opens and $v_a(t)$ switches from -1 to $+1$. The switch times $\mathcal{A}_m^a$ and $\mathcal{B}_m^a$ are given by

$$\mathcal{A}_m^a = mT + \frac{T}{4}(1 + s_a(mT)), \qquad \text{and} \qquad \mathcal{B}_m^a = mT + \frac{T}{4}(3 - s_a(mT)), \qquad (2.1)$$

where the signal wave $s_a(t) = M \cos \omega_s t$ (with amplitude M and frequency ω_s), m is any integer and $T = 2\pi/\omega_c$ is the switching period, with frequency $\omega_c \gg \omega_s$. We describe $v_a(t)$ mathematically as

$$v_a(t) = 1 - 2 \sum_m \psi(t; \mathcal{A}_m^a, \mathcal{B}_m^a),$$

where $\psi(t; t_1, t_2) = 1$ when $t_1 < t_2$ and is zero otherwise. From this expression and (2.1), the Poisson re-summation method determines, from chapter 2,

$$v_a(t) = \sum_{mn} a_{mn} e^{i\Omega_{mn}t},$$

where $\Omega_{mn} = m\omega_c + n\omega_s$ and

$$a_{mn} = \begin{cases} 0, & \text{if } \Omega_{mn} = 0, \\ \frac{2}{i\Omega_{mn}T} J_n\left(\frac{1}{4}\Omega_{mn}MT\right) \left[i^n e^{-3i\Omega_{mn}T/4} - (-i)^n e^{-i\Omega_{mn}T/4}\right], & \text{otherwise,} \end{cases} \qquad (2.2)$$

are the Fourier coefficients.

In order to determine the voltage output of a single-phase inverter that incorporates dead time, we first determine the switch times of the voltage output in section 2.1. Using these switch times, we then determine the voltage output in section 2.2. In section 2.3, we analyse the frequency spectrum of the voltage output of a single-phase inverter that incorporates dead time.
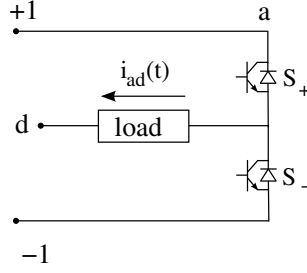
Figure 5.3: *Circuit diagram of a single-phase inverter, where a load is connected between phase-leg a and the neutral point d.*

2.1   Inverter Switching With Dead Time

To determine the switch times of the voltage output $v_a(t)$ of a single-phase inverter that incorporates dead time, we first make some definitions. The switch times of $v_a(t)$ are indicated by

$$\mathcal{A}'_m, \qquad \text{and} \qquad \mathcal{B}'_m,$$

where $m \in \mathbb{Z}$. We recall that at $t = \mathcal{A}'_m$, $v_a(t)$ switches from $+1$ to -1, and at $t = \mathcal{B}'_m$, $v_a(t)$ switches from -1 to $+1$. We assume that $\mathcal{A}'_m < \mathcal{B}'_m$ and $\mathcal{B}'_m < \mathcal{A}'_{m+1}$. We also indicate the length of the dead time by a constant $D \in \mathbb{R}$.

During dead time, $v_a(t) = +1$ or -1, if $i_{ad}(t) < 0$ or > 0, respectively (see section 1.1). Therefore, the switch times $\mathcal{A}'_m$ and $\mathcal{B}'_m$ depend on the polarity of $i_{ad}(t)$. We now examine the polarity of $i_{ad}(t)$ in more detail.

2.1.1   Polarity of $i_{ad}(t)$

Because we examine inverters with highly inductive loads, it is reasonable to assume that $i_{ad}(t) \approx i^l_{ad}(t)$, where $i^l_{ad}(t) = Z^{-1}v^l_{ad}(t)$, where Z is a differential operator determined by the load and $v^l_{ad}(t)$ is the leading low-frequency contribution to the voltage across the load, given by

$$v^l_{ad}(t) = v^l_a(t) = a_{01}e^{i\omega_s t} + a_{0,-1}e^{-i\omega_s t}, \tag{2.3}$$

where a_{01} and $a_{0,-1}$ are given in (2.2). Note that we refer to $i^l_{ad}(t)$ as the *idealised* output current. By taking Taylor series expansions of a_{01} and $a_{0,-1}$ it is easily verified that

$$a_{01} = a_{0,-1} = \frac{M}{2}.$$

Therefore $v^l_{ad}(t) \approx s_a(t)$.

In this thesis, we assume that the load is composed of passive electrical components. Consequently, $i^l_{ad}(t)$ will have different phase and amplitude to $v^l_{ad}(t)$, but the frequency, ω_s, will remain the same. Therefore, because $v^l_{ad}(t) \approx s_a(t)$, it is easily verified that $i^l_{ad}(t) \approx s_a(t-\theta/\omega_s)$, where θ is the phase-shift between $v^l_{ad}(t)$ and $i^l_{ad}(t)$. In order to define the switch times $\mathcal{A}'_m$ and
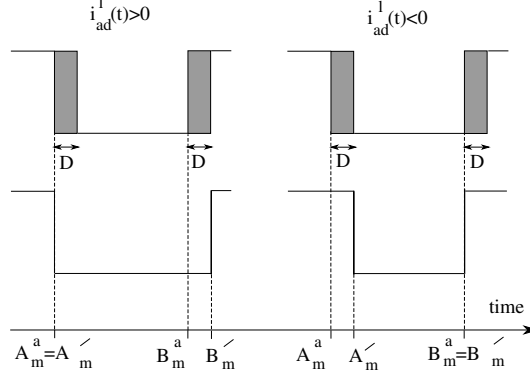
Figure 5.4: *Diagram to show how, across a single switching period, delay-only switching affects the voltage output when $i_{ad}^l(t) > 0$ and $i_{ad}^l(t) < 0$. Dead time of length D, inserted by delay-only switching, is illustrated by shaded areas. The voltage output $v_a(t)$ switches from $+1$ to -1 at $t = \mathcal{A}'_m$, where $\mathcal{A}'_m = \mathcal{A}^a_m$ if $i_{ad}^l(t) > 0$ or $\mathcal{A}'_m = \mathcal{A}^a_m + D$ if $i_{ad}^l(t) < 0$. Similarly, $v_a(t)$ switches from -1 to $+1$ at $t = \mathcal{B}'_m$, where $\mathcal{B}'_m = \mathcal{B}^a_m + D$ if $i_{ad}^l(t) > 0$ or $t = \mathcal{B}'_m = \mathcal{B}^a_m$ if $i_{ad}^l(t) < 0$.*

$\mathcal{B}'_m$, we introduce a function that indicates the polarity of $i_{ad}^l(t)$, given by

$$\Psi(t) = \begin{cases} +1, & \theta < \omega_s t < \theta + \pi, \\ -1, & \theta + \pi < \omega_s t < \theta + 2\pi. \end{cases} \tag{2.4}$$

We now determine the switch times $\mathcal{A}'_m$ and $\mathcal{B}'_m$ explicitly.

2.1.2 Switch Times of an Inverter With Dead Time

In view of section 1.1, and figure 5.4, when inserting dead time to the switching transitions of a single-phase inverter according to delay-only switching, the switch times of $v_a(t)$ are given by

$$\mathcal{A}'_m = \begin{cases} \mathcal{A}^a_m, & \text{if } i_{ad}^l(t) > 0, \\ \mathcal{A}^a_m + D, & \text{if } i_{ad}^l(t) < 0, \end{cases} \quad \text{and} \quad \mathcal{B}'_m = \begin{cases} \mathcal{B}^a_m + D, & \text{if } i_{ad}^l(t) > 0, \\ \mathcal{B}^a_m, & \text{if } i_{ad}^l(t) < 0, \end{cases} \tag{2.5}$$

where $\mathcal{A}^a_m$ and $\mathcal{B}^a_m$ are given in (2.1). Similarly, with reference to figure 5.5, using delay-advance switching, the switch times of $v_a(t)$ are given by

$$\mathcal{A}'_m = \begin{cases} \mathcal{A}^a_m - \frac{D}{2}, & \text{if } i_{ad}^l(t) > 0, \\ \mathcal{A}^a_m + \frac{D}{2}, & \text{if } i_{ad}^l(t) < 0, \end{cases} \quad \text{and} \quad \mathcal{B}'_m = \begin{cases} \mathcal{B}^a_m + \frac{D}{2}, & \text{if } i_{ad}^l(t) > 0, \\ \mathcal{B}^a_m - \frac{D}{2}, & \text{if } i_{ad}^l(t) < 0. \end{cases} \tag{2.6}$$

Therefore, from (2.4), (2.5) and (2.6),

$$\mathcal{A}'_m = \mathcal{A}^a_m + \frac{D}{2}(\delta - \Psi(mT)), \tag{2.7}$$

$$\mathcal{B}'_m = \mathcal{B}^a_m + \frac{D}{2}(\delta + \Psi(mT)), \tag{2.8}$$

where

$$\delta = \begin{cases} 1, & \text{for delay-only switching,} \\ 0, & \text{for delay-advance switching.} \end{cases}$$
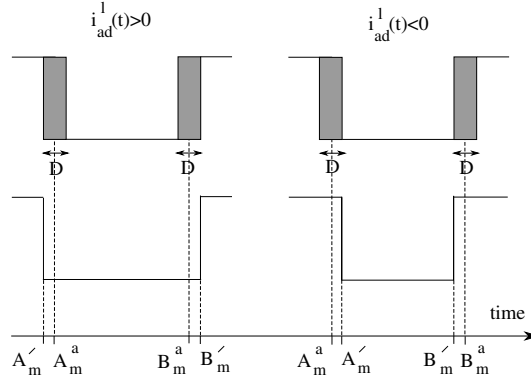
Figure 5.5: *Diagram to show how, across a single switching period, delay-advance switching affects the voltage output when $i_{ad}^l(t) > 0$ and $i_{ad}^l(t) < 0$. Dead time of length D, inserted by delay-only switching, is illustrated by shaded areas. The voltage output $v_a(t)$ switches from $+1$ to -1 at $t = \mathcal{A}_m'$, where $\mathcal{A}_m' = \mathcal{A}_m^a - D/2$ if $i_{ad}^l(t) > 0$ or $\mathcal{A}_m' = \mathcal{A}_m^a + D/2$ if $i_{ad}^l(t) < 0$. Similarly, $v_a(t)$ switches from -1 to $+1$ at $t = \mathcal{B}_m'$, where $\mathcal{B}_m' = \mathcal{B}_m^a + D/2$ if $i_{ad}^l(t) > 0$ or $t = \mathcal{B}_m' = \mathcal{B}_m^a - D/2$ if $i_{ad}^l(t) < 0$.*

Note that, from (2.1), (2.7) and (2.8), the assumption that $\mathcal{A}_m' < \mathcal{B}_m'$ and $\mathcal{B}_m' < \mathcal{A}_{m+1}'$ means that $D < T(1 - M)/2$ in our analysis. In practice, D is usually a few percent of the switching period T (see [25, 27, 29, 34, 64, 78, 93, 111], for example). In chapter 2 we noted that $|M| < 1$, but in this chapter, to allow for D to be a few percent of the switching period, we must have $|M| \leq 0.98$.

2.2   Output Voltage of an Inverter Incorporating Dead Time

We now calculate the voltage output of a single-phase inverter using the Poisson re-summation method following the approach of [34]. The voltage output $v_a(t)$ of a single phase-leg of a PWM inverter incorporating dead time is

$$v_a(t) = 1 - 2\sum_m \psi(t; \mathcal{A}_m', \mathcal{B}_m') \equiv 1 - 2f(t), \tag{2.9}$$

where the switch times A_m' and B_m' are given in (2.7) and (2.8). For slight notational brevity we determine the frequency spectrum of $f(t)$, rather than $v_a(t)$. Taking a Fourier transform of $f(t)$, when $\omega \neq 0$, gives

$$\hat{f}(\omega) = \sum_m \frac{1}{i\omega}(e^{-i\omega\mathcal{A}_m'} - e^{-i\omega\mathcal{B}_m'}).$$

In view of (2.1), (2.7), (2.8) and $s_a(t) = M\cos\omega_s t$, when $\omega \neq 0$,

$$\hat{f}(\omega) = \sum_m \frac{1}{i\omega}e^{-i\omega mT}e^{-i\omega D\delta/2}\bigg(e^{-i\omega T/4}e^{-i\omega(MT\cos\omega_s mT - 2D\Psi(mT))/4}$$
$$-e^{-3i\omega T/4}e^{i\omega(MT\cos\omega_s mT - 2D\Psi(mT))/4}\bigg).$$

We now examine the Fourier series of some exponential terms in $\hat{f}(\omega)$.

2.2.1 Fourier Series for $e^{i\omega(MT\cos\omega_s t - 2D\Psi(t))/4}$

Both $\cos\omega_s t$ and $\Psi(t)$ have a period $2\pi/\omega_s$. Therefore

$$e^{i\omega(MT\cos\omega_s t - 2D\Psi(t))/4} = \sum_n S_n(\omega, D)e^{in\omega_s t},$$

where

$$
\begin{aligned}
S_n(\omega, D) &= \frac{\omega_s}{2\pi}\int_{\theta/\omega_s}^{(2\pi+\theta)/\omega_s} e^{i\omega(MT\cos\omega_s t - 2D\Psi(t))/4}e^{-in\omega_s t}\,dt, \\
&= \frac{\omega_s}{2\pi}\Bigg[\int_{\theta/\omega_s}^{(\pi+\theta)/\omega_s} e^{-in\omega_s t}e^{i\omega MT\cos\omega_s t/4}e^{-i\omega D/2}\,dt \\
&\qquad + \int_{(\pi+\theta)/\omega_s}^{(2\pi+\theta)/\omega_s} e^{-in\omega_s t}e^{i\omega MT\cos\omega_s t/4}e^{i\omega D/2}\,dt\Bigg].
\end{aligned}
$$

Using the Jacobi-Anger expansion [109] we have

$$
\begin{aligned}
S_n(\omega, D) &= \frac{\omega_s}{2\pi}\sum_q i^q J_q\left(\tfrac{1}{4}\omega MT\right)\Bigg[e^{-i\omega D/2}\int_{\theta/\omega_s}^{(\pi+\theta)/\omega_s} e^{-i(n-q)\omega_s t}\,dt \\
&\qquad + e^{i\omega D/2}\int_{(\pi+\theta)/\omega_s}^{(2\pi+\theta)/\omega_s} e^{-i(n-q)\omega_s t}\,dt\Bigg], \\
&= \frac{i^n}{2}J_n\left(\tfrac{1}{4}\omega MT\right)\left(e^{-i\omega D/2} + e^{i\omega D/2}\right) \\
&\qquad + (e^{-i\omega D/2} - e^{i\omega D/2})\sum_{q\neq n}\frac{e^{-i(n-q)\theta}}{2\pi i(n-q)}(1 - e^{-i(n-q)\pi})J_q\left(\tfrac{1}{4}\omega MT\right)i^q, \\
&\equiv i^n J_n\left(\tfrac{1}{4}\omega MT\right)\cos\left(\tfrac{1}{2}\omega D\right) - \sin\left(\tfrac{1}{2}\omega D\right)R_n(\omega), \quad\quad (2.10)
\end{aligned}
$$

where

$$R_n(\omega) = \sum_{q\neq n}\frac{i^q}{\pi(n-q)}e^{-i(n-q)\theta}(1 - (-1)^{n-q})J_q\left(\tfrac{1}{4}\omega MT\right). \quad\quad (2.11)$$

We note that $R_n(\omega)$ is independent of D. Furthermore, from (2.10), $S_n(\omega, 0) = i^n J_n(\tfrac{1}{4}\omega MT)$, and is independent of $R_n(\omega)$. We now return to our Fourier transform $\hat{f}(\omega)$.

2.2.2 Fourier Transform

In view of section 2.2.1, when $\omega \neq 0$,

$$\hat{f}(\omega) = \sum_{mn}\frac{1}{i\omega}e^{-i\omega mT}e^{-i\omega D\delta/2}S_n(\omega, D)\left[e^{-i\omega T/4}(-1)^n - e^{-3i\omega T/4}\right]e^{in\omega_s mT},$$

where $S_n(\omega, D)$ is defined in (2.10). Poisson re-summing $\hat{f}(\omega)$ in m, gives, when $\omega \neq 0$,

$$\hat{f}(\omega) = \sum_{mn}\int_{-\infty}^{\infty}\frac{1}{i\omega T}e^{-i\omega D\delta/2}S_n(\omega, D)\left[e^{-i\omega T/4}(-1)^n - e^{-3i\omega T/4}\right]e^{i\Omega_{mn}t}e^{-i\omega t}\,dt.$$

Therefore,

$$f(t) = \sum_{mn}\frac{1}{i\Omega_{mn}T}e^{-i\Omega_{mn}D\delta/2}S_n(\Omega_{mn}, D)\left[e^{-i\Omega_{mn}T/4}(-1)^n - e^{-3i\Omega_{mn}T/4}\right]e^{i\Omega_{mn}t},$$
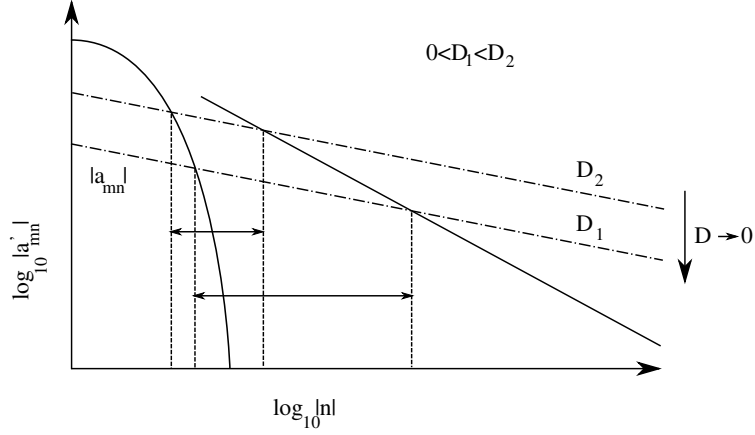
$$-\ 94\ -$$

Figure 5.6: *Schematic plot, for fixed m, of the envelope of a'_{mn}. There are three regimes in n: for small n, large n, and a transition regime between large and small n. The parabola of the small n regime and the slope of the large n regime are indicated by solid lines, with the slope of the transition regime indicated by dot-dash lines. As $D \to 0$ the position of the transition slope is lowered, and the intersections with the small and large n regimes form, respectively, the start and end of the transition regime (indicated by dotted lines). Note that the length of the transition regime increases as $D \to 0$.*

where we the terms in the sum that correspond to $\Omega_{mn} = 0$ are omitted. The contribution to the frequency spectrum of $v_a(t)$ when $\Omega_{mn} = 0$ is the mean value of $v_a(t)$, which is zero (see appendix A.2). Therefore, the voltage output $v_a(t)$ is

$$v_a(t) = \sum_{mn} a'_{mn} e^{i\Omega_{mn}t},$$

where

$$a'_{mn} = \begin{cases} 0, & \text{if } \Omega_{mn} = 0, \\ \dfrac{2}{i\Omega_{mn}T} e^{-i\Omega_{mn}D\delta/2} S_n(\Omega_{mn}, D) \left[e^{-3i\Omega_{mn}T/4} - e^{-i\Omega_{mn}T/4}(-1)^n \right] & \text{if } \Omega_{mn} \neq 0. \end{cases}$$

(2.12)

This reproduces the Fourier series for $v_a(t)$ determined in [34]. It is easily verified, from (2.10) and (2.12), that if $D = 0$, $a'_{mn} = a_{mn}$. The Fourier coefficients a_{mn} (given in (2.2)) of $v_a(t)$ decay rapidly with respect to n, for fixed m (see [49], for example). Specifically, for fixed m, the decay of a_{mn}, with respect to n, is, from Debye's asymptotic expansion of Bessel functions of the first kind [2], proportional to

$$a_{mn} \sim \frac{e^{n(\tanh \alpha - \alpha)}}{\Omega_{mn}\sqrt{2\pi n \tanh \alpha}},$$

where $\operatorname{sech} \alpha = \frac{1}{4}\omega_s MT$. Similarly, from [49], a_{mn} decays rapidly in m, for fixed n.

We now examine a'_{mn} when $D \neq 0$. Because the Fourier coefficients a'_{mn} contain oscillatory terms, for $D \neq 0$, to examine the decay rate of a'_{mn} in n, for fixed m, we examine the envelope of a'_{mn} in n. The envelope of a'_{mn} decays according to three regimes in n, as illustrated in figure 5.6. The three regimes occur for small n, large n and a transition regime between the two. The small

n regime is independent of D, and in this regime $a'_{mn} \approx a_{mn}$. The large n regime only occurs for $D \neq 0$, and in this regime the rate of decay and the envelope of a'_{mn} are independent of D. In the large n regime, from (2.10) and (2.12), $a'_{mn} \approx \Omega_{mn}^{-1} R_n(\Omega_{mn})$, where $R_n(\Omega_{mn})$ is given in (2.11). In the transition regime, from (2.10) and (2.12), $a'_{mn} \approx DR_n(\Omega_{mn})$. Therefore, as $D \to 0$, the amplitude of the envelope of a'_{mn} in the transition regime decreases linearly. Additionally, the n's for which the transition regime begins and ends increase as $D \to 0$.

2.3   Analysis of the Frequency Spectrum of $v_a(t)$

The Fourier coefficients a'_{mn} decay slowly with respect to n (for fixed m) compared to the coefficients a_{mn}, when $D \neq 0$. This means, provided $\omega_c/\omega_s \in \mathbb{Q}$, that each carrier group contributes to each peak in the spectrum of $v_a(t)$ (for an inverter with dead time). Note that if ω_c/ω_s is irrational, each Fourier coefficient has a unique contribution to the frequency spectrum. In this thesis, we plot contributions to the spectrum with magnitude 10^{-5} and greater. Therefore, for numerical purposes, we plot the amplitude,

$$\left| \sum_{k=-N}^{N} a'_{m+k, n-\omega_c k/\omega_s} \right|, \tag{2.13}$$

against the harmonic order, Ω_{mn}/ω_s, in the frequency spectra in this chapter. We truncate the sum at N, where, for all m and n, $|a'_{m\pm N, n\mp\omega_c N/\omega_s}| \geq 10^{-5}$ and $|a'_{m\pm(N+1), n\mp\omega_c(N+1)/\omega_s}| < 10^{-5}$ (as discussed in section 3.2.3 of chapter 3).

Previously, for a single-phase inverter without dead time, the decay of the coefficients a_{mn} means that we truncate the sum of (2.13) at $N = 0$. Therefore, each peak in the spectrum has a contribution from one carrier group, and we identify *low-frequency* components as those corresponding to the $m = 0$ carrier group, and *high-frequency* components as the $m \neq 0$ carrier groups.

When $N \neq 0$ we no longer have these definitions for high and low frequency components because every peak in the frequency spectrum has a contribution from several carrier groups, and it is not obvious where the low-frequency components end, and the high-frequency components begin. Instead we identify low-frequency components of the spectrum as those corresponding to harmonic orders less than $\omega_c/2\omega_s$. Similarly, the high-frequency components correspond to harmonic orders greater than $\omega_c/2\omega_s$. This is the convention used in [69].

We now determine, by examination of a'_{mn} (given in (2.12)), where to truncate the sum in (2.13) to plot spectra for $v_a(t)$ of inverters that incorporate dead time that are accurate up to $O(10^{-5})$. When $D = 0$, $a'_{mn} = a_{mn}$, and, in this case, $N = 0$, and the spectra are identical to the spectra for $v_a(t)$ of inverters without dead time (illustrated in figure 2.5).

In keeping with previous chapters in this thesis and [49], we now plot spectra for $v_a(t)$ when $\omega_c = 21\omega_s$. We also set $D = T/100$. From empirical evidence, when $\omega_c = 21\omega_s$ and $D = T/100$, $|a'_{mn}| < 10^{-5}$ for $|n| > 1000$. Therefore, to plot accurate spectra, we truncate the sum of (2.13) at $N = 48$. When $N = 48$, each peak in the spectrum takes 2.87s to compute using matlab. Note that spectra for $v_a(t)$ when $\delta = 0$ are indistinguishable from spectra for $v_a(t)$ when $\delta = 1$.

(a) $D = T/100$.

(b) $D = T/1000$.

(c) *Without dead time.*
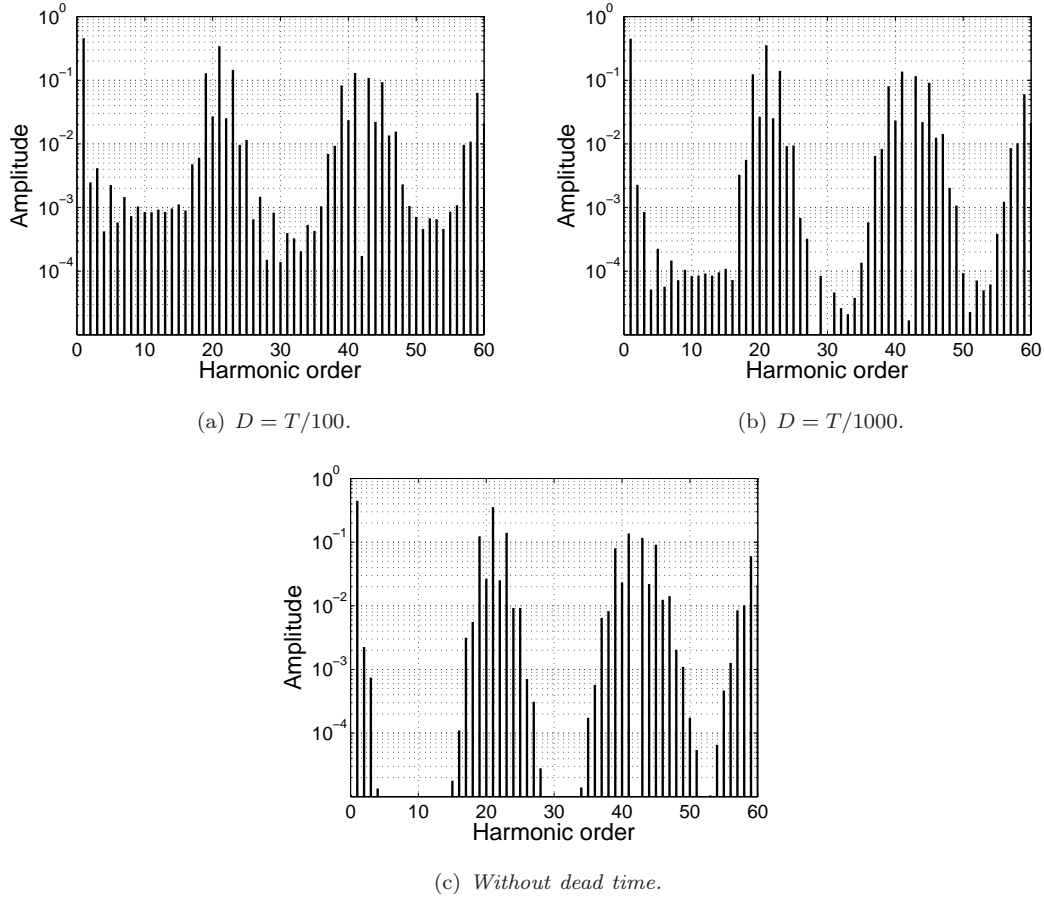
Figure 5.7: *Frequency spectra for the voltage output, $v_a(t)$, of a single-phase inverter, where $M = 0.9$, $\omega_c = 21\omega_s$, $\delta = 1$ and $\theta = \pi/3$.*

Therefore, in this chapter, we produce spectra for $\delta = 1$ only.

Figure 5.7(a) illustrates the spectrum of $v_a(t)$ when $\omega_c = 21\omega_s$ and $D = T/100$. The spectra plotted here agree with those in [34]. Carrier groups with odd m have one dominant central peak, and carrier groups with even m have two dominant central peaks. The leading low-frequency contribution to the spectrum of $v_a(t)$ occurs at ω_s, and the leading high-frequency contribution occurs at ω_c. In other words, the dominant contributions to the spectrum of the voltage output of an inverter with dead time are the same as the dominant contributions for an inverter without dead time. This means that the dominant characteristics of the voltage output of a single-phase inverter with dead time are the same as the dominant characteristics of a single-phase inverter without dead time.

Dead time lasts, in this example, a few percent of the switching period, and, compared to inverters without dead time, there are more visible contributions to the spectrum of $v_a(t)$. This is expected from previous analysis of dead time [25, 27, 29, 64, 78, 93, 111]. Any visible contribution to the spectrum of $v_a(t)$ that is present for inverters with dead time, but not present for inverters without dead time is referred to as *dead time distortion*. The dead time distortion

(a) $\omega_c = 21\omega_s$.

(b) $\omega_c = 101\omega_s$.
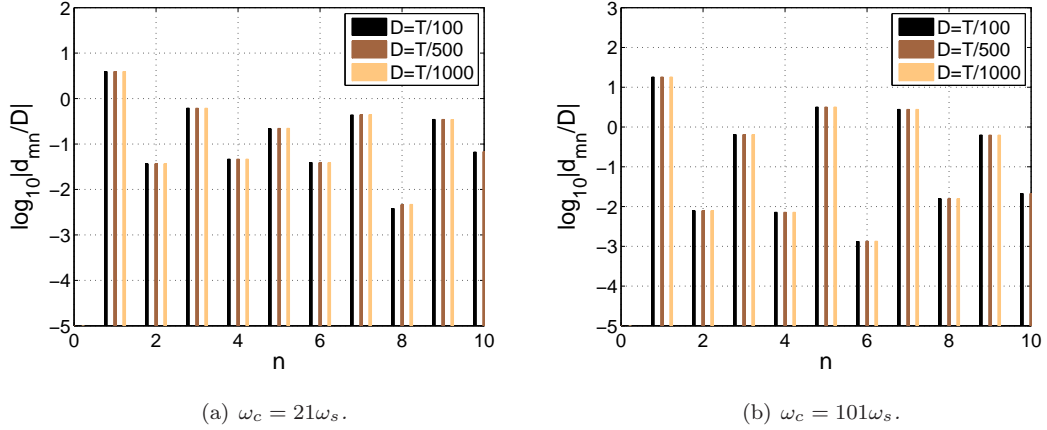
Figure 5.8: *Illustration to show the linearity of the dead time distortion of $v_a(t)$ with respect to D. The vertical axis is the absolute value of the Fourier coefficients of the dead time distortion scaled by D. Here we show a section of the $m = 0$ carrier group for a range of values of D, where $M = 0.9$, $\delta = 1$ and $\theta = \pi/3$.*

is evidenced by comparison of the spectrum of $v_a(t)$ with dead time (shown in figure 5.7(a)) with the spectrum of $v_a(t)$ without dead time (shown in figure 5.7(c)). We describe the dead time distortion mathematically as

$$d(t) = \sum_{mn} d_{mn} e^{i\Omega_{mn}t},$$

where $d_{mn} = a_{mn} - a'_{mn}$. The Fourier coefficients a_{mn} and a'_{mn} are given in (2.2) and (2.12), respectively.

We now examine the effects of varying D on the spectrum of $v_a(t)$. When $\omega_c = 21\omega_s$ and $D = T/1000$, $|a'_{mn}| < 10^{-5}$ for $n > 100$ (from empirical evidence). Therefore, we truncate the sums of (2.13) at $N = 5$ to plot an accurate spectrum. Each contribution to the spectrum of $v_a(t)$ takes 0.35s to compute in matlab. We illustrate the spectrum of $v_a(t)$ when $\omega_c = 21\omega_s$ and $D = T/1000$ in figure 5.7(b). This spectrum is accurate up to $\mathrm{O}(10^{-5})$. Note that the frequencies that have a dominant contribution to the spectrum are not affected by D. The amplitude of the dead time distortion is reduced as $D \to 0$, however, from comparison of figures 5.7(a) and 5.7(b). We now examine the relationship between the amplitude of the dead time distortion and D.

As illustrated in figure 5.8(a), the magnitude of the Fourier coefficients, d_{mn}, of the dead time distortion is linear with respect to the length of the dead time D. In other words, $d_{mn} = \mathrm{O}(D)$ as $D \to 0$. Consequently, as $D \to 0$, the distortion in the output voltage generated by insertion of dead time is reduced. From comparison of figures 5.8(a) and 5.8(b), the amplitude of d_{mn} is affected by the ratio ω_c/ω_s, but the ratio ω_c/ω_s does not affect the property $d_{mn} = \mathrm{O}(D)$ as $D \to 0$.

Finally, we note that, as ω_c/ω_s increases, the numerical cost of plotting spectra decreases. For example, when $D = T/1000$ and $\omega_c = 101\omega_s$, $a'_{mn} \leq 10^{-5}$ for $|n| > 200$. Therefore, for each peak in the spectrum, we only need to sum the contribution from the nearest 5 carrier groups
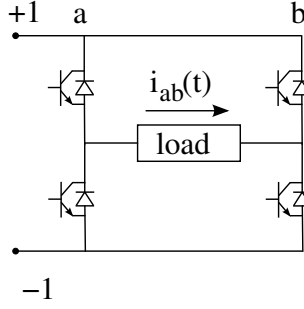
Figure 5.9: *Circuit diagram of a two-phase inverter, where a load is connected between phase-leg a and phase-leg b. The current through the load, $i_{ab}(t)$, is also illustrated here.*

(we require a sum over the nearest 11 carrier groups when $\omega_c = 21\omega_s$ and $D = T/1000$).

3   Two-phase Inverter

In this section we determine frequency spectra for the output voltages of a two-phase inverter with dead time. This extends analysis in [34], where the voltage outputs of a single-phase inverter with dead time were determined. There are two phase-legs in a two-phase inverter (illustrated in figure 5.9), and each phase-leg, a and b, generates a voltage output, $v_a(t)$ and $v_b(t)$, respectively. Additionally, a single output current, $i_{ab}(t)$, is generated through the load.

The switch times of $v_a(t)$ are $\mathcal{A}'_m$ and $\mathcal{B}'_m$. Similarly, the switch times of $v_b(t)$ are $\mathcal{A}''_m$ and B''_m. In order to determine explicit definitions for $\mathcal{A}'_m$, $\mathcal{B}'_m$, $\mathcal{A}''_m$ and B''_m we examine the voltage outputs during dead time. For both phase-legs, the output voltage during dead time depends on the polarity of $i_{ab}(t)$. Therefore, in order to calculate voltage spectra for $v_a(t)$ and $v_b(t)$, we determine the polarity of $i_{ab}(t)$.

We assume that $i_{ab}(t) \approx i^l_{ab}(t)$, where

$$i^l_{ab}(t) = Z^{-1}v^l_{ab}(t) = Z^{-1}(v^l_a(t) - v^l_b(t)).$$

From (2.3), $v^l_a(t) \approx s_a(t)$. Because the signal wave $s_b(t)$ is π radians out of phase with $s_a(t)$, it is easily verified, from (2.3), that $v^l_b(t) \approx -s_a(t)$. Therefore, $v^l_{ab}(t) \approx 2s_a(t)$, and consequently $i^l_{ab}(t) \approx 2s_a(t - \theta/\omega_s)$.

Because the polarity of the $i^l_{ab}(t)$ is the same as the polarity of $i^l_{ad}(t)$ for a single-phase inverter, from section 2.1, the switch times, $\mathcal{A}'_m$ and $\mathcal{B}'_m$, of $v_a(t)$ are given in (2.7) and (2.8), respectively. Similarly, the switch times of $v_b(t)$ are given by

$$\mathcal{A}''_m = \mathcal{A}^b_m + \frac{D}{2}(\delta + \Psi(mT)),$$
$$\mathcal{B}''_m = \mathcal{B}^b_m + \frac{D}{2}(\delta - \Psi(mT)),$$

where $\mathcal{A}^b_m$ and $\mathcal{B}^b_m$ are defined similarly to (2.1), with signal wave $s_b(t) = M\cos(\omega_s t - \pi)$. Thus,

(a) $\omega_c = 21\omega_s$.

(b) $\omega_c = 20\omega_s$.
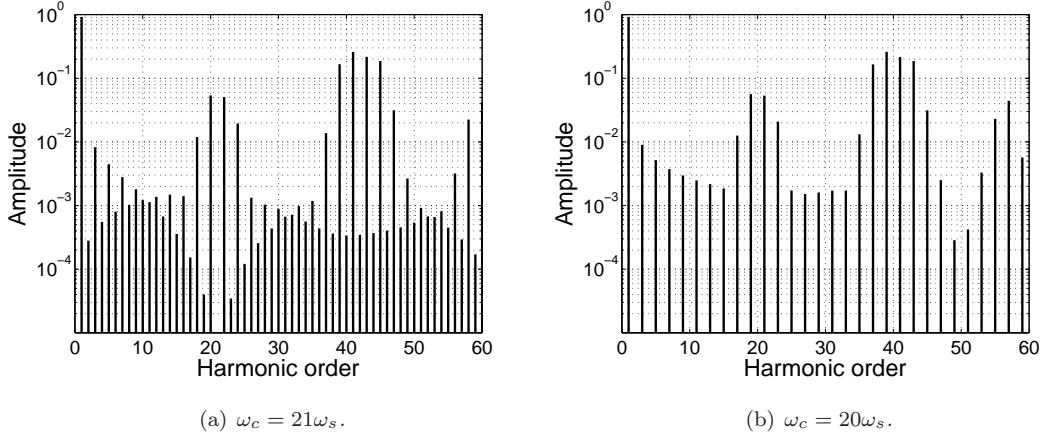
Figure 5.10: *Frequency spectrum of the voltage difference across the load in a two-phase inverter with dead time, where $M = 0.9$, $D = T/100$, $\theta = \frac{\pi}{3}$ and $\delta = 1$.*

from section 2.2, $v_a(t)$ and $v_b(t)$ of a two-phase inverter are

$$v_a(t) = \sum_{mn} a'_{mn} e^{i\Omega_{mn}t}, \qquad \text{and} \qquad v_b(t) = \sum_{mn} a'_{mn} (-1)^n e^{i\Omega_{mn}t},$$

where a'_{mn} is given in (2.12). In addition to $v_a(t)$ and $v_b(t)$, the spectrum for the load voltage (the voltage difference across the load) $v_{ab}(t)$ is also used for filter design. Noting that $v_{ab}(t) = v_a(t) - v_b(t)$, we have

$$v_{ab}(t) = \sum_{mn} a'_{mn} (1 - (-1)^n) e^{i\Omega_{mn}t} \equiv \sum_{mn} v_{mn} e^{i\Omega_{mn}t}.$$

Note that v_{mn} is non-zero when n is odd.

3.1 Analysis of Frequency Spectra for a Two-phase Inverter

The frequency spectra of $v_a(t)$ and $v_b(t)$ are identical, and are plotted in figure 5.7(a) (for $\omega_c = 21\omega_s$ and $D = T/100$). The frequency spectrum of $v_{ab}(t)$ is shown in figure 5.10, where we have plotted two spectra: one for $\omega_c = 21\omega_s$, and one for $\omega_c = 20\omega_s$. When $\omega_c = 21\omega_s$ and $\omega_c = 20\omega_s$, $|v_{mn}| < 10^{-5}$ for $n > 1000$. Therefore, in each of the spectra illustrated in figure 5.10, from (2.13), the amplitude,

$$\left| \sum_{k=-50}^{50} v_{m+k, n - \omega_c k/\omega_s} \right|, \tag{3.1}$$

is plotted against against the harmonic order Ω_{mn}/ω_s, which ensures the spectra are accurate up to $O(10^{-5})$.

In figure 5.10, the leading low-frequency contribution to the spectrum is at ω_s, and the leading high-frequency contributions to the spectrum are at $2\omega_c \pm \omega_s$. From comparison of figures 5.10 and 2.10, considerable low-frequency and high-frequency distortion is generated in the spectrum of the load voltage of a two-phase inverter that incorporates dead time compared to a two-phase
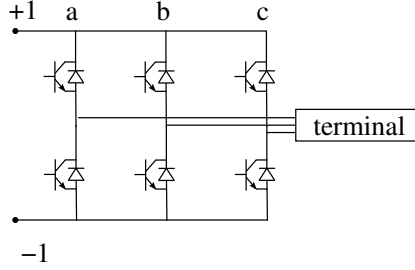
Figure 5.11: *Diagram of a three-phase inverter, where the loads are connected in the part of the circuit labelled 'terminal'. The terminal can be wired in two ways: the Δ configuration and the Y configuration, shown in figure 1.4.*

inverter without dead time. The magnitude of the dead time distortion increases linearly as the length of the dead time, D, increases.

We also note that, from figure 5.10(b), when ω_c is an even multiple of ω_s, there is contribution to the spectrum only when the harmonic order is odd. This is because, when ω_c is an even multiple of ω_s, from (3.1), contribution to the spectrum at odd frequencies comprise v_{mn} in odd n, and contribution to the spectrum at even frequencies comprises v_{mn} in even n. Therefore, in figure 5.10(b) (where ω_c is an even multiple of ω_s), contribution to the spectrum is non-zero for odd frequencies only. Therefore, $v_{ab}(t)$ has maximum harmonic cancellation when ω_c is an even multiple of ω_s.

4 Three-phase Inverter

We now calculate spectra for the output voltages and load voltages of a three-phase inverter with dead time for the first time. A three-phase inverter is illustrated in figure 5.11, where the switches comprise a transistor and a diode connected in parallel.

A three-phase inverter generates three voltage outputs: $v_a(t)$, $v_b(t)$ and $v_c(t)$. The voltage output $v_a(t)$ switches from $+1$ to -1 at $t = \mathcal{A}'_m$, and switches from -1 to $+1$ at $t = \mathcal{B}'_m$. Similarly, the switch times of $v_b(t)$ are $\mathcal{A}''_m$ and $\mathcal{B}''_m$, and the switch times of $v_c(t)$ are $\mathcal{A}'''_m$ and $\mathcal{B}'''_m$. In order to determine the switch times of $v_a(t)$, $v_b(t)$ and $v_c(t)$, we examine what happens to each of the voltage outputs during dead time.

For a three-phase inverter wired in the Δ configuration, the output voltage, $v_a(t)$, during dead time, from Kirchhoff's current law, depends on the polarity of $i^l_{ab}(t) + i^l_{ac}(t)$. It is straightforward to see that

$$
\begin{aligned}
i_{ab}(t) + i_{ac}(t) &= i_{ad}(t) - i_{bd}(t) + i_{ad}(t) - i_{cd}(t), \\
&= 2i_{ad}(t) - i_{bd}(t) - i_{cd}(t).
\end{aligned}
$$

When the loads are equal, as assumed here, the sum of the currents $i_{ad}(t)$, $i_{bd}(t)$ and $i_{cd}(t)$ is zero, therefore

$$
i_{ab}(t) + i_{ac}(t) = 3i_{ad}(t).
$$

Consequently, from section 2.1.1,

$$i_{ab}^l(t) + i_{ac}^l(t) = 3i_{ad}^l(t) \approx 3s_a(t - \theta/\omega_s).$$

Therefore, the polarity of $i_{ab}^l(t) + i_{ac}^l(t)$ is the same as the polarity of $i_{ad}(t)$ in a single-phase inverter. Thus, from section 2.1, the switch times, $\mathcal{A}_m'$ and $\mathcal{B}_m'$ of $v_a(t)$, are given in (2.7) and (2.8), respectively. Through similar reasoning, the switch times of $v_b(t)$ are given by

$$
\begin{aligned}
\mathcal{A}_m' &= \mathcal{A}_m^b + \frac{D}{2}(\delta - \Psi(mT - 2\pi/3\omega_s)), \\
\mathcal{B}_m' &= \mathcal{B}_m^b + \frac{D}{2}(\delta + \Psi(mT - 2\pi/3\omega_s)),
\end{aligned}
$$

where $\mathcal{A}_m^b$ and $\mathcal{B}_m^b$ are defined similarly to (2.1), with signal wave $s_b(t) = M\cos(\omega_s t - 2\pi/3)$. Similarly, the switch times of $v_c(t)$ are given by

$$
\begin{aligned}
\mathcal{A}_m' &= \mathcal{A}_m^c + \frac{D}{2}(\delta - \Psi(mT + 2\pi/3\omega_s)), \\
\mathcal{B}_m' &= \mathcal{B}_m^c + \frac{D}{2}(\delta + \Psi(mT + 2\pi/3\omega_s)),
\end{aligned}
$$

where $\mathcal{A}_m^c$ and $\mathcal{B}_m^c$ are defined similarly to (2.1), with signal wave $s_c(t) = M\cos(\omega_s t + 2\pi/3)$.

The dead time effects on $v_a(t)$ in a three-phase inverter wired in the Y configuration depend on the polarity of $i_{ap}^l(t)$, which, from appendix C,

$$i_{ap}^l(t) = 3i_{ad}^l(t) \approx 3s_a(t - \theta/\omega_s).$$

Similarly,

$$i_{bp}^l(t) \approx 3s_a(t - \theta/\omega_s - 2\pi/3\omega_s), \qquad \text{and} \qquad i_{cp}^l(t) \approx 3s_a(t - \theta/\omega_s + 2\pi/3\omega_s).$$

Therefore, the voltage outputs of a three-phase inverter wired in the Y configuration are identical to the voltage outputs of a three-phase inverter wired in the Δ configuration, provided all the loads are equal.

Therefore, from section 2.2, it is easily verified that the three voltage outputs of a three-phase inverter wired in either the Δ or the Y configuration are given by

$$
\begin{aligned}
v_a(t) &= \sum_{mn} a_{mn}' e^{i\Omega_{mn}t}, & (4.1)
\end{aligned}
$$

$$
\begin{aligned}
v_b(t) &= \sum_{mn} a_{mn}' e^{-2\pi in/3} e^{i\Omega_{mn}t}, & (4.2)
\end{aligned}
$$

$$
\begin{aligned}
v_c(t) &= \sum_{mn} a_{mn}' e^{2\pi in/3} e^{i\Omega_{mn}t}, & (4.3)
\end{aligned}
$$

where a_{mn}' is defined in (2.12). We also determine the load voltages in a three-phase inverter wired in the Δ configuration to be

$$
\begin{aligned}
v_{ab}(t) &= \sum_{mn} v_{mn} e^{i\Omega_{mn}t}, \\
v_{bc}(t) &= \sum_{mn} v_{mn} e^{-2\pi in/3} e^{i\Omega_{mn}t}, \\
v_{ca}(t) &= \sum_{mn} v_{mn} e^{2\pi in/3} e^{i\Omega_{mn}t}.
\end{aligned}
$$

where $v_{mn} = a'_{mn}(1 - e^{-2\pi in/3})$. Similarly, from appendix C, the load voltages of a three-phase inverter wired in the Y configuration are given by

$$v_{ap}(t) = \sum_{mn} v^Y_{mn} e^{i\Omega_{mn}t}, \qquad v_{bp}(t) = \sum_{mn} v^Y_{mn} e^{-2\pi in/3} e^{i\Omega_{mn}t}, \qquad v_{cp}(t) = \sum_{mn} v^Y_{mn} e^{2\pi in/3} e^{i\Omega_{mn}t},$$

where $v^Y_{mn} = a'_{mn}(2 - e^{-2\pi in/3} - e^{2\pi in/3})/3$. Note that both $v_{mn} = 0$ and $v^Y_{mn} = 0$ when n is a multiple of 3, a consequence of the $1 - e^{-2\pi in/3}$ or $2 - e^{-2\pi in/3} - e^{2\pi in/3}$ term.

4.1 Analysis of Frequency Spectra for a Three-phase Inverter

The three voltage outputs of a three-phase inverter (wired in the Δ or Y configuration) are given in (4.1)–(4.3). The frequency spectrum of each of these output voltages is identical (illustrated in figure 5.7(a), for $\omega_c = 21\omega_s$ and $D = T/100$). The different wiring configurations affect the spectra of the load voltages only.

For each wiring configuration there are three load voltages, and all three have an identical frequency spectrum (provided the load impedances are equal). For both a three-phase inverter wired in the Δ configuration and the Y configuration, from (2.13), to plot accurate spectra for the load voltages of inverters wired in the Δ and the Y configurations, the amplitudes

$$\left| \sum_{k=-48}^{48} v_{m+k,n-\omega_c k/\omega_s} \right|, \tag{4.4}$$

are plotted against the harmonic order Ω_{mn}/ω_s. This ensures that the significant contributions to the spectrum from each carrier group are accounted for.

It is easily verified, from (4.4) and because $v_{mn} = 0$ when n is a multiple of 3, provided ω_c is a multiple of $3\omega_s$, frequencies that are a multiple of 3 do not contribute to the spectra of the load voltages of three-phase inverters wired in the Δ or Y configurations. Therefore, the load voltages have maximum harmonic cancellation when ω_c is a multiple of $3\omega_s$.

Because we are examining inverters with equal loads, the three load voltages have identical spectra for three-phase inverters wired in the Δ or Y configuration. We illustrate the spectra of the load voltages for the Δ and the Y configuration in figure 5.12 when $\omega_c = 21\omega_s$ and $D = T/100$. The leading low frequency contribution to the spectrum is at ω_s in both figure 5.12(a) and 5.12(b). There are several dominant high-frequency contributions to the spectrum, at $\omega_c \pm 2\omega_s$ and $2\omega_s \pm \omega_s$. The dead time, D, does not affect which frequencies have a dominant contribution to the spectrum. Similar to a single-phase and two-phase inverter, the amplitude of the dead time distortion is linear in D.

5 Conclusions

In this chapter we have calculated the output voltages of two-phase and three-phase inverters that incorporate dead time, for the first time. We have also calculated the load voltages for two-phase and three-phase inverters. We have calculated the output voltages using the Poisson

(a) Δ *configuration.*   (b) Y configuration
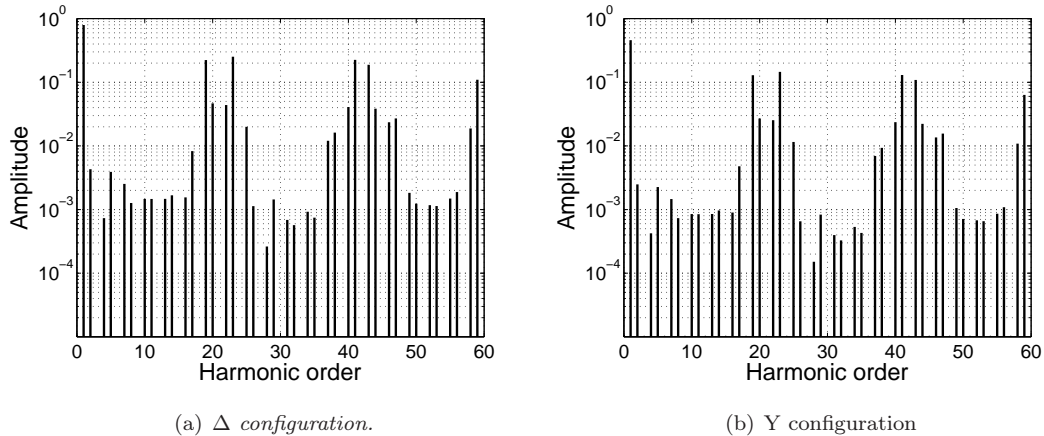
Figure 5.12: *Frequency spectra of voltage differences in a three-phase inverter, where $M = 0.9$, $\omega_c = 21\omega_s$, $D = T/100$, $\theta = \frac{\pi}{3}$ and $\delta = 1$.*

re-summation method, following the approach of [34], where the output voltage of a single-phase inverter with dead time was calculated.

Previous calculations of the dead time effects on the voltage outputs of inverters are limited to a few examples, such as [27, 111]. This is partly due to the analytical difficulty of applying Black's method to determine output voltages. Using Poisson re-summation, as done here and in [34], makes calculation of the voltage outputs with dead time effects less complicated.

In this chapter, we have shown that the dead time effects on the voltage outputs of a single-phase, two-phase and three-phase inverter are identical. Insertion of dead time generates low-frequency distortion in the output voltages of single-phase, two-phase and three-phase inverters, which has been shown previously by experimental and simulated spectra in [25, 27, 29, 34, 64, 78, 93, 111]. The amplitude of the distortion generated by insertion of dead time was found to have a linear relationship with the length of the dead time. In multi-phase inverters, we ascertained that the ratio ω_c/ω_s affects which frequencies contribute to frequency spectra for the load voltages. Specifically, in a two-phase inverter, if ω_c is an even multiple of ω_s, only odd frequencies contribute to the spectrum. Similarly, in a three-phase inverter, if ω_c is a multiple of $3\omega_s$, frequencies that are a multiple of 3 do not contribute to the spectrum.

Input currents have never been calculated analytically for inverters with dead time. In the next chapter we extend our analysis of inverters that incorporate dead time, and calculate the input currents of a single-phase inverter with dead time for the first time.

CURRENT SPECTRA FOR PWM INVERTERS WITH
DEAD TIME

1   Introduction

The effects of dead time on the currents of PWM inverters is documented in [16, 24, 26, 97], for example. These effects have never been calculated analytically, however, due to the algebraic complexity of modelling a PWM inverter with dead time. In this chapter we address this issue, and calculate, for the first time, the input current spectra for an inverter with dead time.

It is known that dead time generates components in the frequency spectrum of output currents (see [26], for example). Consequently, because the input currents are functions of the output currents, dead time also generates components in the spectrum of the input currents. Attempts to quantify the dead time effects on the currents are limited, however. In [97] the output current waveform of a two-phase inverter with dead time is simulated, and the spectrum is determined. It was observed that dead time generates low-frequency components in the spectrum of the output current. In [24] and [16] input current waveforms for three-phase PWM and SVM inverters were simulated. Analysis was purely in the time domain, and negative spikes in the input current were found to be caused by dead time (corroborated by experimental results in [16]). Theoretically, it should be possible to determine spectra from the simulated waveforms in [16, 24].

In this chapter we calculate the input currents of a single-phase inverter with dead time using the single-sum method of [31, 33]. We have also used the single-sum method previously in chapters 3 and 4 of this thesis.

1.1   Structure of Chapter

In section 2 we calculate the output currents of a single-phase inverter that incorporates dead time. We initially present calculations to determine the input currents of a single-phase inverter in section 3 for general output impedances. In section 4 we specialize the calculations of section 3

to determine the input currents of a single-phase inverter for a specific load (namely a series resistive-inductive (RL) load). In section 4 we also present and analyse input current spectra for series RL loads. Finally, in section 5, we sum up our conclusions.

2 Output Currents

In this section we determine the output current of a single-phase inverter that incorporates dead time (a single-phase inverter is illustrated in figure 5.3). Before determining the output current of a single-phase inverter, we recall the output voltage.

The voltage output of a single-phase inverter is known (see [34] and chapter 5), and we use it here to calculate a Fourier series for the output current. From section 2 of chapter 5, the voltage output, $v_a(t)$, is described, mathematically, as

$$v_a(t) = 1 - 2 \sum_m \psi(t; \mathcal{A}'_m, \mathcal{B}'_m), \tag{2.1}$$

where $\psi(t; t_1, t_2) = 1$ when $t_1 < t_2$ and is zero otherwise. The switch times $\mathcal{A}'_m$ and $\mathcal{B}'_m$ are determined by samples of a low-frequency signal wave $s_a(t) = M \cos \omega_s t$ (with amplitude $|M| \leq 0.98$, and frequency ω_s). Here, the samples of the signal wave are taken at uniform intervals to give

$$\begin{aligned}
\mathcal{A}^a_m &= mT + \frac{T}{4}(1 + s_a(mT)) + \frac{D}{2}(\delta - \Psi(mT)), \\
\mathcal{B}^a_m &= mT + \frac{T}{4}(3 - s_a(mT)) + \frac{D}{2}(\delta + \Psi(mT)),
\end{aligned} \tag{2.2}$$

where m is any integer and $T = 2\pi/\omega_c$ is the switching period (with frequency $\omega_c \gg \omega_s$), $D \ll T$ is the length of the dead time,

$$\delta = \begin{cases} 1, & \text{for delay-only dead time,} \\ 0, & \text{for delay-advance dead time.} \end{cases}$$

and

$$\Psi(t) = \begin{cases} +1, & \text{if } \theta < \omega_s t < \theta + \pi, \\ -1, & \text{if } \theta + \pi < \omega_s t < \theta + 2\pi, \end{cases}$$

where θ is the phase shift between $v_a(t)$ and the output current $i_{ad}(t)$. The Fourier series for $v_a(t)$ was calculated in section 2.2 of chapter 5, and is given by

$$v_a(t) = \sum_{mn} a'_{mn} e^{i\Omega_{mn} t},$$

where $\Omega_{mn} = m\omega_c + n\omega_s$. The Fourier coefficients are given by

$$a'_{mn} = \begin{cases} 0, & \text{if } \Omega_{mn} = 0, \\ \dfrac{2}{i\Omega_{mn}T} e^{-i\Omega_{mn}D\delta/2} S_n(\Omega_{mn}, D) \left[e^{-3i\Omega_{mn}T/4} - e^{-i\Omega_{mn}T/4}(-1)^n \right], & \text{if } \Omega_{mn} \neq 0, \end{cases} \tag{2.3}$$

where

$$S_n(\Omega_{mn}, D) = i^n J_n \left(\tfrac{1}{4}\omega MT \right) \cos \left(\tfrac{1}{2}\Omega_{mn}D \right) - \sin \left(\tfrac{1}{2}\Omega_{mn}D \right) R_n(\Omega_{mn}), \tag{2.4}$$

where

$$R_n(\Omega_{mn}) = \sum_{q \neq n} \frac{i^q}{\pi(n-q)} e^{-i(n-q)\theta} (1 - (-1)^{n-q}) J_q \left(\tfrac{1}{4} \Omega_{mn} MT \right).$$

The effects of dead time on the output voltages of an inverter are well documented; in particular, insertion of dead time causes low-frequency distortion and can reduce the magnitude of the output voltage (see [25, 29, 64, 78, 93], for example).

We now calculate the output current, $i_{ad}(t)$, of a single-phase inverter with dead time. For an inverter with general output impedance $Z(\omega)$, the voltage drop across the load is related to the current through the load in the frequency domain by

$$\hat{v}_a(\omega) = Z(\omega) \hat{i}_{ad}(\omega),$$

where $Z(\omega)$ is the output impedance, determined by the load. Therefore the output current is

$$i_{ad}(t) = \sum_{mn} i'_{mn} e^{i\Omega_{mn}t},$$

where the subscript ad denotes the load connection, and

$$i'_{mn} = \frac{a'_{mn}}{Z(\Omega_{mn})}, \tag{2.5}$$

where a'_{mn} is given in (2.3). Note that, because dead time generates significant low-frequency distortion in the voltage outputs (see [34], for example), we expect to see significant low-frequency distortion in the output currents. Furthermore, in [26] it is shown that dead time generates low-frequency distortion in the output currents.

In order to apply the single-sum method, we require expressions for the output currents as discrete switching functions in the time domain. To this end we follow the methodology of [33] and determine an expressions for the output current by examining the current response to a single voltage pulse. Following the calculations of section 2 of chapter 4, the output current of a single-phase inverter with dead time is given by

$$i_{ad}(t) = \frac{1}{Z(0)} - f_{\mathcal{A}}(t) + f_{\mathcal{B}}(t), \tag{2.6}$$

where

$$f_{\mathcal{A}}(t) = \sum_{j=1}^{N} \frac{2}{Z(\omega_j) + \omega_j Z'(\omega_j)} \sum_{m=-\infty}^{\infty} e^{i\omega_j(t-\mathcal{A}'_m)} \psi(t; \mathcal{A}'_m, \infty), \tag{2.7}$$

where ω_j denote the zeros of $\omega Z(\omega)$, for $j = 1, \ldots, N$. We note that $f_{\mathcal{B}}(t)$ is defined similarly to $f_{\mathcal{A}}(t)$.

2.1 Output Current Spectra for a Series RL load

In this section, we analyse the frequency spectrum of the output current of a single-phase inverter with a series RL load. We first determine the specific output impedance $Z(\Omega_{mn})$ for a series RL load before we plot spectra for the output current. We also plot, for comparison, spectra for the

(a) $\gamma = 10$.

(b) $\gamma = 1$.

(c) $\gamma = 0.1$.
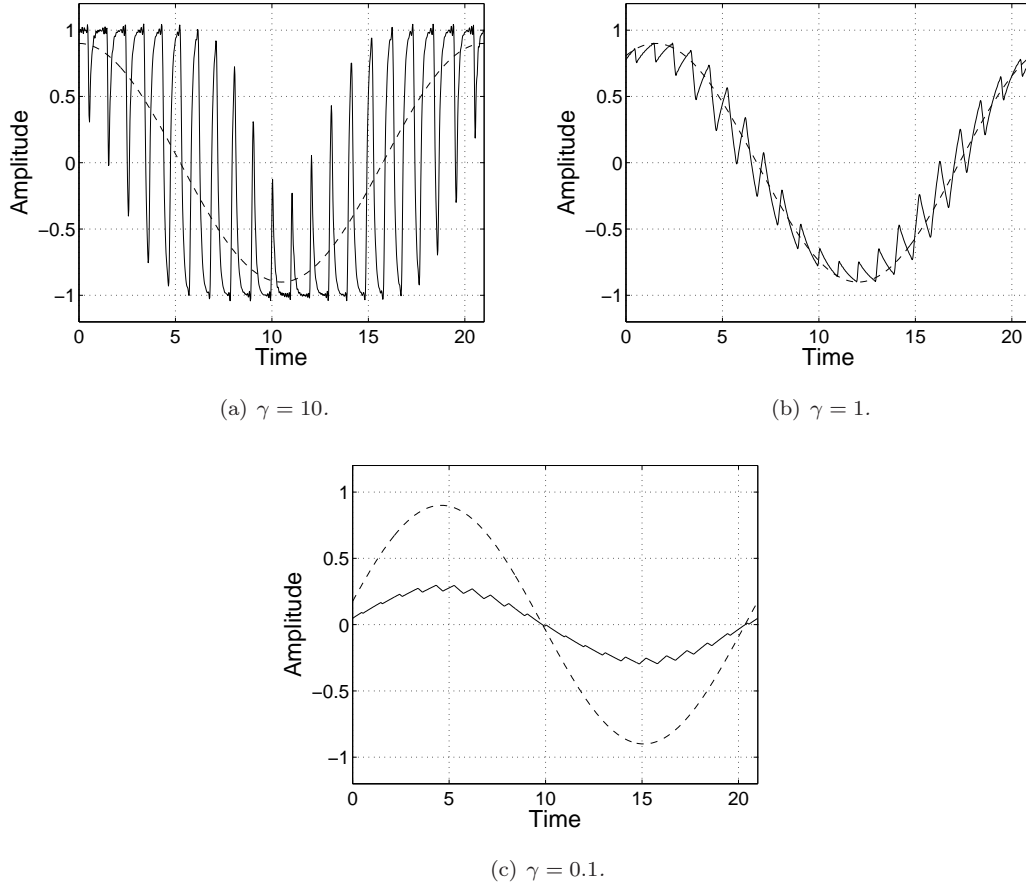
Figure 6.1: *Illustration of the output current (solid lines) for a range of output impedances, where $M = 0.9$, $\omega_c = 21\omega_s$ and $R = 1$. Furthermore, in (a), $L = 0.1$, in (b), $L = 1$, and in (c), $L = 10$. The idealised output current is indicated by dashed lines, and has been scaled to have amplitude 0.9.*

output current of a single-phase inverter without dead time (calculated in chapter 3). Note that the spectra in this section can be determined trivially from the voltage spectra in [34].

The voltage drop across a series RL load determines current in the frequency domain through

$$\hat{v}_a(\omega) = \left[R + i\omega L \right] \hat{\imath}_{ad}(\omega) \equiv Z(\omega)\hat{\imath}_{ad}(\omega). \tag{2.8}$$

Therefore the output impedance, $Z(\Omega_{mn}) = R + i\Omega_{mn}L$, determines, from (2.5),

$$i_{ad}(t) = \sum_{mn} i'_{mn}e^{i\Omega_{mn}t},$$

where,

$$i'_{mn} = \frac{a'_{mn}}{R + i\Omega_{mn}L}, \tag{2.9}$$

and a'_{mn} is given in 2.3. We now discuss some appropriate values of $\gamma = R/L$ for the assumptions that we have made in our model.

2.1.1   Appropriate γ

In previous chapters we have chosen the parameter set $\gamma = 10$, 1 and 0.1 to illustrate the effects of varying γ on current spectra. To remain consistent with previous chapters, and allow for direct comparisons of spectra (where necessary), we want to use the same parameters wherever possible. Our model for inverters with dead time assumes a highly inductive series RL load. For some values of γ we have examined previously, the load is not highly inductive. We now examine which values of γ are suitable for our dead time inverter model.

The voltage output during dead time is dependent of the polarity of the output current, so to asses the suitability of γ we examine the polarity of the actual output current compared to the polarity of our idealised output current. The idealised output current is the output current generated by the dominant low-frequency components of the voltage output (see section 2.1.1 of chapter 5). We illustrate the output current for a range of γ and the idealised output current in figure 6.1. It is evident, from figure 6.1(a), that the polarity of the output current for $\gamma = 10$ is nothing like the polarity of the idealised output current. Therefore, $\gamma = 10$ is not appropriate for the assumptions made in our model. Figures 6.1(b) and 6.1(c) show a good match between the polarity of the actual output current and the idealised output current. Consequently, $\gamma = 1$ or $\gamma = 0.1$ are appropriate parameter values for our model, and we will use these two values of γ in the current spectra we present in this chapter.

2.1.2   Analysis of the Frequency Spectrum

We now analyse the frequency spectrum of the output current of a single-phase inverter with dead time. The Fourier coefficients i'_{mn} decay slowly with respect to n, for fixed m. Therefore, every peak in the frequency spectrum of $i_{ad}(t)$ has a contribution from several carrier groups, provided $\omega_c/\omega_s \in \mathbb{Q}$. In order to plot all the significant contributions from each carrier group to the spectrum, in this section, we plot spectra with amplitude

$$\left| \sum_{k=-29}^{29} i'_{m+k,n-\omega_c k/\omega_s} \right|,$$

against harmonic number Ω_{mn}/ω_s. The sum is truncated at ± 29 because $|i'_{m\pm 29,n\mp\omega_c 29/\omega_s}| < 10^{-5}$ for all m and n.

We plot the spectrum of $i_{ad}(t)$ in figure 6.2 for $\gamma = 1$ and $\gamma = 0.1$ (as discussed in section 2.1.1). Note that, in this chapter, we omit current spectra for $\gamma \gg 1$. This is because our mathematical models for inverters with dead time assume highly inductive loads (small γ). In fact, from figure 6.2, the output current is well approximated by the low-frequency components. Specifically, the dominant low-frequency contribution to the spectrum at ω_s has amplitude at least ten times greater than the next most dominant peak (at ω_c) for the range of γ plotted here.

It is clear, from comparison of figures 6.2(a) and 6.2(b) and figures 6.2(c) and 6.2(d), that dead time generates significant high and low frequency components in the spectrum of the output voltage, compared to inverters without dead time. The presence of additional harmonic components in the output currents generated by dead time is corroborated by the results in [97].

(a) $\gamma = 0.1$ and $\theta = -\pi/2$.

(b) $\gamma = 0.1$, no dead time.

(c) $\gamma = 1$ and $\theta = -\pi/6$.

(d) $\gamma = 1$, no dead time.
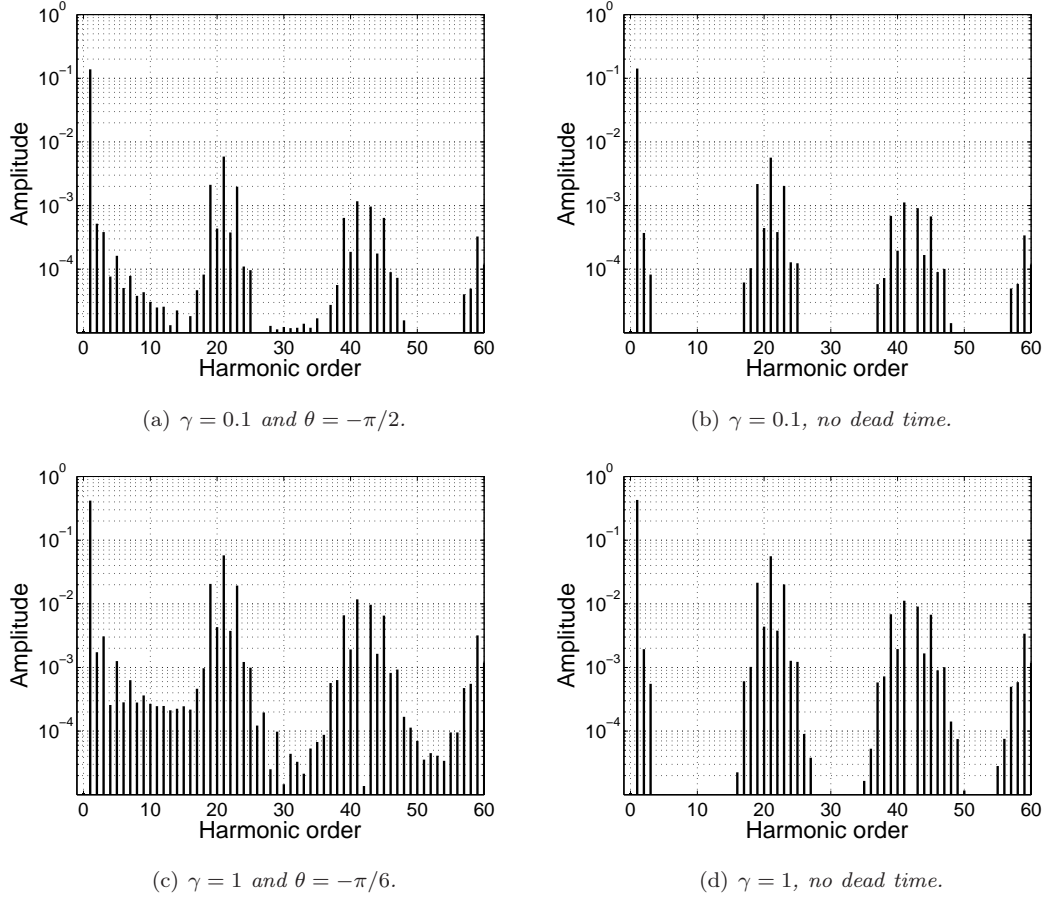
Figure 6.2: *Frequency spectrum of the output current $i_{ad}(t)$ of a single-phase inverter with a series RL load, where $M = 0.9$, $\omega_c = 21\omega_s$, $R = 1$, $D = T/100$ and $\delta = 1$. Additionally, in (a) and (b), $L = 10$, and in (c) and (d), $L = 1$.*

Dead time does not affect which frequencies have a dominant contribution to the spectrum, and the leading low-frequency contribution to the spectrum is at ω_s, and the leading high-frequency contribution to the spectrum is at ω_c. As $L \to \infty$, for fixed R, the amplitude of the high-frequency components in the spectrum is reduced (from comparison of figures 6.2(a) and 6.2(c)). Furthermore, as $L \to \infty$ with R fixed, from comparison of figures 6.2(a) and 6.2(c), the amplitude of the dead time distortion is reduced.

We define the dead time distortion of $i_{ad}(t)$ mathematically as

$$d(t) = \sum_{mn} d_{mn} e^{i\Omega_{mn}t}, \tag{2.10}$$

where

$$d_{mn} = i'_{mn} - i_{mn},$$

where i'_{mn} is given in (2.9), and i_{mn} is given in (2.6) of chapter 3. It is easily verified that $d_{mn} = 0$ when $D = 0$. When $D \neq 0$, the amplitude of the dead time distortion is linear in D, in other words, $d(t) = O(D)$ as $D \to 0$, as illustrated in figure 6.3. Note that $d(t) = O(D)$ as $D \to 0$ for all ratios ω_c/ω_s.
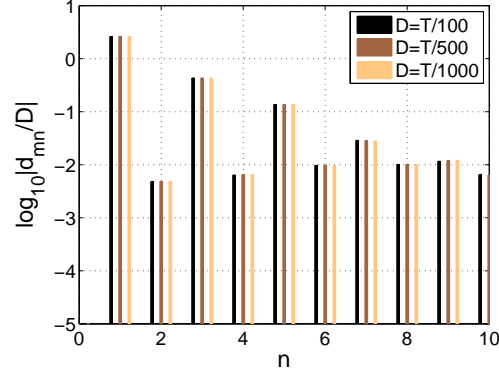
Figure 6.3: *Illustration to show the linearity of the dead time distortion of $i_{ad}(t)$ with respect to D. Here we show a section of the $m = 0$ carrier group for a range of values of D, where $M = 0.9$, $\omega_c = 21\omega_s$, $\gamma = 1$ (specifically $R = L = 1$), $\theta = -\pi/6$ and $\delta = 1$.*

3 Input Currents With General Output Impedance

In this section we calculate the input currents of a single-phase inverter with dead time and general output impedance. We use the single-sum method of [31, 33] to calculate the input currents of a single-phase inverter with dead time. This extends [34], where the output voltages were calculated. Calculation of the input currents is significantly more difficult than calculation of the output voltages. This is because calculation of the input currents requires a double consideration of the switching of the inverter.

By Kirchhoff's current law, the input current drawn from the upper DC source, $I(t)$, is equal to the output current, $i_{ad}(t)$, when the inverter switch is connected to the upper DC source, and is equal to zero when the inverter switch is connected to the lower DC source. In other words,

$$I(t) = i_{ad}(t) \sum_p \psi(t; \mathcal{B}'_p, \mathcal{A}'_{p+1}), \tag{3.1}$$

where $\mathcal{B}'_p$ and $\mathcal{A}'_{p+1}$ are defined in (2.2). Through similar reasoning, the lower input current is

$$I^-(t) = i_{ad}(t) - I(t). \tag{3.2}$$

The output current $i_{ad}(t)$ was readily determined from the output voltage (see section 2). Therefore we only need to calculate one of $I(t)$ or $I^-(t)$.

We choose to calculate $I(t)$. From (3.1) and (2.6), we write the upper input current as

$$I(t) = I_0(t) + I_{\mathcal{A}\mathcal{B}}(t),$$

where

$$I_0(t) = \frac{1}{Z(0)} \sum_p \psi(t; \mathcal{B}'_p, \mathcal{A}'_{p+1}),$$

$$I_{\mathcal{A}\mathcal{B}}(t) = (-f_{\mathcal{A}}(t) + f_{\mathcal{B}}(t)) \sum_p \psi(t; \mathcal{B}'_p, \mathcal{A}'_{p+1}),$$

where $f_{\mathcal{A}}(t)$ and $f_{\mathcal{B}}(t)$ are sum of current responses to the voltage switching from $+1$ to -1, or from -1 to $+1$, respectively, and they are given in (2.7). We now calculate each of $I_0(t)$ and $I_{\mathcal{AB}}(t)$ in turn.

It is straightforward to see that

$$I_0(t) = \frac{1}{2Z(0)}(1 + v_a(t)),$$

where the spectrum of $v_a(t)$ is known (see chapter 5). From examination of $I_{\mathcal{AB}}(t)$ and (2.7), $f_{\mathcal{A}}(t)\psi(t; \mathcal{B}_p, \mathcal{A}_{p+1})$ is nonzero only when $m \leq p$ (similarly for $f_{\mathcal{B}}(t)\psi(t; \mathcal{B}_p, \mathcal{A}_{p+1})$). Therefore

$$
\begin{aligned}
I_{\mathcal{AB}}(t) &= \sum_{j=1}^{N} \frac{2}{Z(\omega_j) + \omega_j Z'(\omega_j)} \sum_p \sum_{m=-\infty}^{p} e^{i\omega_j(t - mT - D\delta/2)} \\
&\quad \times \Bigg[e^{-i\omega_j T/4} e^{-i\omega_j(MT \cos \omega_s mT/4 - D\Psi(mT)/2)} \\
&\qquad - e^{-3i\omega_j T/4} e^{i\omega_j(MT \cos \omega_s mT/4 - D\Psi(mT)/2)} \Bigg] \psi(t; \mathcal{B}'_p, \mathcal{A}'_{p+1}).
\end{aligned}
$$

From examination of the Jacobi-Anger expansion [109],

$$
\begin{aligned}
I_{\mathcal{AB}}(t) &= \sum_{j=1}^{N} \frac{2}{Z(\omega_j) + \omega_j Z'(\omega_j)} \sum_{np} f_p^j(t) e^{-i\omega_j D\delta/2} e^{-3i\omega_j T/4} \\
&\quad \times S_n(\omega_j, D) \Big[e^{i\omega_j T/2}(-1)^n - 1 \Big] \sum_{m=-\infty}^{p} e^{i(-\omega_j + n\omega_s)mT},
\end{aligned}
$$

where $f_p^j(t) = e^{i\omega_j t}\psi(t; \mathcal{B}'_p, \mathcal{A}'_{p+1})$, and $S_n(z, D)$ is given in (2.4). The sum over m can be evaluated explicitly to be

$$\sum_{m=-\infty}^{p} e^{i(-\omega_j + n\omega_s)mT} = \frac{e^{i(-\omega_j + n\omega_s)pT}}{1 - e^{i(\omega_j - n\omega_s)T}}.$$

We now examine $f_p^j(t)$, the components of $I_{\mathcal{AB}}(t)$ that are dependent upon t. The Fourier transform of $f_p^j(t)$ determines

$$
\begin{aligned}
\hat{f}_p^j(\omega) &= \sum_q \frac{1}{i(\omega_j - \omega)} e^{i(\omega_j - \omega)(pT + D\delta/2)} e^{iq\omega_s pT} e^{3i\omega_j T/4} \\
&\quad \times S_q((\omega_j - \omega), D) \Big[e^{i\omega_j T/2 - 5i\omega T/4 + iq\omega_s T}(-1)^q - e^{-3i\omega T/4} \Big],
\end{aligned}
$$

where $S_q(z, D)$ is given in (2.4). Therefore

$$
\begin{aligned}
\hat{I}_{\mathcal{AB}}(\omega) &= \sum_{j=1}^{N} \frac{2}{Z(\omega_j) + \omega_j Z'(\omega_j)} \sum_{npq} \frac{e^{i(n+q)\omega_s pT} e^{-i\omega(pT + D\delta/2)}}{i(\omega_j - \omega)(1 - e^{i(\omega_j - n\omega_s)T})} \\
&\quad \times S_n(\omega_j, D) \Big[e^{i\omega_j T/2}(-1)^n - \Big] S_q((\omega_j - \omega), D) \\
&\quad \times \Big[e^{i\omega_j T/2 - 5i\omega T/4 + iq\omega_s T}(-1)^q - e^{-3i\omega T/4} \Big].
\end{aligned}
$$

The Poisson re-summation formula allows us to identify a Fourier series for $I_{\mathcal{AB}}(t)$. Poisson re-summing in p determines

$$
\begin{aligned}
\hat{I}_{\mathcal{AB}}(\omega) &= \sum_{j=1}^{N} \frac{2}{Z(\omega_j) + \omega_j Z'(\omega_j)} \sum_{mnq} \int_{-\infty}^{\infty} \frac{e^{-i\omega D\delta/2} e^{i\Omega_{m,n+q}t}}{i(\omega_j - \omega)(1 - e^{i(\omega_j - n\omega_s)T})T} \\
&\quad S_n(\omega_j, D)\left[e^{i\omega_j T/2}(-1)^n - \right] S_q((\omega_j - \omega), D) \\
&\quad \left[e^{i\omega_j T/2 - 5i\omega T/4 + iq\omega_s T}(-1)^q - e^{-3i\omega T/4}\right] e^{-i\omega t} \, dt.
\end{aligned}
$$

Therefore

$$
I_{\mathcal{AB}}(t) = \sum_{mn} \mathcal{J}'_{mn} e^{i\Omega_{mn}t},
$$

where

$$
\begin{aligned}
\mathcal{J}'_{mn} &= \sum_{j=1}^{N} \frac{2}{Z(\omega_j) + \omega_j Z'(\omega_j)} \sum_{q} \frac{e^{-i\Omega_{mn}D\delta/2}}{i(\omega_j - \Omega_{mn})(1 - e^{i(\omega_j - (n-q)\omega_s)T})T} \\
&\quad S_{n-q}(\omega_j, D)\left[e^{i\omega_j T/2}(-1)^{n-q} - 1\right] S_q((\omega_j - \Omega_{mn}), D) \\
&\quad \times \left[e^{i(\omega_j/2 - (5\Omega_{mn}/4 - q\omega_s))T}(-1)^q - e^{-3i\Omega_{mn}T/4}\right].
\end{aligned}
\tag{3.3}
$$

Therefore the upper input current is given by

$$
I(t) = \frac{1}{2Z(0)} + \sum_{mn} \mathcal{I}'_{mn} e^{i\Omega_{mn}t},
\tag{3.4}
$$

where

$$
\mathcal{I}'_{mn} = \frac{a'_{mn}}{2Z(0)} + \mathcal{J}'_{mn},
\tag{3.5}
$$

It is easily verified, from (3.2), that the input current drawn from the lower DC source is

$$
I^-(t) = -\frac{1}{2Z(0)} + \sum_{mn} (i'_{mn} - \mathcal{I}'_{mn}) e^{i\Omega_{mn}t}.
$$

We have now calculated a Fourier series for the input currents of a single-phase inverter with dead time and general output impedance. We can determine expressions for specific output impedances from the expressions in this section, without recourse to lengthy analytical calculations for each individual impedance.

4 Input currents for Series RL loads

In this section we determine frequency spectra for the input currents for single-phase inverters with series RL loads using the calculations in section 3. Note that we have calculated output current spectra for a series RL load in section 2.1.

We know from (2.8) that the output impedance of a series RL load is given by $Z(\omega) = R + i\omega L$. Therefore, the zeros of $\omega Z(\omega)$ occur when $\omega = 0$ and when $\omega = iR/L \equiv i\gamma$. Noting that $Z(0) = R$ and $Z(i\gamma) + i\gamma Z'(i\gamma) = -R$, we have, from (3.4),

$$
I(t) = \frac{1}{2R} + \sum_{mn} \mathcal{I}'_{mn} e^{i\Omega_{mn}t},
$$

(a) $\gamma = 0.1$ and $\theta = -\pi/2$.

(b) $\gamma = 0.1$, no dead time.

(c) $\gamma = 1$ and $\theta = -\pi/6$.

(d) $\gamma = 1$, no dead time.
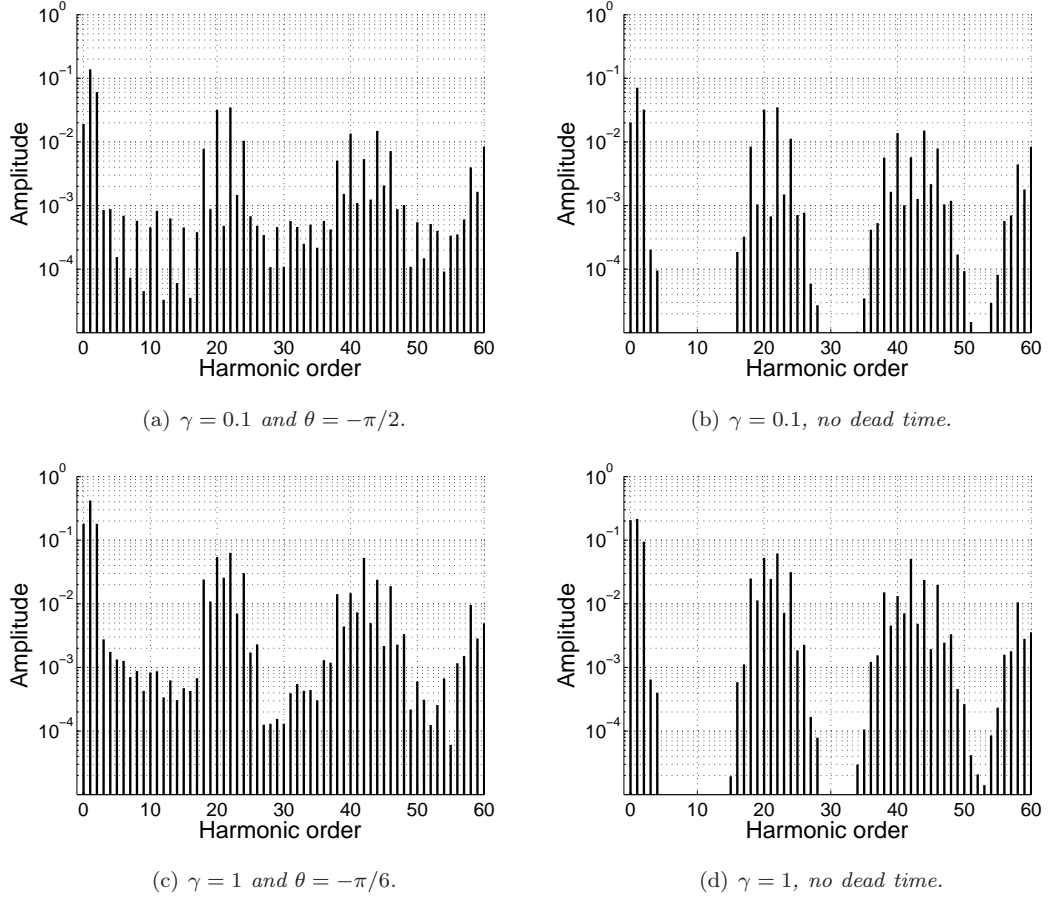
Figure 6.4: *Frequency spectra of the input current $I(t)$ of a single-phase inverter that incorporates dead-time, with a series RL load, where $M = 0.9$, $\omega_c = 21\omega_s$, $R = 1$, $D = T/100$ and $\delta = 1$. Furthermore, in (a) and (b), $L = 10$ and, in (c) and (d), $L = 1$.*

where, from (3.5) and (3.3),

$$
\begin{aligned}
\mathcal{I}'_{mn} &= \frac{a'_{mn}}{2R} - \sum_q \frac{2e^{-i\Omega_{mn}\delta D/2}}{RT(\gamma + i\Omega_{mn})(1 - e^{-(\gamma+i(n-q)\omega_s)T})} S_{n-q}(i\gamma, D)\Big[e^{-\gamma T/2}(-1)^{n-q} - 1\Big] \\
&\quad \times S_q((i\gamma - \Omega_{mn}), D)\Big[e^{-(\gamma/2+i(5\Omega_{mn}/4-q\omega_s))T}(-1)^q - e^{-3i\Omega_{mn}T/4}\Big].
\end{aligned}
\tag{4.1}
$$

The coefficients J_{mn} decay slowly with respect to n (for fixed m).

Provided $\omega_c/\omega_s \in \mathbb{Q}$, for some ratios ω_c/ω_s, several carrier groups will contribute to each peak in the frequency spectrum of $I(t)$. In order to account for all significant contributions to the spectrum (contributions with magnitude $\geq 10^{-5}$), in this section we plot amplitude

$$
\left| \sum_{k=-25}^{25} \mathcal{I}'_{m+k,n-\omega_c k/\omega_s} \right|,
$$

against the harmonic order Ω_{mn}. We illustrate the spectrum of $I(t)$ in figure 6.4 for a few different values of γ.

Figure 6.5: *Illustration to show the relationship between the dead time ripple $r(t)$ (given in (4.2)) and the dead time D. The vertical axis is the log (to the base 10) of the absolute value of the Fourier coefficients of the dead time ripple scaled by D. Here we show the $m = 0$ carrier group for a range of D, where $M = 0.9$, $\omega_c = 21\omega_s$, $\gamma = 1$ (specifically $R = L = 1$), $\theta = -\pi/3$ and $\delta = 1$.*

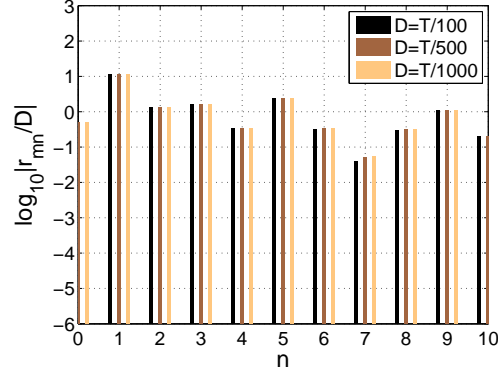As expected (see [75], for example), there is a DC component in the spectrum of the input currents. The dominant low-frequency ripple component is at ω_s, and this is also the dominant contribution to the spectrum of $I(t)$. The dominant high-frequency ripple components are at $\omega_c \pm \omega_s$. Therefore, the dominant current ripple components are the same same for inverters without dead time (by comparison of figures 6.4(a) and 6.4(b), and figures 6.4(c) and 6.4(d)). In fact, for sufficiently small D, the dominant ripple contributions must be the same for the input currents of inverters with and without dead time. For large and unrealistic D (see [78], for example), the dominant contributions might not be the same for the input currents with and without dead time.

It is evident, by comparison of figures 6.4(a) and 6.4(b), and figures 6.4(c) and 6.4(d), that insertion of dead time generates additional current ripple in the spectrum of $I(t)$ (as predicted by [24] and [16], for example). We refer to the additional current ripple as *dead time ripple*. Additionally, we describe the dead time ripple mathematically as

$$r(t) = \sum_{mn} r_{mn} e^{i\Omega_{mn}t}, \tag{4.2}$$

where

$$r_{mn} = \mathcal{I}'_{mn} - \mathcal{I}_{mn}.$$

Note that $\mathcal{I}'_{mn}$ is given in (3.3), and $\mathcal{I}_{mn}$ is given in (2.13) of chapter 3. Note that when $D = 0$, $r_{mn} = 0$ and there is no dead time ripple. When $D \neq 0$, $r_{mn} = \mathrm{O}(D)$ as $D \to 0$(as shown in figure 6.5), and this property is independent of the ratio ω_c/ω_s. Because of the algebraic complexity of the Fourier coefficients r_{mn}, we will not be investigating the relationship between r_{mn} and D any further here.

5   Conclusions

In this chapter we have determined the input currents of a single-phase inverter that incorporates dead time for the first time. We have used the single-sum method of [31, 33] to calculate the input currents. Our analysis ascertained that insertion of dead time generates low-frequency and high-frequency current ripple in the frequency spectrum of the input currents. Furthermore, the amplitude of the current ripple components has a linear relationship with the length of the dead time. The analysis in this chapter provides a progressive expansion of the analysis in [34], where the output voltage of a single-phase inverter with dead time were determined using the Poisson re-summation method.

The reason that input currents have never been calculated for inverters that incorporate dead time before is because mathematical models for inverters with dead time are significantly more complex than those for inverters without dead time. The complex mathematical models make it difficult to use Black's method to calculate the output voltages of an inverter with dead time without making approximations (see [111], for example). This means that the direct method of [40] is difficult to apply to the calculation of input currents, as it relies on using expressions for the output voltages. Black's method and the direct method constitute the standard engineering methods for calculation of output voltages and input currents, respectively.

In this chapter, we also provided calculations of the output current of a single-phase inverter with dead time, which is readily determined from the output voltage (calculated in [34]). As expected from [97], insertion of dead time generates distortion in the output current spectra, which decreases linearly as the length of the dead time decreases. Furthermore, highly inductive series RL loads have minimise the dead time distortion.

Voltage Spectra for SVM Inverters

1 Introduction

Space vector modulation (SVM) is a complex type of PWM. In this chapter we determine the voltage outputs of a SVM inverter, which extends our earlier treatment of a simpler PWM method. The complicated frequency spectra of the voltage outputs of a SVM inverter are calculated here using the Poisson re-summation method. While the spectra of the voltage outputs are known, analysis using the Poisson re-summation is more tractable than previous analysis using Black's method. In addition to this, analysis using the Poisson re-summation method identifies a course for prospective analysis using the single-sum method to calculate current spectra.

Advances in inverter technology in the 1980s introduced a widely used PWM method, known as SVM [51]. SVM is restricted to inverters with three or more phase-legs, and is ideally suited to digital implementation (see [114], for example). In [20, 22, 50] SVM inverters are shown to be advantageous due to reduced current harmonics (compared to standard PWM inverters), thus reducing electromagnetic interference (EMI).

High and low frequency distortion is generated in the frequency spectra of the voltage outputs of a SVM inverter. Black's method has been used to compute Fourier series expressions for the voltage output of a three-phase SVM inverter in [49, 77]. Additionally, papers such as [12, 19] have shown the agreement between theoretical spectra and experimental data. Here we use the Poisson re-summation of [31, 33] to calculate spectra for the voltage outputs of a three-phase SVM inverter.

1.1 Structure of Chapter

In section 2 we discuss how SVM works, as the application of SVM is significantly different to the previous PWM method examined in this thesis. We calculate the frequency spectra of the
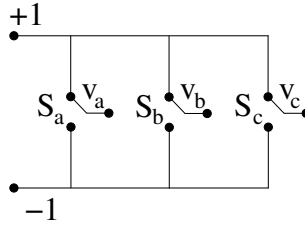
Figure 7.1: *Circuit diagram of a simplistic three-phase inverter, where there are three semiconductor based switches S_a, S_b and S_c. The output leg of each semiconductor switch is denoted V_a, V_b and V_c.*

voltage outputs of a uniformly sampled three-phase SVM inverter in section 3 using the Poisson re-summation method. In section 4, we discuss our conclusions.

2 SVM

We have already examined a three-phase inverter using one PWM technique, and here we examine a three-phase inverter that works using SVM. Similar to a three-phase inverter that uses standard PWM, the low-frequency behaviour of each voltage output, $v_a(t)$, $v_b(t)$ or $v_c(t)$, of a three-phase SVM inverter is a good approximation to the reference wave

$$r_a(t) = M \cos \omega_s t, \quad r_b(t) = M \cos(\omega_s t - 2\pi/3), \quad \text{or} \quad r_c(t) = M \cos(\omega_s t + 2\pi/3),$$

respectively. Unlike standard PWM, for a SVM inverter these reference waves are not the signal waves.

In this section we discuss the signal waves of a SVM inverter, both what they are and how they are determined. In section 2.1, we begin by discussing *space vectors*, which are representations of the switch combinations of an inverter in the complex plane. Then, in section 2.2, we discuss how the space vectors are used to determine the signal waves.

2.1 Space Vectors

In order to determine the signal waves of a three-phase SVM inverter, we begin by examining the switch state of the inverter. A simplistic three-phase inverter is illustrated in figure 7.1, where each phase-leg has just one semiconductor based switch, S_a, S_b and S_c. We denote the position of each switch by 0 or 1, where 0 indicates that the switch is attached to the lower DC source, and the voltage output is -1. Similarly, 1 indicates that the switch is connected to the upper DC source, and the voltage output is $+1$. The configuration in figure 7.1, for example, is [111]. For a three-phase inverter there are only eight possible switch combinations, given by

$$[111], \ [110], \ [101], \ [011], \ [100], \ [010], \ [001], \ [000].$$

We now follow the discussions in [49] to describe how to represent these switch combinations as space vectors.
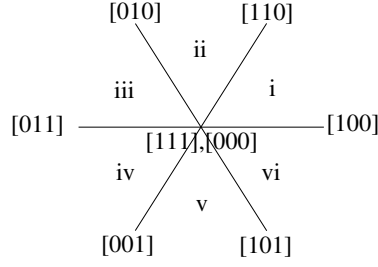
Figure 7.2: *Representation of the eight switch combinations of a three-phase inverter as space vectors.*

Any output of a three-phase inverter can be described in the complex plane by a space vector. The output space vector is given by the Clarke or Park transform (see [5, 21], for example), which tells us that

$$v_{out} = \frac{2}{3}(v_a(t) + v_b(t)e^{2\pi i/3} + v_c(t)e^{-2\pi i/3}) = Me^{i\omega_s t}.$$

From this identity, the eight switch combinations are described by

$$[111] \;\mapsto\; \frac{2}{3}(1 + e^{2\pi i/3} + e^{-2\pi i/3}) = 0,$$

$$[110] \;\mapsto\; \frac{2}{3}(1 + e^{2\pi i/3} - e^{-2\pi i/3}) = \frac{2}{3} + i\frac{1}{\sqrt{3}} = \frac{4}{3}e^{i\pi/3},$$

$$[101] \;\mapsto\; \frac{4}{3}e^{-i\pi/3},$$

$$[011] \;\mapsto\; \frac{4}{3},$$

$$[100] \;\mapsto\; \frac{4}{3},$$

$$[010] \;\mapsto\; -\frac{4}{3}e^{-i\pi/3},$$

$$[001] \;\mapsto\; -\frac{4}{3}e^{i\pi/3},$$

$$[000] \;\mapsto\; 0.$$

Note that the space vectors for [111] and [000] are both 0. From [49], we refer to these two space vectors as *null* space vectors. Similarly, the other six space vectors are called *active* space vectors. We have plotted the space vectors that represent each switch combination in figure 7.2.

2.2   Signal Wave

We now discuss how the signal wave is determined from the space vectors given in section 2.1. In order to do this, we begin by considering a target output space vector voltage $v_{tar} = Me^{i\omega_s t}$ in sector i. We can also express v_{tar} as a sum of the two nearest active space vectors, and in sector i these are the space vectors for [100] and [110] (illustrated in figure 7.2). In order to express v_{tar} in terms of the active space vectors we consider the *duty cycle* associated with each space vector (the duty cycle is the time spent in the switch combination associated with each space vector given as a fraction of the time period under consideration [49]). Let the duty cycles for each space vector be d_{100} and d_{110}.

We have

$$v_{tar} = Me^{i\omega_s t} = \frac{4}{3}d_{100} + \frac{4}{3}e^{i\pi/3}d_{110}.$$

Equating real and imaginary parts gives

$$d_{100} + d_{110}\cos\frac{\pi}{3} = \frac{3M}{4}\cos\omega_s t,$$
$$d_{110}\sin\frac{\pi}{3} = \frac{3M}{4}\sin\omega_s t.$$

Therefore,

$$d_{110} = \frac{3M\sin\omega_s t}{4\sin\frac{\pi}{3}} = \frac{\sqrt{3}M}{2}\sin\omega_s t,$$

$$d_{100} = \frac{3M}{4\sin\frac{\pi}{3}}\left(\cos\omega_s t\sin\frac{\pi}{3} - \sin\omega_s t\cos\frac{\pi}{3}\right) = \frac{3M\sin\left(\frac{\pi}{3} - \omega_s t\right)}{4\sin\frac{\pi}{3}} = \frac{\sqrt{3}M}{2}\sin\left(\frac{\pi}{3} - \omega_s t\right).$$

Note that there is a constraint on these duty cycles:

$$d_{100} + d_{110} \leq 1,$$

so that

$$\frac{\sqrt{3}M}{2}\left(\sin\omega_s t + \sin\left(\frac{\pi}{3} - \omega_s t\right)\right) \leq 0,$$
$$\sqrt{3}M\sin\frac{\pi}{6}\cos\left(\omega_s t - \frac{\pi}{6}\right) = \frac{\sqrt{3}M}{2}\cos\left(\omega_s t - \frac{\pi}{6}\right) \leq 1.$$

Hence we must have

$$M \leq \frac{2}{\sqrt{3}}.$$

This condition is satisfied by the fact that the modulation index $|M| \leq 1$ (from chapter 2).

We now consider the switching in sector i. We suppose the switching sequence

$$[111] \rightarrow [110] \rightarrow [100] \rightarrow [000] \rightarrow [100] \rightarrow [110] \rightarrow [111],$$

and, furthermore, that $d_{111} = d_{000}$. This switching sequence is illustrated in figure 7.3. Because the sum of the duty cycles is equal to 1, we have

$$d_{111} = d_{000} = \frac{1}{2}(1 - d_{110} - d_{100}),$$
$$= \frac{1}{2}\left(1 - \frac{\sqrt{3}M}{2}\cos\left(\omega_s t - \frac{\pi}{6}\right)\right).$$

Therefore, with reference to figure 7.1, the switch S_a switches from the upper DC source to the lower DC source at time

$$t = \left(n + \frac{1}{2}(d_{111} + d_{110} + d_{100})\right)T,$$
$$= nT + \frac{T}{4}\left(1 + \frac{\sqrt{3}M}{2}\cos\left(\omega_s t - \frac{\pi}{6}\right)\right),$$

where $T = 2\pi/\omega_c$ is the switching period, with frequency $\omega_c \gg \omega_s$. Similarly, S_a switches from the lower DC source to the upper DC source at time

$$t = \left(n + d_{000} + \frac{1}{2}(d_{111} + d_{110} + d_{100})\right)T,$$
$$= nT + \frac{T}{4}\left(3 - \frac{\sqrt{3}M}{2}\cos\left(\omega_s t - \frac{\pi}{6}\right)\right).$$

Figure 7.3: *A plot to show the symmetry of the switching times across one switching period for the three PWM waves $v_a(t)$, $v_b(t)$ and $v_c(t)$, in the interval $0 \leq \omega_s mT < \frac{\pi}{3}$*

We note that these are the switch times that would arise from PWM applied to a signal wave

$$\frac{\sqrt{3}M}{2} \cos\left(\omega_s t - \frac{\pi}{6}\right), \qquad \text{for} \qquad 0 \leq \omega_s t \leq \frac{\pi}{3}.$$

We now consider the switching of the inverter in sector ii.

In sector ii the switching sequence is

$$[111] \rightarrow [110] \rightarrow [010] \rightarrow [000] \rightarrow [010] \rightarrow [110] \rightarrow [111].$$

This switching sequence is shown in figure 7.4 for the voltage output $v_a(t)$. Therefore, the switch times of S_a are given by

$$
\begin{aligned}
t &= \left(n + \frac{1}{2}\left(d_{111} + d_{110}\right)\right)T, \\
&= \left(n + \frac{1}{2}\left(\frac{1}{2}\left(1 - d_{110} - d_{010}\right) + d_{110}\right)\right)T, \\
&= \left(n + \frac{1}{4}\left(1 + d_{110} - d_{010}\right)\right)T, \\
&= nT + \frac{T}{4}\left(1 + \frac{\sqrt{3}M}{2}\left(\sin\left(\frac{2\pi}{3} - \omega_s t\right) - \sin\left(\omega_s t - \frac{\pi}{3}\right)\right)\right), \\
&= nT + \frac{T}{4}\left(1 + \frac{3M}{2}\cos\omega_s t\right),
\end{aligned}
$$

and

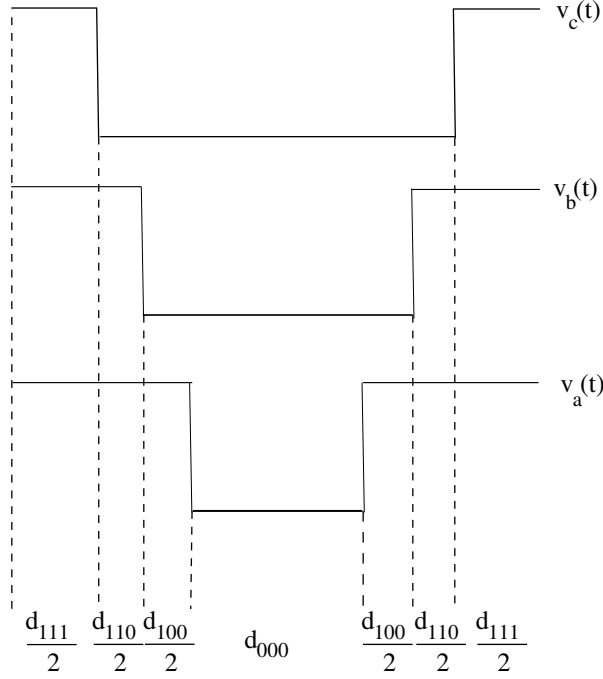$$t = nT + \frac{T}{4}\left(3 - \frac{3M}{2}\cos\omega_s t\right).$$
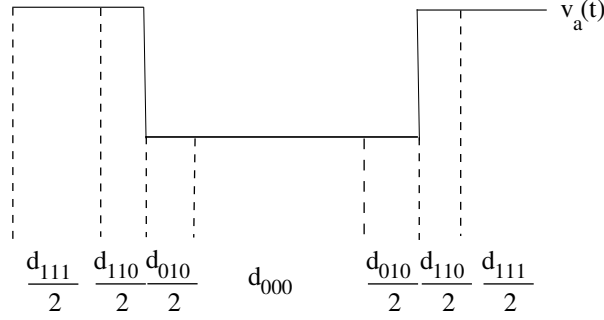
Figure 7.4: *A plot to show the symmetry of the switching times across one switching period for the three PWM waves $v_a(t)$, $v_b(t)$ and $v_c(t)$, in the interval $0 \leq \omega_s mT < \frac{\pi}{3}$*
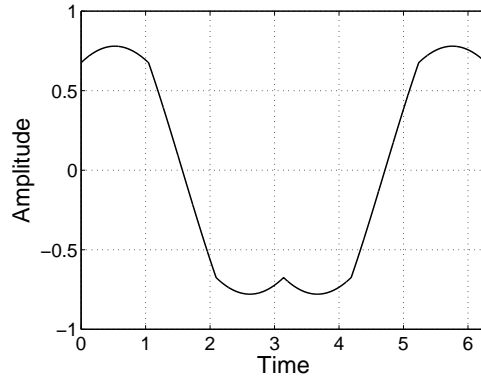
Figure 7.5: *Illustration of the signal wave $s_a(t)$ for a SVM inverter, where $M = 0.9$ and $\omega_s = 1$.*

This corresponds to PWM of a signal $\frac{3M}{2} \cos \omega_s t$ over the interval $\pi/3 \leq \omega_s t \leq 2\pi/3$.

Following a similar process for the remaining four sectors we identify a piecewise $2\pi/\omega_s$-periodic signal wave, given by

$$s_a(t) = \begin{cases} \frac{\sqrt{3}M}{2} \cos \left(\omega_s t - \frac{\pi}{6} \right), & \text{when } 0 \leq \omega_s t \leq \frac{\pi}{3} \text{ and } \pi \leq \omega_s t \leq \frac{4\pi}{3}, \\ \frac{3M}{2} \cos \omega_s t, & \text{when } \frac{\pi}{3} \leq \omega_s t \leq \frac{2\pi}{3} \text{ and } \frac{4\pi}{3} \leq \omega_s t \leq \frac{5\pi}{3}, \\ \frac{\sqrt{3}M}{2} \cos \left(\omega_s t + \frac{\pi}{6} \right), & \text{when } \frac{2\pi}{3} \leq \omega_s t \leq \pi \text{ and } \frac{5\pi}{3} \leq \omega_s t \leq 2\pi. \end{cases} \quad (2.1)$$

The signal wave $s_a(t)$ is illustrated in figure 7.5. Thus, we think of $v_a(t)$ as being determined from PWM applied to the signal wave $s_a(t)$. Similarly, $v_b(t)$ and $v_c(t)$ are determined by PWM applied to the signal waves $s_b(t) = s_a(t - 2\pi/3\omega_s)$ and $s_c(t) = s_a(t + 2\pi/3\omega_s)$, respectively. We have now identified the signal waves for a three-phase SVM inverter.

3 Voltage Outputs of SVM Inverters

We now calculate the voltage outputs, $v_a(t)$, $v_b(t)$ and $v_c(t)$ of a SVM inverter using the Poisson re-summation method. The voltage output $v_a(t)$ of a SVM inverter is described mathematically

as

$$v_a(t) = 1 - 2\sum_m \psi(t; \mathcal{A}_m^a, \mathcal{B}_m^a), \tag{3.1}$$

where $\psi(t; t_1, t_2) = 1$ when $t_1 < t_2$, and is zero otherwise. The voltage outputs $v_b(t)$ and $v_c(t)$ are defined similarly. Because SVM is more amenable to digital implementation, in this chapter we examine inverters that use uniform sampling (which is also more suited to digital implementation [66]). The switch times of $v_a(t)$, for uniform sampling, are

$$\mathcal{A}_m^a = mT + \frac{T}{4}(1 + s_a(mT)), \qquad \text{and} \qquad \mathcal{B}_m^a = mT + \frac{T}{4}(3 - s_a(mT)), \tag{3.2}$$

where m is any integer and the signal wave $s_a(t)$ is given in (2.1). The switch times of $v_b(t)$ and $v_c(t)$ are defined similarly, with respective signal waves $s_b(t) = s_a(t - 2\pi/3\omega_s)$ and $s_c(t) = s_a(t + 2\pi/3\omega_s)$.

We begin by calculating $v_a(t)$. From (3.1),

$$v_a(t) \equiv 1 - 2f(t),$$

where $f(t)$ represents the sum over m. To calculate the spectrum of $v_a(t)$, we initially determine the spectrum of $f(t)$. The Fourier transform of $f(t)$ determines, when $\omega \neq 0$,

$$\hat{f}(\omega) = \sum_m \frac{1}{i\omega}(e^{-i\omega \mathcal{A}_m^a} - e^{-i\omega \mathcal{B}_m^a}).$$

Therefore, from (3.2), when $\omega \neq 0$,

$$\hat{f}(\omega) = \sum_m \frac{e^{-i\omega nT}}{i\omega}(e^{-i\omega T/4}e^{-i\omega T s_a(mT)/4} - e^{-3i\omega T/4}e^{i\omega T s_a(mT)/4}). \tag{3.3}$$

We now determine Fourier series expression for the exponential terms $e^{\pm i\omega T s_a(mT)/4}$.

3.1 Fourier Series for $e^{i\omega T s_a(\tau)/4}$

The signal wave $s_a(\tau)$ is $2\pi/\omega_s$-periodic, therefore,

$$e^{i\omega T s_a(\tau)/4} = \sum_n S_n(\omega)e^{in\omega_s \tau},$$

where

$$\begin{aligned} S_n(\omega) &= \frac{\omega_s}{2\pi} \int_0^{2\pi/\omega_s} e^{i\omega T s_a(\tau)/4}e^{-in\omega_s \tau} \, d\tau, \\ &= \frac{\omega_s}{2\pi} \int_{-\pi/\omega_s}^{\pi/\omega_s} e^{i\omega T s_a(\tau)/4}e^{-in\omega_s \tau} \, d\tau. \end{aligned}$$

From (2.1), we have an alternative expression for $S_n(\omega)$

$$S_n(\omega) = \int_1 + \int_2 + \int_3,$$

where

$$\begin{aligned} \int_1 = \frac{\omega_s}{2\pi}\bigg[&\int_0^{\pi/3\omega_s} e^{i\omega\sqrt{3}MT\cos(\omega_s\tau-\pi/6)/8}e^{-in\omega_s\tau} \, d\tau, \\ &+ \int_{\pi/\omega_s}^{4\pi/\omega_s} e^{i\omega\sqrt{3}MT\cos(\omega_s\tau-\pi/6)/8}e^{-in\omega_s\tau} \, d\tau \bigg], \end{aligned}$$

$$\begin{aligned}
\smallint_2 &= \frac{\omega_s}{2\pi}\Bigg[\int_{\pi/3\omega_s}^{2\pi/3\omega_s} e^{i\omega 3MT\cos\omega_s\tau/8}e^{-in\omega_s\tau}\,\mathrm{d}\tau, \\
&\quad + \int_{4\pi/3\omega_s}^{5\pi/3\omega_s} e^{i\omega 3MT\cos\omega_s\tau/8}e^{-in\omega_s\tau}\,\mathrm{d}\tau\Bigg], \\
\smallint_3 &= \frac{\omega_s}{2\pi}\Bigg[\int_{2\pi/3\omega_s}^{\pi/\omega_s} e^{i\omega\sqrt{3}MT\cos(\omega_s\tau+\pi/6)/8}e^{-in\omega_s\tau}\,\mathrm{d}\tau, \\
&\quad + \int_{5\pi/3\omega_s}^{2\pi/\omega_s} e^{i\omega\sqrt{3}MT\cos(\omega_s\tau+\pi/6)/8}e^{-in\omega_s\tau}\,\mathrm{d}\tau\Bigg].
\end{aligned}$$

To evaluate these integrals, we use the Jacobi-Anger expansion [109]

$$e^{iz\cos(\theta-\theta_0)} = \sum_p J_p(z)e^{ip\theta}e^{ip(\pi/2-\theta_0)}.$$

Hence,

$$\begin{aligned}
e^{i\omega\sqrt{3}MT\cos(\omega_s\tau-\pi/6)/8} &= \sum_p J_p\left(\frac{\sqrt{3}}{8}\omega MT\right)e^{ip\omega_s\tau}e^{\pi ip/3}, \\
e^{i\omega 3MT\cos\omega_s\tau/8} &= \sum_p J_p\left(\frac{3}{8}\omega MT\right)e^{ip\omega_s\tau}e^{\pi ip/2}, \\
e^{i\omega\sqrt{3}MT\cos(\omega_s\tau+\pi/6)/8} &= \sum_p J_p\left(\frac{\sqrt{3}}{8}\omega MT\right)e^{ip\omega_s\tau}e^{2\pi ip/3}.
\end{aligned}$$

Therefore, we are able to re-write $\smallint_1$, $\smallint_2$ and $\smallint_3$ as

$$\begin{aligned}
\smallint_1 &= \sum_p J_p\left(\frac{\sqrt{3}}{8}\omega MT\right)e^{\pi ip/3}\Bigg[\int_0^{\pi/3\omega_s} e^{-i(n-p)\omega_s\tau}\,\mathrm{d}\tau \\
&\qquad\qquad\qquad\qquad\qquad + \int_{\pi/\omega_s}^{4\pi/3\omega_s} e^{-i(n-p)\omega_s\tau}\,\mathrm{d}\tau\Bigg], \qquad (3.4) \\
\smallint_2 &= \sum_p J_p\left(\frac{3}{8}\omega MT\right)e^{\pi ip/2}\Bigg[\int_{\pi/3\omega_s}^{2\pi/3\omega_s} e^{-i(n-p)\omega_s\tau}\,\mathrm{d}\tau + \int_{4\pi/3\omega_s}^{5\pi/3\omega_s} e^{-i(n-p)\omega_s\tau}\,\mathrm{d}\tau\Bigg], \\
\smallint_3 &= \sum_p J_p\left(\frac{\sqrt{3}}{8}\omega MT\right)e^{2\pi ip/3}\Bigg[\int_{2\pi/3\omega_s}^{\pi/\omega_s} e^{-i(n-p)\omega_s\tau}\,\mathrm{d}\tau + \int_{5\pi/3\omega_s}^{2\pi/\omega_s} e^{-i(n-p)\omega_s\tau}\,\mathrm{d}\tau\Bigg].
\end{aligned}$$

After evaluation of the integral in (3.4), we have that

$$\begin{aligned}
\smallint_1 &= \frac{1}{3}i^n J_n\left(\tfrac{\sqrt{3}}{8}\omega MT\right)e^{-in\pi/6} + \sum_{p\neq n}\frac{i^p}{2\pi i(n-p)}J_p\left(\tfrac{\sqrt{3}}{8}\omega MT\right)e^{-ip\pi/6} \\
&\qquad\qquad\qquad\qquad\qquad \times(1+e^{-i(n-p)\pi})(1-e^{-i(n-p)\pi/3}).
\end{aligned}$$

Finding similar expressions for $\smallint_2$ and $\smallint_3$, we determine

$$\begin{aligned}
S_n(\omega) &= \frac{i^n}{3}\Bigg[J_n\left(\tfrac{3}{8}\omega MT\right) + J_n\left(\tfrac{\sqrt{3}}{8}\omega MT\right)(e^{in\pi/6}+e^{-in\pi/6})\Bigg] \\
&\quad + \sum_{p\neq n}\frac{i^p}{2\pi i(n-p)}(1+e^{-i(n-p)\pi})(1-e^{-i(n-p)\pi/3})\Bigg[J_p\left(\tfrac{3}{8}\omega MT\right)e^{-i(n-p)\pi/3} \\
&\qquad + J_p\left(\tfrac{\sqrt{3}}{8}\omega MT\right)e^{-ip\pi/6}\left(1+e^{-2\pi in/3}\right)\Bigg]. \qquad (3.5)
\end{aligned}$$

The Fourier coefficients $S_n(\omega)$ are complex functions of ω, given in terms of sums and differences of Bessel functions. Because of the complexity of $S_n(\omega)$, it is difficult to determine the rate of decay of $S_n(\omega)$ with respect to n.

3.2 Fourier Transform

From section 3.1 and (3.3), the Fourier transform $\hat{f}(\omega)$ is given by, when $\omega \neq 0$,

$$\hat{f}(\omega) = \sum_{mn} \frac{e^{-i\omega mT}}{i\omega} e^{in\omega_s mT} S_n(\omega) \left(e^{-i\omega T/4}(-1)^n - e^{-3i\omega T/4} \right),$$

where $S_n(\omega)$ is given in (3.5). Poisson re-summing in m determines, when $\omega \neq 0$,

$$\hat{f}(\omega) = \sum_{mn} \int_{-\infty}^{\infty} \frac{e^{-i\omega t}}{i\omega T} e^{i\Omega_{mn}t} S_n(\omega) \left(e^{-i\omega T/4}(-1)^n - e^{-3i\omega T/4} \right) \mathrm{d}t.$$

Therefore, when $\Omega_{mn} \neq 0$,

$$f(t) = \sum_{mn} \frac{1}{i\Omega_{mn}T} S_n(\Omega_{mn}) \left(e^{-i\Omega_{mn}T/4}(-1)^n - e^{-3i\Omega_{mn}T/4} \right) e^{i\Omega_{mn}t},$$

where the only frequencies that have a non-zero contribution to $f(t)$ are given by $\Omega_{mn} = m\omega_c + n\omega_s$. Therefore we have determined the contribution to $v_a(t)$ for non-zero Ω_{mn}, and the contribution to $v_a(t)$ when $\Omega_{mn} = 0$ corresponds to the mean value of $v_a(t)$. The mean value of $v_a(t)$ is the mean value of

$$1 - 2\sum_m \psi(t; \mathcal{A}_m^a, \mathcal{B}_m^a),$$

which is zero (from appendix A.1). Therefore

$$v_a(t) = \sum_{mn} a_{mn} e^{i\Omega_{mn}t},$$

where

$$a_{mn} = \begin{cases} 0, & \text{if } \Omega_{mn} = 0, \\ \dfrac{2}{i\Omega_{mn}T} S_n(\Omega_{mn}) \left(e^{-i\Omega_{mn}T/4}(-1)^n - e^{-3i\Omega_{mn}T/4} \right), & \text{if } \Omega_{mn} \neq 0. \end{cases} \tag{3.6}$$

By similar reasoning, the other two voltage outputs of a three-phase SVM inverter are given by

$$v_b(t) = \sum_{mn} a_{mn} e^{-2\pi in/3} e^{i\Omega_{mn}t}, \qquad \text{and} \qquad v_c(t) = \sum_{mn} a_{mn} e^{2\pi in/3} e^{i\Omega_{mn}t},$$

where a_{mn} is given in (3.6). We note that the Fourier coefficients calculated in this chapter differ to those in [49], because our Fourier coefficients have a $1/\Omega_{mn}T$ term, rather than a $1/m\pi^2$ term. Because the Fourier coefficients with $m = 0$ in [49] are not accounted for, it is not clear whether the $1/m\pi^2$ term is a typing or algebraic error.

We also calculate the voltage differences across the three loads in a three-phase SVM inverter. In the Δ configuration a load is connected between each pair of phase-legs (as illustrated in figure 2.9), therefore,

$$\begin{aligned} v_{ab}(t) &= v_a(t) - v_b(t) = \sum_{mn} a_{mn}(1 - e^{-2\pi in/3}) e^{i\Omega_{mn}t} \equiv \sum_{mn} v_{mn} e^{i\Omega_{mn}t}, \\ v_{bc}(t) &= \sum_{mn} v_{mn} e^{-2\pi in/3} e^{i\Omega_{mn}t}, \\ v_{ca}(t) &= \sum_{mn} v_{mn} e^{2\pi in/3} e^{i\Omega_{mn}t}. \end{aligned}$$

In the Y configuration, a load is connected between each phase-leg and a floating point p. Therefore, the load voltages are, from appendix C,

$$
\begin{aligned}
v_{ap}(t) &= v_a(t) - v_p(t) = \sum_{mn} \frac{1}{3} a_{mn} (2 - e^{-2\pi in/3} - e^{2\pi in/3}) e^{i\Omega_{mn}t} \equiv \sum_{mn} v_{mn} e^{i\Omega_{mn}t}, \\
v_{bp}(t) &= \sum_{mn} v_{mn} e^{-2\pi in/3} e^{i\Omega_{mn}t}, \\
v_{cp}(t) &= \sum_{mn} v_{mn} e^{2\pi in/3} e^{i\Omega_{mn}t}.
\end{aligned}
$$

For both three-phase inverters wired in the Δ and the Y configurations, $v_{mn} = 0$ when n is a multiple of 3, a consequence of the $1 - e^{-2\pi in/3}$ or $2 - e^{-2\pi in/3} - e^{2\pi in/3}$ term. The load voltages given here reproduce those calculated in [49].

3.3   Analysis of Frequency Spectra

Before we plot any spectra for the voltage outputs, we first discuss what we plot in the frequency spectrum. Because the Fourier coefficients of the output voltages and load voltages decay slowly with respect to n (for fixed m), for some ratios ω_c/ω_s, several carrier groups contribute to each peak in the voltage spectra (provided $\omega_c/\omega_s \in \mathbb{Q}$). To ensure we account for the contribution from each carrier group, in the section we plot spectra with amplitude

$$
\left| \sum_{k=-25}^{25} a_{m+k, n-\omega_c k/\omega_s} \right|,
$$

(and similarly for v_{mn}) against harmonic number Ω_{mn}. We truncate the sum at ± 25 because, from empirical evidence, $|a_{m\pm k, n\mp\omega_c k/\omega_s}| < 10^{-5}$ and $|v_{m\pm k, n\mp\omega_c k/\omega_s}| < 10^{-5}$ for $k > 25$ for all m and n, and we only plot contributions to the spectrum with amplitude greater than 10^{-5}.

Note that, in this section we omit spectra for a range of ratios ω_c/ω_s. This is because the main features of the spectrum of the voltage outputs or the loads voltages are the same for all ω_c/ω_s.

Because we plot the absolute value of the Fourier coefficients, the voltage outputs $v_a(t)$, $v_b(t)$ and $v_c(t)$ all have identical spectra. We plot the spectra of $v_a(t)$, $v_b(t)$ and $v_c(t)$ in figure 7.6. We include the frequency spectrum of $v_a(t)$ from simulated results, to verify the accuracy of our analytical results. Carrier groups with even m have a single dominant central peak, and carrier groups with odd m have two dominant central peaks. The dominant low-frequency contribution to the spectrum is at ω_s, and the dominant high-frequency contribution to the spectrum is at ω_c. In other words, the dominant contribtuions to the spectrum for the voltage outputs of a SVM inverter are the same as those for a standard PWM inverter. Therefore, the fundamental behaviour of the voltage output of a SVM inverter is similar to the fundamental behaviour of the voltage output of a standard PWM inverter. By comparison of figures 7.6(a) and 7.6(c), the voltage output of a SVM inverter has significantly more high and low frequency components in it's spectrum, however, compared to the spectrum of the voltage output of a standard PWM inverter.

The spectra of the load voltages of a three-phase SVM inverter wired in the Δ and the Y configuration are shown in figure 7.7, where simulated spectra are included (to verify the accuracy

(a) *SVM inverter, theoretical.*

(b) *SVM inverter, simulated.*

(c) *Standard PWM inverter.*
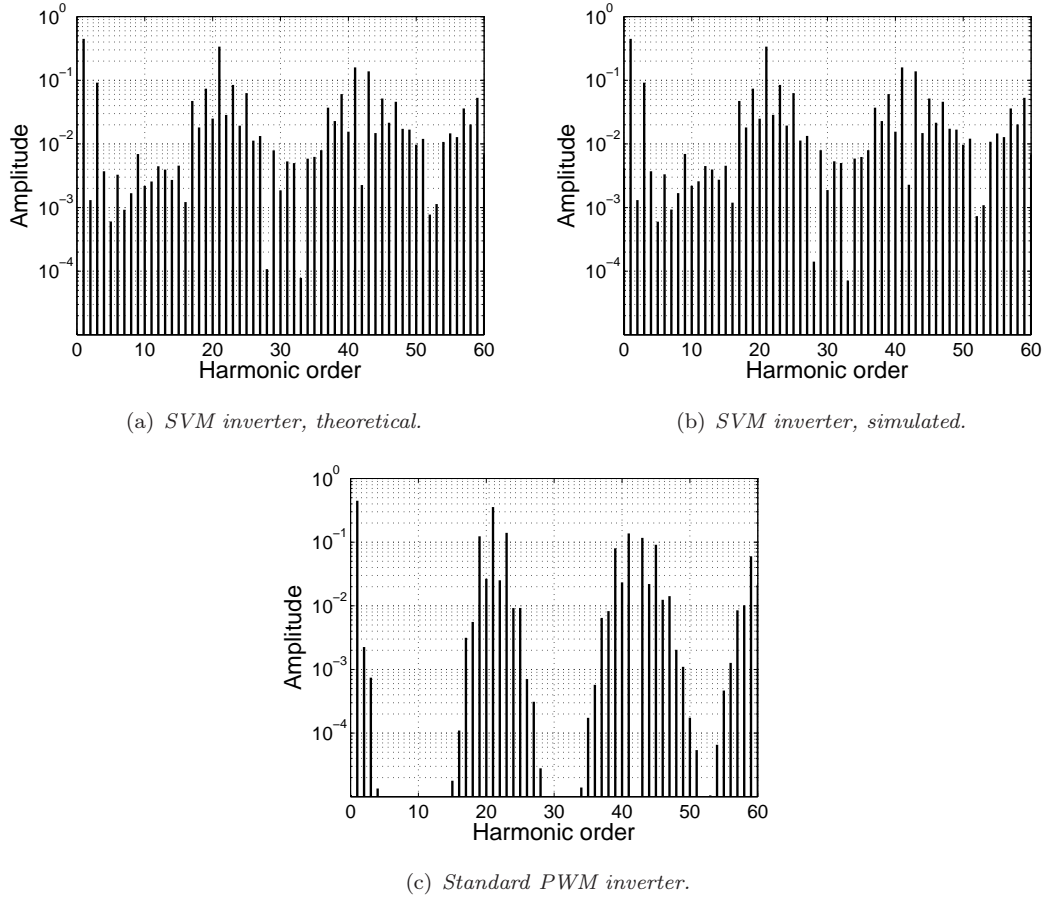
Figure 7.6: *Frequency spectrum of $v_a(t)$, $v_b(t)$ and $v_c(t)$, where $M = 0.9$.*

of our analytical results). Because ω_c is a multiple of $3\omega_s$, there is no contribution to the spectrum when n is a multiple 3. The leading contributions to the spectra of the load voltages of three-phase SVM inverters are the same as the leading contributions to the spectra of the load voltages of standard PWM inverters. SVM inverters generate load voltages with significantly more high and low frequency components in their frequency spectra than the load voltages of standard PWM inverters, however (from comparison of figures 7.7 and 2.11).

Note that, the analytical and simulated spectra in this chapter do not agree with the spectra in [49]. As mentioned in section 3.2, the Fourier coefficients calculated in [49] might contain errors. It is not obvious whether the possible errors in the Fourier coefficients have been carried into the spectra in [49], or if there is another issue (perhaps the peaks in the spectrum are not summed over enough carrier groups).

4   Conclusions

In this chapter we have determined frequency spectra for the voltage outputs and load voltages of a three-phase SVM inverter. These spectra are known, having been previously calculated using

(a) Δ *configuration, analytical*

(b) Δ *configuration, simulated*

(c) *Y configuration, analytical*

(d) *Y configuration, simulated*
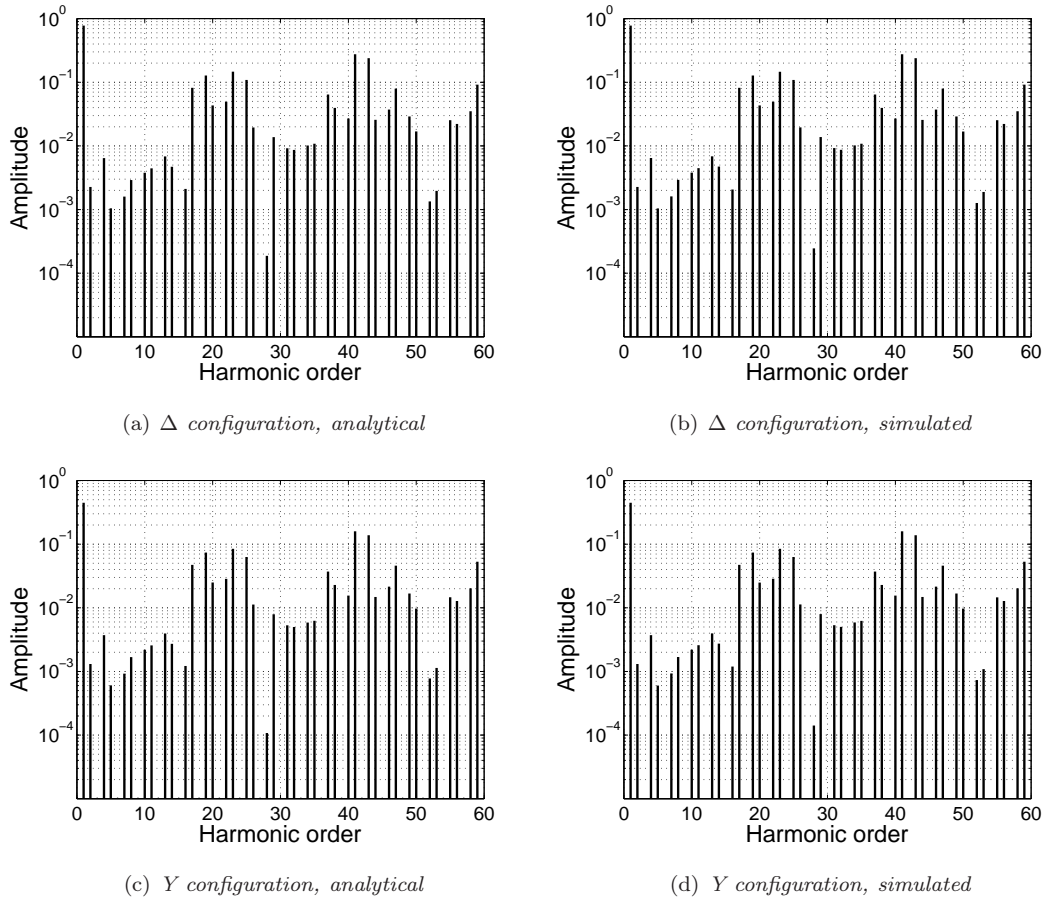
Figure 7.7: *Frequency spectrum of the load voltages of a three-phase SVM inverter, where $M = 0.9$.*

Black's method in [49] and [77]. Black's method is algebraically complex, as to calculate each Fourier coefficient a double integral is required. In this chapter, however, we have used the, more direct, Poisson re-summation method of [31, 33] to calculate spectra. It is evident, by comparison of calculations in this chapter, and calculations in [49], that the Poisson re-summation method reduces the algebraic complexity of calculating voltage spectra, thereby reducing the possibility of errors in the calculation.

Our analytical results using the Poisson re-summation method have been substantiated with Matlab simulations of the output voltages and load voltages of a three-phase SVM inverter. The analytical and simulated results conform with each other, and our results agree with [19, 77]. Our simulated results do not agree with the analytical results in [49], however.

Significant high and low frequency components are generated in the voltage outputs of a three-phase SVM inverter in comparison with a three-phase PWM inverter. It is claimed in [20, 22, 50], however, that use of SVM reduces current harmonics (thus reducing EMI, for example). The work in this chapter provides an introduction for calculations in the next chapter, where the single-sum method is used to calculate current spectra to complement the experimental results of [20, 22, 50].

Current Spectra for SVM Inverters

1 Introduction

In this chapter we determine current spectra for SVM inverters. In particular, we calculate input current spectra, which have only been calculated previously for SVM inverters with highly inductive series resistive-inductive (RL) loads. Series RL loads are a good approximation to a wide variety of loads, such as motor based loads (see [86], for example). The work in this chapter extends analysis to a greater variety of loads (highly resistive series RL loads, for example, which are widely studied [71, 86]).

The outputs of a wide variety of SVM inverters are well known analytically (see [19, 20, 22, 49, 50, 77, 89]). Analysis in [11, 20] has shown that inverters that use SVM generate output currents with more desirable ripple components compared to inverters that use standard PWM techniques. Consequently, the input currents of SVM inverters should have more desirable ripple components than the input currents of inverters that use standard PWM techniques. Input current spectra are not as well known, however.

There are a few example of simulated and analytical calculations of the input currents of SVM inverters. Input current spectra have been calculated in [60] for inverters with highly inductive series RL loads. The calculations in [60] are made feasible by approximating the output currents as sinusoidal. Additionally, input current waveforms have been simulated in [47], and it should be possible to determine spectra by taking fast Fourier transforms of the simulated waveforms. Therefore, previous calculations are either limited to highly inductive series RL loads, or give no immediate insight into the spectrum of the input currents. We address these issues in this chapter.

1.1 Structure of Chapter

In section 2 we determine output current spectra using the output voltages determined in chapter 7. We use the single-sum method of [31, 33] in section 3 to calculate the input currents of a

three-phase SVM inverter with a series RL load. We summarise the findings of this chapter in section 4.

2 Output Currents

The output currents of SVM inverters are well known in [11, 19, 20, 22, 49, 50, 77, 89]. We calculate the input currents of a SVM inverter in the next section, and we reproduce the results of [11, 20] here as an intermediate step.

To calculate output current spectra, we first recall the voltage outputs (determined in chapter 7). The voltage outputs of a three-phase SVM inverter are described as

$$v_o(t) = 1 - 2\sum_m \psi(t; \mathcal{A}_m^o, \mathcal{B}_m^o),$$

where o may represent any of the output phases, a, b, or c. The switch times of the voltage outputs are, for uniform sampling,

$$\mathcal{A}_m^o = mT + \frac{T}{4}(1 + s_o(mT)), \quad \text{and} \quad \mathcal{B}_m^o = mT + \frac{T}{4}(3 - s_o(mT)), \tag{2.1}$$

where m is any integer, $T = 2\pi/\omega_c$ is the switching period (and ω_c the switching frequency), and the signal wave $s_o(t)$ is, from section 2.2 of chapter 7,

$$s_o(t) = \begin{cases} \frac{\sqrt{3}M}{2}\cos\left(\omega_s t + \phi_o - \frac{\pi}{6}\right), & \text{when } 0 \leq \omega_s t + \phi_o \leq \frac{\pi}{3} \text{ and } \pi \leq \omega_s t + \phi_o \leq \frac{4\pi}{3}, \\ \frac{3M}{2}\cos(\omega_s t + \phi_o), & \text{when } \frac{\pi}{3} \leq \omega_s t + \phi_o \leq \frac{2\pi}{3} \text{ and } \frac{4\pi}{3} \leq \omega_s t + \phi_o \leq \frac{5\pi}{3}, \\ \frac{\sqrt{3}M}{2}\cos\left(\omega_s t + \phi_o + \frac{\pi}{6}\right), & \text{when } \frac{2\pi}{3} \leq \omega_s t + \phi_o \leq \pi \text{ and } \frac{5\pi}{3} \leq \omega_s t + \phi_o \leq 2\pi, \end{cases}$$

with frequency $\omega_s \ll \omega_c$, and phase ϕ_o (more specifically, $\phi_a = 0$, $\phi_b = -2\pi/3$ and $\phi_c = 2\pi/3$). Furthermore, we calculated, in section 3 of chapter 7, a Fourier series for the voltage outputs, given by

$$v_o(t) = \sum_{mn} a_{mn} e^{i\Omega_{mn}t} e^{in\phi_o},$$

where $\Omega_{mn} = m\omega_c + n\omega_s$, and

$$a_{mn} = \frac{2}{T}Q_n(\Omega_{mn}).$$

We introduce $Q_n(\omega)$ for later convenience, and it is defined as

$$Q_n(\omega) = \frac{1}{i\omega}S_n(\omega)((-1)^n e^{-i\omega T/4} - e^{-3i\omega T/4}), \tag{2.2}$$

where, from section 3.1 of chapter 7,

$$\begin{aligned} S_n(\omega) &= \frac{i^n}{3}\left[J_n\left(\tfrac{3}{8}\omega MT\right) + J_n\left(\tfrac{\sqrt{3}}{8}\omega MT\right)\left(e^{in\pi/6} + e^{-in\pi/6}\right)\right] \\ &\quad + \sum_{p \neq n}\frac{i^p}{2\pi i(n-p)}(1 + e^{-i(n-p)\pi})(1 - e^{-i(n-p)\pi/3})\left[J_p\left(\tfrac{3}{8}\omega MT\right)e^{-i(n-p)\pi/3}\right. \\ &\quad \left. + J_p\left(\tfrac{\sqrt{3}}{8}\omega MT\right)e^{-ip\pi/6}\left(1 + e^{-2\pi in/3}\right)\right]. \end{aligned} \tag{2.3}$$

We determine the output currents from these voltage outputs.

In this chapter we examine inverters with series RL loads. As described in [52], in the frequency domain

$$\hat{V}(\omega) = Z(\omega)\hat{I}(\omega),$$

where, for a series RL load [38, 81],

$$Z(\omega) = R + i\omega L.$$

Therefore, for a three-phase SVM inverter wired in the Δ configuration (illustrated in figure 2.9), the three output currents are

$$
\begin{aligned}
i_{ab}(t) &= \sum_{mn} i_{mn}^{\Delta} e^{i\Omega_{mn}t}, \\
i_{bc}(t) &= \sum_{mn} i_{mn}^{\Delta} e^{i\Omega_{mn}t} e^{-2\pi in/3}, \\
i_{ca}(t) &= \sum_{mn} i_{mn}^{\Delta} e^{i\Omega_{mn}t} e^{2\pi in/3},
\end{aligned}
$$

where

$$i_{mn}^{\Delta} = \frac{(1 - e^{-2\pi in/3})a_{mn}}{R + i\Omega_{mn}L}.$$

Similarly, from appendix C, the output currents of a three-phase SVM inverter wired in the Y configuration (illustrated in figure C.1) are given by

$$
\begin{aligned}
i_{ap}(t) &= \sum_{mn} i_{mn}^{Y} e^{i\Omega_{mn}t}, \\
i_{bp}(t) &= \sum_{mn} i_{mn}^{Y} e^{i\Omega_{mn}t} e^{-2\pi in/3}, \\
i_{cp}(t) &= \sum_{mn} i_{mn}^{Y} e^{i\Omega_{mn}t} e^{2\pi in/3},
\end{aligned}
$$

where

$$i_{mn}^{Y} = \frac{(2 - e^{-2\pi in/3} - e^{2\pi in/3})a_{mn}}{3(R + i\Omega_{mn}L)}.$$

Note that the $1 - e^{-2\pi in/3}$ and $2 - e^{-2\pi in/3} - e^{2\pi in/3}$ terms indicate, respectively, that i_{mn}^{Δ} and i_{mn}^{Y} are zero when n is a multiple of 3. We now analyse the frequency spectrum of the output currents of three-phase inverters wired in both the Δ and the Y configuration.

The form of the spectrum for the output currents depends on whether $\omega_c/\omega_s \in \mathbb{Q}$ or not. If $\omega_c/\omega_s \notin \mathbb{Q}$, each contribution to the spectrum at Ω_{mn} is unique. If, however $\omega_c/\omega_s \in \mathbb{Q}$, multiple choices of m and n give rise to the same Ω_{mn}. In this case we sum over all the possible contributions to the spectrum at Ω_{mn}. To ensure that all contributions to the spectrum with magnitude equal to or greater than 10^{-5} are accounted for, we plot the amplitude

$$\left| \sum_{k=-25}^{25} i_{m+k,n-\omega_c k/\omega_s}^{\Delta} \right|,$$

(and similarly for i_{mn}^{Y}) against the harmonic order Ω_{mn}/ω_s. We illustrate spectra for the output currents of three-phase inverters wired in the Δ and Y configuration in figure 8.1 for a range of ratios $\gamma = R/L$. Note that, in figure 8.1, because ω_c/ω_s is a multiple of 3, there is no contribution to the spectra for harmonic orders that are a multiple of 3.

(a) Δ *configuration, $\gamma = 1$*

(b) *Y configuration, $\gamma = 1$*

(c) Δ *configuration, $\gamma = 10$*

(d) *Y configuration, $\gamma = 10$*

(e) Δ *configuration, $\gamma = 0.1$*
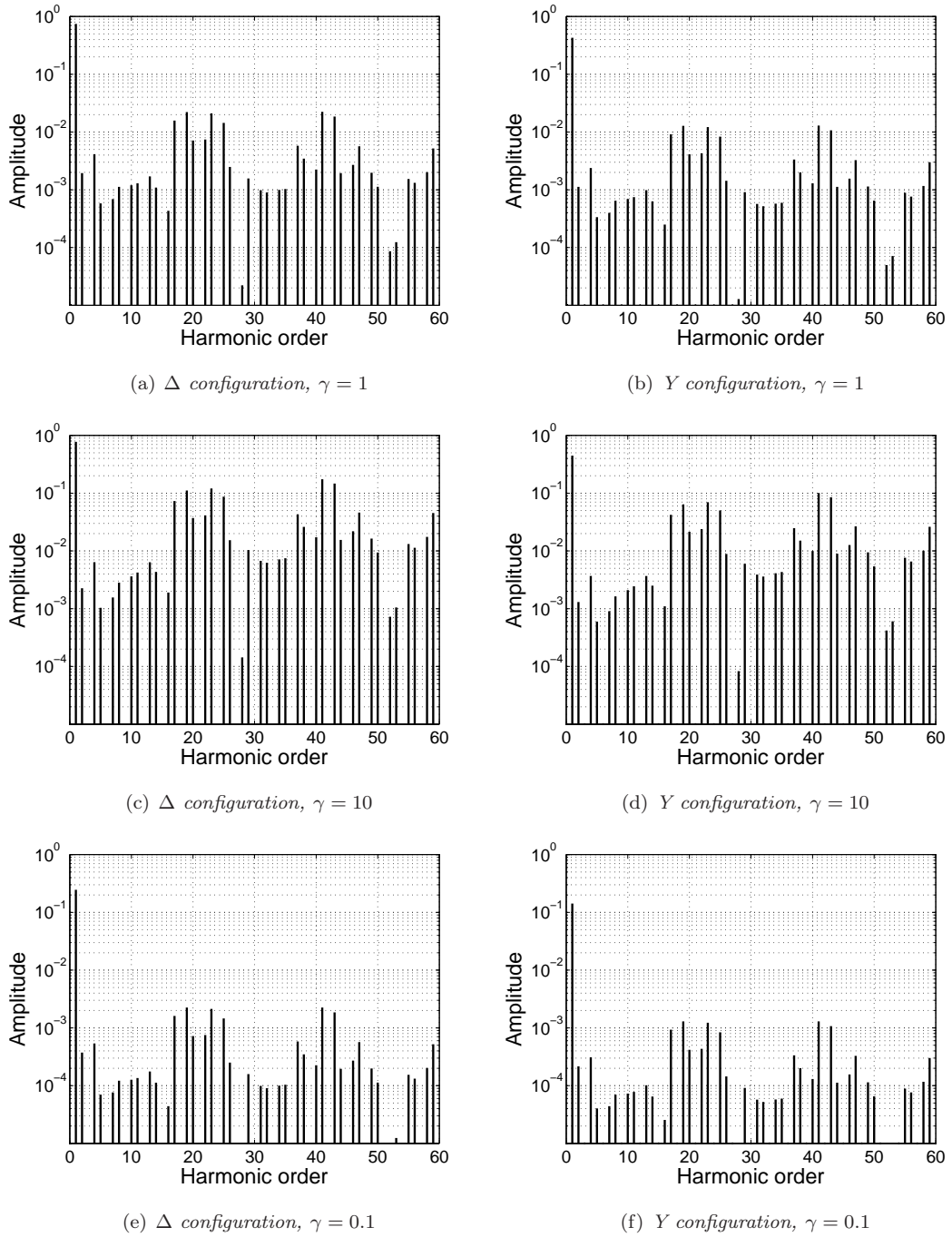
(f) *Y configuration, $\gamma = 0.1$*

Figure 8.1: *Frequency spectrum of the output currents of a three-phase SVM inverter, where $M = 0.9$, $\omega_c = 21\omega_s$ and $R = 1$. Furthermore, in (a) and (b), $L = 1$, in (c) and (d), $L = 0.1$, and in (e) and (f), $L = 10$.*

In this chapter we refer to *high-frequency* components as those with harmonic order greater than $\omega_c/2\omega_s$, and *low-frequency* components as those with harmonic order less than $\omega_c/2\omega_s$. This conforms to the precepts set out in [69].

It is evident, from comparison of figures 8.1(a), 8.1(c) and 8.1(e) with figures 8.1(b), 8.1(d) and 8.1(f), that output current spectra for a three-phase inverter wired in the Δ configuration are similar to output current spectra of a three-phase inverter wired in the Y configuration. Differences between output current spectra in the two configurations are limited to the non-dominant contributions to the spectrum. The similarity between the Δ and the Y configuration is predicted in [54], for example.

As expected from [11, 20], the dominant low-frequency contribution to the spectrum of the output currents is independent of γ, and occurs at ω_s. Similarly, the dominant high-frequency contributions to the spectrum occur at $\omega_c \pm 2\omega_s$ and at $2\omega_c \pm \omega_s$.

It was also observed in [11, 20] that as $L \to \infty$ with fixed R, the non-dominant low-frequency components and the high-frequency components in the current spectra asymptote to zero, and we provide further evidence of this here. Furthermore, we have shown that as $L \to 0$, for fixed R, the output current spectra approximate the load voltage spectra (where the magnitude of the peaks are scaled by R), as expected (see [11, 20], for example).

3 Input Currents

Although analysis of the input currents of SVM inverters with highly inductive series RL loads has been carried out previously in [60], in practice inverters with highly resistive series RL loads are important (see [71, 86], for example). In this section we extend analysis of input currents to SVM inverters with highly resistive series RL loads.

All the calculations in this section are for three-phase SVM inverters wired in the Δ configuration with series RL loads. We also assume that all load impedances are equal. Provided all loads are equal, the input current drawn from the upper DC source has identical frequency spectrum to the input current drawn from the lower DC source (see [40], for example). Therefore, in this section we calculate the upper input current only.

There are two commonly used methods for calculating the input currents: the direct method of [40], and the single-sum method of [31, 33]. We have used both of these methods previously in this thesis. As discussed in chapter 3 and [31], the direct method is algebraically simple compared to the single-sum method, but determines Fourier series with Fourier coefficients that converge slowly compared to coefficients determined using the single-sum method. Therefore, in this section, we use the single-sum method to calculate the input currents.

So far in this chapter, calculations using the single-sum method have been predominantly in the time domain. In [33], calculations using the single-sum method are performed largely in the frequency domain. Therefore, to illustrate the versatility of the single-sum method we follow the approach of [33] here. We begin by examining the input current generated by a single voltage pulse, and then superpose these input current responses in section 3.1. Then, in section 3.2, we

determine a Fourier series for the upper input current from the sum of input current responses. Finally, in section 3.3, we plot input current spectra for a range of output impedances.

3.1 Input Current Generated by a Single Voltage Pulse

In this section we determine (in the frequency domain) the upper input current by considering the input current generated by a single voltage pulse, and then superpose these input current responses. As described in [33], we begin by considering the output current generated by a single voltage pulse, and then examine the contribution to the input current from the output current response. Superposing all possible input current contributions from output current responses to a single voltage pulse will give the full input current.

A single voltage pulse is described as

$$v_m^o(t) = \psi(t; \mathcal{A}_m^o, \mathcal{B}_m^o),$$

where $o = a, b, c$ and the switch times $\mathcal{A}_m^o$ and $\mathcal{B}_m^o$ are given in (2.1). In the frequency domain, this voltage pulse is

$$\hat{v}_m^o(\omega) = \hat{\psi}(\omega; \mathcal{A}_m^o, \mathcal{B}_m^o) = \frac{2}{i\omega}[e^{-i\omega\mathcal{A}_m^a} - e^{-i\omega\mathcal{B}_m^a}]. \tag{3.1}$$

From [52], the corresponding output current is

$$\hat{i}_m^o(\omega) = \frac{1}{Z(\omega)}\hat{v}_m^o(\omega) = \frac{1}{Z(\omega)}\hat{\psi}(\omega; \mathcal{A}_m^o, \mathcal{B}_m^o),$$

where $Z(\omega) = R + i\omega L$ for a series RL load (see [38, 81], for example). Therefore, from section 2 of chapter 4, the output current response to a single voltage pulse $v_m^o(t)$ is

$$i_m^o(t) = \begin{cases} 0, & \text{if } t < \mathcal{A}_m^o, \\ \frac{1}{R}(1 - e^{-\gamma(t - \mathcal{A}_m^o)}), & \text{if } \mathcal{A}_m^o < t < \mathcal{B}_m^o, \\ \frac{1}{R}(e^{-\gamma(t - \mathcal{B}_m^o)} - e^{-\gamma(t - \mathcal{A}_m^o)}), & \text{if } t > \mathcal{B}_m^o. \end{cases}$$

In other words, the output current response to a single voltage pulse switches on at $t = \mathcal{A}_m^o$, is driven to $1/R$ in the interval $\mathcal{A}_m^o < t < \mathcal{B}_m^o$, and decays to 0 for $t > \mathcal{B}_m^o$.

If the upper input line connects to the output of phase-leg o during the interval $\mathcal{A}_p^o < t < \mathcal{B}_p^o$, then the corresponding contribution to the upper input current is

$$I_{mp}^o(t) = \psi(t; \mathcal{A}_p^o, \mathcal{B}_p^o)i_m^o(t).$$

By the convolution theorem [58], this contribution to the input current is given in the frequency domain as

$$\hat{I}_{mp}^o(\omega) = \frac{1}{2\pi}\hat{\psi}(\omega; \mathcal{A}_p^o, \mathcal{B}_p^o)\left(\frac{1}{Z(\omega)}\hat{\psi}(\omega; \mathcal{A}_m^o, \mathcal{B}_m^o)\right).$$

Writing the output impedance as

$$Z(\omega) = iL(\omega - i\gamma), \qquad \text{where} \qquad \gamma = \frac{R}{L},$$

we have, from (3.1),

$$\hat{I}_{mp}^o(\omega) = \frac{1}{\pi i}\int_{-\infty}^{\infty}\frac{(e^{-i(\omega-\omega')\mathcal{A}_p^a} - e^{-i(\omega-\omega')\mathcal{B}_p^a})(e^{-i\omega'\mathcal{A}_m^a} - e^{-i\omega'\mathcal{B}_m^a})}{L\omega'(\omega' - \omega)(\omega' - i\gamma)}\,d\omega'. \tag{3.2}$$

Note that the only true pole in (3.2) is at $\omega' = i\gamma$. As in [33], (3.2) is evaluated using residue calculus (more specifically, using contour integration and Cauchy's residue theorem [1]).

There are three cases to consider for the integral in (3.2), which depend on where the intervals $[\mathcal{A}_m^o, \mathcal{B}_m^o]$ and $[\mathcal{A}_p^o, \mathcal{B}_p^o]$ fall in relation to each other. As described in [33], the three cases are:

Case 1, $[\mathcal{A}_p^o, \mathcal{B}_p^o]$ precedes $[\mathcal{A}_m^o, \mathcal{B}_m^o]$, thus

$$\hat{I}_{mp}^o(\omega) = 0;$$

Case 2, $[\mathcal{A}_p^o, \mathcal{B}_p^o]$ follows $[\mathcal{A}_m^o, \mathcal{B}_m^o]$, thus

$$\hat{I}_{mp}^o(\omega) = \frac{1}{L}\hat{\psi}(\omega - i\gamma; \mathcal{A}_p^o, \mathcal{B}_p^o)\hat{\psi}(i\gamma; \mathcal{A}_m^o, \mathcal{B}_m^o); \tag{3.3}$$

Case 3, $[\mathcal{A}_p^o, \mathcal{B}_p^o]$ coincides with $[\mathcal{A}_m^o, \mathcal{B}_m^o]$, thus

$$\hat{I}_{mp}^o(\omega) = \frac{1}{R}\left(\hat{\psi}(\omega; \mathcal{A}_p^o, \mathcal{B}_p^o) - e^{\gamma \mathcal{A}_p^o}\hat{\psi}(\omega - i\gamma; \mathcal{A}_p^o, \mathcal{B}_p^o)\right). \tag{3.4}$$

We now obtain the upper input current by summing over all intervals $[\mathcal{A}_m^o, \mathcal{B}_m^o]$ and $[\mathcal{A}_p^o, \mathcal{B}_p^o]$ and over the three outputs a, b and c. In other words,

$$\hat{I}(\omega) = \sum_{o=a,b,c}\sum_{mp}\hat{I}_{mp}^o(\omega).$$

From the discussion above, and noting that the summand is 0 if $p < m$,

$$\hat{I}(\omega) = \hat{I}_{mm}(\omega) + \hat{I}_{m,m+r}(\omega), \tag{3.5}$$

where

$$\hat{I}_{mm}(\omega) = \sum_o\sum_m\hat{I}_{mm}^o(\omega), \tag{3.6}$$

$$\hat{I}_{m,m+r}(\omega) = \sum_o\sum_m\sum_{r=1}^{\infty}\hat{I}_{m,m+r}^o(\omega). \tag{3.7}$$

We now examine each of $\hat{I}_{mm}(\omega)$ and $\hat{I}_{m,m+r}(\omega)$ in order to determine a Fourier series for the input current $I(t)$.

3.2 Fourier Series

In the following analysis, we repeatedly encounter quantities of the form

$$\hat{\psi}(\omega; \mathcal{A}_m^o, \mathcal{B}_m^o) = e^{-i\omega mT}\sum_n Q_n^o(\omega)e^{in\omega_s mT},$$

$$= e^{-i\omega mT}\sum_n Q_n(\omega)e^{in\omega_s mT}e^{in\phi_o}, \tag{3.8}$$

where $Q_n(\omega)$ is given in (2.2). We use this identity to interpret $\hat{I}_{mm}(\omega)$ and $\hat{I}_{m,m+r}(\omega)$.

3.2.1 $\hat{I}_{mm}(\omega)$

The expression $\hat{I}_{mm}(\omega)$ is the sum of all contributions to the input current from single voltage pulses when the intervals $[\mathcal{A}_m^o, \mathcal{B}_m^o]$ coincide with the intervals $[\mathcal{A}_p^o, \mathcal{B}_p^o]$. Therefore, from (3.6) and (3.4), we have

$$\hat{I}_{mm}(\omega) \;\; = \;\; \hat{I}_1(\omega) - \hat{I}_2(\omega),$$

where

$$\hat{I}_1(\omega) \;\; = \;\; \frac{1}{R} \sum_o \sum_m \hat{\psi}(\omega; \mathcal{A}_m^o, \mathcal{B}_m^o), \tag{3.9}$$

$$\hat{I}_2(\omega) \;\; = \;\; \frac{1}{R} \sum_o \sum_m e^{\gamma \mathcal{A}_m^o} \hat{\psi}(\omega - i\gamma; \mathcal{A}_m^o, \mathcal{B}_m^o). \tag{3.10}$$

Use of the identity in (3.8) allows us to identify an alternative expression for $\hat{I}_1(\omega)$, which is, from (3.9),

$$\hat{I}_1(\omega) \;\; = \;\; \frac{1}{R} \sum_o \sum_{mn} e^{-i\omega mT} Q_n(\omega) e^{in\omega_s mT} e^{in\phi_o},$$

From use of the Poisson re-summation formula, we have

$$\hat{I}_1(\omega) \;\; = \;\; \frac{1}{R} \sum_o \sum_{mn} Q_n(\omega) e^{in\phi_o} \int_{-\infty}^{\infty} e^{2\pi i m\tau} e^{i\tau T(-\omega + n\omega_s)} \, d\tau,$$

$$= \;\; \frac{2\pi}{R} \sum_o \sum_{mn} Q_n(\omega) e^{in\phi_o} \delta(2\pi m + n\omega_s T - \omega T),$$

$$= \;\; \frac{2\pi}{RT} \sum_{mn} Q_n(\omega) \delta(\omega - \Omega_{mn}) \sum_o e^{in\phi_o}.$$

The sum over phase-legs gives

$$\sum_o e^{in\phi_o} = 1 + e^{-2\pi in/3} + e^{2\pi in/3}, \tag{3.11}$$

which is non-zero when n is a multiple of 3 only. Therefore,

$$\hat{I}_1(\omega) = \frac{6\pi}{RT} \sum_{mn} Q_{3n}(\omega) \delta(\omega - \Omega_{m,3n}).$$

We now examine $\hat{I}_2(\omega)$ in more detail.

We start our analysis of $\hat{I}_2(\omega)$ by noting that, from (2.1)

$$e^{\gamma \mathcal{A}_m^o} \;\; = \;\; e^{\gamma mT} e^{\gamma T(1 + s_o(mT))/4}.$$

Furthermore, from the analysis in section 3.1 of chapter 7,

$$e^{\gamma \mathcal{A}_m^o} \;\; = \;\; e^{\gamma T/4} e^{\gamma mT} \sum_n (-1)^n S_n(i\gamma) e^{in\omega_s mT} e^{in\phi_o},$$

where $S_n(\omega)$ is given in (2.3). We also have, from (3.8),

$$\hat{\psi}(\omega - i\gamma; \mathcal{A}_m^o, \mathcal{B}_m^o) \;\; = \;\; e^{-i\omega mT} e^{-\gamma mT} \sum_k Q_k(\omega - i\gamma) e^{ik\omega_s mT} e^{ik\phi_o}.$$

Thus, from (3.10),

$$
\begin{aligned}
\hat{I}_2(\omega) &= \frac{1}{R}\sum_o\sum_m e^{\gamma T/4}e^{-i\omega mT}\sum_n(-1)^n S_n(i\gamma)\sum_k Q_k(\omega-i\gamma)e^{i(n+k)\omega_s mT}e^{i(n+k)\phi_o}, \\
&= \frac{1}{R}\sum_o\sum_{mnk} e^{\gamma T/4}(-1)^k S_k(i\gamma)Q_{n-k}(\omega-i\gamma)e^{i(n\omega_s-\omega)mT}e^{in\phi_o}.
\end{aligned}
$$

Poisson re-summing in m determines

$$
\hat{I}_2(\omega) = \frac{2\pi}{RT}\sum_{mn}\delta(\omega-\Omega_{mn})\left[\sum_k e^{\gamma T/4}(-1)^k S_k(i\gamma)Q_{n-k}(\omega-i\gamma)\right]\sum_o e^{in\phi_o},
$$

and, from (3.11),

$$
\hat{I}_2(\omega) = \frac{6\pi}{RT}\sum_{mn}\delta(\omega-\Omega_{m,3n})\left[\sum_k e^{\gamma T/4}(-1)^k S_k(i\gamma)Q_{3n-k}(\omega-i\gamma)\right].
$$

Therefore,

$$
\hat{I}_{mm}(\omega) = \frac{6\pi}{RT}\sum_{mn}\delta(\omega-\Omega_{m,3n})\left[Q_{3n}(\omega)-\sum_k e^{\gamma T/4}(-1)^k S_k(i\gamma)Q_{3n-k}(\omega-i\gamma)\right]. \tag{3.12}
$$

Note that the the $\delta(\omega-\Omega_{m,3n})$ term indicates that the only frequencies with a non-zero contribution to $I_{mm}(t)$ are of the form $\Omega_{m,3n}$. We now examine $\hat{I}_{m,m+r}(\omega)$.

3.2.2 $\hat{I}_{m,m+r}(\omega)$

The term $\hat{I}_{m,m+r}(\omega)$ is the sum of all the contributions to the input current from single voltage pulses when the interval $[\mathcal{A}_m^o, \mathcal{B}_m^o]$ precedes the interval $[\mathcal{A}_p^o, \mathcal{B}_p^o]$. In this case, we have, from (3.7) and (3.3),

$$
\hat{I}_{m,m+r}(\omega) = \frac{1}{L}\sum_o\sum_m\sum_{r=1}^{\infty}\hat{\psi}(\omega-i\gamma;\mathcal{A}_{m+r}^o,\mathcal{B}_{m+r}^o)\hat{\psi}(i\gamma;\mathcal{A}_m^o,\mathcal{B}_m^o).
$$

From (3.8),

$$
\begin{aligned}
\hat{I}_{m,m+r}(\omega) &= \frac{1}{L}\sum_o\sum_m\sum_{r=1}^{\infty}e^{-i\omega mT}e^{-ir(\omega-i\gamma)T}\sum_{np}Q_n(\omega-i\gamma)Q_p(i\gamma)e^{in\omega_s(m+r)T} \\
&\qquad\qquad\qquad\qquad \times e^{ip\omega_s mT}e^{i(n+p)\phi_o}, \\
&= \frac{1}{L}\sum_o\sum_{mnp}\sum_{r=1}^{\infty}e^{-i(\omega-(n+p)\omega_s)mT}e^{-i(\omega-i\gamma-n\omega_s)rT}Q_n(\omega-i\gamma) \\
&\qquad\qquad\qquad\qquad \times Q_p(i\gamma)e^{i(n+p)\phi_o}, \\
&= \frac{1}{L}\sum_o\sum_{mnp}\frac{e^{-i(\omega-(n+p)\omega_s)mT}}{e^{-i(\omega-i\gamma-n\omega_s)T}-1}Q_n(\omega-i\gamma)Q_p(i\gamma)e^{i(n+p)\phi_o}, \\
&= \frac{1}{L}\sum_o\sum_{mnp}\frac{e^{-i(\omega-n\omega_s)mT}}{e^{-i(\omega-i\gamma-p\omega_s)T}-1}Q_p(\omega-i\gamma)Q_{n-p}(i\gamma)\sum_o e^{in\phi_o}.
\end{aligned}
$$

Applying the Poisson re-summation formula determines

$$
\hat{I}_{m,m+r}(\omega) = \frac{2\pi}{LT}\sum_{mn}\delta(\omega-\Omega_{mn})\left[\sum_p\frac{Q_p(\omega-i\gamma)Q_{n-p}(i\gamma)}{e^{-i(\omega-i\gamma-p\omega_s)T}-1}\right]\sum_o e^{in\phi_o}.
$$

Summing over o, we have, from (3.11),

$$\hat{I}_{m,m+r}(\omega) \quad = \quad \frac{6\pi}{LT} \sum_{mn} \delta(\omega - \Omega_{m,3n}) \left[\sum_p \frac{Q_p(\omega - i\gamma)Q_{3n-p}(i\gamma)}{e^{-i(\omega-i\gamma-p\omega_s)T} - 1} \right].$$

As for $I_{mm}(t)$, the only frequencies with a non-zero contribution to $I_{m,m+r}(t)$ are of the form $\Omega_{m,3n}$ (as indicated by the $\delta(\omega - \Omega_{m,3n})$ term in $\hat{I}_{m,m+r}(\omega)$). We now combine our expressions for $\hat{I}_{m,m+r}(\omega)$ and $\hat{I}_{mm}(\omega)$ to determine $\hat{I}(\omega)$.

3.2.3 $I(t)$

The Fourier transform of the input current drawn from the upper DC source is, from (3.5), and sections 3.2.1 and 3.2.2,

$$\hat{I}(\omega) \quad = \quad \frac{6\pi}{T} \sum_{mn} \delta(\omega - \Omega_{m,3n}) \left[\frac{1}{R} \left(Q_{3n}(\omega) - \sum_k e^{\gamma T/4}(-1)^k S_k(i\gamma)Q_{3n-k}(\omega - i\gamma) \right) \right.$$
$$\left. + \frac{1}{L} \sum_p \frac{Q_p(\omega - i\gamma)Q_{3n-p}(i\gamma)}{e^{-i(\omega-i\gamma-p\omega_s)T} - 1} \right].$$

Note that the $\delta(\omega - \Omega_{m,3n})$ term indicates that the only frequencies with a non-zero contribution to the input currents are of the form $\Omega_{m,3n}$. Therefore, the upper input current $I(t)$ has Fourier series

$$I(t) = \sum_{mn} \mathcal{I}_{m,3n} e^{i\Omega_{m,3n}t},$$

where

$$\mathcal{I}_{m,3n} \quad = \quad \frac{3}{RT} \left[Q_{3n}(\Omega_{m,3n}) - \sum_k e^{\gamma T/4}(-1)^k S_k(i\gamma)Q_{3n-k}(\Omega_{m,3n} - i\gamma) \right.$$
$$\left. + \gamma \sum_p \frac{Q_p(\Omega_{m,3n} - i\gamma)Q_{3n-p}(i\gamma)}{e^{-i(\Omega_{m,3n-p}-i\gamma)T} - 1} \right]. \qquad (3.13)$$

The evaluation of each Fourier coefficient requires two separate infinite sums over k and p. Furthermore, the $Q_n(\omega)$ and $S_n(\omega)$ terms require a further infinite sum to be evaluated.

Finally, we note that it is trivial to determine further input currents from the upper input current $I(t)$ calculated in this section. For example, the input current drawn from the lower DC source of a three-phase SVM inverter is equal to minus the upper input current (see [49], for example). Similarly, the input currents of a three-phase inverter wired in the Y configuration are equal to the input currents determined here, divided by three (see appendix C and [44], for example).

3.3 Analysis of the Frequency Spectrum

In this section we present frequency spectra for the upper input current of a three-phase SVM inverter with a series RL load. Because the Fourier coefficients of $I(t)$ decay slowly with respect to n (for fixed m), when $\omega_c/\omega_s \in \mathbb{Q}$ multiple carrier groups contribute to each peak in the frequency spectrum. We are interested in peaks with magnitude 10^{-5} and greater, therefore each peak in the spectrum is a sum over Fourier coefficients, truncated so that all contributions
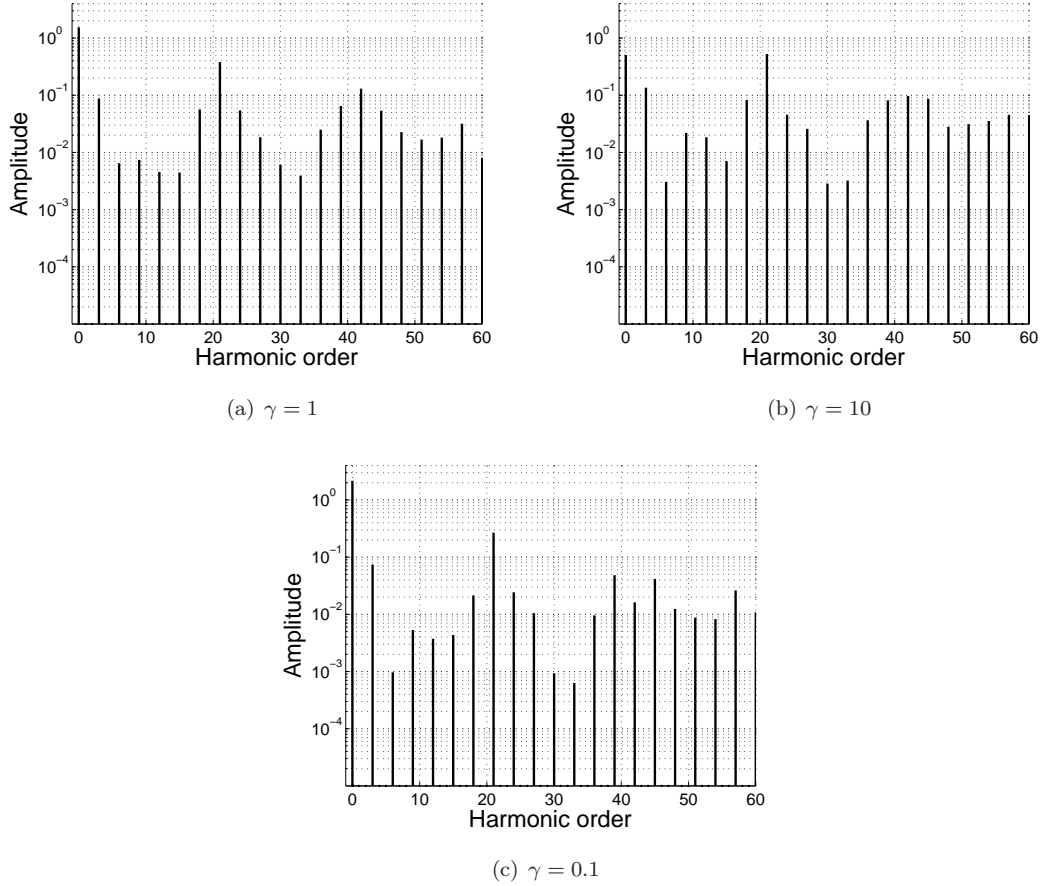
(a) $\gamma = 1$

(b) $\gamma = 10$

(c) $\gamma = 0.1$

Figure 8.2: *Frequency spectrum of the input currents of a three-phase SVM inverter wired in the Δ configuration, where $M = 0.9$, $\omega_c = 21\omega_s$ and $R = 1$. Furthermore, in (a), $L = 1$, in (b), $L = 0.1$, and in (c), $L = 10$.*

with magnitude 10^{-5} and greater are accounted for. Thus, in the spectra in this section we plot the amplitude

$$\left| \sum_{k=-25}^{25} I_{m+k,n-\omega_c k/\omega_s} \right|,$$

where I_{mn} is given in (3.13), against the harmonic order Ω_{mn}/ω_s. Because we plot spectra with $\omega_c = 21\omega_s$ (in other words $\omega_c/3\omega_s \in \mathbb{Z}$) and, from (3.13), I_{mn} is non-zero when n is a multiple of 3 only, there is contribution to the spectra when the harmonic order is a multiple of 3 only. If $\omega_c/3\omega_s \notin \mathbb{Z}$, there will be contributions at all harmonic orders. We illustrate the spectrum of $I(t)$ for a range of ratios γ in figure 8.2.

We now examine the effects of altering the impedances on the spectrum of $I(t)$. For all γ, there is a dominant DC component, as expected (see [75], for example). The DC component increases in magnitude as $L \to \infty$, for fixed R. Additionally, for all γ, the dominant low-frequency ripple component is at $3\omega_s$, and the dominant high-frequency ripple component is at ω_c. As $L \to 0$, for fixed R, the current ripple components increase in magnitude, and the peak at ω_c becomes increasingly dominant. We also note that the number of peaks in each carrier group

with magnitude 10^{-5} and greater decreases as $L \to \infty$, for fixed R.

4   Conclusions

In this chapter we have determined frequency spectra for the input current of three-phase SVM inverters with series RL loads. This work extends [60], where spectra were determined for three-phase SVM inverters with highly inductive series RL loads.

The reason calculation of input currents for SVM inverters is limited to [60] is because the mathematical models for SVM inverters are more complex than those for inverters that use standard PWM techniques. In this chapter we have used the single-sum method of [31, 33] to calculate the input currents, as it derives Fourier series for the input currents with coefficients that converge faster than the Fourier coefficients calculated using the alternative direct method [40]. We have also demonstrated the flexibility of the single-sum method in this chapter. Calculations using the single-sum method are predominantly in the frequency domain here, similar to the calculations in [33]. This is an alternative approach to the previous calculations using the single-sum method in chapters 3, 4 and 6 and in [31].

We have calculated, using the single-sum method, closed form expressions for the input currents of a three-phase inverter with a series RL load for the first time here, allowing for immediate identification of the harmonic content of the input current waveform. We demonstrated, in this chapter, that the amplitude of the current ripple components is reduced for series RL loads where the inductance is greater than the resistance.

9

Conclusions

In this thesis we have used alternative methods of Fourier analysis to those used in engineering literature to calculate closed-form expressions for the currents and voltages of various PWM inverters. Output voltages are well known (see [17–19, 31, 46, 48, 49, 77, 83, 111], for example), but there are very few examples of input current calculations (see [31, 40], for example). Our analysis fell into two main categories: use of the Poisson re-summation method to calculate output voltages, and use of the single-sum method to calculate input currents. Both the Poisson re-summation method and the single-sum method have been used previously in [31, 33], and they are used in this thesis because they are better than the standard methods used in engineering literature.

We demonstrated in chapter 2 that the Poisson re-summation method is more compact than the conventional Black's method [14], and determines identical results. The common method used to calculate input currents is the direct method, used in [40, 71, 86, 94]. The direct method is more straightforward than the algebraically complex single-sum method, but determines Fourier series for the input currents that converge slowly in comparison to those found using the single-sum method, as shown in chapter 3. Therefore, the algebraic complexity of the single-sum method is advantageous, because a practitioner plotting input current spectra from Fourier coefficients derived using the single-sum method will require less computational processing power than using coefficients found using the direct method.

While the exposition of the Poisson re-summation method and the single-sum method is of great importance in this thesis, the calculation of previously unknown (or approximated) spectra for inverters with dead time or SVM inverters is more important. The voltages and currents of inverters with dead time are generated with additional undesirable components in their spectrum, compared to inverters without dead time (see [26, 34], for example). Analysis of the additional components is limited. This is because the mathematical models for inverters with dead time are more complex than those for inverters without dead time, and consequently deriving spectra is more difficult. In particular, the voltage outputs of a two-phase PWM inverter with dead time have only been calculated by making approximations that lead to errors in the voltage spectra

in [111] previously. We have addressed this in this thesis, calculating the voltage outputs of two-phase and three-phase PWM inverters with dead time for the first time. These calculations are made feasible by the Poisson re-summation method. Furthermore, use of the single-sum method has enabled us to calculate the input currents of a single-phase PWM inverter that incorporates dead time for the very first time here. The input currents of SVM inverters have only been calculated for inverters with highly inductive series resistive-inductive (RL) loads previously [60]. We have addressed this issue in this thesis, extending analysis to a further range of series RL loads.

We now discuss our analysis using the Poisson re-summation method, which we have used in chapters 2, 5 and 7. Because the mathematical models for PWM inverters with dead time and SVM inverters are complex, we first examined PWM inverters without dead time in chapter 2 as an intermediate step to introduce the Poisson re-summation method. The voltage outputs of single-phase, two-phase and three-phase PWM inverters without dead time are well known using Black's method (see [49], for example). The relative compactness of the Poisson re-summation method was demonstrated in chapter 2 of this thesis, where the voltage outputs of single-phase, two-phase and three-phase PWM inverters were calculated using both the Poisson re-summation method and Black's method.

The theoretical results of chapter 2 have been verified with simulated spectra. The agreement between analytical spectra calculated using the Poisson re-summation method, and spectra generated by taking fast Fourier transforms of simulated voltage output waveforms is very good.

The calculations of chapter 2 presented the key steps in the Poisson re-summation method, which meant that the calculations in chapter 5 (where the Poisson re-summation method was used to calculate output voltages for inverters with dead time) could be more direct. The voltage outputs for single-phase PWM inverters with dead time have been calculated previously in [34] using the Poisson re-summation method, but in practice two-phase and three-phase inverters are more widely used (see [95], for example). Calculation of output voltages for two-phase and three-phase PWM inverters with dead time is limited. In chapter 5 we rectified this, and used the Poisson re-summation method to calculate, for the first time, the voltage outputs of two-phase and three-phase PWM inverters that incorporate dead time.

The calculations in chapter 5 are analytically complex compared to the calculations of chapters 2. Despite this complexity, however, the calculations are more compact using the Poisson re-summation compared to the algebraically involved Black's method (by comparison with calculations in [111]).

SVM inverters are also widely used, but analysis of the voltage outputs is limited to a few examples in [19, 49, 77] because the mathematical models for SVM inverters are complex compared to the mathematical models for standard PWM inverters. We demonstrated, in chapter 7, that protracted calculations using Black's method to determine the voltage outputs of a SVM inverter without dead time in [49] are significantly reduced using the Poisson re-summation method. We also derived spectra for the voltage outputs of a SVM inverter by taking fast Fourier transforms of simulated output waveforms. The agreement between analytical and simulated spectra confirmed that our calculations of voltage spectra for a three-phase SVM inverter using the Poisson

re-summation method are correct.

The output currents are readily determined from the output voltages, provided the load is known. Therefore, from the voltage outputs calculated in chapters 2, 5 and 7 for a range of PWM and SVM inverters, we have calculated the equivalent output currents in chapters 3, 6 and 8. While these are valuable results, the calculation of input currents is of greater importance.

Calculation of input currents is difficult because input currents switch between the output currents in a complex way. There are two methods used to calculate the input currents: the direct method [40], and the single-sum method [31]. In this thesis we mainly used the single-sum method, because Fourier coefficients for the input currents derived using the single-sum method converge quickly compared to coefficients derived using the direct method. The single-sum method is more algebraically complex than the direct method, however.

Previously, analysis using the single-sum method has been used to determine input current spectra for single-phase and two-phase inverters with series RL loads in [31]. In practice, analysis of three-phase inverters is important (see [50], and the references within), and we analyse the input currents of a three-phase inverter in chapter 3. Specifically, we calculated the input currents of a three-phase PWM inverter with a series RL load using the single-sum method for the first time. This substantially improves the results of [40, 86, 94], where the input currents of a three-phase PWM inverter are derived using the direct method. We also reproduced the results of [31] in chapter 3 to illustrate the key steps in the single-sum method. Furthermore, we calculated input current spectra for a single-phase PWM inverter using the direct method (reproducing calculations in [40]), in order to demonstrate the merits of both methods to a practitioner. The accuracy of the analytical results in chapter 3 has been verified by comparison with results generated by numerical simulations of the inputs of single-phase, two-phase and three-phase PWM inverters.

In chapter 4, we calculated the input currents of single-phase, two-phase and three-phase PWM inverters with general output impedance. This generalises the results of [31, 40, 86, 94]. Additionally, spectra for input currents for PWM inverters with a specific output impedance can be readily determined from the calculations of chapter 4. Therefore, time consuming analysis is avoided for future applications of the single-sum method for loads not examined in this thesis.

In chapter 6 we used the single sum method to calculate input currents for a PWM inverter with dead time, which built on simpler calculations in chapters 3 and 4 for PWM inverters without dead time. Specifically, in chapter 6, we determined the input currents of a single-phase PWM inverter with dead time for the first time. The dead time effects on the input currents was found to have a complex relationship with the length of the dead time for inverters with series RL loads. These results are important for the design of input filters for single-phase PWM inverters with dead time. We note that the single-sum method could be extended to calculate the input currents of two-phase and three-phase PWM inverters with dead time.

In chapter 8 we used the single-sum method to calculate input currents for three-phase SVM inverters with series RL loads. So far, the input currents of SVM inverters have only been calculated by approximating the output currents as sinusoidal (see [60], for example), and the

analytical results are limited to highly inductive series RL loads. We have addressed this here, and provided results for all series RL loads. It should also be possible to extend the calculations of chapter 8 to incorporate other load types, such as resistive only or series resistive-inductive-capacitive (RLC) loads (see [33, 105], for example).

There are a wide range of other PWM inverter designs that have not been considered in the scope of our research. For these inverter designs, use of the Poisson re-summation method and the single-sum method could potentially determine previously unknown spectra, or reduce the algebraic complexity of previous calculations. For example, in [83], output voltage spectra for a PWM inverter with a multiple-frequency signal wave are determined using Black's method. The Poisson re-summation method would significantly reduce the algebraic complexity of the calculations in [83]. Furthermore, the single-sum method potentially allows for calculation of input current spectra for the inverter designs discussed in [83]. There are also many multi-phase PWM inverter designs that have not been examined in this thesis (we have examined two-phase and three-phase PWM inverters). In [72, 73], there are a range of multi-phase PWM inverters for which our methods could easily be applied to determine voltage spectra at a reduced analytical cost, and determine input current spectra for the first time.

SVM inverters with dead time have not yet been examined analytically, even though they are widely used [8, 108]. The effects of dead time on the output voltages of SVM inverters have been documented in [68], and use of the Poisson re-summation method could potentially determine voltage spectra to complement these findings. The effects of dead time on the input currents of SVM inverters has been examined previously in [24], however, spectra for the input currents have never been calculated analytically. It should be possible to apply the single-sum method to SVM inverters with dead time in order to determine unknown input current spectra.

In this thesis, the voltages and currents of PWM inverters that incorporate dead time were all determined with the assumption that the load is highly inductive, and with a limit on the length of the dead time. While these assumptions are entirely reasonable, the results of our analysis are limited to certain inverter designs. More analysis is required for PWM inverters that have highly resistive series RL loads and resistive only loads, for example. Calculations are also required that allow for longer dead time.

PWM is not only used to convert DC power supplies to AC supplies, it also has many other applications. Thus, research using the Poisson re-summation and single-sum method has wider applications. For example, PWM is used in high-fidelity audio amplifiers because naturally sampled PWM does not generate low-frequency distortion, and the Poisson re-summation method has been used to calculate spectra for class-D audio amplifiers (see [32], and, more recently, [113], for example).

There are other fields that use PWM, where application of the Poisson re-summation method and the single-sum method might be of interest. In [104] PWM is used in fibre optic communications because it has the benefit of being able to mix digital and analogue signals with ease. PWM devices have also been used to send neurological signals from the brain to muscles otherwise unusable due to paralysis [28]. More recently, PWM has been integral to the design of tablet PC's [9, 10] and modern mobile phones [56]. This is because PWM devices have low power loss,

and can efficiently use power from a limited battery supply.

Average Values

1 Average Value of $v_x(t)$

If we let I be the average value of $v_x(t)$, then

$$
\begin{aligned}
I &= \lim_{r \to \infty} \frac{1}{2r} \int_{-r}^{r} v_x(t)\, \mathrm{d}t, \\
&= \lim_{r \to \infty} \frac{1}{2r} \int_{-r}^{r} \left(1 - 2 \sum_{m} \psi(t; \mathcal{A}_m^x, \mathcal{B}_m^x)\right) \mathrm{d}t,
\end{aligned}
$$

where $\mathcal{A}_m^x$ and $\mathcal{B}_m^x$ are defined similarly to (2.4) of chapter 2, with signal wave $s_x(t) = M \cos(\omega_s t + \phi)$, for some phase ϕ. Therefore,

$$
\begin{aligned}
I &= \lim_{N \to \infty} \frac{1}{2NT} \sum_{m=-N}^{N-1} \int_{mT}^{(m+1)T} \left(1 - 2 \sum_{n} \psi(t; \mathcal{A}_n^x, \mathcal{B}_n^x)\right) \mathrm{d}t, \\
&= \lim_{N \to \infty} \frac{1}{2NT} \sum_{m=-N}^{N-1} \int_{mT}^{(m+1)T} \left(1 - 2\psi(t; \mathcal{A}_m^x, \mathcal{B}_m^x)\right) \mathrm{d}t, \\
&= \lim_{N \to \infty} \frac{1}{2NT} \sum_{m=-N}^{N-1} \left[T + 2\mathcal{A}_m^x - 2\mathcal{B}_m^x\right], \\
&= \lim_{N \to \infty} \frac{1}{2N} \sum_{m=-N}^{N-1} \left[1 - (1 - s_x(mT))\right], \\
&= \lim_{N \to \infty} \frac{1}{2N} \sum_{m=-N}^{N-1} s_x(mT). \quad\quad\quad\quad (\text{A1-1})
\end{aligned}
$$

Substituting in the expression for the signal wave, we have

$$
\begin{aligned}
\sum_{m=-N}^{N-1} s_x(mT) &= \sum_{m=-N}^{N-1} M \cos(\omega_s mT + \phi), \\
&= M \frac{\sin(\omega_s(N-1/2)T + \phi) - \sin(\omega_s(-N-1/2)T + \phi)}{2 \sin(\omega_s T/2)}, \quad (\text{A1-2})
\end{aligned}
$$

provided the denominator is not 0. Since $\sin \omega_s T/2 = \sin \pi \omega_s/\omega_c$ is always non-zero in this thesis because we assume that $\omega_c > \omega_s$ (consequently ω_s/ω_c never takes an integer value), the denominator will never be zero.

It is clear that equation (A1-2) is a real-valued bounded function in N. Therefore, from (A1-1), in the limit $N \to \infty$, $I = 0$.

2 Average Value of $v_x(t)$ Incorporating Dead Time

Similar to the previous section, we let I be the average value of $v_x(t)$, then

$$
\begin{aligned}
I &= \lim_{r \to \infty} \frac{1}{2r} \int_{-r}^{r} v_x(t) \, \mathrm{d}t, \\
&= \lim_{r \to \infty} \frac{1}{2r} \int_{-r}^{r} \left(1 - 2 \sum_m \psi(t; \mathcal{A}'_m, \mathcal{B}'_m) \right) \mathrm{d}t,
\end{aligned}
$$

where $\mathcal{A}'_m$ and $\mathcal{B}'_m$ are defined similarly to (2.7) and (2.8) of chapter 5, respectively, with signal wave $s_x(t) = M \cos(\omega_s t + \phi)$, for some phase ϕ. Therefore,

$$
\begin{aligned}
I &= \lim_{N \to \infty} \frac{1}{2NT} \sum_{m=-N}^{N-1} \frac{1}{2NT} \int_{mT}^{(m+1)T} \left(1 - 2\psi(t; \mathcal{A}'_m, \mathcal{B}'_m) \right) \mathrm{d}t, \\
&= \lim_{N \to \infty} \frac{1}{2N} \sum_{m=-N}^{N-1} (M \cos \omega_s mT + D\Psi(mT)),
\end{aligned}
$$

From the previous section, we know that

$$
\lim_{N \to \infty} \frac{1}{2N} \sum_{m=-N}^{N-1} s_x(mT) = 0.
$$

Therefore, we now examine

$$
\lim_{N \to \infty} \frac{D}{2N} \sum_{m=-N}^{N-1} \Psi(mT).
$$

Using the Poisson re-summation formula, we have

$$
\begin{aligned}
\sum_{m=-N}^{N-1} \Psi(mT) &= \frac{1}{T} \sum_{m=-N}^{N-1} \int_{-\infty}^{\infty} e^{2\pi imt/T} \Psi(t) \, \mathrm{d}t, \\
&= \frac{1}{T} \sum_{m=-N}^{N-1} \int_{-\infty}^{\infty} e^{im\omega_c t} \Psi(t) \, \mathrm{d}t.
\end{aligned}
$$

The Fourier transform of a low-frequency function ($\Psi(t)$) at a high frequency ($im\omega_c t$) is equal to zero. Thus we have

$$
I = 0,
$$

in other words, the average value of $v_x(t)$ is equal to zero.

CONVERTING BETWEEN REAL AND COMPLEX FOURIER SERIES

In this thesis we derive complex Fourier series for all of our voltage outputs and input/output currents. Engineering texts, such as [49], tend to have voltages and currents written in terms of real Fourier series, so here we record the relationship between the coefficients in real and complex Fourier series. In other words we document how to convert between a real-valued function

$$F(t) = \sum_{mn} F_{mn} e^{i\Omega_{mn}t}, \tag{B-1}$$

and

$$
\begin{aligned}
F(t) &= \frac{1}{2}A_{00} + \sum_{m=1}^{\infty}(A_{m0}\cos m\omega_c t + B_{m0}\sin m\omega_c t) \\
&\quad + \sum_{n=1}^{\infty}(A_{0n}\cos n\omega_s t + B_{0n}\sin n\omega_s t) \\
&\quad + \sum_{m=1}^{\infty}\sum_{n}{}'(A_{mn}\cos \Omega_{mn}t + B_{mn}\sin \Omega_{mn}t), \tag{B-2}
\end{aligned}
$$

where $\sum_{n}'$ is the sum over all n from $-\infty$ to ∞ except 0.

From the Fourier series written in (B-1) and (B-2) we have that (for $m > 0$, or $m = 0$ and $n > 0$)

$$F_{mn}E^{i\Omega_{mn}t} + F_{-m,-n}e^{i\Omega_{-m,-n}t} = 2\mathbb{R}e(F_{mn}e^{i\Omega_{mn}t}) = A_{mn}\cos \Omega_{mn}t + B_{mn}\sin \Omega_{mn}t.$$

It is evident from $F_{mn} = \overline{F_{-m,-n}}$ that

$$2\overline{F_{-m,-n}} = 2F_{mn} = A_{mn} - iB_{mn},$$

and $2F_{00} = A_{00}$. This concludes how to convert between equivalent real and complex Fourier series.

Equivalence of Δ and Y Wiring Configurations

In this appendix we illustrate the equivalence of the Δ and the Y wiring configuration of a three-phase inverter, following the accounts in [44]. For a three-phase inverter wired in the Y configuration, each phase-leg is connected to a floating point p by a load, as illustrated in figure C.1. By Kirchhoff's current law, if phase-leg a is connected to the upper DC source, the contribution to $I(t)$ from phase-leg a is $I_a(t) = i_{ap}(t)$, and if phase-leg a is connected to the lower DC source, $I_a(t) = 0$. In other words,

$$I_a(t) = i_{ap}(t) \sum_m \psi(t; \mathcal{B}_m^a, \mathcal{A}_{m+1}^a),$$

where $\mathcal{B}_m^a$, $\mathcal{A}_{m+1}^a$ are defined similarly to (2.4) of chapter 2 for PWM inverters, and similarly to (3.2) of chapter 7 for SVM inverters. Note that the contributions to the input current $I_b(t)$ and $I_c(t)$ from phase-leg b and c, respectively, are defined similarly to $I_a(t)$. Therefore,

$$I(t) = \sum_m \left[i_{ap}(t)\psi(t; \mathcal{B}_m^a, \mathcal{A}_{m+1}^a) + i_{bp}(t)\psi(t; \mathcal{B}_m^b, \mathcal{A}_{m+1}^b) + i_{cp}(t)\psi(t; \mathcal{B}_m^c, \mathcal{A}_{m+1}^c) \right], \qquad \text{(C-1)}$$

where $\mathcal{B}_m^b$, $\mathcal{A}_{m+1}^b$ and $\mathcal{B}_m^c$, $\mathcal{A}_{m+1}^c$ are defined similarly to $\mathcal{B}_m^a$, $\mathcal{A}_{m+1}^a$.
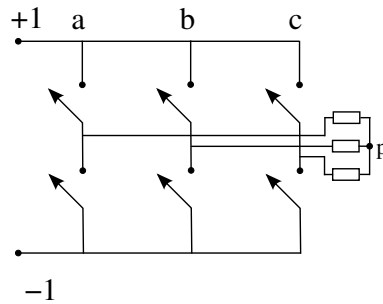

Figure C.1: *Circuit diagram of a three-phase inverter wired in the Y configuration.*

We now examine the output currents $i_{ap}(t)$, $i_{bp}(t)$, and $i_{cp}(t)$. Assuming that all load impedances are equal we have, from [52],

$$v_a(t) - v_p(t) = Zi_{ap}(t), \qquad v_b(t) - v_p(t) = Zi_{bp}(t), \qquad v_c(t) - v_p(t) = Zi_{cp}(t),$$

where Z is a differential operator, and $v_p(t)$ is the voltage of the floating point p. The sum of all the output currents is zero, in other words

$$i_{ap}(t) + i_{bp}(t) + i_{cp}(t) = 0.$$

Therefore

$$v_p(t) = \frac{1}{3}(v_a(t) + v_b(t) + v_c(t)).$$

This means that the output current $i_{ap}(t)$ can be written as

$$
\begin{aligned}
i_{ap}(t) &= Z^{-1}(v_a(t) - v_p(t)), \\
&= Z^{-1}\frac{1}{3}(2v_a(t) - v_b(t) - v_c(t)).
\end{aligned}
$$

The current generated by the voltage output $v_a(t)$ is $i_{ad}(t) = Z^{-1}v_a(t)$ (similarly for $v_b(t)$ and $v_c(t)$). Therefore, the output current $i_{ap}(t)$ is given by

$$
\begin{aligned}
i_{ap}(t) &= \frac{1}{3}(2i_{ad}(t) - i_{bd}(t) - i_{cd}(t)), \\
&= \frac{1}{3}(i_{ab}(t) - i_{ca}(t)).
\end{aligned}
$$

Similarly,

$$i_{bp}(t) = \frac{1}{3}(i_{bc}(t) - i_{ab}(t)), \qquad i_{cp}(t) = \frac{1}{3}(i_{ca}(t) - i_{bc}(t)).$$

Substituting in these equations for $i_{ap}(t)$, $i_{bp}(t)$ and $i_{cp}(t)$ we have, from (C-1),

$$I(t) = \frac{1}{3}(I_{ab}(t) + I_{bc}(t) + I_{ca}(t)),$$

where $I_{ab}(t)$ is given in (4.5) of chapter 3, and $I_{bc}(t)$, $I_{ca}(t)$ are defined similarly. Therefore, from (4.4) of chapter 3, the input currents of a three-phase inverter wired in the Y configuration are equal to a third of the input currents wired in the delta configuration, and thus have equivalent frequency spectra (subject to the appropriate scaling). More generally, a three-phase inverter wired in the Δ configuration is equivalent to a three-phase inverter wired in the Y configuration if the impedances are as those given in figure C.2.

We also note that, for a three-phase inverter wired in the Y configuration, the voltage differences across the load are given by

$$v_{ap}(t) = v_a(t) - v_p(t) = \tfrac{1}{3}\sum_{mn} a_{mn}(2 - e^{-2\pi in/3} - e^{2\pi in/3})e^{i\Omega_{mn}} \equiv \sum_{mn} v_{mn}e^{i\Omega_{mn}t},$$

$$v_{bp}(t) = \sum_{mn} v_{mn}e^{-2\pi in/3}e^{i\Omega_{mn}t}, \qquad\qquad v_{cp}(t) = \sum_{mn} v_{mn}e^{2\pi in/3}e^{i\Omega_{mn}t},$$

where a_{mn} are the Fourier coefficients of the voltage output $v_a(t)$, calculated in chapter 2 for PWM inverters without dead time, chapter 5 for PWM inverters with dead time and in chapter 7 for SVM inverters.
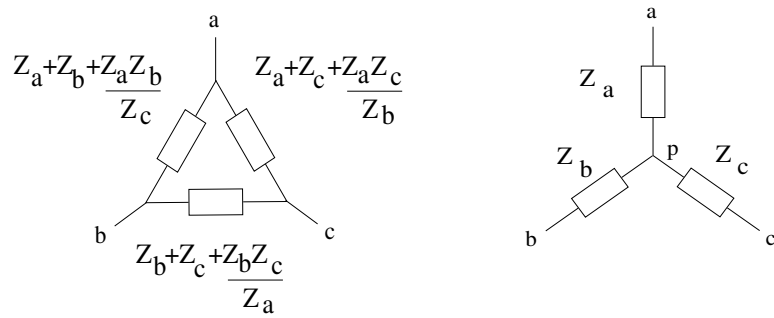
$$Z_a+Z_b+\frac{Z_aZ_b}{Z_c}$$

$$Z_a+Z_c+\frac{Z_aZ_c}{Z_b}$$

$$Z_b+Z_c+\frac{Z_bZ_c}{Z_a}$$

Figure C.2: *Circuit diagrams to illustrate the relationship between the load impedances of equivalent Δ and Y configurations.*

References

[1] M. J. Ablowitz and A. S. Fokas. *Complex Variables Introduction and Applications*, volume 2. Cambridge University Press, 2003.

[2] M. Abramowitz and I. A. Stegun. *Handbook of Mathematical Functions with Formulas, Graphs and Mathematical Tables.* New York: Dover, 1972.

[3] I. Adamson and R. Kennedy. *Sinclair and the "Sunrise" Technology.* London, Penguin Books, 1986.

[4] H. Akagi. Active harmonic filters. In *Proceedings of the IEEE*, volume 93, December 2005.

[5] J.M. Aller, A. Bueno, and T. Pagá. Power system analysis using space-vector transformation. *IEEE Trans. on Power Systems*, 17, 2002.

[6] S. W. Amos and M. James. *Principles of Transistor Circuits.* Newnes, 9th edition, 2000.

[7] T. M. Apostol. *Mathematical Analysis.* Addison-Wesley, 1974.

[8] C. Attaianese, V. Nardi, and G. Tonasso. A novel SVM strategy for VSI dead-time-effect reduction. *IEEE Trans. on Ind. Electr.*, 41:1667–1674, 2005.

[9] Y-W. Bai and H-C. Chen. Design and implementation of low-power tablet PCs. In *International Symosium on Consumer Electronics (ISCE)*, September 2011.

[10] Y-W. Bai and C-Y. Tsai. Design and implementation of a low-power workstation. In *Canadian Conference on Electrical and Computer Engineering (CCECE)*, May 2009.

[11] A. Bakhshai, G. Joos, J. Espinoza, and H. Jin. Fast space vector modulation based on a neurocomputing digital signal processor. In *Applied Power Electronics Conference and Exposition (APEC)*, February 1997.

[12] M. Bierhoff, F. W. Fuchs, and S. Pischke. Theoretical output current spectra of three phase current source converters. In *EPE on Power Electr. and Appl.*, 2005.

[13] M. H. Bierhoff and F. W. Fuchs. DC-link harmonics of three-phase voltage-source converters influenced by the pulse width-modulation strategy - an analysis. *IEEE Trans. on Ind. Elec.*, 55:2085–2092, 2008.

[14] H. S. Black. *Modulation Theory*. Van Nostrand, New York, 1953.

[15] D. Bodanis. *Electric Universe*. Abacus, 2006.

[16] S. B. Bodkhe and M. V. Aware. Robust method for stator current reconstruction from DC link in a sensorless induction motor drive. *International Journal of Engineering Science and Technology*, 2:87–99, 2010.

[17] S. R. Bowes. New sinusoidal pulsewidth-modulated inverter. *Proc. IEE*, 122(11):1279–1285, 1975.

[18] S. R. Bowes. Novel approach to the analysis and synthesis of modulation processes in power converters. *Proc. IEE*, 122(5):507–513, 1975.

[19] J. T. Boys and P. G. Handley. Harmonic analysis of space vector modulated PWM waveforms. *IEE Proc.*, 137:197–204, 1990.

[20] H. W. Van Der Broeck, H.C. Skudelny, and G. V. Stanke. Analysis and realisation of a pulsewidth modulator based on voltage space vectors. *IEE Trans. on Ind. App.*, 24:142–150, 1988.

[21] H. W. Van Der Broek, H-C. Skudelny, and G. V. Stanke. Analysis and realization of a pulsewidth modulator based on voltage space vectors. *IEEE Trans. on Ind. Applicat.*, 24, 1988.

[22] S. L. Capitaneanu, B. De Fornel, M. Fadel, J. Faucher, and A. Almeida. Graphical and algebraic synthesis for PWM methods. *EPE Journal*, 11(3), 2001.

[23] R. S Carrow. *Electrician's Technical Reference: Variable Frequency Drives*. Delmar Cengage Learning, 2000.

[24] C. C. Chan, K. T. Chan, and Y. Li. A novel dead-time vector approach to analysis of DC link current in PWM inverter drives. In *IEEE Conference and Exposition on Power Electronics*, February 1997.

[25] L. Chen and F. Z. Peng. Dead-time elimination for voltage source inverters. *IEEE Trans. on Power Electr.*, pages 574–580, 2008.

[26] L. Chenguang and S. Qiang. Study on the dead-time effection in PWM inverter control of electric vehicle's motor. In *International Conference on Power Electronics Systems and Applications (PESA)*, June 2011.

[27] F. Chierchie and E. E. Paolini. Analytical and numerical analysis of dead-time distortion in power inverters. In *Proceedings of the Argentine School of Micro-Nanoelectronics, Technology and Applications*, pages 6–11, 2010.

[28] H. J. Chizeck, P. E. Crago, and L. S. Kofman. Robust closed-loop control of isometric muscle force using pulsewidth modulation. *IEEE Trans. on Biomedical Eng.*, 35:510–517, 1988.

[29] Jung-Soo Choi, Ji-Yong Yoo, Seung-Won Lim, and Young-Seok Kim. A novel dead-time minimisation algorithm of the PWM inverter. In *Ind. App. Conf.*, volume 4, pages 2188–2193, 1999.

[30] P. Colwell. *Solving Kepler's Equation over Three Centuries*. Willman-Bell, 1993.

[31] S. M. Cox. Voltage and current spectra for a single-phase voltage-source inverter. *IMA J. App. Math.*, 74:782–805, 2009.

[32] S. M. Cox and B. H. Candy. Class-D audio amplifiers with negative feedback. *SIAM J. App. Math.*, 66:468–488, 2006.

[33] S. M. Cox and S. C. Creagh. Voltage and current spectra for matrix power converters. *SIAM J. App. Math.*, 69:1415–1437, 2009.

[34] S. M. Cox and D. C. Moore. Dead-time effects on the voltage spectrum of a PWM inverter. submitted, 2011.

[35] S. M. A. Cruz, M. Ferreira, A. M. S. Mendes, and A. J. Marques Cardoso. Analysis and diagnosis of open-circuit faults in matrix converters. *IEEE Trans. on Ind. Electr.*, 58:1648–1661, 2011.

[36] P. A. Dahono, Y. Sato, and T. Kataoka. Analysis and minimization of ripple components of input current and voltage of PWM inverters. *IEE Trans. on Ind. App.*, 32:945–950, 1996.

[37] D. M. Divan and G. Skibinski. Zero-switching-loss inverters for high-power applications. *IEEE Trans. on Ind. Appl.*, 25:634–643, 1989.

[38] K. Dobson, D. Grace, and D. Lovett. *Collins Advanced Science – Physics*. Collins Educational, 3rd edition, 2008.

[39] R. Dugan, S. Santoso, M. F. F. Mcgranaghan, and H. W. Beaty. *Electrical Power Systems Quality*. McGraw-Hill, 2nd edition, 2002.

[40] P. D. Evans and R. J. Hill-Cottingham. DC link current in PWM inverters. *IEE Proc.*, 133:217–224, 1986.

[41] G. Fedele and D. Frascino. Spectral analysis of a class of DC-AC PWM inverters by Kapteyn series. *IEEE Trans. on Power Electronics*, 25:839–849, 2010.

[42] W. M. Flanagan. *Handbook of Transformer Design and Applications*. McGraw-Hill Professional, 2nd edition, 1993.

[43] G. Franzo, M. Mazzucchelli, L. Puglisi, and G. Sciutto. Analysis of PWM techniques using uniform sampling in variable-speed electrical drives with large speed range. *IEEE Trans. on Ind. App.*, 1A-21:966–974, 2003.

[44] J. J. Grainger and W. D. Stevenson Jr. *Power System Analysis*. McGraw-Hill, 1994.

[45] D. A. Grant and R. Seiner. Ratio changing in pulse-width-modulated inverters. *IEEE Proc. on Electric Power Applications*, 128:243–248, 1981.

[46] R. A. Guinee and C. Lynden. A single Fourier series technique for the simulation and analysis of asynchronous pulse width modulation in motor drive systems. *Circuits and Sytems ISCAS*, 6:653–656, 1998.

[47] C. Guo-Qiang. A new method to building simulation model for space-vector-modulation and two-level three-phase inverter. In *International Conference on Computer Research and Development (ICCRD)*, March 2011.

[48] D. G. Holmes. A general analytical method for determining the theoretical harmonic components of carrier based PWM strategies. *Ind. App. Conf. IEEE*, 2:1207–1214, 1998.

[49] D. G. Holmes and T. A. Lipo. *Pulse Width Modulation for Power Converters*. Wiley Interscience, 2003.

[50] J. Holtz. Pulse width modulation - a survey. *IEEE Trans. on Ind. Electronics*, 39:410–420, 1992.

[51] J. Holtz and S. Stadfeld. A predictive controller for the stator current vector of AC machines fed from a switched voltage source. In *Conf. Rec. IPEC Conf.*, pages 1665–1675, 1983.

[52] P. Horowitz and W. Hill. *The Art of Electronics*, volume 2. Cambridge University Press, 1989.

[53] N. Ida. *Engineering Electromagnetics*. Springer, 2 edition, 2007.

[54] W. D. Stevenson Jr. *Elements of Power System Analysis*, volume 4. McGraw Hill Higher Education, 1982.

[55] N. Kanekawa, E. H. Ibe, T. Suga, and Y. Uematsu. *Dependibility in Electron Systems: Mitigation of Hardware Failures, Soft Errors, and Electro-Magnetic Disturbances*. Springer, 1st edition, 2010.

[56] K. Karthikeyan, J. Jaisheela, M. D. Kumar, and K. S. Kumar. Sinusoidal PWM signal generation using TMS320C6711 DSP for power control in mobile phones. In *International Conference on Process Automation, Control and Computing (PACC)*, July 2011.

[57] J. G. Kassakian, M. F. Schlecht, and G. C. Verghese. *Principles of Power Electronics*. Addison-Wesley, 1991.

[58] Y. Katznelson. *An Introduction to Harmonic Analysis*. Cambridge University Press, 3rd edition, 2004.

[59] L-H. Kim, N-K. Hahm, W-C. Lee, Y-C. Kim, C-Y. Won, and Y-R. Kim. Analysis of a new PWM method for conducted EMI reduction in a field oriented controlled induction motor. In *IEEE App. Power Electr. on Electromagnetic Compatability*, pages 204–210, 2006.

[60] J. W. Kolar and S. D. Round. Analytical calculation of the RMS current stress on the DC-link capacitor of voltage-PWM converter systems. *IEE Proc.-Electr. Power Appl.*, 153:535–543, 2006.

[61] H. J. Kuno. Rise and fall time calculations of junction transistors. *IEEE Trans. on Electron Devices*, 11:151–155, 1964.

[62] J. S. Lai and F. Z. Peng. Multilevel converters – a new breed of power converters. *IEEE Trans. on Ind. App.*, 32:509–517, 1996.

[63] D. Leggate, J. Pankau, D. Schlegel, R. Kerkman, and G. Sibinski. Reflected waves and their associated current. In *IEEE Industry Applications Society*, October 1998.

[64] Jong-Lick Lin. A new approach of dead-time compensation for PWM voltage inverters. *IEEE Trans. on Circuits and Systems*, 49:476–483, 2002.

[65] C. V. Loan. *Computational Frameworks for the Fast Fourier Transform (Frontiers in Applied Mathematics)*. Society for Industrial Mathematics, 1987.

[66] B. Lojek. *History of Semiconductor Engineering*. Springer, 2007.

[67] J. Luszcz and K. Iwan. Conducted EMI propogation in inverter-fed AC motor. *Electr. Power Quality and Utilisation*, 2:47–51, 2006.

[68] X. Mao, R. Ayyanar, and A. K. Jain. Dead time effect in two-level space vector PWM voltage source inverters with large current ripple. In *Twenty-Sixth Annual IEEE Applied Power Electronics Conference and Exposition (APEC)*, March 2011.

[69] M. Margaliot and G. Weiss. The low-frequency distortion in D-class amplifiers. *IEEE Trans. on Circuits and Systems–II: Express Beliefs*, 57:772–776, 2010.

[70] A. Mariscotti. Analysis of the DC-link current spectrum in voltage source inverters. *IEEE Trans. on Circuits and Systems*, 49:484–491, 2002.

[71] C. Marouchos, M.K. Darwish, and M. El-Habrouk. New mathematical model for analysing three-phase controlled rectifier using switching functions. *IET Power Electron.*, 3:95–110, 2010.

[72] B. P. McGrath. *Topologically independent modulation of multilevel inverters*. PhD thesis, Monash University, 1997.

[73] B. P. McGrath and D. G. Holmes. Multicarrier PWM strategies for multilevel inverters. *IEEE Trans. on Ind. Electr.*, 49:858–867, 2002.

[74] B. P. McGrath and D. G. Holmes. A general analytical method for calculating inverter DC-link current harmonics. *IEEE Trans. on Ind. App.*, 45:1851–1859, 2009.

[75] N. Mohan, W. P. Robbins, and T. M. Undeland. *Power Electronics: Converters, Applications and Design.* John Wiley and Sons, 3rd edition, 2003.

[76] T. Mouton and B. Putzeys. Understanding the PWM nonlinearity: single sided modulation. *IEEE Trans. on Power Electr.*, 99, 2011. Accepted for publication.

[77] J. F. Moynihan, M. G. Egan, and J. M. D. Murphy. Theoretical spectra of space-vector modulated waveforms. *IEE Proc.-Electr. Power App.*, 145:17–24, 1998.

[78] Y. Murai, T. Watanabe, and H. Iwasaki. Waveform distortion and correction circuit for PWM inverters with switching lag-times. *IEEE Trans. on Ind. App.*, IA-23:881–886, 1987.

[79] K. M. Muttaqi and M. E. Haque. Electromagnetic interference generated from fast switching power electronic devices. *International Journal of Innovations in Energy Systems and Power*, 3:19–26, 2008.

[80] A. Nabae, I. Takahashi, and H. Akagi. A new neutral-point-clamped PWM inverter. *IEEE Trans. on Ind. App.*, IA-17:518–523, 1981.

[81] J. W. Nilsson and S. Riedel. *Electronic Circuits*, volume 7. Prentice Hall, 2004.

[82] R. O-Hayre, S-W. Cha, W. Colella, and F. B. Prinz. *Fuel Cell Fundamentals.* John Wiley and Sons, 2nd edition, 2009.

[83] M. Odavic, M. Sumner, P. Zanchetta, and J. C. Clare. A theoretical analysis of the harmonic content of PWM waveforms for multiple-frequency modulators. *IEEE Trans. on Power Electr.*, 25:131–141, 2010.

[84] The Institution of Engineering and Technology. *Requirements for Electrical Installations: BS 7671:2008.* IET, 17th edition, 2008.

[85] C-T. Pan, C-M. Lai, and Y-L. Juan. Output current ripple-free PWM inverters. *IEEE Trans. on Circuits and Systems – II*, 57:823–827, 2010.

[86] Young-Wook Park, Dong-Choon Lee, and Jul-Ki Soek. Spectral analysis of DC link ripple currents in three-phase AC/DC/AC PWM converters feeding AC machines. In *The 27th Annual Conf. of IEEE Ind. Electr. Society*, pages 1055–1060, 2001.

[87] C. Pascual. *All-digital audio amplifier.* PhD thesis, University of Illinois, 2000.

[88] C. Pascual, Z. Song, P. T. Krein, D. V. Sarwate, P. Midya, and W. J. Roeckner. High-fidelity PWM inverter for digital audio amplification: spectral analysis, real-time DSP implementation, and results. *IEEE Trans. on Power Electr.*, 18:473–486, 2003.

[89] D. C. Pham, S. Huang, and K. Huang. Modelling and simulation of current source inverters with space vector modulation. In *Internation Conference on Electrical Machines and Systems (ICEMS)*, October 2010.

[90] M. A. Pinsky. *Introduction to Fourier Analysis and Wavelets.* American Mathematical Society, 2009.

[91] H. Polinder, F. F. A. van der Pijl, G-J. de Vilder, and P. J. Tavner. Comparison of direct-drive and geared generator concepts for wind turbines. *IEEE Trans. on Energy Conversion*, 21:725–733, 2008.

[92] IEEE Standards Information Network/IEEE Press. *The Authoritative Dictionary of IEEE Standards Terms (IEEE 100).* IEEE, 7th edition, 2000.

[93] T. Reiter, D. Polenov, H. Pröbstle, and H-G Herzog. PWM dead-time optimisation method for automotive multiphase DC/DC-converters. *IEEE Trans. on Power Electr.*, 25:1604–1614, 2010.

[94] F. Renken. Analytic calculation of the DC-link capacitor current for pulsed three-phased inverters. In *Proc. 11th Int. Conf. Power Elec. Motion Control*, 2004.

[95] J. Rodriguez, J. S. Lai, and F. Z. Peng. Multilevel inverters: A survey of topologies, controls, and applications. *IEEE Trans. on Ind. Electr.*, 49:724–738, 2002.

[96] J. D. Ryder. *Electronic Fundamentals and Applications.* Pitman, 4th edition, 1970.

[97] R. Shan, X. Xiao, Z. Yin, and Q. Liu. Compensation strategy of switching dead-time effect based on frequency domain model. In *IEEE Conference on Industrail Electronics and Applications (ICIEA)*, June 2010.

[98] K. Singh. *Engineering Mathematics Through Applications.* Palgrave Macmillian, 2nd edition, 2011.

[99] Z. Song and D. V. Sarwate. The frequency spectrum of pulse width modulated signals. *Signal Processing*, 83:2227–2258, 2003.

[100] E. M. Stein and G. Weiss. *Introduction to Fourier Analysis on Euclidean Spaces.* Princeton University Press, 1971.

[101] J. K. Steinke. Switching frequency optimal PWM control of a three-level inverter. *IEEE Trans. on Power Electr.*, 7:487–496, 1992.

[102] D. S. Stephens. Lightweight aircraft transformers. *Transactions of the American Institute of Electrical Engineers*, 68:1073–1078, 1949.

[103] N. Storey. *Electronics: A Systems Approach.* Prentice Hall, 4th edition, 2009.

[104] S. Y. Suh. Pulse width modulation for analog fiber-optic communications. *IEEE Journal of Lightwave Technology*, LT-5:102–112, 1987.

[105] K. T. Tang and E. G. Friedman. Delay and pwoer expressions characterizing a CMOS inverter driving an RLC load. In *IEEE International Symposium on Circuits and Systems*, May 2000.

[106] J. A. Taufiq and J. Xiaoping. Fast accurate computation of the DC-side harmonics in a traction VSI drive. *IEE Proc.*, 136:176–187, 1989.

[107] R. Wang, K. Roy, and C-K. Koh. Short-circuited power analysis of an inverter driving an RLC load. In *IEEE International Symposium on Circuits and Systems*, May 2001.

[108] Y. Wang, Z. Lu, H. Wen, and Y. Wang. Dead-time compensation based in the inproved space vector modulation strategy for matrix converter. In *IEEE Power Electronics Specialists Conference*, June 2005.

[109] G. N. Watson. *A Treatise on the Theory of Bessel Functions*, volume 2. Van Nostrand, New York, 2006.

[110] A. Williams. *Microcontroller Projects with Basic Stamps*. Cmp Books, 1999.

[111] C. M. Wu, Wing hong Lau, and H. S. Chung. Analytical techniques for calculating the output harmonics of an H-bridge inverter with dead time. *IEEE Trans. on Circuits and Systems*, pages 617–627, 1999.

[112] J. Yu, M. T. Tan, S. M. Cox, and W. L. Goh. Time-domain analysis of intermodulation distortion of closed-loop class D amplifiers. *IEEE Trans. on Power Electr.*, 99, 2011. Accepted for publication.

[113] J. Yu, M. T. Tan, W. L. Goh, and S. M. Cox. A dual feed-forward carrier modulated 2nd-order class-D amplifier with improved THD. *IEEE Trans. on Circuits and Systems II: Express Beliefs*, 2012. Accepted for publication.

[114] K. Zhou and D. Wang. Relationship between space-vector modulation and three-phase carrier-based PWM: A comprehensive analysis. *IEEE Trans. on Ind. Electr.*, 49:186–196, 2002.